Misalignment Insensitive Wireless Power Transfer System for Powering Implanted Biomedical Devices

A Thesis Report Submitted to
Indian Institute of Technology Ropar
in Partial Fulfilment of the Requirements for the
Degree of

DOCTOR OF PHILOSOPHY

by

Vivek Kumar Srivastava

2019EEZ0027

under the guidance of

Dr. Ashwani Sharma

Department of Electrical Engineering

Indian Institute of Technology Ropar

Rupnagar-140001, Punjab, India

May 2024

Dedicated to my Parents, Brother, Wife, and Supervisor.

Declaration of Originality

I hereby declare that the work which is being presented in the thesis entitled **Misalignment Insensitive Wireless Power Transfer System for Powering Implanted Biomedical Devices** has been solely authored by me. It presents the result of my own independent investigation/research conducted during the time period from December 2019 to April 2024 under the supervision of Dr. Ashwani Sharma, Assistant Professor, Indian Institute of Technology, Ropar. To the best of my knowledge, it is an original work, both in terms of research content and narrative, and has not been submitted or accepted elsewhere, in part or in full, for the award of any degree, diploma, fellowship, associateship, or similar title of any university or institution. Further, due credit has been attributed to the relevant state-of-the-art and collaborations (if any) with appropriate citations and acknowledgments, in line with established ethical norms and practices. I also declare that any idea/data/fact/source stated in my thesis has not been fabricated/ falsified/ misrepresented. All the principles of academic honesty and integrity have been followed. I fully understand that if the thesis is found to be unoriginal, fabricated, or plagiarized, the Institute reserves the right to withdraw the thesis from its archive and revoke the associated Degree conferred. Additionally, the Institute also reserves the right to appraise all concerned sections of society of the matter for their information and necessary action (if any). If accepted, I hereby consent for my thesis to be available online in the Institute's Open Access repository, inter-library loan, and the title & abstract to be made available to outside organizations.

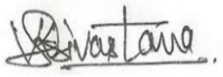

Signature

Name: Vivek Kumar Srivastava
Entry Number: 2019EEZ0027
Program: Doctor of Philosophy (Ph.D.)
Department: Electrical Engineering
Indian Institute of Technology Ropar
Rupnagar, Punjab 140001

Date: 06/05/2024

Acknowledgement

First and foremost, I express my gratitude to Lord Shri Sita-Ram for their blessings and unwavering support, which have empowered me to persevere and progress through all facets of my life. I extend heartfelt appreciation to my supervisor, Dr. Ashwani Sharma, for imparting vast knowledge and nurturing my passion for research. His invaluable emotional backing during the challenging phases of my initial research remains etched in my memory, and I am forever beholden to him. Additionally, I also extend my gratitude to the esteemed members of my doctoral committee, Dr. Ramachandra Sekhar, Dr. Brijesh Kumbhani, and Dr. Neha Sardana, for their perceptive feedback and suggestions aimed at enhancing the quality of my research endeavors. Furthermore, I appreciate the unwavering support and provision of essential resources from the Director, Deans, Heads of Departments, and faculty at the Indian Institute of Technology Ropar, which facilitated seamless progress in my research pursuits. My journey toward earning a Ph.D. was enriched by meaningful discussions with my esteemed senior and best friend, Dr. Ananth Bharadwaj, and I also want to thank him for his support. I extend my gratitude to my fellow members at the Antenna and Microwave Research lab - Sagar Jain, Suraj Gupta, Parul Rattanpal, Sundeep Kumar, Vikas Kumar Malav, Shivam Bansal, and Aman Raj, for their invaluable assistance and support throughout my Ph.D. journey. I owe a debt of gratitude to my parents, Mr. Rajesh Kumar Srivastava and Mrs. Deepa Srivastava, whose unwavering love and guidance have molded me into the person I am today, capable of navigating life's challenges. Special appreciation is extended to my younger brother, Mr. Abhishek Kumar Srivastava, for his steadfast support, which eased my path towards completing my Ph.D. Finally, I offer heartfelt thanks to my beloved wife, Shivangi Srivastava, for her boundless love and unwavering encouragement. Her dedication to reviewing and editing my thesis has been instrumental in my academic journey.

Certificate

This is to certify that the thesis entitled **Misalignment Insensitive Wireless Power Transfer System for Powering Implanted Biomedical Devices**, submitted by **Vivek Kumar Srivastava (2019EEZ0027)** for the award of the degree of **Doctor of Philosophy** of Indian Institute of Technology Ropar, is a record of bonafide research work carried out under my guidance and supervision. To the best of my knowledge and belief, the work presented in this thesis is original and has not been submitted, either in part or full, for the award of any other degree, diploma, fellowship, associateship or similar title of any university or institution.

In my opinion, the thesis has reached the standard fulfilling the requirements of the regulations relating to the Degree.

Signature of the Supervisor(s)
Dr. Ashwani Sharma
Department of Electrical Engineering
Indian Institute of Technology Ropar
Rupnagar, Punjab 140001
Date: 06/05/2024

Lay Summary

The primary focus of this thesis is to tackle diverse misalignment challenges encountered in wireless charging for biomedical implant devices. To achieve this objective, the scholar harnesses the potential of magnetic field-forming techniques to analyze and develop multiple transmitter and receiver coils. These coils not only rectify misalignment issues but also streamline circuit complexity and cost. As a pioneering contribution to the research field, the researcher undergoes an evolutionary process and explores various field-forming approaches targeting different misalignment scenarios. He designed multiple transmitter antennas to implement the investigated fields and subsequently introduced an innovative antenna capable of mitigating all potential misalignment challenges using a single transmitter antenna. Furthermore, the researcher delves into receiver coil design, surpassing existing literature studies by effectively addressing misalignment problems.

Acronyms

2−D Two Dimensional

3−D Three Dimensional

AC Alternating Current

AM Amplitude Modulation

AR Axial Ratio

DSB-SC Double-Sideband Suppressed-Carrier

DSO Digital Storage Oscilloscope

EM Electromagnetic

EP Evolutionary Process

FDA Frequency-Divisional Approach

H-field Magnetic-field

HFSS High Frequency Structure Simulator

MPT Microwave Power Transfer

MRC Magnetic Resonance Coupling

NF Near-Field

PTE Power Transfer Efficiency

PU Percentage Uniformity

RMS Root Mean Square

Rx Receiver

Rxs Receivers

SNR Signal-to-Noise Ratio

TDA Time-Divisional Approach

TDM Time-Division Multiplexing

Tx Transmitter

Txs Transmitters

VNA Vector Network Analyzer

WPT Wireless Power Transfer

Abstract

Wireless power transfer (WPT), a concept dating back to Nikola Tesla's innovations over a century ago, has recently gained increased attention, especially in biomedical realms like charging pacemakers, wireless endoscopic capsules, neural and cochlear implants, retinal prostheses, etc. Despite its flexibility, safety, and aesthetics advantages, practical WPT systems encounter challenges, notably misalignment between transmitter (Tx) and receiver (Rx) coils in biomedical implants. This thesis proposes a solution using field-forming techniques to mitigate misalignment issues in Tx design. Additionally, it explores optimizing Rx antennas to efficiently capture the magnetic field generated by conventional Tx setups, addressing misalignment problems in biomedical implants and other applications.

The thesis is structured into eight chapters. In Chapter 1, the fundamentals of the near-field WPT system are explored, encompassing a discussion on various potential research challenges inherent to the WPT system. Moreover, this chapter identifies the most important issue, which forms the focal point of this thesis. It also undertakes an intensive investigation of existing solutions available in the literature. Concurrently, Chapter 2 provides the mathematical background essential for analyzing and modelling WPT systems employing field-forming techniques. This chapter outlines the closed-form equations for conventionally used coil structures and defines the various design parameters. Meanwhile, Chapter 3 focuses on establishing a mathematical framework for examining 3−D rotating H-fields, with particular emphasis on mitigating angular misalignment problems, notably in the context of charging biomedical implants. In contrast, Chapter 4 presents the inception of a novel methodology, amalgamating traditional field-forming techniques with switching control to obtain an orientation-insensitive WPT system. This method necessitates only a single sinusoidal source instead of the multiple modulated sources requisite in the traditional 3−D rotating H-field method. Subsequently, Chapter 5 introduces a magnetic localization method tailored for tracking both the position and orientation of a mobile receiver employed in biomedical implants. A thorough investigation draws a comparison between the existing technique centered on frequency-divisional approaches and a novel time-divisional approach aimed at mitigating circuit complexity and system cost. Chapter 6 marks an integration of previously proposed localization techniques with magnetic beamforming to address diverse misalignment challenges using a single Tx antenna, an innovative approach unexplored in near-field WPT applications. Here, a machine-learning model is adopted to localize the Rx, while particle swarm optimization is employed to effectively shape the desired magnetic beam. Employing a single excitation source and switching circuitry, the proposed Tx is energized, thus reducing circuit complexity and system cost. Finally, Chapter 7 introduces a novel Rx structure optimized to harness both longitudinal and lateral field components effectively for addressing misalignment issues. The proposed Rx is realized using multi-layer PCB technology, which encapsulates all circuit elements within the antenna structure, making it a compact, robust, and cost-effective solution poised as an ideal option for wirelessly

powering biomedical implants and wearable devices. Furthermore, a use case is proposed for other applications, such as drone charging. Finally, Chapter 8 concludes the thesis and explores future development avenues to enhance proposed methodologies.

Keywords: 3−D polarization; angular misalignment; coil; lateral misalignment; localization; longitudinal misalignment; magnetic beam forming; magnetic field forming; magnetic resonance coupling; multi-coil antenna; wireless power transfer.

List of Publications

OUTCOME FROM THIS THESIS

Patent

Patent−1

V. K. Srivastava and A. Sharma, **"TITLE: POWER TRANSFER SYSTEM AND METHOD FOR OPTIMIZING MISALIGNMENT FACTORS IN THEREOF."** (Patent filed with Indian patent office on 03-04-2022: Application No. 202211020100)

Patent−2

V. K. Srivastava, and A. Sharma, **"TITLE: STEERABLE MAGNETIC BEAM FORMING FOR BIOMEDICAL IMPLANTS."** (Patent filed with Indian patent office on 16/07/2024: Application No. 202411054346)

Transactions/Journal

Article−1

V. K. Srivastava, A. Ahmad and A. Sharma, "A Machine Learning Assisted Localization and Magnetic Field Forming for Wireless Powering of Biomedical Implant Devices," submitted in *IEEE Transactions/Journals.*

Article−2

V. K. Srivastava and A. Sharma, "An Optimized Switching Integrated Transmitter Pad for Generating Orthogonal H-Field Components to Localize Implanted Devices," in *IEEE Journal of Electromagnetics, RF and Microwaves in Medicine and Biology*, doi: 10.1109/JERM.2024.3409423.

Article−3

V. K. Srivastava and A. Sharma, "A Coil Rectenna Array Design to Harvest All H-Field Components for Lateral Misalignment Tolerant Wireless Powering of Bio-Medical Implant Devices," in *IEEE Journal of Electromagnetics, RF and Microwaves in Medicine and Biology*, doi: 10.1109/JERM.2024.3351751.

Article−4

V. K. Srivastava and A. Sharma, "A Planar Switching Integrated Quadrant Coil Antenna to Form Widespread Switched Polarized H-Field for Misalignment Resilient WPT System," in *IEEE Transactions on Antennas and Propagation*, vol. 70, no. 11, pp. 10294-10303, Nov. 2022, doi: 10.1109/TAP.2022.3195554.

Article−5

V. K. Srivastava, A. Bharadwaj and A. Sharma, "A Multicoil Array Transceiver Antenna Design for Touchless Hygienic Artificial Human Interfacing," in *IEEE Transactions on Antennas and Propagatio*n, vol. 70, no. 10, pp. 8911-8921, Oct. 2022, doi: 10.1109/TAP.2022.3177534.

Article−6

V. K. Srivastava and A. Sharma, "Switched Polarized H-Field Forming Using a Planar

Switchable Double-Dumbbell Coil Antenna for Orientation-Oblivion Wireless Power Transfer," in *IEEE Transactions on Antennas and Propagation*, vol. 70, no. 6, pp. 4234-4242, June 2022, doi: 10.1109/TAP.2022.3140499.

Article–7

V. K. Srivastava, A. Sharma, and A. Bharadwaj, "A Planar Distributed Multicoil Antenna to Generate 3-D Ellipsoidally Polarized H-Field for Angular Misalignment Tolerant WPT System," in *IEEE Transactions on Antennas and Propagation*, vol. 70, no. 4, pp. 2969-2978, April 2022, doi: 10.1109/TAP.2021.3137477.

Article–8

V. K. Srivastava and A. Sharma, "Optimized 3-D Polarized H-Field Forming for Orientation-Insensitive Wireless Power Transfer Systems," in *IEEE Transactions on Antennas and Propagation*, vol. 69, no. 8, pp. 4999-5007, Aug. 2021, doi: 10.1109/TAP.2021.3060140.

Article–9

A. Sharma and **V. K. Srivastava**, "A Switched Planar Multicoil Transmitter Antenna Designed With Nonuniform H-Field Forming for Small Device Localization," in *IEEE Transactions on Antennas and Propagation*, vol. 70, no. 11, pp. 10261-10269, Nov. 2022, doi: 10.1109/TAP.2022.3195449.

Conference Proceeding

Article–1

V. K. Srivastava, A. Bharadwaj and A. Sharma, "A Planar Distributed Receiver Coil Antenna Array to Encapsulate Vertical and Lateral H-Fields for Drone Wireless Charging," 2023 17^{th} *European Conference on Antennas and Propagation (EuCAP)*, Florence, Italy, 2023, pp. 1-5, doi: 10.23919/EuCAP57121.2023.10133370.

Article–2

V. K. Srivastava, S. Kumar and A. Sharma, "3D Polarized Field-Forming for Mitigation of Angular Misalignment Problem in Microwave Power Transfer Systems," 2021 *IEEE* 19^{th} *International Symposium on Antenna Technology and Applied Electromagnetics (ANTEM)*, 2021, pp. 1-2, doi: 10.1109/ANTEM51107.2021.9518942.

Article–3

V. K. Srivastava, A. Sharma and A. Bharadwaj, "A Magnetic Resonance Coupling Based Touchless Pad for Human-Computer Interfacing," 2020 IEEE 15^{th} *International Conference on Industrial and Information Systems (ICIIS)*, 2020, pp. 601-605.

OTHER COLLABORATIVE WORK

Patent–1

A. Bharadwaj, **V. K. Srivastava**, A. Sharma, and C. C. Reddy, **"TITLE: DUAL-MODE ANTENNA WITH NON-UNIFORM COIL ARRAY FOR WIRELESS POWER TRANSMISSION AND METHOD THEREOF."** (Patent

filled with Indian office on 25-03-2021: Application No. 202111013157)

Transactions/Journal

Article−1

A. Bharadwaj, **V. K. Srivastava**, A. Sharma and C. C. Reddy, "A Tilted-Orthogonal Receiver Coil Antenna to Improve Misalignment Tolerance in WPT Systems," in *IEEE Transactions on Antennas and Propagation*, vol. 70, no. 12, pp. 11434-11441, Dec. 2022.

Article−2

A. Bharadwaj, **V. K. Srivastava**, A. Sharma and C. C. Reddy, "A Switchable Multicoil Antenna With Booster Coil to Improve Coverage in WPT Systems," in *IEEE Transactions on Antennas and Propagation*, vol. 70, no. 4, pp. 2490-2498, April 2022.

Article−3

A. Sharma, A. Bharadwaj and **V. K. Srivastava**, "An Analytical Framework to Design Planar Transmitting Array Antennas to Mitigate Lateral Misalignment in Wireless Power Transfer Systems," in *IEEE Transactions on Antennas and Propagation*, vol. 69, no. 9, pp. 5559-5569, Sept. 2021.

Conference Proceeding

Article−1

A. Bharadwaj, **V. K. Srivastava**, C. C. Reddy and A. Sharma, "Design Methodology of Near-Field Transmitter Coil Antenna for Maximizing Efficiency of the WPT System," 2023 *17th European Conference on Antennas and Propagation (EuCAP)*, Florence, Italy, 2023, pp. 1-5.

Article−2

A. Bharadwaj, **V. K. Srivastava**, A. Sharma and C. C. Reddy, "A Novel Trapezoidal Multi-Coil Antenna for Wireless Charging of Electric Vehicles," 2020 *IEEE 15th International Conference on Industrial and Information Systems (ICIIS)*, RUPNAGAR, India, 2020, pp. 13-17.

Article−3

R. Pudur and **V. K. Srivastava**, "Performance Study of Electronic Load Controller for Integrated Renewable Sources," 2018 *2nd International Conference on Electronics, Materials Engineering & Nano- Technology (IEMENTech)*, Kolkata, 2018, pp. 1-6.

Contents

List of Figures

List of Tables

Chapter 1

Introduction

1.1 Wireless Power Transfer and its Classification

The concept of Wireless Power Transfer (WPT) revolves around the transmission of electrical energy from a designated source to a respective load, all achieved without the reliance on any physical connection but rather through the utilization of electromagnetic waves. This process necessitates the utilization of two specifically designated antennas, known as transmitter (Tx) and receiver (Rx) coils. The Tx antenna is situated on the source end, while the Rx antenna is positioned at the load end, facilitating the seamless energy flow between the two points. This technology is further classified into three distinct categories based on the range of power transmission, namely far-field radiative, near-field radiative, and near-field reactive systems, as exemplified in Figure 1.1. Far-field radiative

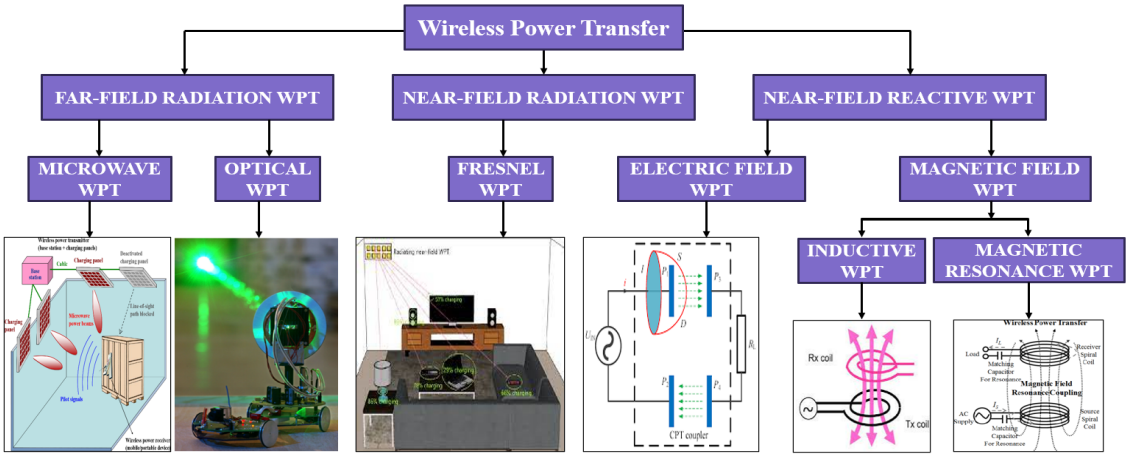

Figure 1.1: Classification of modern WPT Systems.

WPT embodies energy transmission for large distances by harnessing electromagnetic waves such as microwaves and laser beams. Despite its potential, this technology is in its initial stage primarily due to the perceived hazards posed by high-power microwaves and laser beams to living organisms. Conversely, near-field WPT (NF-WPT) can be bifurcated into radiative and reactive field regions. The radiative near-field, also known as the Fresnel region, involves the transmission of low-power microwaves through antennas, rendering it suitable for energizing biomedical devices, microsensor nodes, and low-power domestic appliances. Meanwhile, the reactive near-field comprises electric field-based and magnetic field-based WPT mechanisms adopted for medium to high-power applications. Capacitive

WPT relies on the electric field coupling between Tx and Rx metal plates, which raises safety concerns as the human body may become polarized under the influence of electric fields. Furthermore, nearby stray metal objects can significantly diminish the electric-field coupling between Tx-Rx coil metal plates, decreasing power transfer efficiency (PTE).

Conversely, magnetic field-based WPT operates on the principles of Faraday's law of electromagnetic induction, wherein the Tx-Rx coils are categorized into Inductive and Magnetic Resonant WPT systems. The notable benefits of employing a magnetic field-based WPT system include its provision of features such as high flexibility, convenience, aesthetic appeal, safety, and spatial liberation that are unattainable through traditional plugin charging methods. Additionally, the magnetic fields generated by Inductive WPT have minimal impact on living organisms, considering the predominant absence of magnetic properties in terrestrial life forms. Nonetheless, Inductive WPT encounters reduced coupling as the transfer distance extends from short to medium ranges, primarily attributed to significant magnetic flux leakage arising from the absence of resonance between Tx-Rx coils.

MIT researchers conducted a comprehensive study of a magnetic resonance coupling (MRC) based WPT system, with the goal of overcoming the mentioned challenges by improving the coupling Tx and Rx coils. The MRC approach involves compensating for the reactance of Tx-Rx coils through the utilization of an external capacitor network operating at a specific single-tone frequency. This innovative technique has emerged as the foremost effective and reliable method for wireless power transmission, garnering substantial attention in research endeavors, particularly within the scope of this thesis, due to its remarkable capability to efficiently transfer power across medium distances.

1.2 Potential Applications Building Block of NF-WPT

In light of this technological advancement, the potential applications employing NF-WPT for charging biomedical devices are meticulously showcased in Figure 1.2. This illustrative figure vividly portrays the contemporary charging schemes tailored for diverse biomedical applications, including but not limited to cardiac pacemakers, endoscopic capsules, implanted neural stimulators, prosthetic hands, cochlear implants, retinal prostheses, and smart arenas for biomedical experimentation.

Furthermore, the comprehensive blueprint of an NF-WPT system is meticulously presented in Figure 1.3, delineating the various research domains inherent in a typical WPT system. These encompass inverter and other power electronic converter design, impedance matching network for Tx and Rx antenna design, rectifier and load circuitry design, and coil antenna design. The associated losses in these areas are illustrated in Figure 1.4, highlighting that the majority of losses stem from coil design due to diminished coupling between Tx and Rx antennas. This underscores the need for innovative Tx-Rx antenna designs to mitigate reduced mutual coupling, thus serving as the driving force behind this research endeavor.

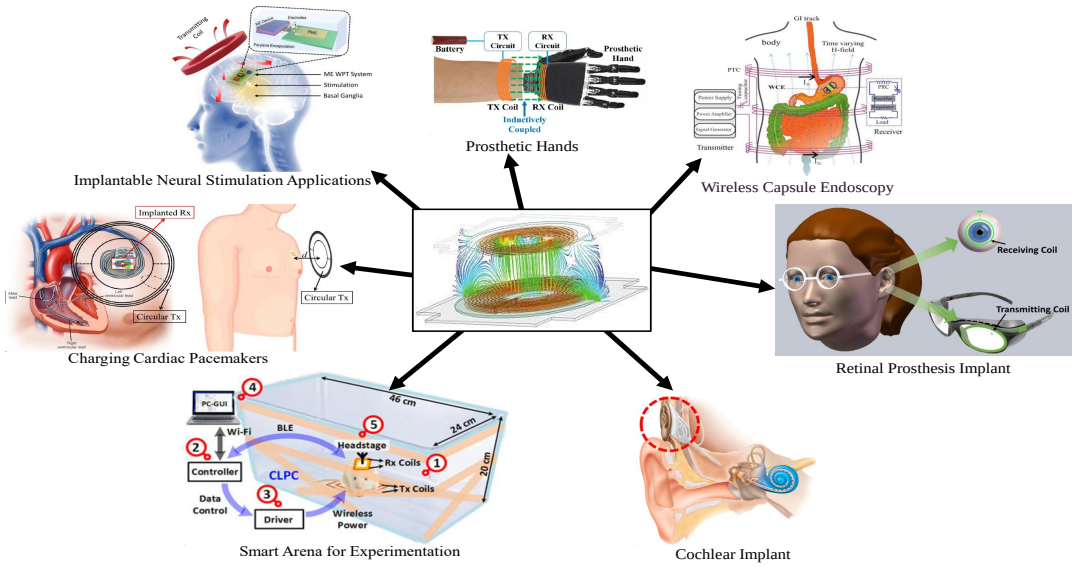

Figure 1.2: Potential applications of WPT in biomedical. [1, 2, 3, 4, 5, 6]

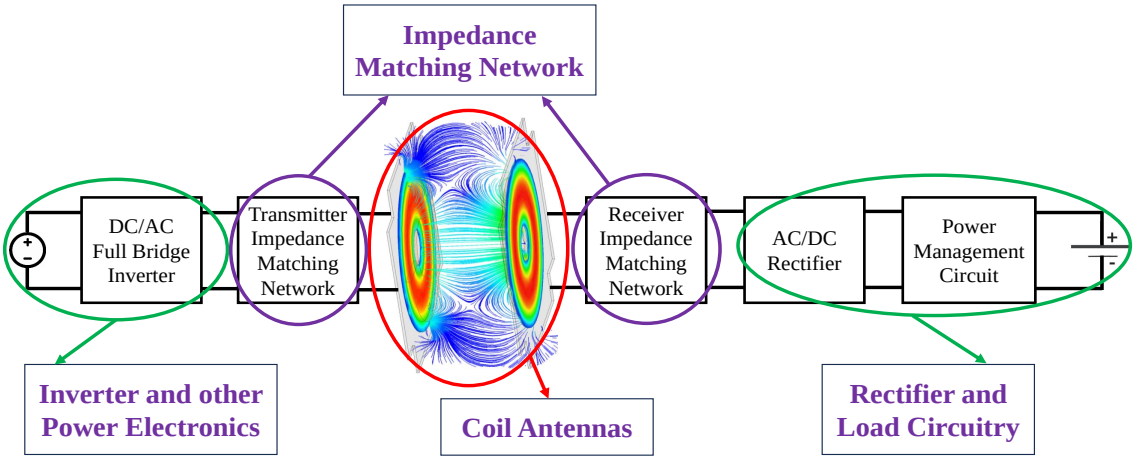

Figure 1.3: Building block of near-field WPT system.

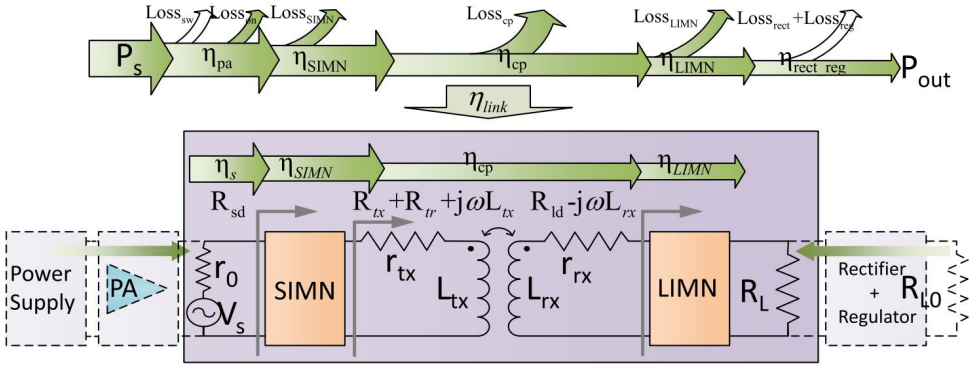

Figure 1.4: Losses associated with various research areas. [3]

1.3 Reason Behind Referring Near-Field Coils as Antennas

One question that may arise in the reader's mind is why near-field coils are referred to as antennas in this thesis. This ambiguity is addressed by examining the concept of a well-known Hertzian dipole antenna, which typically has an electrical length of $\frac{\lambda}{50}$. This length is similar to the dimensions of near-field coils. In a Hertzian dipole antenna, the current distribution is uniform. Nonetheless, this type of antenna is not widely used in practical applications because it is not very efficient at radiating energy and tends to generate more reactive fields. Building Hertzian dipole antennas can also be quite challenging. Interestingly, the drawbacks of Hertzian dipole antennas can be turned into advantages by finding applications that need low radiation efficiency and high reactive fields. Near-field coils with electrical lengths within the range of $\frac{\lambda}{50}$ showcase the desired characteristics. Since 2007, the development of near-field wireless charging technology has provided a practical use for these coils. Additionally, making near-field coils is relatively simple due to their operations at lower frequencies. Considering the shared characteristics between Hertzian dipole antennas and near-field coils, it is appropriate to use the term antenna when talking about Tx-Rx coils.

1.4 Problem encountered while charging medical devices

Charging biomedical implant devices poses a significant challenge due to misalignment between the Tx and implanted Rx components. Ideally, the Rx coil should align coaxially with the charging platform, i.e., Tx. However, practical implementations often deviate from this ideal scenario, resulting in misalignments categorized as angular, lateral, and longitudinal, as illustrated in Figure 1.5. These misalignments lead to reduced

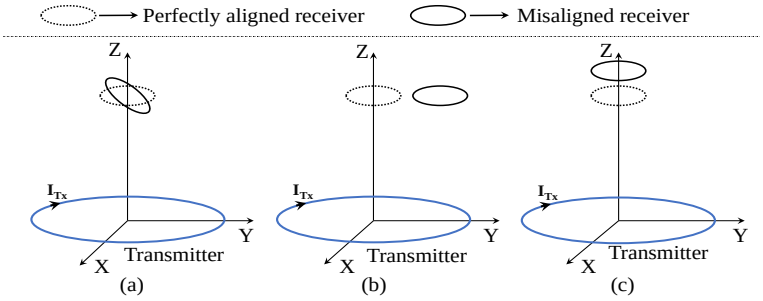

Figure 1.5: Possible misalignment existing between Tx and implanted Rx (a) angular, (b) lateral, (c) longitudinal.

coupling between the Tx and implanted Rx, consequently impacting PTE. Among these misalignment types, angular misalignment is particularly common in biomedical implant applications, occurring when the Rx coil rotates from its intended orientation. Conversely, lateral misalignment results from horizontal displacement of the Rx relative to the Tx, while longitudinal misalignment occurs when the Rx moves away from the Tx axis. Thus, the primary focus of this thesis is to mitigate these challenges by designing both Tx and

Rx antennas to optimize alignment and improve PTE.

1.5 Root Cause Behind the Misalignment Problem

The underlying cause of these misalignment issues stems from the lack of the necessary H-field component at the Rx location, which a conventional Tx typically generates. For instance, when the conventional circular coil Tx, as illustrated in Figure 1.5, is activated with excitation current I_{Tx}, the resulting H-field distribution at the Rx plane is depicted in Figure 1.6, which illustrates that the H_z component is present at the center of the Tx coil but absent at the edges. In contrast, the maximum values of the H_x and H_y components are found at the edges and absent at the center.

To illustrate how the absence of magnetic field components leads to misalignment issues, let us consider a simple scenario of angular misalignment in a typical WPT system. Initially, the Rx is positioned perfectly aligned at a distance of (0, 0, h) from the Tx, as depicted in Figure 1.7(a). In this setup, the area vector ($\mathbf{A}$) of the Rx is oriented along the Z-axis. Thus, only the H_z component of the H-field is sufficient to power up the Rx. However, in the presence of angular misalignment of the Rx coil, where the orientation of the Rx changes to $\theta = 45°$ as shown in Figure 1.7(b), the Rx coil captures both the H_y and H_z components. Nonetheless, due to the absence of the H_y component at the center of the Rx coil as depicted in Figure 1.6(b), only a reduced component of H_z will be present at the Rx, resulting in a variation in output power from the Rx. Furthermore, as the orientation of the Rx changes further to $\theta = 90°$ as presented in Figure 1.7(c), the Rx attempts to harness only the H_y component. However, the absence of this field component results in zero output power. This can also be exemplifies from Figure 1.8 under different misalignment cases. This underscores the fact that the output power obtained at the Rx depends solely on the misalignment problem and needs to be addressed to maintain consistent power delivery to the charging device.

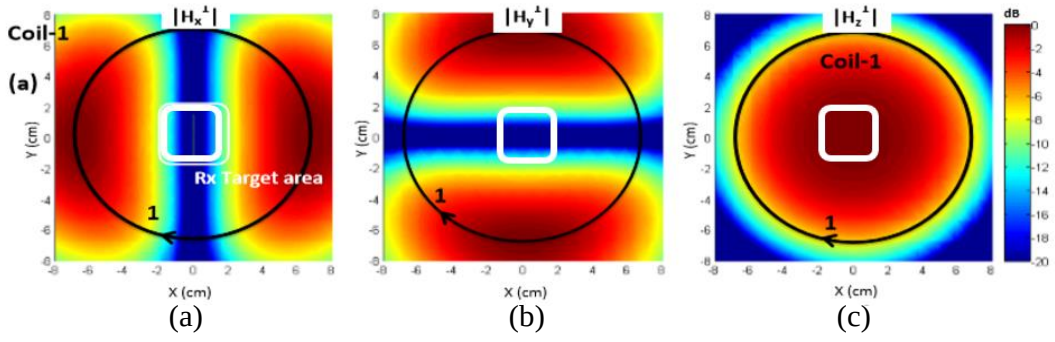

Figure 1.6: Magnetic field distribution from a conventionally adopted Tx. [7]

One potential solution to mitigate the mentioned misalignment issue is to generate three orthogonal H-field components (H_x, H_y, H_z) at all the lateral locations in the Rx plane. To achieve this, a newly engineered Tx is devised for powering the Rx irrespective of its position or orientation, as illustrated in Figure 1.9.

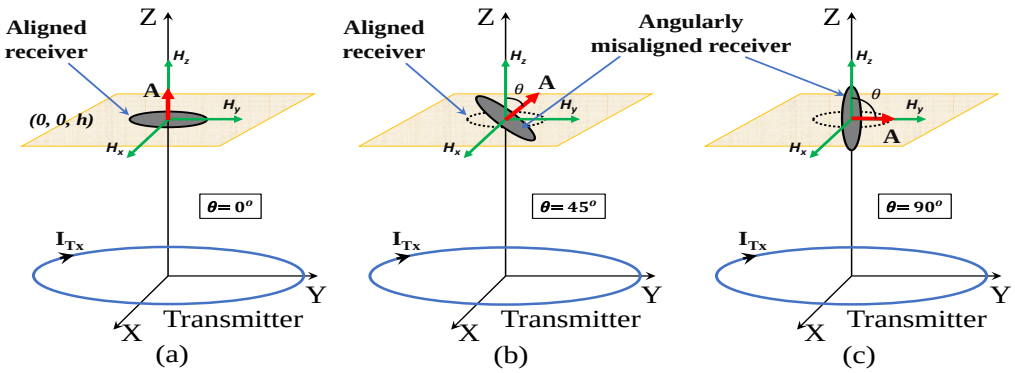

Figure 1.7: A simple case of angular misalignment between Tx and Rx (a) perfectly aligned ($\theta = 45°$), (b) misaligned ($\theta = 0°$), (c) misaligned ($\theta = 90°$).

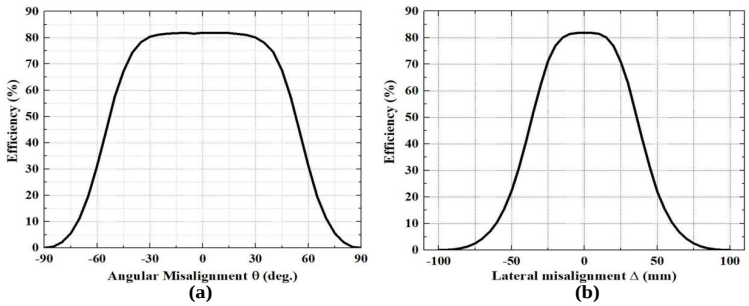

Figure 1.8: Performance degradation under the misalignment cases (a) angular, (b) lateral. [13]

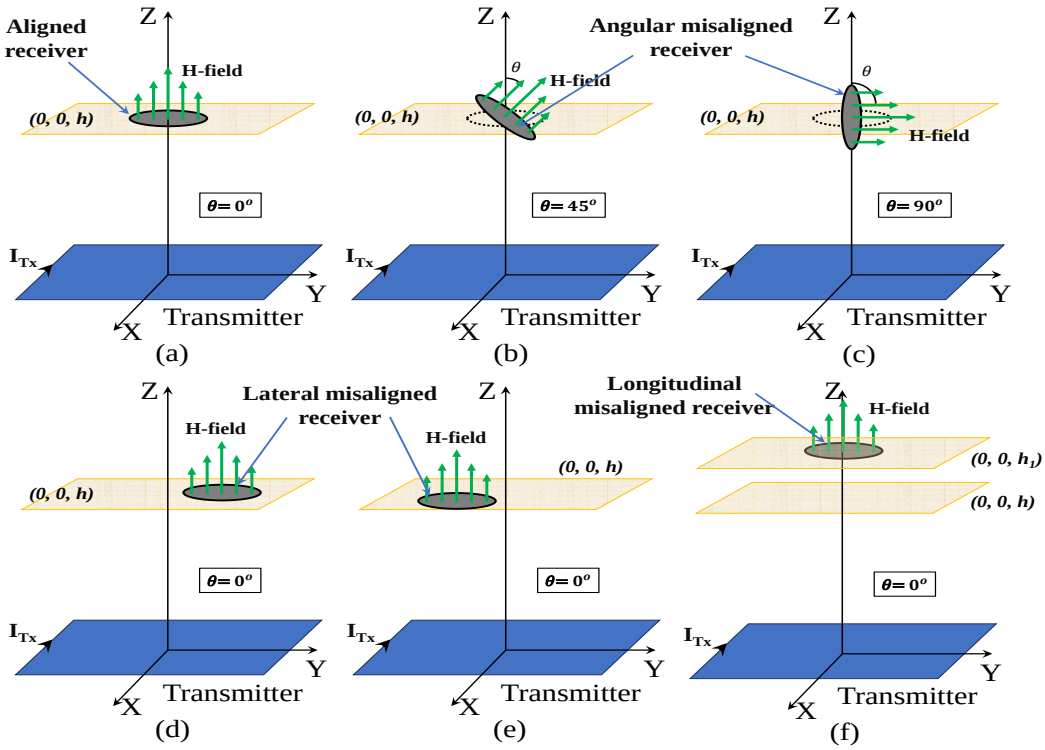

Figure 1.9: Possible solution for misalignment mitigation.

1.6 Literature Survey

Extensive research has been undertaken to thoroughly analyze the existing literature, encompassing a range of designs and methodologies, which have been meticulously organized into distinct clusters. These clusters outline different categories, beginning with field-forming transmitters (Txs) specifically engineered for WPT, followed by those tailored for localization purposes. Subsequently, there is an exploration of the integration of field-forming Txs with the localization Txs. Finally, the analysis concludes with a presentation of magnetic field harvesting Rx antennas designed for biomedical implants. Through this systematic approach, a comprehensive understanding of the various aspects of Tx design and functionality is attained, laying a robust foundation for further exploration and innovation in this field.

1.6.1 Field Forming Transmitter for Wireless Power Transfer

The primary challenge encountered in biomedical implant applications often revolves around mitigation of misalignment problems as discussed in the preceding chapter. Targeting solely the lateral misalignment problem, a mechanical arrangement integrated with sensing coils as shown in Figure 1.10(a) is proposed in [8] to re-align the Tx coil, resulting in a less reliable, less durable, and cost-ineffective solution [9]. Therefore, the

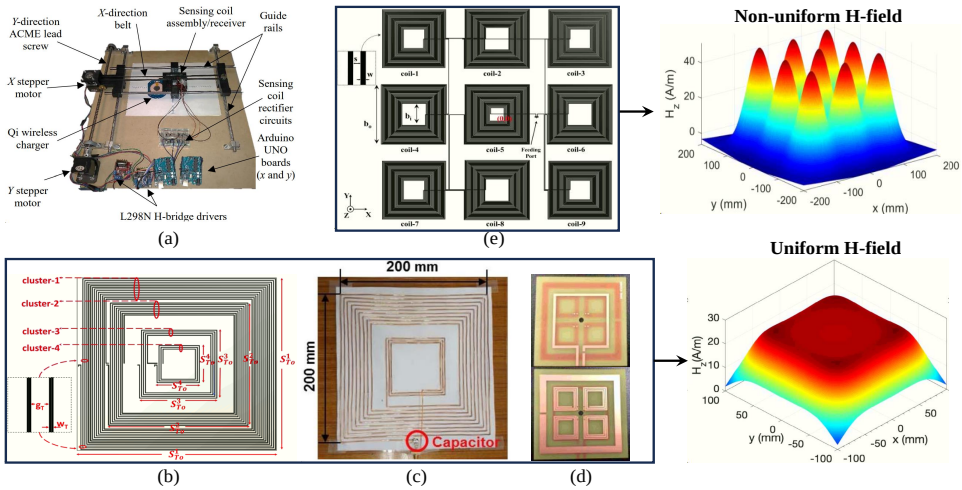

Figure 1.10: Solution proposed for mitigating lateral misalignment problems.

conventionally used Tx antennas were subsequently redesigned to generate a widespread uniform H-field distribution in the Rx plane. To accomplish this, various designs of the Tx antennas are available in the literature. For instance, non-uniformly distributed turn coil [10], asymmetrical coil [11], and resonator coil array [12] antennas as depicted in Figure 1.10(b,c,d) are designed to generate a widespread uniform H-field distribution. In contrast, a non-uniform H-field distribution generated from a Tx coil array [9] can also be exploited for the purpose illustrated in Figure 1.10(e). To emphasize that the immediately mentioned antennas are designed to target only the lateral misalignment while the angular misalignment problem is completely ignored. Therefore, these designs are unsuitable for applications where the angular movement of the Rx antenna is very likely.

Several literary works have been proposed to counter the angular misalignment problem for generating various combinations of H-field components at the Rx location. For instance, a 3−D complex Tx antenna structure, as shown in Figure 1.11(a) is presented in [13], but the misalignment problem is not completely eliminated. The Tx designs presented in [14]

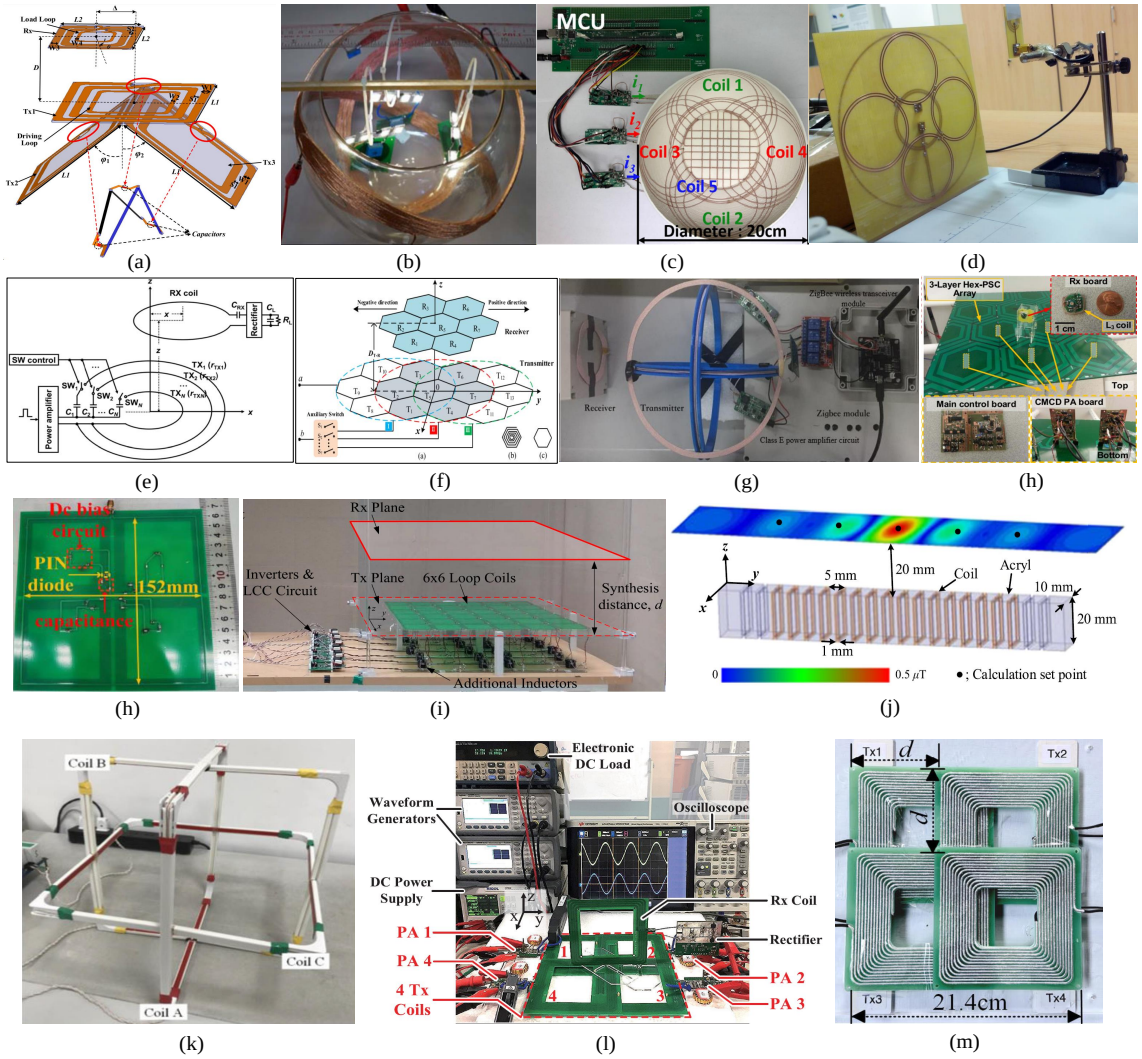

Figure 1.11: Field forming Txs for mitigating various misalignment problems.

consist of orthogonally placed coils having identical currents. However, the arrangement produces orthogonal H-field components to compensate for the reduction in flux linkage due to the Rx rotation. It generates a linearly polarized H-field in a resultant direction, hence, unable to mitigate the angular misalignment. In contrast, the Tx coils presented in [15, 16] are fed with currents having equal amplitudes but 90° phase difference to produce circularly polarized H-field. The oscillating H-field in two dimension (2−D) rotates in a plane and induces a consistent voltage in the Rx coil whose area vector direction is restricted in the same plane. Essentially, the circularly polarized H-field is able to resolve the angular misalignment problem but only for the Rx rotating in a specific plane. Similarly, [17] presents a study of 2−D H-field polarization. Therefore, investigation of the WPT system for 3−D H-field distributions is necessary.

We note here that the polarization is the main cause of the angular misalignment problem.

Therefore, to allow the Rx orientation at any angle, generating a rotating H-field covering all directions in 3−D is necessary. This can be achieved using the current control method [18] by feeding various coils of the Tx with different current waveforms. Amplitude Modulated (AM) signals (e.g., Double Side Band Suppressed Carrier (DSB-SC) signals) are used as excitation currents to realize rotating H-field in 3−D [18, 19] using three orthogonal shaped Tx structure, as depicted in Figure 1.11(b). However, a variation in PTE is observed with angular misalignment of the Rx in all the cases. The rotating H-field vector generated in [20] corresponds to a 3−D polarization depicting a spherical shape. Nevertheless, these presented structures have a 3−D spherical shape. Thus, the Rx is intended to hang at the center of the 3−D Tx, which is impractical for a real application.

To provide ease of Rx placement, a bowl-shaped Tx for charging small electronic devices, as provided in Figure 1.11(c) is proposed in [21, 22]. However, the field distribution generated by these 3−D Tx antennas is non-uniformly distributed and needs to be optimized to mitigate the angular misalignment problem. Moreover, being 3−D structured antennas, they could be more favorable for many applications and constitute an inherent difficulty for manufacturing. Therefore, a planar Tx antenna having advantages like simplicity, reliability, cost-effectiveness, and providing angular misalignment tolerance is sought [7]. Considering this, a twisted loop antenna with sub-coils of distributed diameter is proposed to achieve a uniform PTE for arbitrarily oriented Rx coil antennas in [23]. However, the design is unable to generate three orthogonal field components optimally. This implies that the angular misalignment problem persists in the design. In contrast, the authors in [7] have presented an H-field forming technique using a planar multicoil Tx antenna designed to address the angular misalignment problem as demonstrated in Figure 1.11(d). Though the planar two port Tx designed in [7] is able to produce three orthogonal H-field components, the feeding of two sinusoidal sources having 90° phase difference leads to the formation of a 2−D elliptically polarized H-field in the Rx region. This implies that a planar Rx, whose area vector is perpendicular to the plane of the 2−D rotating H-field, is unable to receive any power. Moreover, the utilization of multiple sources to generate the 2−D or 3−D polarized H-field inherently increase the circuit complexity. Thus a better and alternate approach is sought to completely mitigate the angular misalignment problem and serve as the first objective of this thesis. Moreover, time-domain switching could reduce circuit complexity compared to sophisticated modulated current-control methods. In this regard, integrating the field-forming technique with switching control appears to be a rousing approach that is minimally attended in the literature to achieve an orientation-insensitive WPT system.

Previously, the switching control has been explored by [24, 25] in conjunction with a Tx antenna to direct the H-field flux in the desired location while reducing the leakage in other places. For this purpose, [24] proposes a time-division multiplexing (TDM) approach to transfer power wirelessly for separately excited DC motor drives. Whereas, in [25], a TDM-based control is proposed to simultaneously track the power flow and efficiency in a multi-Rx WPT system. Similarly, in [26], a digital Tx antenna with several parallel

coils is proposed to address distance and lateral misalignment problems as depicted in Figure 1.11(e), whereas, switchable antenna structures are adopted as a hexagonal Tx coil array [27] for the lateral misalignment and illustrated in Figure 1.11(f). These works demonstrate the use of switching in the WPT system, however, the mitigation of angular misalignment is not targeted. In contrast, the angular misalignment problem is partially addressed by time-sharing controlled 3−D Tx proposed in [28] as shown in Figure 1.11(g) using a quasi-omnidirectional WPT system to detect and power the Rx coil optimally. Moreover, the mitigation of lateral misalignment is not targeted in the presented works. In contrast, a planar Tx coil antenna consisting of three hexagonal spiral overlapping layers as exhibiting in Figure 1.11(h) is designed to generate robust lateral and longitudinal fields for powering randomly oriented multiple Rx coils in [29]. However, the PTE is found inconsistent due to varying longitudinal field intensity for specific Rx coil orientations, and also, the antenna structure is very complex. Moreover, a high permittivity metamaterial slab inserted between the Tx and Rx antennas [30], however, the misalignment problems are partially addressed due to forming inadequate H-field distributions in the Rx plane. This demonstrates that the misalignment problem has yet to be resolved.

The previous studies indicate that the simultaneous mitigation of misalignment problems requires generating widespread uniform H-field components (for lateral misalignment) along with an optimal 3−D ellipsoidally polarized H-field (for angular misalignment) throughout the desired Rx plane. Forming such an intricate field distribution using conventional design methods is highly cumbersome. A field-forming antenna design with inherent switching control is an alternative approach to independently control over the three orthogonal H-field components. Thus, the requirement for mitigating the misalignment problems together reduces to generating the widespread distributions of the three H-field components in a switchable manner at the Rx plane. Hence, a new Tx design approach with simplified switching operation and the capability of generating an adequate field distribution is required to overcome both the misalignment problems simultaneously and is served as the second objective of this thesis.

To comprehensively mitigate all potential misalignments, i.e., angular, lateral, and longitudinal misalignment, a distinct approach to field forming is required. One potential solution to this challenge is directing the magnetic beam toward the intended Rx direction. Furthermore, shaping the magnetic beam in this manner also helps for mitigating the issue of significant flux leakage, commonly occurring in the conventional field forming techniques such as 3−D rotating H-field for angular misalignment mitigation and widespread distribution of H-field for lateral misalignment problem, as highlighted in previous studies. To accomplish the magnetic beam forming, two commonly utilized methods for directing the magnetic beam are passive and active control schemes [31]. The former relies on a low-reluctance magnetic core to guide the magnetic beam, while the latter involves regulating excitation currents for individual coils within the coil array. Focusing on the active control scheme, one technique embraces incorporating additional circuit components, such as variable capacitors or inductors in series, as demonstrated

in Figure 1.11(h,i) to manage the excitation phase delivered to the coils arrays and adjust the magnetic beam direction [32, 33, 34]. However, employing additional circuit components will disrupt the coil tuning. Alternatively, employing multiple excitation sources for powering the coil array offers another approach for constructing the magnetic beam. For instance, magnetic beam shaping in a single dimension by linearly arranging a group of coils and two-dimensional field shaping using a planar array of coils, shown in Figure 1.11(i,j) as presented in [35, 36] and [34], respectively. Nonetheless, these designs overlook the mutual coupling between adjacent coils, which can impact field-forming operations. Three-orthogonal coil Tx excited by three distinct sources as depicted in Figure 1.11(k) is proposed in [37], demonstrating effective field orientation control to address the coupling issue and ensure smooth field forming operation. However, the three-dimensional nature of Tx coils limits its applicability for charging biomedical implants. In response, a planar Tx coil array with overlapping coils is suggested in [38, 39] and demonstrated in Figure 1.11(l,m), utilizing multiple excitations to regulate current flow to the Tx coils. Furthermore, the methodology under discussion fails to address the issue of localizing a mobile Rx, a vital aspect to consider prior to deploying magnetic beams, especially in fields like biomedical implants and charging endoscopic capsules. Consequently, there is a need to explore a newly designed Tx that integrates both localization and shaping of magnetic beams to tackle all potential misalignments, which constitutes another objective of this thesis.

1.6.2 Field Forming Transmitter for Localization

Previous studies have addressed the misalignment problems by proposing various magnetic field-forming Tx antennas. Nevertheless, the presented structures suffer from enormous flux leakage once the Rx is settled down. As an alternate approach to mitigate flux leakage is to shape the desired magnetic beam directly at the Rx location. However, accurately determining the position and orientation of a moving Rx is essential before constructing a magnetic beam toward it. Therefore, the relevant literature on this topic is compiled and presented below.

Sensing the position remotely and tracking the movement is crucial for localizing the position of a moving object. Various techniques adopted for this purpose include vision-based [40, 41], mechanical sensor-based [40, 42], and magnetic field (H-field) based [43] sensing systems. The vision-based systems [44, 45] require a digital camera and complex data processing algorithms as demonstrated in Figure 1.12(a), which are susceptible to ambient conditions like background light, presence of objects, and mobility. Due to this, these systems have limitations of high cost, low latency, and low sensing accuracy. In contrast, the mechanical sensor-based systems [40, 46, 47, 48] impose wearable hand gloves comprising a variety of sensors such as bend, stretch, and inertial sensors that are less affected by ambient conditions as presented in Figure 1.12(b). However, a bulky data processing and communication unit is attached to the hand, posing significant discomfort. Besides this, the inherent problems associated with the sensors, such as the

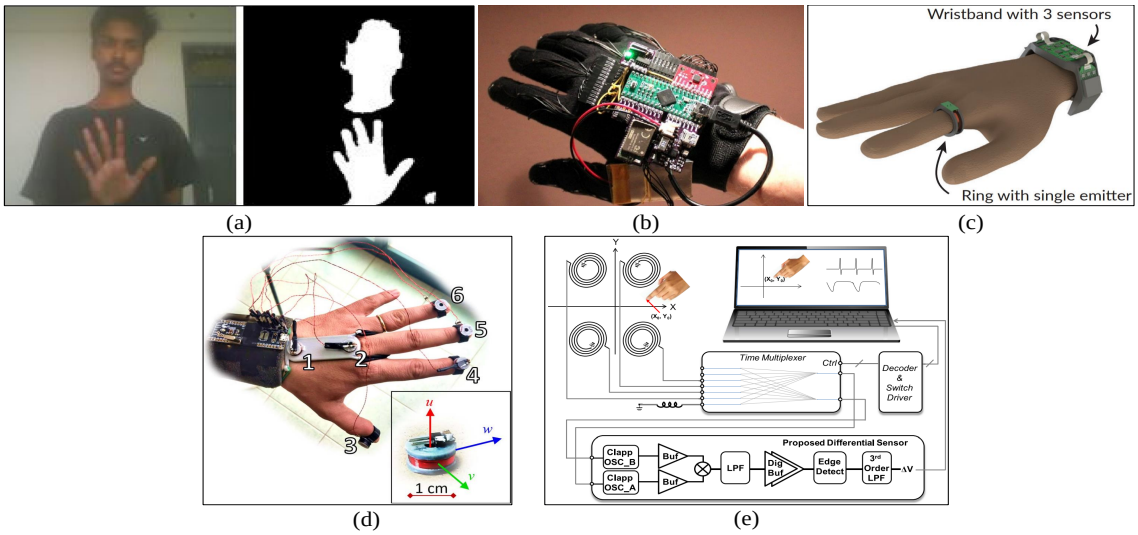

Figure 1.12: Prominent localization schemes proposed in literary works.

aging effect, inconsistent sensitivity, sluggish response, and incompatibility of rigid sensors with flexible gloves, make the sensor-based systems ineffective.

To avoid the aforementioned limitations, the H-field based sensing systems are adopted in which two approaches are considered, first: using permanent magnets and hall-effect sensors or sensing coils, second: exploiting MRC using coil antennas. In the first approach, the hall-effect sensor array or EM coils and permanent magnets are used as hand wearables, e.g., rings and wristbands, to track the hand movements [49, 50, 51] as shown in Figure 1.12(c). These systems have inconsistent accuracy due to the permanent magnets losing strength with time. Similarly, the hand tracking system proposed in [52] comprises magnetic nodes attached to all the fingertips given in Figure 1.12(d). Complex wired connections affixed on the user's hand are used to transfer the sensed data, which is again not user-friendly. To overcome this problem, the fingertip tracking system proposed in [53] uses no wearable but two probing coils located in the sensing platform to sense the change in impedance shift due to the presence of the user's finger as a dielectric presented in Figure 1.12(e). The highly complex circuitry and frequent calibration requirements are the system's limitations which render it as cost-ineffective solution. The need for frequent calibration can be avoided by adopting the second approach of an MRC-based system using coil antennas for localization purposes.

For instance, 2−coil MRC-based positioning systems are proposed to detect axial and rotatory movements of the shaft in [54, 55] and to detect the finger movements in [56]. These systems consist of a few spatially distributed coils embedded in a stationary Tx platform and a moving Rx coil attached to the hand finger whose output signals are processed for localization. Therefore, the data processing units are placed with the user's hand, resulting in user discomfort. Although the immediately mentioned systems utilize a 2−coil MRC-based technique for localization, they need to be optimized to exploit the full potential of the MRC approach. Moreover, the presented schemes are not targeting to simultaneously determining both the position and orientation is necessary for tracking

and tracing various applications including navigation of intra-body medical instruments (wireless endoscopy capsule), motion tracking, ubiquitous computing, virtual reality etc.

The magnetic localization technique is most popular for determining a moving object's position and orientation due to its high speed, accuracy, and simple realization for short ranges [57]. In principle, the magnetic localization techniques involve sensing the magnetic fields originating from an excitation source realized either by permanent magnets or coil antennas, which classifies the systems into two types: permanent magnet tracking and magnetic coil tracking [58, 59, 60]. Based on the former type, the object embedded with a permanent magnet is localized by capturing the generated fields using external systems like gradiometer [61], magnetic sensors [58], a cubical array of sensors [62], and planar sensor array [63] as demonstrated in Figure 1.13(a,b,c). Alternatively, the magnetic sensors can be embedded in the object [64, 65], and permanent magnets act as external sources. However, the permanent magnet-based systems are less reliable for tracking mobile objects due to interference from the earth's magnetic field and surrounding magnetic materials [66]. In contrast, the magnetic coil tracking systems are robust where specific frequency signals are generated by field excitation sources (coil antennas), filtered out by the Rx coil, and processed further for localization [57].

Various sensor systems exist in the literature to localize a planar Rx coil (single-axis magnetic dipole) integrated with the object. For instance, sensor units are developed consisting of multiple loop coils and gradiometers in [67, 68], three-bar antennas in [69], two orthogonal coils in [70], and three orthogonal coils in [71], as depicted in Figure 1.13(d,e,f,g), however, only the position in 1−D or 2−D is estimated. In [72], the

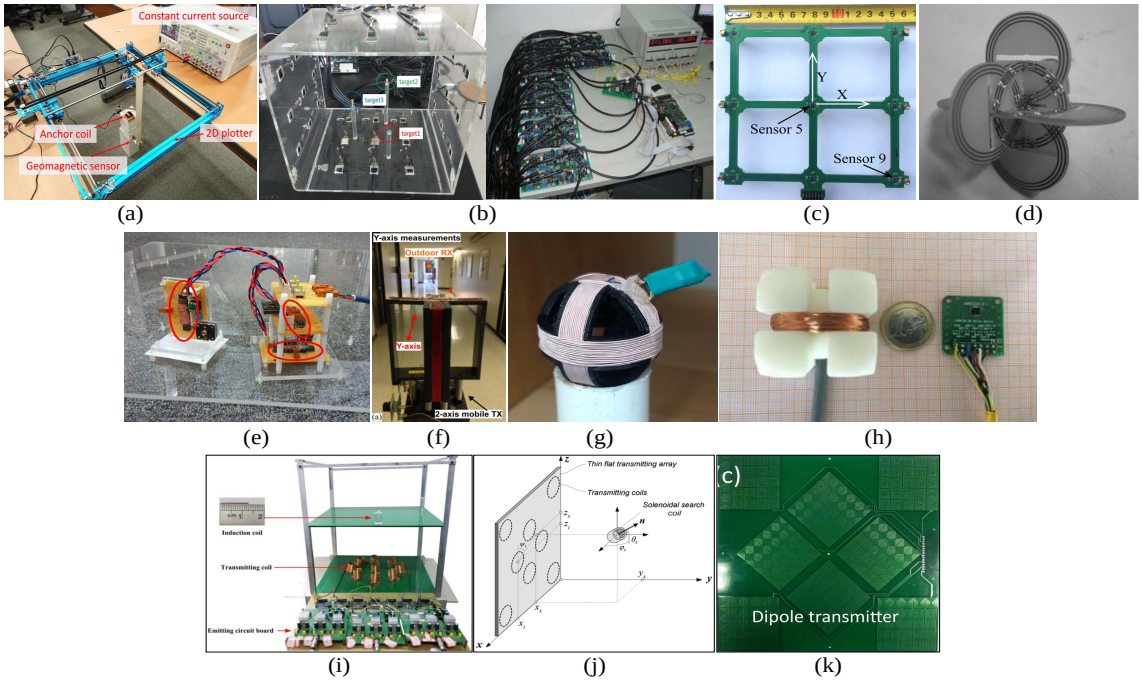

Figure 1.13: Various Txs and Rx designs for localizing both position and orientation of a Rx.

position and orientation are acquired using a uni-axial transmitting coil and a tri-axial

magnetometer sensor as shown in Figure 1.13(h). Similarly, a tetrahedron-shaped Tx consisting of six coils is used in [73] for this purpose. In [74], orthogonally placed Tx and Rx are presented to determine the range and orientation of the sensing object. The drawback of such systems is that the structure of Txs or receivers (Rxs) adopts 3−D shapes, while planar structures are preferred for ease of fabrication and convenience of space. As a result, the system consisting of a planar multi-coil Tx and a small planar Rx coil as a sensor embedded in the object is an appealing solution.

The planar multi-coil Tx designs comprising of a set of eight or more distributed coils are employed previously in [75, 76, 77, 78, 79] to monitor both position and orientation of the object containing a small Rx coil as demonstrated in Figure 1.13(i,j,k). These systems are based on the frequency-divisional approach in which all the Tx coils are driven simultaneously and excited with multiple frequency signals. At the Rx, multiple channels are demodulated, and various frequency components are extracted; this roots to shortcomings of this approach, such as high complexity due to the requirement of multiple frequency sources, inter-channel interference, and frequency mismatching [79]. Moreover, a costly and complex feeding network is required consisting of eight or more excitation circuits along with input ports [77, 79]. Similarly, a time-divisional approach that is adopted in [80] uses a large Tx array consisting of 64 coils excited sequentially; however, it requires 64 input ports and a highly complex feeding network. To address the limitations, a novel switched planar multi-coil Tx antenna with enhanced localization accuracy is aimed as the third objective of this thesis.

1.6.3 Integration of Localization and Wireless power transfer

Until now, the literature has primarily concentrated on developing individual Tx designs to address localization and wireless powering separately. However, to achieve efficient power transfer, it is imperative to address these challenges simultaneously. Targeting this, a bowl-shaped Tx antenna fed with time-controlled amplitude-modulated signals is presented in [81], which identifies the position and orientation of the Rx and delivers power in the intended direction. However, like the 3−D rotating H-field approach, these systems require multiple modulated sources, therefore, exhibit complex and cost-inefficient systems. Furthermore, no existing literary works have been found that concurrently tackle both of these issues. This indicates a substantial research opportunity in this field, which is why it has been adopted as a novel research area to be explored further in this thesis.

1.6.4 Magnetic Field Harvesting Receiver Antennas for Biomedical Implants

Until now, the emphasis has been on harnessing the capabilities of the Tx and designing its structure to address misalignment challenges. However, the potential of the Rx has yet to be explored. Therefore, the subsequent objective is to create an innovative Rx capable of utilizing all the H-field components generated by a conventional Tx. The currently using planar Rx coil antenna only captures the H-field component perpendicular

to its cross sectional area while neglecting others, resulting in sub optimal utilization of available H-field components. Consequently, these Rx structures are underutilized and require an engineered Rx coil structure to effectively harness all the H-field components. A few state-of-the-art works emphasize the Rx design to enhance the WPT performance. For instance, in [82], a Rx antenna with three orthogonal coils is presented, whereas [83] proposed two series-connected perpendicular bipolar coils along with a unipolar Rx coil for simultaneous power and data transmission as shown in Figure 1.14(a,b). Nevertheless, the presented designs mainly target the reduction in cross-talk between the coil antennas to transmit data effectively, and no focus is placed on the misalignment problem. In contrast, [84] and [85] presented a DDQ-shaped pickup coil and a Rx coil array, respectively, as depicted in Figure 1.14(c) for electric vehicle applications, which are unsuitable for biomedical implants and wearable device applications.

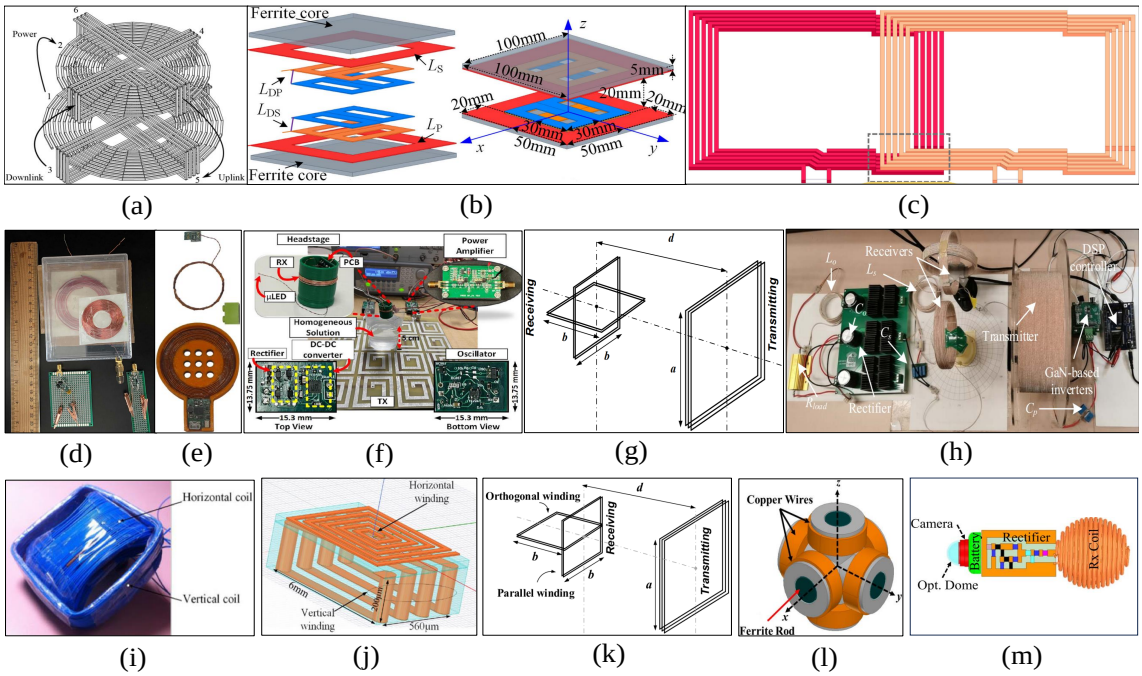

Figure 1.14: Prominent Rx designs present in literary works.

Targeting specifically biomedical devices, a planar rectifier Rx is adopted in [86, 87] as presented in Figure 1.14(d,e) to facilitate power transfer to an implanted device. Similarly, a 3−D printed cylindrical Rx as shown in Figure 1.14(f), is introduced in [88] to power a freely moving rodent. Nevertheless, these solutions do not specifically address misalignment issues. Although the impact of misalignment between loosely coupled coils is analyzed in [89], a mitigation strategy is not provided. Recognizing this gap, several Rx coil structures have been put forth in the existing literature to address these challenges. For instance, two equal orthogonally placed Rx coils are reported at the Rx side for capturing the two orthogonal H-field components in [90, 91], whereas, two non-identical orthogonal Rx coils are presented in [92, 93] to harness power from the Tx coil as demonstrated in Figure 1.14(g,h,i,j), respectively. Since the two orthogonal coils partially encapsulate

the three H-field components, a significant variation results in the misalignment output response. To counter this problem, a T-shaped Rx structure is presented in [94] that contains non-identical turns in two orthogonal Rx coils, in contrast, a 3−D cross-type Rx is proposed in [95] as given in Figure 1.14(k,l). Similarly, in [96], a spherical-shaped Rx is presented for implantable devices and shown in Figure 1.14(m). However, these 3−D Rx structures severely limit their applications where planar Rx antennas are sought. Thus, as far as the authors are concerned, the complete mitigation of the lateral misalignment problem with a small planar Rx has yet to be achieved in state-of-the-art designs. Although a few literary works such as [90, 92, 93] tried to address the problem, mitigation is accomplished along a single direction of misalignment. This motivates the proposed work to investigate a compact coil rectenna array design to harness the three orthogonal H-field components generated by the conventional Tx coil to mitigate the lateral misalignment problem.

1.7 Thesis Objective

Based on the literature survey discussed above, the main challenges that need to be tackled include eliminating the 3−D structure, handling multiple excitations, reducing significant flux leakage, localize the Rx and addressing various misalignments such as angular, lateral, and longitudinal misalignments. To tackle these challenges identified in the literature survey, the objectives of the thesis have been subdivided into various sub-objectives (SO), which have undergone an evolutionary process aimed at designing Tx-Rx coil antennas using the field-forming technique for bio-medical implant application, as outlined below:

1. **SO−1:** Investigate an optimal rotating magnetic field for angular misalignment mitigation and generate using a planar Tx.
2. **SO−2:** Examine a switching integrated planar Tx for targeting angular and lateral misalignment simultaneously.
3. **SO−3:** Inspect a planar Tx that localizes the position and orientation of an arbitrarily placed Rx.
4. **SO−4:** Explore a planar Tx that simultaneously localizes and constructs a magnetic beam toward a Rx.
5. **SO−5:** Develop a Rx antenna design to overcome the misalignment issue.

The accomplishments of the above mentioned sub-objectives are listed in Table 1.1.

1.8 Thesis Outline

1. **Chapter-1:** This chapter provides an overview of the fundamental principles behind NF-WPT systems and explores their potential applications in biomedical implants.

Table 1.1: Challenges encountered through the evolutionary process.

	Problem Encountered						
Objectives	3−D Structure	Multiple Excitation	Flux Leakage	Localization	Angular Misalignment	Lateral Misalignment	Longitudinal Misalignment
SO−1	✓	✗	✗	✗	✓	✗	✗
SO−2	✓	✓	✗	✗	✓	✓	✗
SO−3	✓	✓	✗	✓	✗	✗	✗
SO−4	✓	✓	✓	✓	✓	✓	✓
SO−5	✓	✓	✗	✗	✗	✓	✗

Note: ✓ denotes target achieved, ✗ denotes target not achieved.

Subsequent discussions address the array of research challenges encountered. Following this, a thorough investigation of existing solutions documented in the literature is undertaken, with a systematic organization of these works to address previously outlined challenges. Furthermore, the chapter includes an outline of the thesis.

2. **Chapter-2:** This chapter discusses the significance of comprehending the theory behind resonant NF-WPT systems to fulfill the objectives outlined in the preceding chapter. It introduces closed-form magnetic-field equations for different coil configurations and design parameters, which are subsequently utilized for the analytical modeling of the proposed WPT system. Additionally, this chapter provides the discussion on voltage calculation and the evaluation of PTE.

3. **Chapter-3:** This chapter is centered on establishing a mathematical framework to examine various 3−D rotating H-fields, with a specific focus on resolving angular misalignment challenges, especially in charging biomedical implants. It aims to optimize the distribution of rotating magnetic fields at the Rx region to improve the tolerance of angular misalignment. Additionally, the chapter introduces two distinct Tx coil designs aimed for achieving the optimal 3−D rotating H-fields and also validates the optimal field in the far-field regime.

4. **Chapter-4:** This chapter presents the development of a novel methodology that combines a traditional field-forming technique with switching control to create an orientation-insensitive WPT system. This overrides the previous conception of perceiving the 3−D rotating H-field forming as the last resort to completely eliminate the angular misalignment problem. Instead, a switched polarized H-field approach is proposed, necessitating only a single sinusoidal source as opposed to the multiple modulated sources required by the traditional 3−D rotating H-field method. Furthermore, this switched polarization concept is expanded to cover a broader Rx range, effectively addressing both lateral and angular misalignment challenges simultaneously. Finally, the chapter introduces two distinct Tx antenna designs tailored to implement this switched polarized H-field approach.

5. **Chapter-5:** This chapter introduces a magnetic localization method for tracking both the position and orientation of a mobile Rx used in biomedical implants. Through an extensive review of existing literature focusing on frequency-divisional

approaches, a new technique called the time-divisional approach is proposed for magnetic localization. This new method aims to reduce the circuit complexity and system cost. A comparative analysis between the previously employed approach and the proposed one is conducted to showcase the efficacy of the proposed methodology. Additionally, three distinct antenna structures are outlined: one is designed solely for position tracking, while the other two are capable of tracking both position and orientation simultaneously.

6. **Chapter-6:** This chapter explores an integration of localization and magnetic beamforming to tackle various misalignment challenges using a single Tx antenna, a novel approach not previously explored in near-field WPT applications. To achieve this, a machine-learning model is developed to localize the Rx by collecting voltage samples using a time-divisional method. Additionally, particle swarm optimization is employed to determine the optimal excitations for the Tx array, effectively shaping the desired magnetic beam. Furthermore, a single excitation source and switching circuitry are utilized to activate multiple coils within the proposed Tx, reducing circuit complexity and system cost. Finally, the chapter introduces a novel Tx design featuring an overlapping coil structure, addressing all potential misalignment issues and other challenges identified in existing literature, thus representing a significant advancement in the field.

7. **Chapter-7:** Previous chapters focused on designing a field-forming Tx to address misalignment issues with a planar Rx. However, the planar Rx does not efficiently capture available H-field components. This chapter introduces a novel Rx structure optimized to harvest both longitudinal and lateral field components, effectively tackling misalignment. It also examines identical and non-identical orthogonal Rx coil structures to assess the impact of lateral misalignment. The integrated coil rectenna array with a single DC output port is realized using multi-layer PCB technology, with all circuit elements integrated within the antenna structure. This compact, robust, and cost-effective solution is ideal for wirelessly powering biomedical implants and wearable devices. A use case is also proposed for other applications, such as drone charging.

8. **Chapter-8:** This chapter conducts a comparative analysis of the various approaches proposed in the study and offers overall conclusions of this thesis. Additionally, potential avenues for future development are explored to further improve upon the proposed methodologies.

Chapter 2

Theoretical Framework for MRC based WPT

To achieve the goals outlined in the previous chapter, it is vital to have a deep understanding of the theory behind the resonant near-field WPT system. Therefore, this chapter aims to improve comprehension of the mathematical analysis involved in a typical MRC-based WPT system. The theoretical analysis mainly focuses on explaining the closed-form equation of the magnetic field distribution produced by standard coil structures. Additionally, this chapter covers the determination of various coil design parameters, calculating induced voltage (V_{ind}) using Faraday's Law of Electromagnetic Induction, and assessing PTE using circuit law. Ultimately, this chapter lays the groundwork for analyzing the coil structures discussed in subsequent chapters.

2.1 Magnetic Field from Conventional Coil Structure

The standard coil configurations adopted for analyzing WPT are circular and square coils. A closed-form equations are required to analyze the magnetic field generated by these coil configurations analytically. Those closed form solutions are listed here and utilized later to further analyze the system.

2.1.1 Magnetic field generated from a circular coil at the center

The instantaneous magnetic field ($h(t)$) produced by a conventional circular Tx coil having radius r_{Tx}, available turns N_{Tx} and carrying an instantaneous current $i(t)$ at the coil's center is formulated using Biot Savart's Law [97] as

$$h(t) = \frac{N_{Tx} i(t)}{2 r_{Tx}}. \tag{2.1}$$

However, the magnetic field equation presented in (2.1) is applicable only at the center of Tx coil. To further analyze a Tx generated magnetic field in the near by Rx region, closed-form solution is required.

2.1.2 Closed-Form Magnetic Field Equation for a Circular Coil

To formulate the field distribution, a single-turn circular coil of radius r_{Tx} is considered as the Tx antenna located at (x_{Tx}, y_{Tx}, z_{Tx}), as depicted in Figure 2.1. The Tx coil is excited by a sinusoidal source, resulting in a current $I_{Tx}e^{j\psi}$ flowing through the Tx coil, where

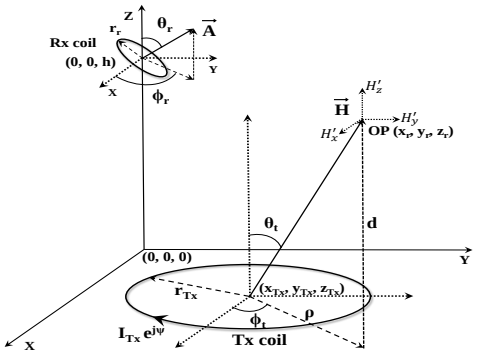

Figure 2.1: Analytical modeling of H-field due to a single turn circular coil.

I_{Tx} is the peak value, and ψ is the initial phase of the current excitation. The current excitation generates H-field distribution around the Rx area, which induces a voltage in the Rx coil located at (0, 0, h). An analytical model of the H-field generated by the Tx coil and originating from a current-carrying loop is utilized for this purpose.

Consider an arbitrary observation point (OP) with coordinates (x_r, y_r, z_r) at which the H-field is determined. The relative distances and angle quantities (ρ, d, ϕ_t), as defined in Figure 2.1, are obtained as

$$\left.\begin{aligned} &\rho = \sqrt{(x_r - x_{Tx})^2 + (y_r - y_{Tx})^2}, d = (z_r - z_{Tx}), \\ &\phi_t = \tan^{-1}\left[\frac{(y_r - y_{Tx})}{(x_r - x_{Tx})}\right]. \end{aligned}\right\} \tag{2.2}$$

The peak value of orthogonal projections H'_x, H'_y, and H'_z of the H-field vector along X, Y, and Z axis, respectively, at OP shown in Figure 2.1 are formulated as [7]

$$\begin{aligned} H_\rho &= \frac{I_{Tx}e^{j\psi}d}{2\pi\rho\sqrt{(r_{Tx}+\rho)^2+d^2}}\left[\frac{r_{Tx}^2+\rho^2+d^2}{(r_{Tx}-\rho)^2+d^2}E(p) - K(p)\right], \\ H'_x &= H_\rho\cos\phi_t, \qquad H'_y = H_\rho\sin\phi_t, \\ H'_z &= \frac{I_{Tx}e^{j\psi}}{2\pi\sqrt{(r_{Tx}+\rho)^2+d^2}}\left[\frac{r_{Tx}^2-\rho^2-d^2}{(r_{Tx}-\rho)^2+d^2}E(p) + K(p)\right]. \end{aligned} \tag{2.3}$$

Where $K(p)$ and $E(p)$ are defined as complete elliptic integrals of the first and second kind, respectively, and p is calculated as $\sqrt{\frac{4r_{Tx}\rho}{(r_{Tx}+\rho)^2+d^2}}$. Thus, the total H-field components generated at the Rx region due to N_{Tx} turns present in the Tx coil is given as

$$H_x(x_r, y_r, z_r) = \sum_{j=1}^{N_{Tx}} H'_x, \quad H_y(x_r, y_r, z_r) = \sum_{j=1}^{N_{Tx}} H'_y, \quad H_z(x_r, y_r, z_r) = \sum_{j=1}^{N_{Tx}} H'_z. \tag{2.4}$$

2.1.3 Closed Form Magnetic Field Equation for a Square Coil

The H-field produced by a single-turn square coil, with a side length of S_{Tx}, positioned at (x_{Tx}, y_{Tx}, z_{Tx}) and carrying current $I_{Tx}e^{j\psi}$, is further analytically modeled. This is illustrated in Figure 2.2. The H-field generated at any arbitrary point Rx (x_r, y_r, z_r) is formulated using the closed-form solution for the H-field equation as [98].

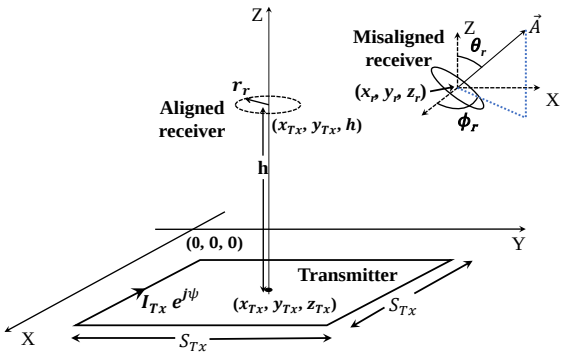

Figure 2.2: Analytical modeling of H-field due to a single turn square coil.

$$
\begin{aligned}
H'_x &= \frac{I_{Tx}e^{j\psi}}{4\pi}\sum_{k=1}^{4}\left\{\frac{(-1)^{k+1}(z_{Tx}-z_r)}{q_k(q_k+P_k)}\right\}\\
H'_y &= \frac{I_{Tx}e^{j\psi}}{4\pi}\sum_{k=1}^{4}\left\{\frac{(-1)^{k+1}(z_{Tx}-z_r)}{q_k(q_k+(-1)^{k+1}Q_k)}\right\}\\
H'_z &= \frac{I_{Tx}e^{j\psi}}{4\pi}\sum_{k=1}^{4}\left\{\frac{(-1)^{k}P_k}{q_k[q_k+(-1)^{k+1}Q_k]}-\frac{Q_k}{q_k[q_k+P_k]}\right\},
\end{aligned}
\tag{2.5}
$$

$$
\begin{aligned}
q_1 &= \sqrt{P_1^2+Q_1^2+(z_{Tx}-z_r)^2}, \quad q_2 = \sqrt{P_2^2+Q_2^2+(z_{Tx}-z_r)^2},\\
q_3 &= \sqrt{P_3^2+Q_3^2+(z_{Tx}-z_r)^2}, \quad q_4 = \sqrt{P_4^2+Q_4^2+(z_{Tx}-z_r)^2},\\
P_1 &= P_2 = \frac{S_{Tx}}{2}+y_r-y_{Tx}, \quad P_3 = P_4 = -\frac{S_{Tx}}{2}+y_r-y_{Tx},\\
Q_1 &= -Q_4 = \frac{S_{Tx}}{2}+x_r-x_{Tx}, \quad Q_2 = -Q_3 = \frac{S_{Tx}}{2}-x_r+x_{Tx}.
\end{aligned}
$$

Thus, the total H-field components generated at the Rx region due to N_{Tx} turns present in the Tx coil is given as

$$
H_x(x_r,y_r,z_r) = \sum_{j=1}^{N_{Tx}} H'_x, \quad H_y(x_r,y_r,z_r) = \sum_{j=1}^{N_{Tx}} H'_y, \quad H_z(x_r,y_r,z_r) = \sum_{j=1}^{N_{Tx}} H'_z. \tag{2.6}
$$

The total H-field is defined as a vector summation of these evaluated H-field components and given as $\vec{H} = H_x\hat{x} + H_y\hat{y} + H_z\hat{z}$. Here, the total H-field is the phasor quantity, as the excitation current is represented in phasor. For obtaining a time-varying H-field, conversion of phasor quantity into time-domain is required as [99]

$$
\vec{h}(t) = Re\{\vec{H}e^{j\omega t}\} = h_x(t)\hat{x} + h_y(t)\hat{y} + h_z(t)\hat{z}. \tag{2.7}
$$

Here, ω is the working frequency (rad/sec) of the sinusoidal source.

2.2 Induced Voltage Evaluation

Once the H-field at the Rx region is known, further V_{ind} obtained at the Rx is defined by Faraday's law of electromagnetic induction as the rate of change of flux linkage as

$$
V_{ind}(t) = -N_r\frac{d\Phi(t)}{dt}. \tag{2.8}
$$

Here, N_r is the turns present in the Rx coil and Φ is the magnetic flux defined as a dot product of the magnetic flux density $\vec{B}$ and the Rx area vector $\vec{A}$ i.e. $\Phi(t) = \vec{B(t)}.\vec{A} = \mu_o\vec{h(t)}.\vec{A}$, μ_o is the permeability of free space. The Rx area vector is given by $\vec{A} = A_x\hat{i} + A_y\hat{j} + A_z\hat{k}$ where $A_x = A\sin\theta_r\cos\phi_r$, $A_y = A\sin\theta_r\sin\phi_r$, and $A_z = A\cos\theta_r$, are

the area projections along x, y, and z-axis, respectively. Using these relations in (2.8), the induced voltage is obtained as

$$V_{ind}(t) = -N_r \mu_o \frac{d}{dt}\Big[h_x(t)A_x + h_y(t)A_y + h_z(t)A_z\Big]. \tag{2.9}$$

Here, $h_x(t)$, $h_y(t)$, $h_z(t)$ are the instantaneous magnetic field components as defined in (2.7). Thus, the Root Mean Square (RMS) value of V_{ind}, V_r is evaluated using the expression

$$V_r^2 = 2f\left[\int_o^{\frac{1}{2f}} V_{ind}^2(t)dt\right] \tag{2.10}$$

Here, f is the operating frequency in Hertz.

2.3 Coil Design Parameters of a Conventional Circular Coil

Once the V_r in the Rx coil is known, to further evaluate the PTE, the coil design parameter is required. In a typical WPT system, various parameters of the coil antennas influence the power transmission between the Tx and the Rx includes mutual inductance (M), self-inductance (L), parasitic capacitance (C_t), and coil resistance (R_{ac}). Therefore, to formulate the PTE, equivalent circuit parameters of the coils need to be analyzed.

Mutual inductance

The V_{ind} in the Rx coil determines the mutual inductance (M) between the Tx and the Rx coils, when Tx carrying a peak current of I_{Tx} and calculated using Faraday's law of electromagnetic induction as [100]

$$M = \frac{V_{ind}}{\omega I_{Tx}} \tag{2.11}$$

Self-inductance of the multi-turn coil

The total self inductance (L) of a multi-turn coil having a total N_{Tx} turns is determined by summation of self inductance L_m of individual m^{th} turn and mutual inductance M_{mn} between each pair of m^{th} and n^{th} turns. In this manner, L is defined as

$$L = \sum_{m=1}^{N_{Tx}} L_m + \sum_{m=1}^{N_{Tx}} \sum_{n=1}^{N_{Tx}} M_{mn} \tag{2.12}$$

and the L_m and M_{mn} are calculated using [101]

$$\begin{aligned} L_m &= \mu_o r_m \left[ln\left(\frac{16r_m}{w}\right) - 2\right] \\ M_{mn} &= \mu_o \sqrt{r_m r_n}\frac{2}{\gamma}\left[\left(1 - \frac{\gamma^2}{2}\right)K(\gamma) - E(\gamma)\right]. \end{aligned} \tag{2.13}$$

Here, R_m and R_n are the radius of m^{th} and n^{th} turns, w denotes the strip width of the printed coil, and $\gamma = 2\sqrt{r_m r_n}/(r_m + r_n)$.

Parasitic capacitance between different turns of a coil

The parasitic capacitance (C_t) between two adjacent turns of a coil is composed of two different capacitances that exist between the air (C_{air}) and the substrate (C_{subs}) of a printed circuit board (PCB) [102] , which is defined as

$$C_t = C_{air} + C_{subs} \approx (\alpha\varepsilon_{air} + \beta\varepsilon_{subs})\varepsilon_0 \frac{t}{g} l_g. \tag{2.14}$$

Where l_g is the air gap length, t is the thickness of track strip, g is the separation between adjacent tracks, $\alpha = 0.9$ and $\beta = 0.1$ are the constants for air ($\epsilon_{air} = 1$) and FR4 substrate ($\epsilon_{subs} = 4.4$).

Resistance of a multi-turn coil

Total DC resistance of a multi-turn coil is defined as $R_{DC}= \frac{l_c}{\sigma a}$. Where, σ is the conductivity of material, l_c is total conductive length and a is cross-sectional area of the track. Under higher frequencies, the current distribution in the coil tracks is non-uniform due to skin and proximity effects. Due to the former, the current is mainly confined near the surface of the wire, whereas, the latter results in the non-uniform current distribution along the tracks because of the coupling in the adjacent turns. Therefore, the R_{ac} of a coil is given by [103]

$$R_{ac} = R_{skin} + R_{prox}, \tag{2.15}$$

where, R_{skin} and R_{prox} represents resistances due to skin and proximity effects, respectively, and determined by [102, 103]

$$\begin{aligned} R_{skin} &= \frac{t}{\delta(1 - e^{-\frac{t}{\delta}})} R_{DC}, \\ R_{prox} &= \frac{1}{10} R_{DC} \left(\frac{\omega}{\omega_{crit}} \right)^2, \\ \omega_{crit} &= \frac{3.1}{\mu_0} \frac{s + w}{w^2} R_{sheet}. \end{aligned} \tag{2.16}$$

Here, δ is the skin depth defined as $\sqrt{2/(\mu_o \omega \sigma)}$, ω_{crit} is the critical angular frequency at which current crowding becomes significant, μ_0 is the permeability of air, and R_{sheet} is the metal sheet resistance of the track.

2.4 The PTE and S21 calculation

The PTE, which is realized in terms of $S21$ parameters between the Tx and Rx coils as $|S21|^2$ can be formulated as [104]

$$S21 = \frac{j2\omega M \sqrt{R_s R_l}}{(R_1 + R_s)(R_2 + R_l) + (\omega M)^2}, \tag{2.17}$$

where, R_1, R_2 are the parasitic resistances of the Tx and the Rx coils and R_s, R_l are the source and load resistances, respectively.
By substituting M from (2.11) in (2.17), we obtain

$$S21 = \frac{j2V_{ind} I_{Tx} \sqrt{R_s R_l}}{I_{Tx}^2 (R_1 + R_s)(R_2 + R_l) + V_{ind}^2}. \tag{2.18}$$

2.5 Summary

This chapter is dedicated to deepening our understanding of the theory behind the resonant near-field WPT system. It focuses on improving comprehension of the mathematical analysis of a typical MRC-based WPT system, particularly explaining the closed-form equation of the magnetic field distribution generated by standard coil structures. Additionally, it addresses determining various coil design parameters, calculating induced voltage using Faraday's Law, and assessing Power Transfer Efficiency using circuit law, which serves as the foundation for analyzing and designing coil structures.

Chapter 3

Rotating Magnetic Field Forming Transmitters

SO−1: *Investigate an optimal rotating magnetic field for angular misalignment mitigation and generate using a planar Tx.*

This chapter introduces a mathematical model of a typical WPT system that generates a 3−D rotating H-field to mitigate the angular misalignment problem, particularly in charging biomedical implants. Various 3−D rotating H-fields are demonstrated, and their effects on the angular misalignment of the Rx are analyzed. To enhance the system's tolerance to angular misalignment, the 3−D rotating H-field is optimized to determine the optimally polarized H-field distribution at the Rx region. Additionally, this chapter discusses the development and optimization of two distinct Tx coil designs, labeled Design−1A and Design−1B, which fulfill the objectives outlined in SO−1 as defined in Section 1.7. Furthermore, the proposed optimal field is validated in the far-field microwave power transfer (MPT) regime as Design−1C.

3.1 Evolution of 3-D Rotating Magnetic Field Using 3-D Shaped Transmitter (Design-1A)

To analyze a 3−D rotating H-field, the proposed WPT system contains two inductively coupled Tx and Rx units as depicted in Figure 3.1. The Tx is made of three coils having radius r_{Tx}, number of turns N_{Tx}, and instantaneous current excitations $i_x(t)$, $i_y(t)$ and $i_z(t)$ with peak amplitude I_{Tx}^x, I_{Tx}^y and I_{Tx}^z, respectively. The Tx coils are arranged orthogonally in space to generate three orthogonal H-field components with peak value H_x, H_y, and H_z and having instantaneous value of $h_x(t)$, $h_y(t)$, and $h_z(t)$ at the Rx location. As shown in Figure 3.1, a small planar Rx coil having a cross-sectional area A, number of turns N_r, and inclination angles θ_r and ϕ_r from z-axis and x-axis, respectively, is centered at the origin. The oscillating H-fields originated from the three orthogonal Tx coils are evaluated at the origin using Biot Savart Law, presented in (2.1) and defined as

$$h_x(t) = \frac{N_{Tx} i_x(t)}{2r_{Tx}}, h_y(t) = \frac{N_{Tx} i_y(t)}{2r_{Tx}}, h_z(t) = \frac{N_{Tx} i_z(t)}{2r_{Tx}}. \tag{3.1}$$

Hence, the resultant H-field vector $\vec{h}(t)$ generated at the Rx is given by $\vec{h}(t) = h_x(t)\hat{x} + h_y(t)\hat{y} + h_z(t)\hat{z}$ which induces a voltage V_{ind} in the Rx coil defined as (2.9). By substitution

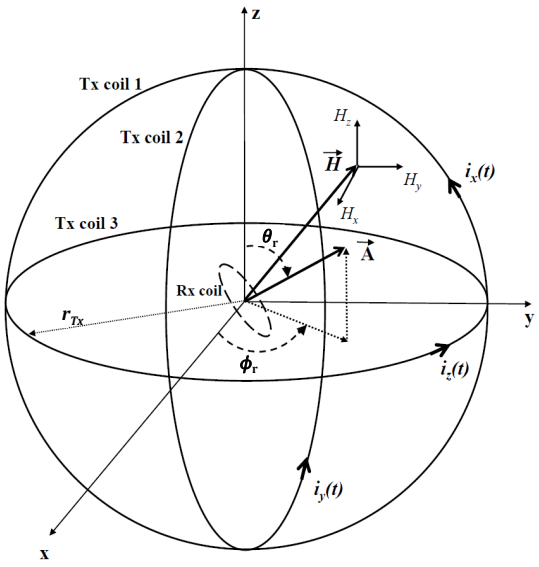

Figure 3.1: A WPT system consisting of three orthogonal transmitter and a planar receiver.

from (3.1), (2.9) yields an expression of V_{ind} as a function of excitation currents in the Tx coils as

$$V_{ind}(t) = -\left(\frac{N_{Tx}N_r\mu_o A}{2r_{Tx}}\right)\frac{d}{dt}\Big[i_x(t)\sin\theta_r\cos\phi_r + i_y(t)\sin\theta_r\sin\phi_r + i_z(t)\cos\theta_r\Big]. \tag{3.2}$$

The V_{ind} given by (3.2) determines the total power delivered to the Rx. The effectiveness of a WPT system is ultimately measured by its performance metrics, specifically PTE, which is defined as the ratio of power delivered to the Rx load to the total input power of the Tx. However, the power delivered to the load relies on RMS value of the V_{ind}, V_r, before rectification at the Rx. Hence, to achieve an optimal PTE, the V_r is the ultimate parameter to be enhanced. It is observed from (3.2) that the current excitations $i_x(t)$, $i_y(t)$, and $i_z(t)$ in the Tx coils along with the Rx coil orientation θ_r and ϕ_r determine V_r value. Moreover, it is apparent from (3.1) that due to the time varying excitation currents, the $\vec{h}(t)$ varies in time and has a time varying vector direction. Hence, the trajectory of the tip of the vector $\vec{h}(t)$ (defined as polarization of the H-field) depends on the current excitations and may adopt various shapes. The H-field polarization affects the PTE at the Rx and a specific polarization of $\vec{h}(t)$ may result in a maximum PTE for a specific inclination θ_r and ϕ_r of the Rx coil. However, when the Rx changes its orientation, the PTE may degrade significantly resulting in angular misalignment problem. To understand this, the effect of H-field polarization (2−D and 3−D) in WPT systems is studied next.

3.1.1 Effect of H-field polarization in WPT systems

The angular misalignment problem is analyzed by studying the H-field polarization at the Rx location. Depending on the Tx coil excitations and correspondingly generated rotating fields at the Rx, 2−D and 3−D H-field polarizations may exist.

2-D H-field polarization

In case only two Tx coils, i.e., Coil−1 and Coil−2 in Figure 3.1 are excited (with currents of amplitudes I_{Tx}^{x} and I_{Tx}^{y}, and phase difference $\Delta\psi$), the oscillating H-field generated at the Rx location will be 2−D polarized. To categorize polarizations, Axial Ratio (AR) is defined as a ratio of major axis to minor axis length. This results in linear, circular, and elliptical polarizations. For $\Delta\psi = n\pi$ where n is an integer, a linearly polarized H-field is generated and the corresponding H-field trace is illustrated in Figure 3.2(a) for $I_{Tx}^{x} = I_{Tx}^{y}$. The AR is infinite for the linearly polarized H-field which oscillates in a single direction

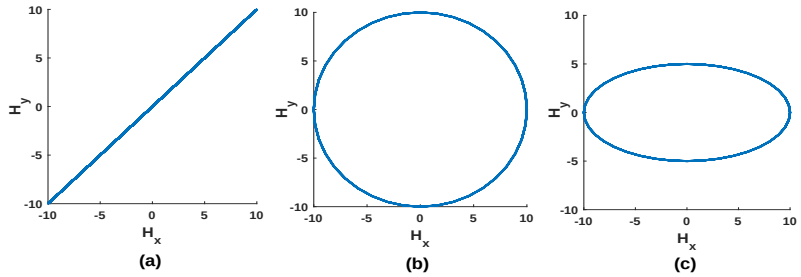

Figure 3.2: 2−D polarization (a) Linear (b) Circular (c) Elliptical.

restricting the Rx area vector to always align with that direction to efficiently capture the field. Figure 3.3(a) reveals the directional nature of the linearly polarized H-field, which

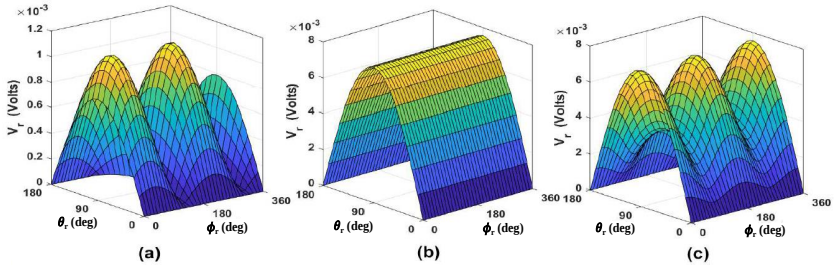

Figure 3.3: Induced voltage variation due to 2−D polarized H-fields (a) Linear (b) Circular (c) Elliptical.

shows that the V_r varies with both θ_r and ϕ_r. For $I_{Tx}^{x} = I_{Tx}^{y}$ and the phase difference ($\Delta\psi$) between the sources are $\Delta\psi = (\frac{1}{2} + n)\pi$, the H-field is circularly polarized. The phase shift between excitation currents generates a rotating H-field at the Rx as presented in Figure 3.2(b). The AR for a circular polarization is unity and the H-field rotates in x-y plane with equal intensity. This allows the Rx to capture H-field equally in any orientation ϕ_r but restrict inclination $\theta_r = 90°$ for a maximum V_r. Figure 3.3(b) shows V_r variation for the circular polarization, and proves that the induced voltage is invariant in ϕ_r but varies with θ_r. Similarly, for $I_{Tx}^{x} \neq I_{Tx}^{y}$ and $\Delta\psi = (\frac{1}{2} + n)\pi$, the H-field is elliptically polarized as shown in Figure 3.2(c) for I_{Tx}^{x}= 1A and $I_{Tx}^{y} = 0.5$ A. The AR for elliptically polarized H-field is greater than unity indicating that the field captured by the Rx is non-uniform and depends on orientation in ϕ_r, this can be verified by the corresponding V_r result shown in Figure 3.3(c).

Since $i_z(t) = 0$ for 2−D polarization, we derive from (3.2) that V_{ind} reduces to zero for $\theta_r = 0°$. Therefore, we conclude that by generating the 2−D polarized H-field, the

orientation problem in θ_r always persists. Since the 3−D polarization generates a rotating H-field in three dimension, the Rx can be placed in any orientation. Hence, a 3−D polarized H-field is necessary to completely mitigate the angular misalignment problem.

3-D H-field polarization

The 3−D polarized H-field can be generated by using the Tx consisting of three orthogonal coils and controlling the excitation currents in the individual coil shown in Figure 3.1. To realize rotating H-field in 3−D, we use AM signals to excite the Tx coils. Note that the DSB-SC excitation is included in the general AM signal as a special case. The AM currents in the Tx Coil−1, −2, and −3, respectively, can be formulated as

$$\left.\begin{aligned} i_x(t) &= I^x_{Tx}[(1-m) + m\cos(\omega_m t)]\cos(\omega_c t + \psi_c), \\ i_y(t) &= I^y_{Tx}[(1-m) + m\cos(\omega_m t + \psi_m)]\cos(\omega_c t + \psi_c), \\ i_z(t) &= I^y_{Tx}\cos(\omega_c t), \end{aligned}\right\} \tag{3.3}$$

where, m is the modulation index ($0 \leq m \leq 1$), ω_m is the angular modulating frequency ($2\pi f_m$ rad/sec), ω_c is the angular carrier frequency ($2\pi f_c$ rad/sec) here $f_m = 500$Hz and $f_c = 6.78$MHz, ψ_m and ψ_c are the phase difference in the modulating and the carrier signals, respectively. To generate AM signal efficiently, the frequencies should satisfy $\omega_c >> \omega_m$. By controlling the excitation current parameters given in (3.3), various 3−D polarizations of H-field governed by (3.1) can be generated. In this study, we present some general shapes formed by 3−D polarization and their effect on WPT performance is analyzed subsequently.

Drum shaped 3-D polarization

For the AM signals excited with conditions $I^x_{Tx} = I^y_{Tx} = I^z_{Tx}$, $m = 1$, $0 < \psi_c \leq \pi/6$, and $0 < \psi_m \leq \pi/2$, in (3.3), a drum shaped 3−D polarized H-field is realized at the Rx location. The resultant H-field trace for $\psi_c = \psi_m = \pi/4$ and $I^z_{Tx} = 1$ A is shown in Figure 3.4(a).

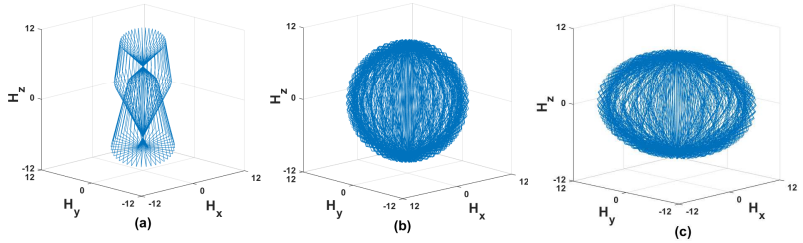

Figure 3.4: 3−D polarized H-fields (a) Drum (b) Spherical (c) Ellipsoidal.

Spherical 3-D polarization

For excitation conditions $I^x_{Tx} = I^y_{Tx} = I^z_{Tx}$, $m = 1$, $\psi_c = \psi_m = \pi/2$, a spherically polarized H-field is generated at the Rx as depicted in Figure 3.4(b) for $I^z_{Tx} = 1$ A. This excitation is same as DSB-SC case presented in [18, 19] to generate spherically rotating H-field vector.

Ellipsoidal 3-D polarization

To generate an ellipsoidally polarized H-field, the conditions for excited AM signals are $m = 1$, $\psi_m = \pi/2$, $\psi_c = \pi/2$, and except $I^x_{Tx}, I^y_{Tx}, I^z_{Tx}$ are not equal. Figure 3.4(c) presents an example of an ellipsoidal polarization for $I^x_{Tx} = 1.2$ A, $I^y_{Tx} = 1.4$ A, and $I^z_{Tx} = 0.82$ A. A complete analysis of the effect of 3−D polarized fields on angular misalignment in WPT systems is presented next.

3.1.2 Analysis of 3-D Polarized H-field

Induced voltage calculation

Once the Tx is excited with the AM signals $i_x(t)$, $i_y(t)$, and $i_z(t)$ defined in (3.3), the V_{ind} in the Rx coil is found using (3.2) which by substitution converts to

$$V_{ind}(t) = -\left(\frac{N_{Tx}N_r\mu_o A}{2r_{Tx}}\right)\frac{d}{dt}\Big[I^x_{Tx}[(1-m)+m\cos(\omega_m t)]\cos(\omega_c t+\psi_c)\sin\theta_r\cos\phi_r + I^y_{Tx}[(1-m)+ m\cos(\omega_m t+\psi_m)]\cos(\omega_c t+\psi_c)\sin\theta_r\sin\phi_r + I^z_{Tx}\cos(\omega_c t)\cos\theta_r\Big]. \tag{3.4}$$

After expanding and rearranging the terms in (3.4), the final V_{ind} is given by (3.5). The

$$V_{ind}(t) = \left(\frac{N_{Tx}N_r\mu_o A}{2r_{Tx}}\right)\Big[I^x_{Tx}[(1-m)\omega_c\sin(\omega_c t+\psi_c) + \frac{m}{2}(\omega_c+\omega_m)\sin((\omega_c+\omega_m)t) + \frac{m}{2}(\omega_c-\omega_m)\sin((\omega_c-\omega_m)t)]\sin\theta_r\cos\phi_r + I^y_{Tx}[(1-m)\omega_c\sin(\omega_c t+\psi_c) + \frac{m}{2}(\omega_c+\omega_m)\sin((\omega_c+\omega_m)t+ (\psi_c+\psi_m)) + \frac{m}{2}(\omega_c-\omega_m)\sin((\omega_c-\omega_m)t+(\psi_c-\psi_m))]\sin\theta_r\sin\phi_r + I^z_{Tx}\sin(\omega_c t)\cos\theta_r\Big]. \tag{3.5}$$

RMS value of V_{ind}, V_r is evaluated using (2.10) considering $f = f_m$, where $f_m = \frac{\omega_m}{2\pi}$ is the fundamental frequency of the induced voltage. By solving (3.5) and (2.10), the square of V_r in the Rx is formulated as (3.6). The steps to obtain (3.6) are omitted here for

$$V_r^2 = \left(\frac{N_{Tx}N_r\mu_o A}{2r_{Tx}}\right)^2\Big[(I^x_{Tx})^2(\omega_c^2\frac{(1-m)^2}{2} + \frac{m^2}{4}(\omega_c^2+\omega_m^2))\sin^2\theta_r\cos^2\phi_r + (I^y_{Tx})^2(\omega_c^2\frac{(1-m)^2}{2} + \frac{m^2}{4}(\omega_c^2+\omega_m^2))\sin^2\theta_r\sin^2\phi_r + \frac{(I^z_{Tx})^2}{2}\omega_c^2\cos^2\theta_r + I^x_{Tx}I^z_{Tx}(1-m)\omega_c^2\frac{\cos\psi_c}{2}\sin\theta_r\cos\theta_r\cos\phi_r + I^y_{Tx}I^z_{Tx}(1-m)\omega_c^2\frac{\cos\psi_c}{2}\sin\theta_r\cos\theta_r\sin\phi_r + I^x_{Tx}I^y_{Tx}(\omega_c^2\frac{(1-m)^2}{2} + \frac{m^2}{2}(\omega_c^2+\omega_m^2)\cos\psi_m)\sin^2\theta_r\cos\phi_r\sin\phi_r\Big]. \tag{3.6}$$

brevity. It is apparent that the expression of V_r is consisting of θ_r and ϕ_r dependent terms, and excited AM signal parameters. Therefore, the V_r is determined by the kind of polarization as well as the orientation of the Rx coil. The effect of 3−D polarizations on angular misalignment is analyzed subsequently.

Effect of 3−D H-field polarization

The WPT performance and variation in the V_r for 3−D polarization cases, i.e., drum, spherical, and ellipsoidal are now analyzed. For the drum-shaped polarization, the

corresponding excitation current parameters provided in Chapter 3.1.1 are substituted in (3.6) and the corresponding RMS induced voltage V_r^{D} is obtained as

$$(V_r^{\mathrm{D}})^2 = \left(\frac{N_{Tx}N_r\mu_o A I_{Tx}^z}{2r_{Tx}}\right)^2 \left[\frac{1}{4}(\omega_c^2+\omega_m^2)\sin^2\theta_r + \frac{1}{2}\omega_c^2\cos^2\theta_r + \frac{1}{2}(\omega_c^2+\omega_m^2)\cos\psi_m\sin^2\theta_r\cos\phi_r\sin\phi_r\right]. \tag{3.7}$$

The expression shows that the V_r^{D} varies with θ_r and ϕ_r. The V_r^{D} for the polarization shown in Figure 3.4(a) is calculated using (3.7) and plotted in Figure 3.5(a) which shows a high variation with θ_r and ϕ_r. Hence, the WPT performance is not consistent in case

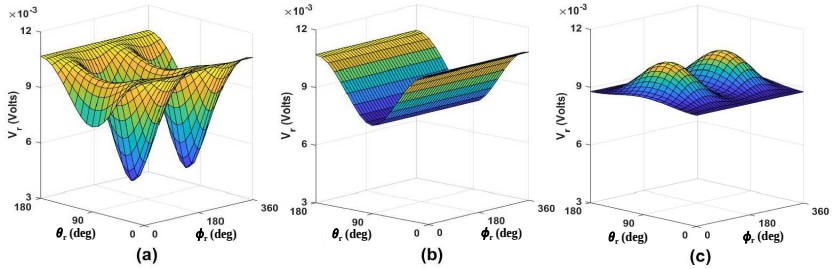

Figure 3.5: The V_r for 3−D polarized H-field (a) Drum (b) Spherical (c) Ellipsoidal.

of angular misalignment of the Rx coil. Similarly, the performance corresponding to the spherical polarization is analyzed by inserting excitation current parameters from Section 3.1.1 in (3.6). The RMS induced voltage V_r^{S} for this case is obtained as

$$(V_r^{\mathrm{S}})^2 = \left(\frac{N_{Tx}N_r\mu_o A I_{Tx}^z}{2r_{Tx}}\right)^2 \left[\frac{1}{4}(\omega_c^2+\omega_m^2)\sin^2\theta_r + \frac{1}{2}\omega_c^2\cos^2\theta_r\right] \tag{3.8}$$

which shows that V_r^{S} becomes independent of ϕ_r, however, it still varies with θ_r. The calculated V_r^{S} corresponding to the polarization is shown in Figure 3.4(b) is plotted in Figure 3.5(b) demonstrating that the V_r^{S} variation for the spherically polarized H-field is reduced as compared to the drum-shaped polarization though the angular misalignment problem is still persistent. To achieve uniform power delivery in any orientation of the Rx coil, the V_r should be independent of θ_r as well as ϕ_r. This motivates us to investigate an optimal polarization of H-field to completely mitigate the angular misalignment problem as presented subsequently.

3.1.3 Proposed 3-D Polarized H-field Forming

To mitigate angular misalignment problem, our investigation reveals an ellipsoidal 3−D polarization defined in Chapter 3.1.1 as a potential solution. The parameters of excited AM currents of (3.3) to generate a general ellipsoidal polarization are defined in Chapter 3.1.1 as $m=1$, $\psi_m=\pi/2$, $\psi_c=\pi/2$, and except $I_{Tx}^x, I_{Tx}^y, I_{Tx}^z$ are not equal. These parameter values are substituted in (3.6) and the V_r for ellipsoidal polarization is given by

$$(V_r^E)^2 = \left(\frac{N_{Tx}N_r\mu_o A}{2r_{Tx}}\right)^2 \left[\frac{(I_{Tx}^x)^2}{4}(\omega_c^2+\omega_m^2)\sin^2\theta_r\cos^2\phi_r + \frac{(I_{Tx}^z)^2}{4}(\omega_c^2+\omega_m^2))\sin^2\theta_r\sin^2\phi_r + \frac{(I_{Tx}^z)^2}{2}\omega_c^2\cos^2\theta_r\right]. \tag{3.9}$$

This can be inferred by analyzing the ellipsoidal polarization presented in Figure 3.4(c) whose corresponding V_r calculated using (3.9) is shown in Figure 3.5(c). By comparison, Figure 3.5 reveals that the variation in the V_r for the ellipsoidal polarization is small as compared to that of the drum and the spherical polarizations. However, this particular ellipsoidal case does not result in a V_r independent of θ_r and ϕ_r. Therefore, our goal next is to optimize the ellipsoidal polarization to completely remove angular misalignment problem of the Rx.

Analytical optimization of the ellipsoidal polarization

For analysis, let the current amplitudes are defined as $I_{Tx}^x = kI, I_{Tx}^y = kI, I_{Tx}^z = I$ satisfying the amplitude condition for ellipsoidal case, where amplitude factor k is a parameter of optimization. This reduces the V_r expression of (3.9) for ellipsoidal polarization to

$$(V_r^E)^2 = \left(\frac{N_{Tx}N_r\mu_o AI}{2r_{Tx}}\right)^2 \left[\frac{1}{4}(\omega_c^2+\omega_m^2)k^2\sin^2\theta_r + \frac{1}{2}\omega_c^2\cos^2\theta_r\right]. \tag{3.10}$$

Note that the judiciously chosen current amplitude condition results in a V_r that is independent of ϕ_r. Further, the expression is rearranged to

$$(V_r^E)^2 = \left(\frac{N_{Tx}N_r\mu_o AI}{2r_{Tx}}\right)^2 \left[\frac{1}{4}((\omega_c^2+\omega_m^2)k^2 - 2\omega_c^2)\sin^2\theta_r + \frac{1}{2}\omega_c^2\right]. \tag{3.11}$$

To obtain the V_r independent of θ_r, the initial terms in (3.11) should vanish, this evolves the condition on amplitude factor k as

$$(\omega_c^2+\omega_m^2)k^2 - 2\omega_c^2 = 0, \quad \Rightarrow \quad k_{opt} = \sqrt{\frac{2}{1+\left(\frac{\omega_m}{\omega_c}\right)^2}}. \tag{3.12}$$

The optimal amplitude factor k_{opt} is determined by (3.12) which is depending solely on frequencies of the AM signal. In our case, since $\omega_c >> \omega_m$ for the AM signal, the optimal amplitude factor can be approximately obtained as $k_{opt} = \sqrt{2}$. Hence, to completely eliminate the angular misalignment problem, the analytical optimization proposed here proves that the excitation current amplitudes should be dictated by optimal relation $I_{Tx}^x = \sqrt{2}I, I_{Tx}^y = \sqrt{2}I, I_{Tx}^z = I$ and other parameters must have values $m = 1$, $\psi_m = \pi/2$, $\psi_c = \pi/2$. This results in an optimized ellipsoidal polarization and completely remove the angular misalignment problem of the Rx. Next, to verify the analytically obtained optimization results, a numerical optimization study is conducted.

Numerical optimization and parametric study

To mitigate the angular misalignment completely, the standard deviation σ_{V_r} of V_r with respect to θ_r and ϕ_r should be minimized. In the numerical optimization study, all possible 3−D polarization cases are covered. For that, we have considered five optimization variables, i.e., k, $I = I_{Tx}^z$, m, ψ_m and ψ_c and the desired objective function with constraints

is defined,

$$\begin{aligned} \underset{k,I,m,\psi_c,\psi_m}{\text{minimize}} \quad & \sigma_{V_r(k,I,m,\psi_c,\psi_m)} \\ \text{subject to} \quad & 0 \leq k \leq 2,\ 0 \leq m \leq 1, \\ & 0 \leq I \leq I_0,\ \overline{V_r} = \overline{V_0}, \\ & 0 \leq \psi_c \leq \pi/2,\ 0 \leq \psi_m \leq \pi/2 \end{aligned} \tag{3.13}$$

where $I_0 = 2A$ is the current amplitude limit for I_{Tx}^z (correspondingly limiting the amplitudes of I_{Tx}^x and I_{Tx}^y), $\overline{V_0}$ is the desired mean $\overline{V_r}$ of V_r averaged over θ_r and ϕ_r. A parametric study is performed to analyze variation of σ_{V_r} with the optimization parameters k, I, m, ψ_c and ψ_m.

Parametric study result

The variation of σ_{V_r} with respect to the optimization variables is presented in Figure 3.6. For instance, Figure 3.6(a), (b), and (c) shows the variation of σ_{V_r} versus k for various

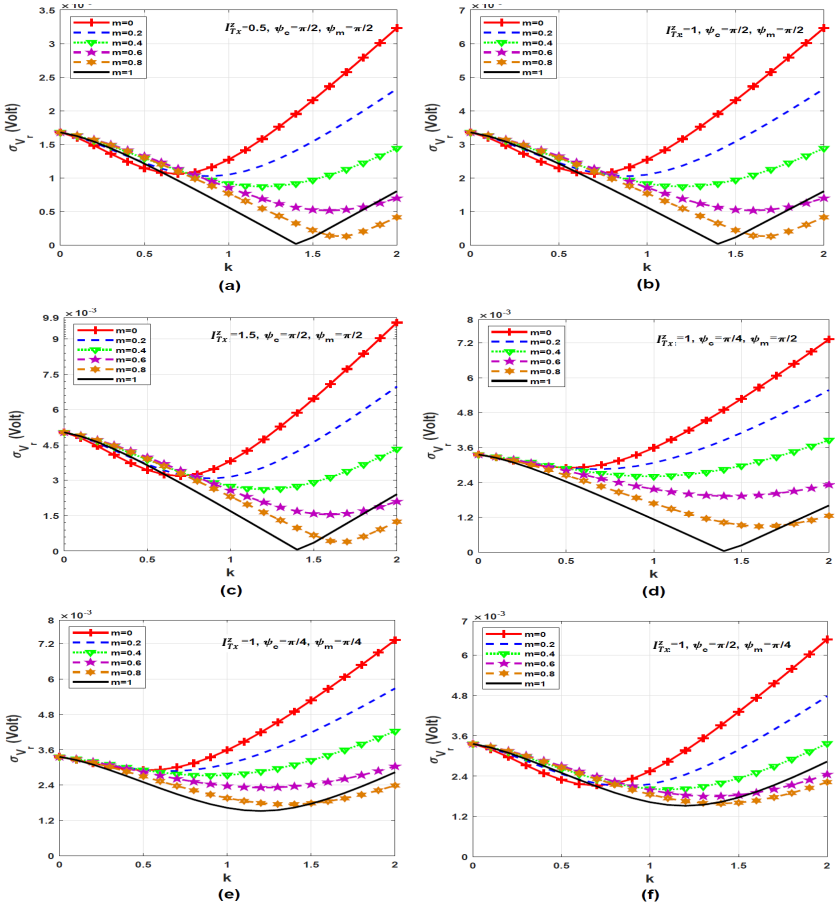

Figure 3.6: Parametric results for varying the optimization variables.

values of m and I_{Tx}^z for a particular $\psi_c = \psi_m = \pi/2$. The plot shows that a minimum (close to zero) σ_{V_r} is achieved for $m = 1$ and $k = 1.41 = \sqrt{2}$. Similarly, from Figure 3.6(b) and (d), we observe that the optimal m and k values remain the same for different ψ_c, however, the minimum value of σ_{V_r} increases with lower ψ_c. The same is noted for ψ_m variation from Figure 3.6(d) and (f) that the minima of σ_{V_r} rises when ψ_m is reduced. Furthermore, by comparing the results of Figure 3.6(e) and (f), we infer that σ_{V_r} does

not attain a minima if ψ_c and ψ_m are less than $\pi/2$. This suggests that $\psi_c = \psi_m = \pi/2$ represents the optimal solution to minimize the σ_{V_r}.

To analyze the effect of I^z_{Tx}, we note from (3.10) that V_r varies linearly with I^z_{Tx}, the dependency is shown in Figure 3.7 in terms of σ_{V_r} and $\overline{V_r}$. The optimized parameter

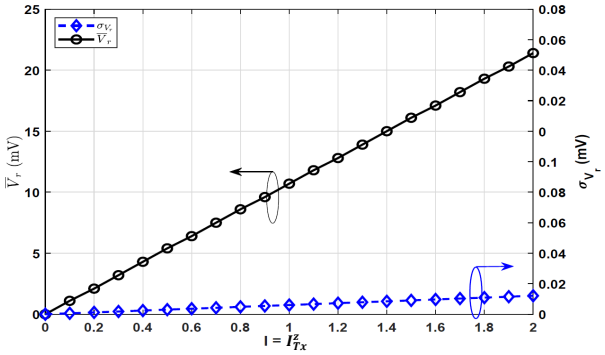

Figure 3.7: Variation of $\overline{V}_r$ and σ_{V_r} with respect to I^z_{Tx}.

values for this result are set as $k = \sqrt{2}$, $m = 1$, and $\psi_m = \psi_c = \pi/2$. It is observed that $\overline{V_r}$ and σ_{V_r} both increase with I^z_{Tx}, however, the increment in σ_{V_r} is negligibly small in μV and still attains a minima to fulfill the objective function. Therefore, the choice of parameter I^z_{Tx} depends only on the $\overline{V_r}$ requirement.

In this study, for a fair comparison of the polarization schemes, $\overline{V_0} = 9.3$ mV is chosen which corresponds to the $\overline{V_r}$ of the spherically polarized field shown in Figure 3.5(b). To achieve the same $\overline{V_r}(= \overline{V_0} = 9.3$ mV) for the proposed optimal ellipsoidal polarization, the corresponding amplitude parameter is calculated from Figure 3.7 as $I = I^z_{Tx} = 0.87$ A.

Numerical evaluation

As a proof, the formulated optimization problem of (3.13) is solved using commercial software MATLAB. By utilizing optimization tool, a genetic algorithm is run to find a global optimal solution. The objective function given in (3.13) is incorporated in the algorithm and the optimization parameters are assigned with the limits. The algorithm terminates successfully after 71 iterations attaining the objective function values as $\sigma_{V_r} = 0.01$ mV and $\overline{V}_r = 9.3$ mV. The optimized parameter values are revealed as $k = 1.463$, $m = 0.965$, $I^z_{Tx} = 0.87$ A, $\psi_c = 1.481$ rad and $\psi_m = 1.543$ rad which are in close approximation to the values obtained from the analytical optimization presented in Chapter 3.1.3.

Analytical result of the optimal polarization

The analytically obtained and numerically verified solution of (3.13) results in an optimal ellipsoidal polarization eliminating the angular misalignment problem and shown in Figure 3.8(a). The V_r performance of the proposed ellipsoidally polarized H-field is analyzed in Figure 3.8(b) for all the Rx inclinations. The results show a negligible variation of V_r with θ_r and ϕ_r implying mitigation of angular misalignment problem.

To compare the performance of various 3−D polarizations, respective $\overline{V}_r$ and σ_{V_r} are calculated with respect to θ_r and ϕ_r. In addition, to compare peak variation in V_r, the

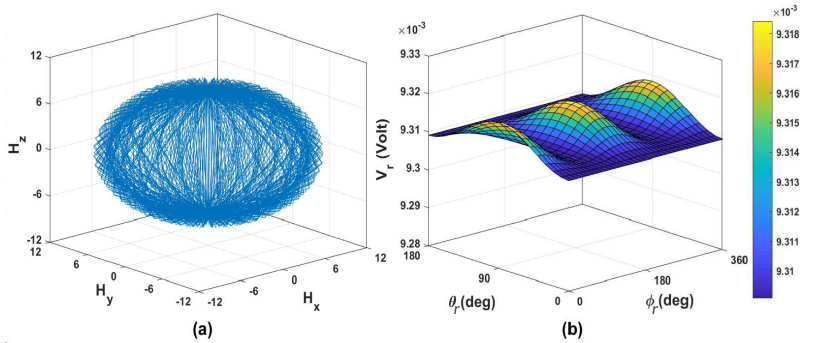

Figure 3.8: Optimized ellipsoidally polarized H-field and corresponding V_r variation.

difference between maximum to minimum V_r value is found as $V_{max} - V_{min}$. Table 3.1 summarizes the results corresponding to the drum-shaped, spherical, and ellipsoidal

Table 3.1: Performance comparison of various 3−D polarizations.

3D polarization	$V_{max} - V_{min}$ (mV)	$\overline{V}_r$ (mV)	σ_{V_r} (mV)
Drum-shaped	6.500	9.3	1.600
Spherical	3.100	9.3	1.100
Ellipsoidal(not optimized)	1.800	9.3	0.505
Ellipsoidal (optimized)	0.013	9.3	0.003

(not-optimized) polarizations presented in Figure 3.5, and proposed optimized ellipsoidal result presented in Figure 3.8(b). The data in Table 3.1 show that the peak variation $V_{max} - V_{min}$ of the drum-shaped, spherical, and ellipsoidal (not-optimized) polarizations are 6.5 mV, 3.1 mV, and 1.8 mV, respectively, showing a high variation in V_r for the three cases. In addition, the σ_{V_r} values for these cases are 1.6 mV, 1.1 mV, and 0.5 mV, respectively, where the former shows the highest variation. Essentially, the proposed ellipsoidal (optimized) polarization outperforms others with a peak variation $V_{max} - V_{min} =$ 0.013 mV and $\sigma_{V_r} =$ 0.003 mV, proving that the V_r variation is minimum in the proposed case. For a fair comparison, $\overline{V}_r =$ 9.3 mV is the same in all the cases implying an equal average power delivery. Hence, the optimized ellipsoidally polarized H-field is proved to be a solution to mitigate angular misalignment which delivers constant power at the Rx in any orientation.

3.1.4 Simulation and Results

The analytical results presented in Chapter 3.1.3 are verified by simulations using commercial software Ansys EM Suite 19.1. The Tx and Rx coils shown in Figure 3.1 are designed in Ansys Maxwell and the structure is imported in Ansys Simplorer for circuit simulation. Figure 3.9 presents the simulation setup consisting of resonating capacitor in series with each coil and modulators to generate required excitations. Two AM signals and one carrier signal as defined in (3.3) of desired frequency at the Tx is generated. Sinusoidal sources of corresponding frequencies 500 Hz and 6.78 MHz are used to generate AM signals feeding the two Tx coils and a sinusoidal excitation of 6.78 MHz is used to excite the third Tx coil. The excitation current amplitudes are controlled using resistors placed in series of the coils to generate spherical and ellipsoidal H-field polarizations. The setup is simulated for various orientations of the Rx coil and the induced voltage at the Rx is observed.

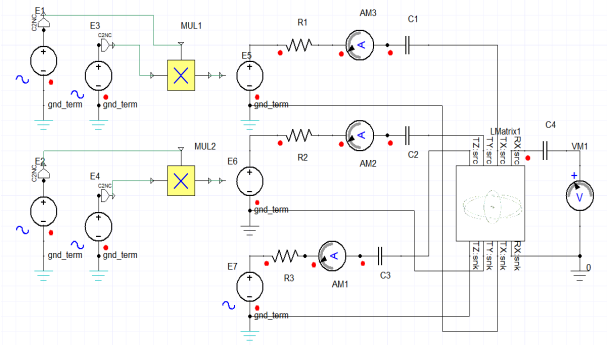

Figure 3.9: Simulation model of the WPT system in Ansys Simplorer.

The results are presented in Figure 3.10 showing the variation of V_r with θ_r for various

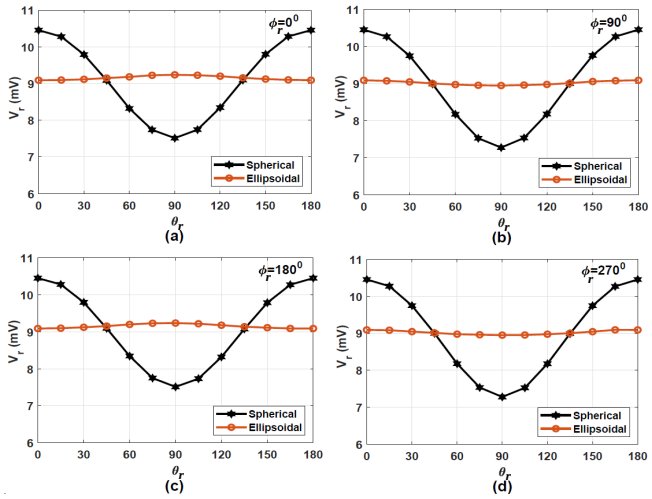

Figure 3.10: Simulation results of the spherical and optimized ellipsoidal polarizations.

values of ϕ_r. The simulated results corroborate the analytical results of Figure 3.5(b) and Figure 3.8(b) and demonstrate that, for the same V_r, the spherical H-field polarization has a high variation in V_r with a peak to peak 2.94 mV, whereas, the ellipsoidal H-field polarization has a reduced peak variation to 0.14 mV. This implies that the simulated result shows a small variation of V_r for proposed ellipsoidally polarized H-field as compared to the spherically polarized H-field. Experimental verification is conducted subsequently.

3.1.5 Experimental Verification

To validate the results, the WPT system of Figure 3.1 is realized consisting of three orthogonal Tx coils (r_{Tx} = 50 mm and N_{Tx} = 10) made of litz wire, which contain 25 strands of 47 gauges. Using the same wire, the Rx coil (r_r = 3 mm and N_r = 60) is fabricated and placed at the center of the Tx as demonstrated in Figure 3.11. The unloaded coil impedance is measured using Agilent Vector Network Analyzer (VNA) (PNA-L N5230C). The measured values of resistance and inductance are 1.93 Ω and 26.22 μH for each Tx coil and 1.69 Ω and 24.19 μH for the Rx coil, respectively. A matching network is connected to each coil to resonate them at the operating frequency. The complete hardware setup of the WPT system is shown in Figure 3.11. The three Tx coils

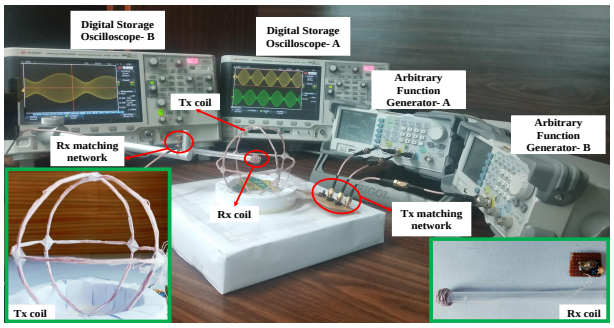

Figure 3.11: Experimental setup of the WPT system.

are excited using two synchronized dual channel Rigol function generators (DG1062Z). To measure the V_r at the Rx port, Keysight DSO (DSOX2022A) is utilized. The function generator-A excites two AM signals as visualized from DSO-A. Whereas, the function generator-B generates sinusoidal carrier signal. The output V_r of the Rx coil is measured using DSO-B. Figure 3.12 plots the normalized V_r recorded for various orientations of the Rx coil. The results show a good agreement between the measured and simulated

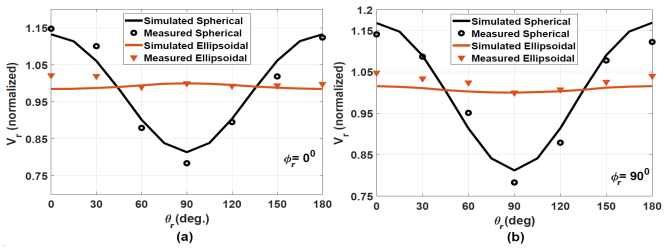

Figure 3.12: Measured result for angular misalignment (a) ϕ_r= 0° (b) ϕ_r= 90°.

data and verify the performance of proposed scheme. For comparison, σ_{V_r} is evaluated for ϕ_r= 0° and ϕ_r= 90° for spherical and ellipsoidal polarizations. Figure 3.12, the σ_{V_r} is evaluated as 0.14 mV measured and 0.08 mV simulated value for the proposed ellipsoidal H-field polarization whereas 1.24 mV measured and 1.13 mV simulated values are obtained for spherical H-field polarization. Hence, the proposed optimized polarization achieves a V_r which is nearly invariant to the Rx orientation. As a result, the performance remains consistent in case of the proposed 3−D polarization irrespective of the angular misalignment of the Rx. However, the 3−D Tx structure presented has several drawbacks, such as its inability to be directly used for biomedical implants and mass production. These limitations can be addressed by employing a 2−D Tx structure presented subsequently.

3.2 System Configuration of Planar Transmitter Antenna (Design-1B)

To generate a 3−D polarized H-field distribution at the Rx location, amplitude modulated (AM) excitations are utilized. Since, the excitation current determines the distribution of instantaneous H-field originated by a coil, the AM modulated field projections to generate

3−D rotating H-field are formulated as

$$\left.\begin{aligned} h_x(t) &= H_x \cos(\omega_m t)\sin(\omega_c t),\\ h_y(t) &= H_y \sin(\omega_m t)\sin(\omega_c t),\\ h_z(t) &= H_z \cos(\omega_c t). \end{aligned}\right\} \tag{3.14}$$

Here, the peak amplitudes H_x, H_y and H_z at the Rx region is obtained using (2.3). To generate these components defined in (3.14), a planar multicoil Tx is proposed here. Figure 3.13 illustrates the schematic view of the proposed design comprising a total

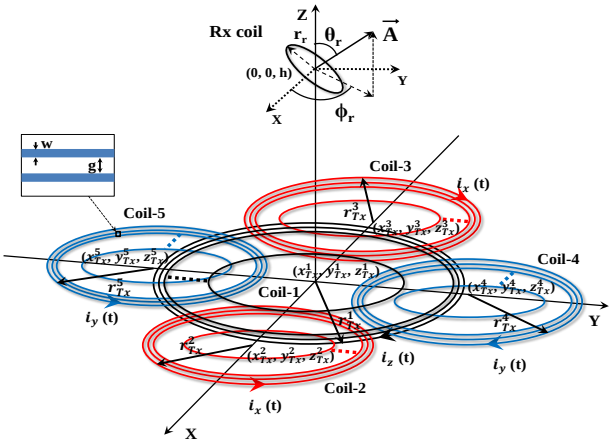

Figure 3.13: Planar multicoil antenna to produce 3−D polarized H-field.

of five multi-turn planar coils distributed in space. Each coil-i $\forall$i $\in$ [1, 5] has location $(x^i_{Tx}, y^i_{Tx}, z^i_{Tx})$ and radius r^i_{Tx} as shown in Figure 3.13. For an efficient field forming at the Rx location, the excitation current and geometrical parameters of the individual coil are controlled. Since the Rx is located at (0, 0, h) as shown in Figure 3.13, coil−1 alone is sufficient to form $h_z(t)$ field at the Rx location. Whereas to produce $h_x(t)$ component at the Rx location, coil−2 and coil−3 carry currents with opposite circulation as depicted in Figure 3.13, this incorporates 180° phase shift in the excitation current, thus resulting a generation of $h_x(t)$ component at the Rx location (0, 0, h) from Fleming's right-hand rule. Similarly, coil−4 and coil−5 produce the $h_y(t)$ component at the Rx location. Moreover, the presence of anti-parallel turn coils minimizes the mutual coupling between the proposed Tx antenna. Further derivation of an optimal H-field condition for the proposed planar multicoil antenna V_{ind} is analyzed subsequently.

3.2.1 Condition for Generating Optimal 3-D Polarization

For the scenario shown in Figure 3.13, the V_{ind} in the Rx coil is evaluated using (2.9). To simplify the analysis further, it is assumed that the Rx is very small compared to the Tx depicted in Figure 3.13. This condition implies a uniform H-field throughout the Rx

dimension. The substitution of (3.14) in (2.9) results in V_{ind} formulation as

$$V_{ind}(t,\theta_r,\phi_r) = -N_r\mu_o\Bigg[\frac{H_xA_x}{2}\Big((\omega_c+\omega_m)\cos((\omega_c+\omega_m)t)+(\omega_c-\omega_m)\cos((\omega_c-\omega_m)t)\Big)+\frac{H_yA_y}{2}\Big((\omega_c+\omega_m)\sin((\omega_c+\omega_m)t)-(\omega_c-\omega_m)\sin((\omega_c-\omega_m)t)\Big)-H_zA_z\omega_c\sin(\omega_ct)\Bigg]. \tag{3.15}$$

It is noted from (3.15) that the V_{ind} solution is a function of the Rx orientation (θ_r, ϕ_r). To completely mitigate the angular misalignment problem, the V_{ind} should be independent of θ_r and ϕ_r. To analyze this, the V_{ind} for various orientations of the Rx coil is investigated.

For $\theta_r = 0°$ & $\phi_r = 0°$

This case corresponds to perfectly aligned Rx ($A_x = A_y = 0$ and $A_z = A$) which is coplanar to the Tx. Under this condition only $h_z(t)$ contributes to the V_{ind} in the Rx coil, hence, using (3.15), it is derived as

$$V_{ind}(t,0^\circ,0^\circ) = N_r\mu_oH_zA\omega_c\sin(\omega_ct). \tag{3.16}$$

The RMS value of V_r is evaluated using the expression (2.10). Hence, the V_r value for the perfectly aligned Rx case (V_r^z) is evaluated as

$$V_r^z = \frac{N_r\mu_oH_zA}{2}\sqrt{2\omega_c^2}. \tag{3.17}$$

For $\theta_r = 90°$ & $\phi_r = 0°$

For this case, the area projections have values $A_x = A$, $A_y = A_z = 0$ and only $h_x(t)$ contributes to the $V_{ind}(t)$ which is determined from (3.15) as

$$V_{ind}(t,90^\circ,0^\circ) = -\frac{N_r\mu_oH_xA}{2}\Big[(\omega_c+\omega_m)\cos((\omega_c+\omega_m)t)+(\omega_c-\omega_m)\cos((\omega_c-\omega_m)t)\Big]. \tag{3.18}$$

The RMS value for this case, V_r^x, is evaluated using (2.10) in (3.18) by assuming $\omega_c = n\omega_m$, where n is an integer and obtained as

$$V_r^x = \frac{N_r\mu_oH_xA}{2}\sqrt{(\omega_c^2+\omega_m^2)}. \tag{3.19}$$

For $\theta_r = 90°$ & $\phi_r = 90°$

Similar, for this case, the area projections are $A_x = 0$, $A_y = A$, and $A_z = 0$ and only $h_y(t)$ contributes to the $V_{ind}(t)$ and found using (3.15)

$$V_{ind}(t,90^\circ,90^\circ) = -\frac{N_r\mu_oH_yA}{2}\Big[(\omega_c+\omega_m)\sin((\omega_c+\omega_m)t)-(\omega_c-\omega_m)\sin((\omega_c-\omega_m)t)\Big]. \tag{3.20}$$

The RMS value for this case, V_r^y, is obtained by using (2.10) and (3.20) as

$$V_r^y = \frac{N_r\mu_oH_yA}{2}\sqrt{(\omega_c^2+\omega_m^2)}. \tag{3.21}$$

To eliminate the θ_r and ϕ_r dependency of V_r, the expressions (2.10), (3.19), and (3.21) are equated to each other so that the V_r is equal in all the three orientations. By solving this the optimal H-field condition obtained are

$$H_x = H_y = H_z\sqrt{\frac{2\omega_c^2}{(\omega_c^2+\omega_m^2)}}. \tag{3.22}$$

The derived optimal field conditions of (3.22) show that to mitigate angular misalignment problem completely, the optimized 3-D polarization is an ellipsoidal polarization since $H_z \neq H_x$ and $H_z \neq H_y$. The proposed antenna is optimized to form the optimal 3-D ellipsoidally polarized H-field adhering to the conditions derived in (3.22).

3.2.2 Analytical optimization of the proposed transmitter

To obtain maximum $S21$ between the Tx and Rx coils, the Tx coil parameters such as coil radius (r_{Tx}^i), number of turns (N_{Tx}^i), strip width (w_{Tx}^i) and spacing between the turns (g_{Tx}^i) for coil-i $\forall$i $\in$ [1, 5] are optimized in accordance to the formulated problem defined as

$$\begin{aligned}
&\underset{r_{Tx}^i, N_{Tx}^i, w_{Tx}^i, g_{Tx}^i}{\text{Maxmize}} \quad S21(r_{Tx}^i, N_{Tx}^i, w_{Tx}^i, g_{Tx}^i) \\
&\text{subject to} \\
&r_{Tx}^1 \leq 70 \text{ mm},\ r_{Tx}^2, r_{Tx}^3, r_{Tx}^4, \text{and } r_{Tx}^5 \leq 29 \text{ mm}, \\
&H_x = H_y = H_z\sqrt{\frac{2\omega_c^2}{(\omega_c^2+\omega_m^2)}}, \text{and} \left(\omega_c L - \frac{1}{\omega_c C}\right) > 0.
\end{aligned} \tag{3.23}$$

Here, r_{Tx}^1 is restricted to 70 mm such that coil-1 can form maximum H-field at the Rx location (0, 0, 50) mm from (2.3). To avoid any electrical shorting between tracks of different coils, their locations are set carefully. For this purpose, coils are spatially distributed, i.e., coil-1 is placed at the origin (backside of PCB), whereas all other coils are located in z = 1.6 mm plane (front side of PCB). The coils $2-5$ are distributed as shown in Figure 3.13 with their centers having coordinates (41, 0), (-41, 0), (0, 41) and (0, -41) in mm, respectively. This allows a maximum radius of 29 mm for these coils to constrain the maximum antenna size to 140 mm. Moreover, the last constraint in the optimization problem of (3.23) corresponds to the reactance criteria for determining sign change of net reactance value, which is obtained by calculating the inductance and capacitance analytically using (2.12) and (2.14) for various coil parameters. This reactance criterion is imposed to refrain the optimized coil from adopting a very high number of turns and become capacitive. This is because, under high-frequency operation, the capacitive effect in a multi-turn coil may dominate. The reason for discarding such Tx coil solutions working in a capacitive region is due to the requirement of a complex matching network which further leads to wastage in the form of electric field.

To optimize the Tx coil antenna, a parametric sweep is performed using MATLAB 2019a. For this, a planar Rx coil presented in having diameter= 20 mm, and the number of turns= 6 is considered where the track width and gap are set as 0.5 mm in accordance to the fabrication limits of the available PCB prototyping machine. During the parametric study,

the optimization procedure calculates the coil parameters for different coils as formulated in Section 2.3 and determined using (2.12), (2.13), and (2.14). The optimization procedure begins to optimize the coils $2-5$ to maximize the $S21$ parameter calculated using (2.18). The reason behind optimizing the coils $2-5$ prior to the coil-1 is that the maximum H_x and H_y that the optimized coils $2-5$ will generate, the coil-1 alone is able to generate sufficient H_z such that the field condition given in (3.22) is satisfied, but the converse may not be true because of the space limitation of the coils $2-5$. Once the coils $2-5$ are optimized, the optimal H-field for the coil-1 is found from (3.22), and the optimal parameters of the coil-1 are then evaluated. The parametric study results obtained by the design procedure are presented in the following.

Parametric Study Results

To satisfy the field condition $H_x = H_y$ in (3.22), the coils 2-5 must be identical, therefore, their design parameters are also same and considered as r_{Tx}^2, w_{Tx}^2, g_{Tx}^2, and N_{Tx}^2. Figure 3.14 demonstrates the normalized plots of $S21$ by varying coils $2-5$ parameters. Figure 3.14(a) shows the variation of $S21$ versus g_{Tx}^2 for various values of N_{Tx}^2, where

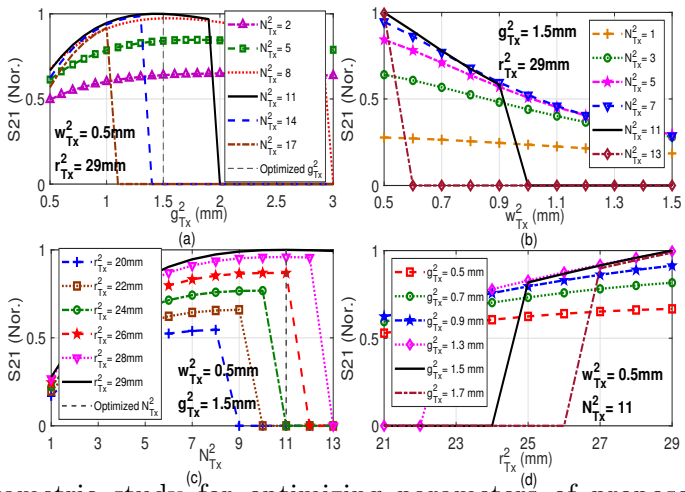

Figure 3.14: Parametric study for optimizing parameters of proposed Tx coil $2-5$. Normalized $S21$ versus (a) g_{Tx}^2, (b) w_{Tx}^2, (c) N_{Tx}^2, and (d) r_{Tx}^2.

$w_{Tx}^2 = 0.5$ mm and $r_{Tx}^2 = 29$ mm. The result shows that a maximum $S21$ is achieved at the optimized values $g_{Tx}^2 = 1.5$ mm and $N_{Tx}^2 = 11$. Figure 3.14(b) shows variation of $S21$ versus w_{Tx}^2 for different values of N_{Tx}^2 when $g_{Tx}^2 = 1.5$ mm and $r_{Tx}^2 = 29$ mm. This result indicates that the maximum $S21$ is achieved for a minimum w_{Tx}^2 and at $N_{Tx}^2 = 11$. Due to the fabrication limits of the available PCB prototyping machine, the minimum possible $w_{Tx}^2 = 0.5$ mm is selected. Similarly, Figure 3.14(c) illustrates the $S21$ variation with N_{Tx}^2 for different values of r_{Tx}^2 at $w_{Tx}^2 = 0.5$ mm and $g_{Tx}^2 = 1.5$ mm. This plot shows that the $S21$ is optimized for $r_{Tx}^2 = 29$ mm and $N_{Tx}^2 = 11$ is chosen because the increment in $S21$ is almost constant beyond $N_{Tx}^2 > 11$. Figure 3.14(d) describes the variation of $S21$ versus r_{Tx}^2 for different values of g_{Tx}^2 while $w_{Tx}^2 = 0.5$ mm and $N_{Tx}^2 = 11$. The result indicates that the maximum $S21$ is achieved for $r_{Tx}^2 = 29$ mm and $g_{Tx}^2 = 1.5$ mm. Corresponding to these optimized parameters of the coils $2-5$ as $r_{Tx}^2 = 29$ mm, $N_{Tx}^2 = 11$, $w_{Tx}^2 = 0.5$ mm, and $g_{Tx}^2 = 1.5$ mm, the values of H_x and H_y are obtained using (2.3) at the Rx

location as $H_x = H_y = 11.46$ A/m. To satisfy the optimal field condition of (3.22), the required H_z field is calculated to be 8.10 A/m. To generate this H_z field, the coil−1 is optimized by allowing 1% variation in the analytically obtained H_z value. Figure 3.15 shows parametric study of the coil−1 optimization. Figure 3.15(a) plots the variation

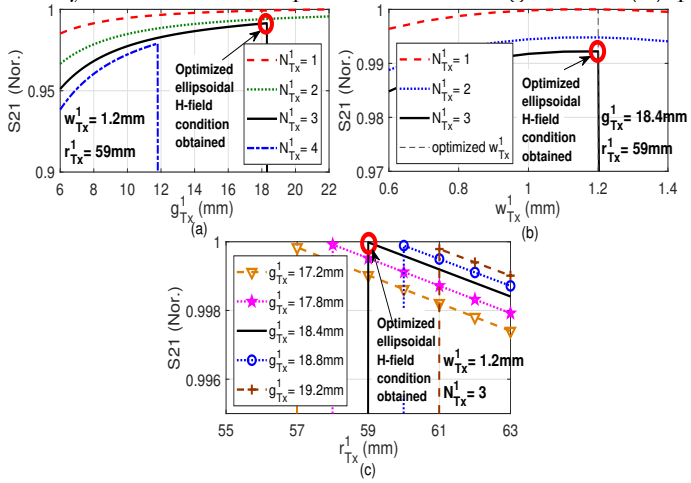

Figure 3.15: Parametric study for optimizing the proposed Tx coil-1. Normalized S21 versus (a) g^1_{Tx}, (b) w^1_{Tx}, and (c) r^1_{Tx} for various N^1_{Tx}.

of $S21$ versus g^1_{Tx} for different values of N^1_{Tx}, where $w^1_{Tx} = 1.2$ mm, and $r^1_{Tx} = 59$ mm. This plot indicates that the optimized ellipsoidal H-field condition is satisfied for $g^1_{Tx} = 18.4$ mm and $N^1_{Tx} = 3$. Figure 3.15(b) includes variation of $S21$ versus w^1_{Tx} for different values of N^1_{Tx} indicating the optimized ellipsoidal H-field condition achieved for $w^1_{Tx} = 1.2$ mm and $N^1_{Tx} = 3$. Similarly, Figure 3.15(c) shows that the maximum $S21$ and the optimized ellipsoidal H-field condition both are simultaneously achieved for $r^1_{Tx} = 59$ mm and $g^1_{Tx} = 18.4$ mm. The parameters resulted from the complete parametric study of coil-1 results in $H_z = 8.05$ A/m generated at the receiver location. The optimized parameters of all the coils in the proposed Tx antenna with maximum and minimum radius of $r^i_{Tx}(out)$ and $r^i_{Tx}(in)$ respectively, is summarized in Table 3.2.

Table 3.2: Optimized coil parameters of the proposed antenna

Coil	$r^i_{Tx}(out)$ (mm)	$r^i_{Tx}(in)$ (mm)	N^i_{Tx}	w^i_{Tx} (mm)	g^i_{Tx} (mm)
Coil-1	59	20	3	1.2	18.4
Coil-2 to -5	29	9	11	0.5	1.5

Analytical Results

The H-field distributions in the Rx plane generated by the proposed Tx coil having optimized parameters listed in Table 3.2 is depicted in Figure 3.16. Figure 3.16(a) shows field formation due to coil−1, which shows only H_z component is present at the Rx location. In contrast, coils $2-3$ forms H_x, as shown in Figure 3.16(b). Similarly, H_y due to coils $4-5$ is illustrated in Figure 3.16(c). This shows that the proposed multicoil Tx antenna is able to generate three orthogonal components of H-field at the Rx location as depicted in Figure 3.16(d) over the fields shown in Figure 3.16(a) of the conventional single coil Tx antenna. The total H-field vector distributions plotted at different progressive time instants are shown in Figure 3.16(e) signifying the rotating H-field with time. By using

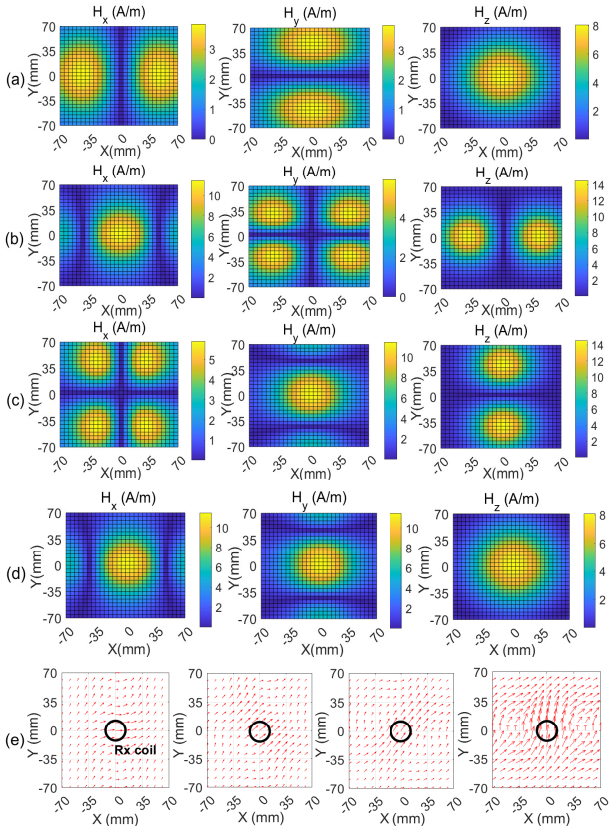

Figure 3.16: Field forming from Tx (a) coil−1, (b) coils $2-3$, (c) coils $4-5$, (d) proposed planar multicoil Tx, (e) H-field vector at progressive time instants.

(3.14), the rotating H-field components are calculated and further used in (3.15) to evaluate V_{ind} in the Rx coil. Figure 3.17 shows the polarization study and variation of V_r under

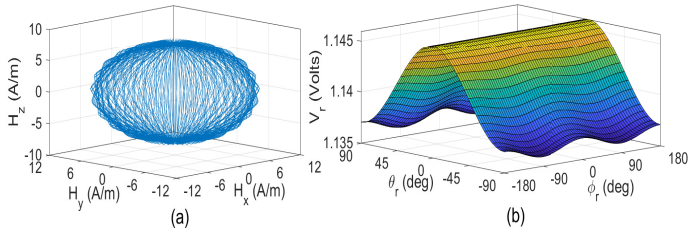

Figure 3.17: Analyzing proposed Tx (a) 3−D ellipsoidally polarized H-field and (b) V_r variation in the misaligned Rx coil having orientation (θ_r, ϕ_r).

different Rx misalignment conditions. From Figure 3.17(a) it is observed that the 3−D ellipsoidally polarized H-field is formed at the Rx location, hence can eliminate angular misalignment problem. Figure 3.17(b) shows the analytically obtained V_r variation for different θ_r and ϕ_r implying a minimal variation in the induced voltage, therefore, the power received by the Rx coil in any orientation is almost same. Further verification of these results is provided in the next section.

3.2.3 The Proposed Antenna Realization

The proposed design presented in Figure 3.13 with optimized parameters provided in Table 3.2 with a planar Rx coil is realized in Printed Circuit Board (PCB) technology. For this purpose, a double-sided FR4 substrate of thickness, $t = 1.6$ mm, relative dielectric

constant $\epsilon_r = 4.4$, loss tangent $\tan\delta = 0.02$, and 0.017 mm of copper deposition is utilized. Figure 3.18 shows the PCB layout of the proposed Tx design. The antenna has three

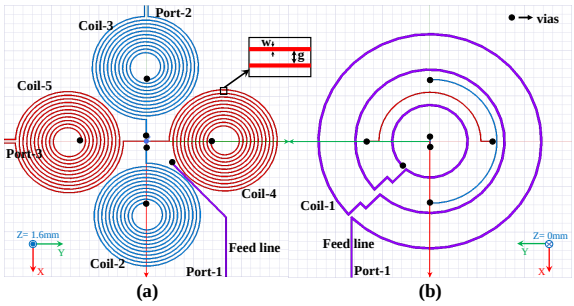

Figure 3.18: The proposed Tx antenna PCB layout (a) front view and (b) back view.

ports and fed with signals defined in (3.14). The coil-1 is fed by port-1 as shown in Figure 3.18. The coils $2-3$ are connected in series through vias such that the current circulation is opposite from each other and fed using common port-2. Similarly, the coils $4-5$ are excited through port-3 and connected in series to obtain opposite current circulation. As apparent from the back view of the layout, these series connections are implemented using two semi-circular printed jumpers to connect the two oppositely placed coils. The connections of the front and the backside of the printed tracks of the Tx coils are made through vias as depicted in Figure 3.18 indicated by solid dots. This layout is implemented, and the analytical results obtained in Section 3.2.2 are verified by using commercial software Ansys EM Suite 19.1. This simulated design is then used for verification of H-field forming at the Rx location. Figure 3.19 illustrates the variation of the

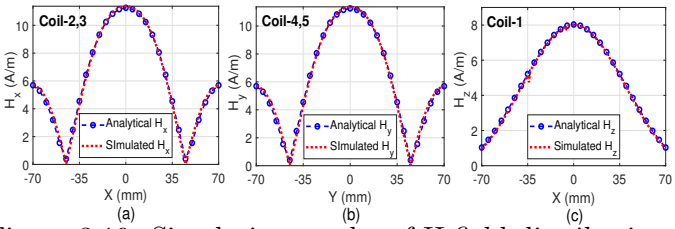

Figure 3.19: Simulation results of H-field distributions.

H-field originated by the proposed Tx antenna in the Rx plane, and the simulated results are found corroborating well with the analytical results. The peak H-field generated at the Rx center has values $H_x = 11.37$ A/m, $H_y = 11.37$ A/m, and $H_z = 8.02$ A/m satisfying the condition (3.22). This validates that the proposed multicoil antenna is able to generate three orthogonal H-field components of desired amplitude to mitigate the angular misalignment problem. The design is experimentally validated subsequently.

3.2.4 Fabrication and experimental results

To validate the design, the proposed Tx antenna is fabricated using a PCB prototyping machine in the laboratory. The fabricated prototype of the proposed Tx antenna along with the Rx coil is shown in Figure 3.20. The input impedances of the unloaded (without resonating capacitors) coils are obtained using an Agilent VNA (PNA-L N5230C). The measured impedance (in Ω) values at different ports of the Tx and the Rx is provided

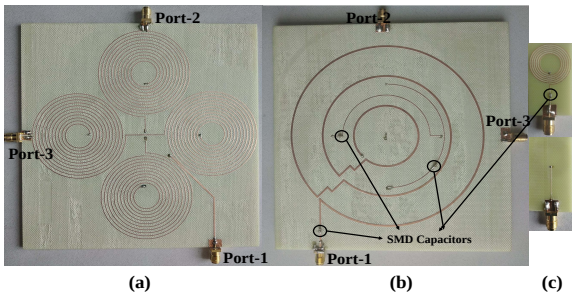

Figure 3.20: Fabricated prototypes view of (a) the Tx front, (b) the Tx back and (c) the Rx front and back.

in Table 3.3. Corresponding to these impedance values, the required capacitances

Table 3.3: Measured coil impedance at different ports.

Port-1	Port-2	Port-3	Port-Rx
0.95 + j6.72	7.5 + j55.97	7.7 + j55.93	1.72 + j5.1

to resonate the proposed Tx and the Rx coils at the system operating frequency are evaluated as $C_{reso}^{port1} = 1.75$ nF, $C_{reso}^{port2} = 0.21$ nF, $C_{reso}^{port3} = 0.21$ nF, and $C_{reso}^{portRx} = 2.30$ nF. The corresponding SMD capacitors are inserted in series with the coils as shown in Figure 3.20. To demonstrate the effectiveness of the proposed antenna to mitigate the angular misalignment problem, the used WPT experimental setup is shown in Figure 3.21. To excite the Tx ports, two synchronized dual-channel Rigol function generators (DG1062Z) are employed. Whereas V_r is measured at the Rx port using Keysight Digital Storage Oscilloscope (DSOX2022A). Here, the function generator-A

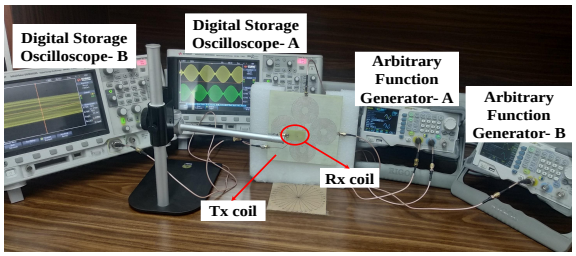

Figure 3.21: Experimental setup of the WPT system.

generates two AM signals and excites port−2 and port−3 of the Tx as shown in DSO-A. At the same time, the function generator-B excites the port-1 of the Tx with a carrier signal. The V_r at the Rx coil is measured using DSO-B. Figure 3.22 shows the measured

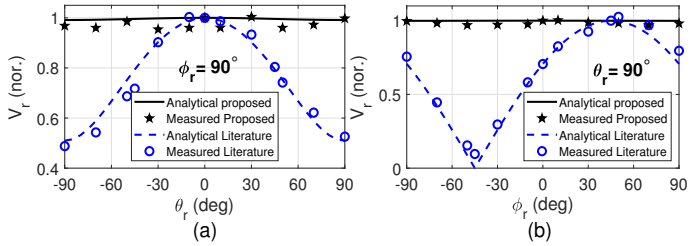

Figure 3.22: Measured V_r in the Rx for angular misalignment (a) $\phi_r = 0°$ (b) $\phi_r = 90°$.

result of V_r variation for different Rx orientations. The comparison of the proposed Tx with the previous design available in the literature [7] is performed. The calculated standard deviation (σ_{V_r}) in the V_r for the literature design is 0.2247 V in all the orientations, whereas, for the proposed Tx, σ_{V_r} is 0.0034 V. The V_r of the literature design shows 98.48%

higher variation over the proposed design. This proves that the proposed antenna has a minimal variation in the V_r compared to the literature design. The link efficiency of the proposed system, when the Rx coil is aligned in $\theta_r = \phi_r = 0°$, is 17.10% for the resistances of the Tx coil−1 and Rx coil evaluated as 0.97Ω and 1.64Ω, respectively. The efficiency is compared with that obtained by the single Tx coil as presented in [7]. The evaluated link efficiency is 5.72% for the single coil when the Rx coil is in perfect alignment with the Tx; this implies an improvement in PTE by the proposed design due to $S21$ optimization in Figure 3.15. Hence, the proposed Tx coil antenna designed in planar technology has the potential to produce optimal 3−D polarized H-field at the Rx location and allows the Rx to rotate freely. As a result, the power transfer performance remains consistent irrespective of the angular misalignment of the Rx coil by the use of the optimized 3−D ellipsoidal polarization generated using the proposed planar antenna design. Further validation of 3−D rotating H-field in far-field regime is presented subsequently.

3.3 Impact of 3-D Rotating Field Forming in Far-Field Regime (Design-1C)

The proposed MPT system consists of three RF showers placed at the three walls of the room, whereas, the IoT node is assumed at the center of the room and allowed to rotate freely in any (θ_r, ϕ_r) orientation as demonstrated in Figure 3.23. All the antennas are

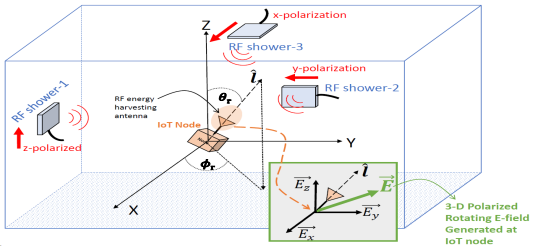

Figure 3.23: The proposed MPT system to generated 3−D polarized E-field.

assumed linearly polarized, and each RF shower is deployed to generate one orthogonal E-field component at the IoT node, i.e., E_z generated by shower−1, E_y by the shower−2, and E_x by the shower−3. Here, for generating 3−D rotating E-field, the RF shower−2 and −3 are excited with amplitude modulated (DSB-SC) signals having phase difference of 90°, and the RF shower−1 is fed with a sinusoidal carrier signal defined as

$$\begin{aligned} v_x(t) &= V_x \cos(\omega_m t)\sin(\omega_c t), \\ v_y(t) &= V_y \sin(\omega_m t)\sin(\omega_c t), \\ v_z(t) &= V_z \cos(\omega_c t). \end{aligned} \tag{3.24}$$

where V_x, V_y, and V_z are the peak amplitudes of the excitation voltages, ω_m is the modulating angular frequency ($2\pi f_m$ rad/sec), ω_c is the carrier angular frequency ($2\pi f_c$ rad/sec), here $f_m = 10$MHz and $f_c = 5.8$GHz. The E-field orthogonal vector components (E_x, E_y and E_z) generated by the RF shower antennas at the IoT node location are demonstrated in the inset of Figure 3.23. Due to these three source excitations, the

total resulting E-field vector ($\vec{E}$) of the three orthogonal components is achieved as a 3−D polarized rotating field. Analysis and result verification of the proposed system is presented in the subsequent section.

3.3.1 Analytical and Simulation Results

The proposed system is analytically modeled in MATLAB 2019a. For analysis purpose dipole antenna (length = 23.3 mm) is assumed as a Rx IoT node and patch antennas are utilized as RF shower placed at a distance of 200 mm from the Rx node as shown in Figure 3.23. The patch antenna is realized on FR4 substrate ($\epsilon_r = 4.4$, $\tan\delta = 0.0024$, thickness (h) = 1.6 mm) having parameters listed in Table. 3.4. The E-field pattern for a patch

Table 3.4: Patch antenna parameters (in mm) used at the RF shower.

Length(L)	Width(W)	Inset Gap(G_f)	Inset length(L_f)	Feed Width(W_f)
11.757	15.73	0.6	3.87	3.1

antenna is given in [105] as

$$\vec{E} = \frac{K_0 h W E_0}{\pi r} e^{-jk_0 r} \left(\frac{\sin k_0 h/2}{k_0 h/2} \right) \hat{n}. \tag{3.25}$$

From our previous study, a 3−D ellipsoidal polarization ($V_x = V_y = \sqrt{2}V_z$) is found as the optimal solution to mitigate the angular misalignment in near-field WPT systems. In this study, we assume that the same is valid for the far-field MPT systems and prove the same by analyzing the polarization results. The 3−D polarization result thus obtained is demonstrated in Figure 3.24(a). Further, the power received (P_r) by the dipole antenna

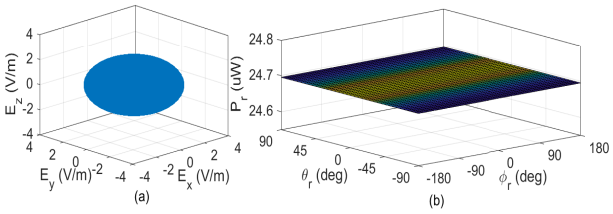

Figure 3.24: Analytical Results (a) Optimal ellipsoidal E-field 3−D polarization (b) Power Received (P_r) in different orientations of the IoT node.

is evaluated by first calculating the induced voltage as $V_{ind} = \vec{E} \cdot \vec{l}$ from the inset of Figure 3.23 by considering a uniform field intensity along the dipole due to far-fields. The received P_r in the IoT node for various orientations is shown in Figure 3.24(b). The result demonstrates that the received power is almost invariant to the IoT orientation hence mitigated angular misalignment problem completely.

The result is verified using Ansys EM Suite 2020$R2$. First, the proposed scenario of Figure 3.23 is implemented in Ansys HFSS as demostrated in Figure 3.25(a). Thereafter, the HFSS structure is imported in Ansys Simplorer for circuit simulation where excitation sources are implemented as shown in Figure 3.25(b). The circuit simulation setup has two AM signals and one carrier signal in accordance with (3.24) at the Tx side. The sinusoidal

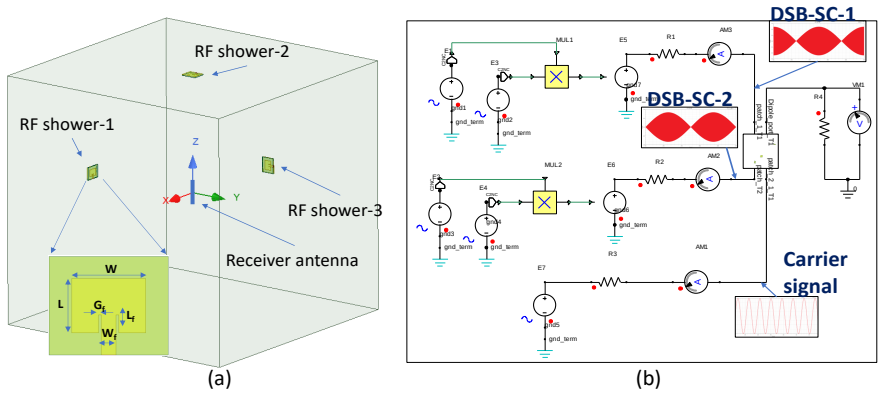

Figure 3.25: Simulation Model (a) System model design in Ansys HFSS (b) Circuit simulation setup in Ansys simplorer.

carrier signal of 5.8 GHz frequency and modulating sinusoidal source of 10 MHz is used to generate AM signals feeding the two patch antennas, and a sinusoidal excitation of 5.8 GHz is used to excite the third patch antenna. The transmitted waves are shown in Figure 3.25(b) in their corresponding feed lines. For comparison purposes, circular polarization (2−D) is considered in an additional setup in which only a circularly polarized antenna is used at the location of the RF shower−3. The setups are simulated for various orientations of the Rx antenna, and the results of P_r measured in the output load are compared in Figure 3.26. It is inferred from the results that, though the circularly polarized RF shower

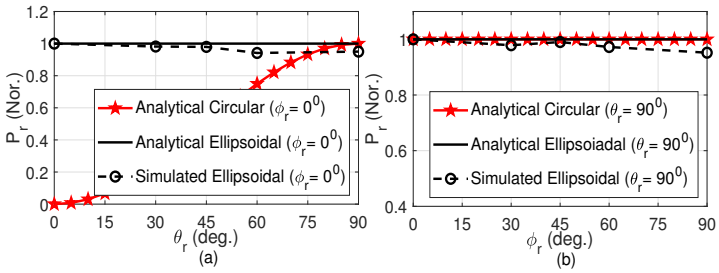

Figure 3.26: Results for different orientations of the IoT node rotating in (a) xoz plane (b) xoy plane.

can mitigate angular misalignment in xoy plane (shown in Figure 3.26(b)) but it still persists in xoz plane (shown in Figure 3.26(a)). Whereas, the proposed 3−D optimal ellipsoidal E-field is able to achieve consistent power delivery to the IoT node in all the orientations. The simulation results are found corroborating with the analytical results, and a slight mismatch can be attributed to the assumption of perfectly matched antennas and uniform incident field intensity in the analytical study. Hence, the proposed 3−D polarized field-forming technique using distributed antenna system is proved to be an effective technique to implement an orientation-insensitive MPT system.

3.4 Summary

In this chapter, the angular misalignment problem present in WPT systems is addressed by investigating various 3−D polarization of the H-field. For this purpose, a 3−D Tx is operated with the required amplitude modulated signals to generate 3−D polarized H-field at the Rx location as exemplified in Design−1A. A complete analysis of the induced voltage in the Rx due to various polarizations (2−D and 3−D) is presented. The previous work indicated the spherically polarized H-field as an intuitive solution to improve power transfer in any orientation of the receiver. However, this work proved that this scheme could not totally mitigate the angular misalignment problem. A parametric study was conducted with the analytically obtained relations and optimization problem was formulated which, as a result, revealed an ellipsoidal polarization to eliminate the problem completely. A proper comparison between the performances of various 2−D and 3−D polarizations is conducted. The results proved that the proposed ellipsoidal polarization outperforms the other polarizations in terms of invariance of the induced voltage in all the orientations of the Rx. Specifically, the standard deviation (peak variation) of rms induced voltage shown by spherical polarization as 1.1 mV (3.1 mV) is reduced to 0.003 mV (0.013mV) by the proposed optimal ellipsoidal polarization. The analytically obtained results are corroborated with the simulation results. In addition, the results are then verified experimentally showing a good agreement with the simulated results. This proves the usefulness of the proposed analysis in the design of WPT systems where uniform power delivery is expected in all the orientations of the receiver. Though, a spherical transmitter is utilized in Design−1A for demonstration, the proposed 3−D polarization study is valid for any Tx antenna structure which is validated in Design−1B.

Furthermore, the proposed optimized 3−D ellipsoidally polarized H-field to address the angular misalignment problem is targeted to generate using a planar multi-coil antenna as demonstrated in Design−1B. The proposed analytical framework of 3−D rotating H-field forming reveals a design with five spatially distributed coils in the proposed planar antenna structure. The antenna having three ports is excited with two amplitude modulated signals and a carrier signal same as provided in Design−1A and optimized to achieve a maximum $S21$ between the Tx and the Rx antennas. The tolerance to angular misalignment is investigated by observing the RMS value of the induced voltage in the Rx coil of any orientation. The analytical results are verified experimentally, showing that the proposed design, although planar, is able to form a 3−D polarized H-field which powers the receiver in any orientation. As compared to a previous 2−port antenna, which was proposed to generate three orthogonal H-field components, the proposed antenna outperforms to mitigate angular misalignment problems. This is due to the optimal 3−D ellipsoidally polarized H-field generated by the proposed antenna compared to the previous design, which produces only 2−D polarization. The results indicate that the standard deviation in RMS induced voltage for the previous design is 0.2247V, whereas, for the proposed design, it is 0.0034V. This concludes that the proposed design showcases a very high

misalignment tolerance with a percentage deviation in RMS induced voltage as 98.48% lower than the previous design. This proves the usefulness of the proposed antenna as a simple and planar design to resolve the angular misalignment problem in WPT systems.
To further validate the performance of proposed 3−D rotating H-field in far-field regime, the angular misalignment problem present in the microwave power transfer system is targeted. The received power in various orientations of the IoT node is analyzed in Design−1C, and the results are verified with a commercially used EM simulator. The comparison study results showed an inconsistent power transmission for a circularly polarized (2−D) antenna. Whereas, the proposed 3−D polarized E-field forming technique has the potential to completely mitigate the angular misalignment problem and results in an orientation-insensitive system.
However, generating a 3−D rotating H-field requires multiple excitations and suffers from abundance flux leakage problems, thus necessitating a new field-forming technique, as presented subsequently.

[0]**CHAPTER OUTCOMES:**

[1]. **V. K. Srivastava** and A. Sharma, "Optimized 3-D Polarized H-Field Forming for Orientation-Insensitive Wireless Power Transfer Systems," in *IEEE Transactions on Antennas and Propagation*, vol. 69, no. 8, pp. 4999-5007, Aug. 2021, doi: 10.1109/TAP.2021.3060140.
[2]. **V. K. Srivastava**, A. Sharma and A. Bharadwaj, "A Planar Distributed Multicoil Antenna to Generate 3-D Ellipsoidally Polarized H-Field for Angular Misalignment Tolerant WPT System," in *IEEE Transactions on Antennas and Propagation*, vol. 70, no. 4, pp. 2969-2978, April 2022, doi: 10.1109/TAP.2021.3137477.
[3]. **V. K. Srivastava**, S. Kumar and A. Sharma, "3D Polarized Field-Forming for Mitigation of Angular Misalignment Problem in Microwave Power Transfer Systems," 2021 *IEEE 19th International Symposium on Antenna Technology and Applied Electromagnetics (ANTEM)*, Winnipeg, MB, Canada, 2021, pp. 1-2, doi: 10.1109/ANTEM51107.2021.9518942.

Chapter 4

Switched Magnetic Field Forming Transmitter

SO−2: *Examine a switching integrated planar Tx for targeting angular and lateral misalignment simultaneously.*

This chapter focuses on the development of a transmitter capable of forming a switched magnetic field, aiming to tackle both angular and lateral misalignment issues. The initial section of this chapter provides a comprehensive overview of the evolution of switched magnetic fields using a planar transmitter, while the latter part focuses on designing a novel transmitter intended to generate a widespread distribution of switched polarized magnetic fields across the receiver region. Additionally, it discusses the evolution and optimization of two distinct Tx antennas, referred to as Design−2A and Design−2B, which align with the objectives outlined in SO−2 as discussed in Section 1.7.

4.1 System Description of Switched Polarized Magnetic Field Forming Transmitter (Design−2A)

The proposed planar Tx antenna for generating a switched polarized H-field is modelled for analysis and depicted in Figure 4.1. The antenna comprises three sets of coils, each

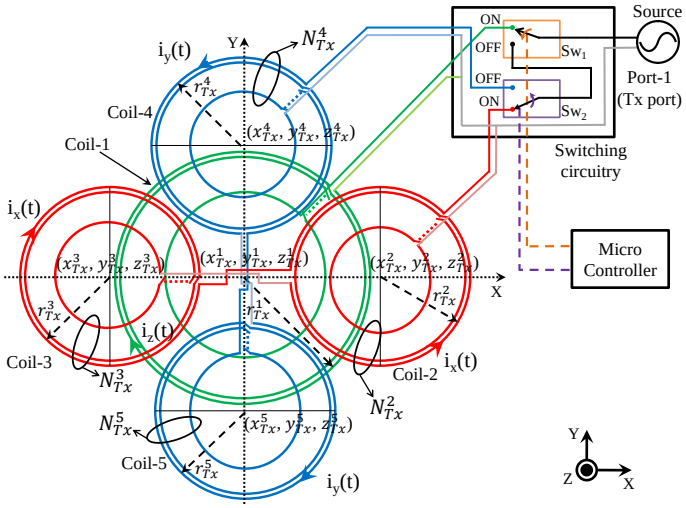

Figure 4.1: Proposed Tx antenna schematic to generate switched polarized H-field.

responsible for generating one orthogonal H-field component at the Rx location, the same

as presented in Figure 3.13. In the first set, an axial Coil−1 is located at the origin and excited with a current $i_z(t)$ to produce the H_z. Whereas, the second set consists of a planar dumbbell shape coil which is a conjunction of Coil−2 and Coil−3 connected in series and distributed in space as shown in Figure 4.1. The Coils $2-3$ are connected in such a manner that the current $i_x(t)$ flows in opposite circulations through these coils, hence, their constructive interference generates H_x at the Rx located on z-axis. Similarly, the third set has another planar dumbbell shape coil composed of series connected Coils $4-5$ which are excited with oppositely circulating current $i_y(t)$ to generate H_y component. Hence, a total five spatially distributed coils labeled as Coil−i are present each having radius r^i_{Tx}, available turns N^i_{Tx}, strip width w^i_{Tx}, spacing between the turns g^i_{Tx} and located at $(x^i_{Tx}, y^i_{Tx}, z^i_{Tx})$, respectively, where $i \in \{1,2,..5\}$. Moreover, the placement of the coils is judiciously done to generate three orthogonal components of the H-field at the Rx location and to avoid any possibility of electrical shorting. For instance, the Coil−1 lies in a different z-plane than the double dumbbell coils to eliminate electrical shorting, similar to Design−1A as demonstrated in Figure 3.13. The only difference between the two designs presented in Figure 3.13 and Figure 4.1 is the excitation provided to the Tx. Where Design−1A requires multiple sources with multi-tone excitation signals for generating 3−D rotating H-field, the system presented in Design−2A needs only a single sinusoidal excitation. Along with the three coil sets (one axial and two dumbbell), a switching circuit is integrated with the antenna design having two SPDT switches, Sw_1 and Sw_2 to realize three states, as depicted in Figure 4.1, respectively generating H_z, H_x, and H_y components. A microcontroller can be used to control the switching period of these switches for generating the proposed switched polarized H-field to mitigate angular misalignment problem as presented in the next section.

4.1.1 Evolution of Switched Polarized H-field Forming

In the proposed approach to mitigate angular misalignment, the three coil sets are switched to generated orthogonal H-field components independently in different time slots within T_s duration which is periodically repeated. The switching periods of Sw_1 and Sw_2 along with the switching states are illustrated in Figure 4.2 , where the Coils $2-3$ are switched

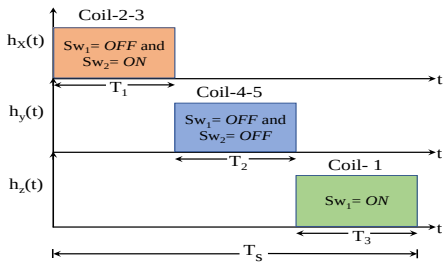

Figure 4.2: Switching sequence to generate switched polarized H-field.

ON for T_1 duration generating h_x, the Coils $4-5$ for T_2 duration generating h_y, and the Coil−1 for T_3 duration to generate h_z. The switching states for the three time slots are:

$\mathrm{Sw}_1 = OFF$ and $\mathrm{Sw}_2 = ON$ during T_1, $\mathrm{Sw}_1 = OFF$ and $\mathrm{Sw}_2 = OFF$ for T_2 duration, and for T_3 switching duration, $\mathrm{Sw}_1 = ON$ independent of the Sw_2 state. This forms switched polarization of the resultant H-field at the Rx location which needs to be optimized such that the power delivery is independent to the Rx orientation. The resultant H-field in one switching period $0 \leq t \leq T_s$, where $T_s = T_1 + T_2 + T_3$, for the sinusoidal source can be formulated by using unit step function $u(t)$ as

$$\begin{aligned}\vec{h}(t) =& H_x \cos(\omega t)[u(t) - u(t - T_1)]\hat{x} + H_y \cos(\omega t)[u(t - T_1) - u(t - (T_1 + T_2))]\hat{y} + H_z \cos(\omega t) \\ & [u(t - (T_1 + T_2)) - u(t - (T_1 + T_2 + T_3))]\hat{z}.\end{aligned} \tag{4.1}$$

Here, H_x, H_y, and H_z are the peak value of the H-field generated by the Coils $2-3$, Coils $4-5$, and Coil -1, respectively, at the Rx location evaluated from (2.3). This switched polarized H-field induces a voltage in the Rx coil and the instantaneous value of V_{ind} is obtained by substituting (4.1) into (2.9) as

$$\begin{aligned}V_{ind}(t, \theta_r, \phi_r) =& - N_r \mu_o \frac{d}{dt}\Big[H_x A_x \cos(\omega t)[u(t) - u(t - T_1)] + H_y A_y \cos(\omega t)[u(t - T_1) \\ & - u(t - (T_1 + T_2))] + H_z A_z \cos(\omega t)[u(t - (T_1 + T_2)) - u(t - (T_1 + T_2 + T_3))]\Big].\end{aligned} \tag{4.2}$$

Since the average power delivered to the load directly depends upon the RMS value V_r of the V_{ind} and evaluated using (2.10) as

$$V_r = \sqrt{\frac{1}{T_s}\int_o^{T_s} V_{ind}^2(t, \theta_r, \phi_r)dt}. \tag{4.3}$$

Following some mathematical manipulations (not included here for brevity) to solve for V_r^2 results in

$$V_r^2 = \frac{(N_r \mu_o A)^2}{2T_s}\Big[H_x^2 T_1 \sin^2\theta_r \cos^2\phi_r + H_y^2 T_2 \sin\theta_r^2 \sin^2\phi_r + H_z^2 T_3 \cos^2\theta_r\Big]. \tag{4.4}$$

To note from (4.4) that the V_r^2 is a function of the Rx orientation (θ_r, ϕ_r). To obtain the V_r^2 independent of θ_r and ϕ_r, the following field constraint must to be satisfied

$$H_x^2 T_1 = H_y^2 T_2 = H_z^2 T_3 \tag{4.5}$$

which simplifies (4.4) into a constant V_R^2 as

$$V_r^2 = \frac{(N_r \mu_o A)^2 H_x^2 T_1}{2T_s}. \tag{4.6}$$

The condition in (4.5) represents an important constraint to design an orientation-oblivion WPT system. The constraint implies the need of an effective control over the switching periods (T_1, T_2, and T_3) for a given H-field distribution generated by any arbitrary antenna which can form orthogonal H-field components (H_x, H_y, and H_z). The switching periods should be controlled such that the product of the squared H-field component with corresponding switching duration, i.e., $H_x^2 T_1$, $H_y^2 T_2$, and $H_z^2 T_3$, must remain constant. For instance, any Tx antenna which generates unequal H-field components in a switchable

manner can be used to completely mitigate angular misalignment problem provided that the switching duration is optimally controlled to satisfy (4.5). Therefore, several antenna solutions can exist corresponding to different unequal H-field combinations with their respective optimal switching states. The converse is also true that for a given unequal switching duration ($T_1 \neq T_2 \neq T_3$), the antenna must be designed to generate optimal unequal H-field satisfy (4.5) to give $H_x \neq H_y \neq H_z$. However, to generate unequal field components, either unequal excitations are fed to the coils or this is directly incorporated in the antenna design process to produce unequal H-field components. The limitation of the former lies in requirement of multiple sources of excitation or additional attenuator with each coil. This increases the system complexity and cost. Whereas, the latter way is much simpler in a manner that any unoptimized antenna design produces unequal H-field components. Therefore, the generation of unequal H-field components is straight forward, however, not optimized for WPT performance. Another way to satisfy (4.5) is by selecting an equal switching duration i.e. $T_1 = T_2 = T_3 = \frac{T_s}{3}$, this supports a symmetrical antenna structure as well as limits the antenna size by imposing the equal H-field criteria. However, designing the antenna to produce $H_x = H_y = H_z$ is challenging since these components are generated by three different distributed coils set, therefore, an optimization is required to incorporate the field condition within the design process itself. In addition, the same optimization should also include the WPT performance improvement as the objective function. This is adopted as design objective in the proposed work where the switching period and the respective H-field constraint are

$$T_1 = T_2 = T_3 = \frac{T_s}{3}, \qquad H_x = H_y = H_z, \tag{4.7}$$

and the corresponding V_r at the Rx coil is obtained from (4.6)-(4.7) as

$$V_r = \frac{N_r \mu_o A H_z}{\sqrt{6}}. \tag{4.8}$$

Given this H-field criteria, the proposed antenna is optimized.

4.1.2 Optimization of Proposed Antenna

The proposed Tx antenna as modelled in Figure 4.1 is optimized to obtain a maximum $S21$ between the Tx and Rx antennas. As defined in (2.18), the $S21$ depends upon various design parameters such as r^i_{Tx}, N^i_{Tx}, g^i_{Tx}, and w^i_{Tx}. The formulated objective function for the proposed antenna design is defined as

$$\begin{aligned} &\max_{r^i_{Tx}, N^i_{Tx}, g^i_{Tx}, w^i_{Tx}} \quad S21(r^i_{Tx}, N^i_{Tx}, g^i_{Tx}, {}^i_{Tx}) \\ &\text{subject to} \\ &r^1_{Tx} \leq 70\text{mm}, \; r^2_{Tx}, r^3_{Tx}, r^4_{Tx}, \text{and } r^5_{Tx} \leq 29\text{mm}, \\ &\quad H_x = H_y = H_z, \quad \text{and} \quad (X_L - X_C) > 0. \end{aligned} \tag{4.9}$$

As design constraints, the maximum coil dimension is limited to restrict the maximum size of the Tx antenna to 140 mm. For this, the r^1_{Tx} is restricted to 70 mm such that it can generate maximum field at the Rx location (0, 0, 50) mm. Whereas, the maximum radius

of the double dumbbell coils is limited to 29 mm with center coordinates (41, 0), (−41, 0), (0, 41), and (0, −41) mm for the Coils $2-5$, respectively, to avoid any electrical shorting. Moreover, the Coil−1 is placed on the bottom layer (at $z = 0$) and other coils on the top layer of the PCB (at $z = 1.6$ mm). Apart from this, a reactance criterion ($X_L - X_C$), where X_L and X_C corresponds to the inductive and capacitive reactance, is imposed in (4.9) to limit the maximum turn possible in a coil such that the coil functions in inductive region only. This avoids unnecessary power loss and complex matching network requirement if the designed coil exhibits capacitive reactance.

Parametric Optimization of the Proposed Antenna

The optimization problem (4.9) for the Tx antenna design is analytically solved using computational tool MATLAB 2021a. The Rx coil parameters with radius $r_r = 10$ mm, turns $N_r = 6$, $g_r = 0.5$ mm and $w_r = 0.5$ mm is adopted for optimization. The design of the Tx antenna is initiated by optimizing first the double dumbbell coils (Coils $2-5$). This is because the maximum lateral H-fields (H_x & H_y) generated by the corresponding coils are always inferior to the H_z field generated by the equivalent Coil−1 alone. However, converse is not always true because of the lower space available for the Coils $2-5$ parametric variation. Succeeding the optimization of the Coils $2-5$, the Coil−1 is optimized to satisfy the H-field constraint presented in (4.5).

Because of the H-field criteria $H_x = H_y$, the double dumbbell coils, Coils $2-5$, are symmetrically identical and share the same values of the design parameters r^i_{Tx}, N^i_{Tx}, g^i_{Tx} and w^i_{Tx}. Therefore, only the Coil−2 notations suffice to present the parametric analysis. The normalized $S21$ variation within time-slot T_1 is plotted in Figure 4.3 with

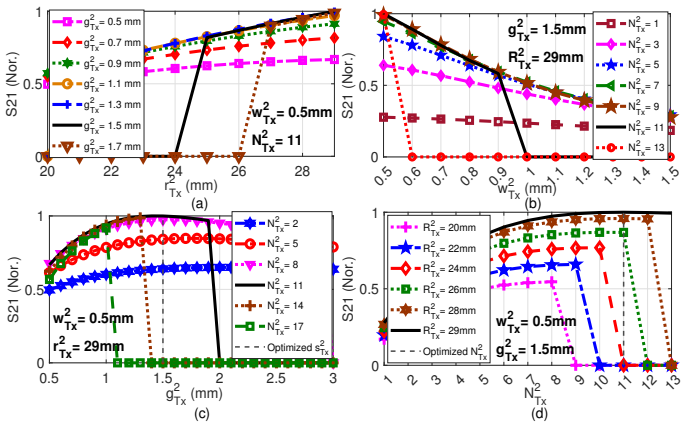

Figure 4.3: Parametric study of the double dumbbell Coils $2-5$ of proposed antenna.

respect to the design parameters of the Coil-2. Figure 4.3(a) shows the $S21$ versus r^2_{Tx} for various g^2_{Tx} values when $w^2_{Tx} = 0.5$ mm and $N^2_{Tx} = 11$. The plots indicate that the $S21$ increases with r^2_{Tx}, however, near lower r^2_{Tx} values, the $S21$ is intentionally substituted to zero due to space limitation confronted for maintaining $N^2_{Tx} = 11$ in case of higher g^2_{Tx} values. Hence, the maximum $S21$ is obtained for $r^2_{Tx} = 29$ mm and $g^2_{Tx} = 1.5$ mm. The parametric study for the $S21$ versus w^2_{Tx} is presented in Figure 4.3(b) showing a

decaying $S21$ with w^2_{Tx} for various values of N^2_{Tx} and $g^2_{Tx} = 1.5$ mm and $r^2_{Tx} = 29$ mm. For higher values of N^2_{Tx}, since the coil becomes capacitive, the $S21$ is substituted to zero to satisfy the reactance constraint of (4.9). The result suggests to prefer a minimum w^2_{Tx} and $N^2_{Tx} = 11$ to maximize the $S21$. A minimum possible $w^2_{Tx} = 0.5$ mm is selected based on the minimum fabrication limit of the available facility in the laboratory. Similarly, Figure 4.3(c) presents the parametric study of the $S21$ versus g^2_{Tx} for various N^2_{Tx} and $w^2_{Tx} = 0.5$ mm and $r^2_{Tx} = 29$ mm. The plots illustrate the existence of the particular optimal g^2_{Tx} and N^2_{Tx} for which the $S21$ is maximized as $g^2_{Tx} = 1.5$ mm and $N^2_{Tx} = 11$. Furthermore, Figure 4.3(d) exhibits the $S21$ variation with N^2_{Tx} for various r^2_{Tx} showing an increasing $S21$ value with higher N^2_{Tx} and r^2_{Tx}. The abrupt drops visible in the plots at higher N^2_{Tx} are due to infeasibility of inserting too many turns within a limited dimension of the coil. This concludes that optimal $S21$ is achieved for $r^2_{Tx} = 29$ mm, $N^2_{Tx} = 11$, $g^2_{Tx} = 1.5$ mm, and $w^2_{Tx} = 0.5$ mm. Using these optimized parameters of the Tx Coils $2-5$ in the field formulation of (2.3) gives the calculated values $H_x = H_y = 11.46$ A/m for $I_{Tx} = 1$ A.

To generate an equal H_z by the Tx Coil-1 within time-slot T_3 to satisfy the equal field constraint of the objective (4.9), the design parameters r^1_{Tx}, N^1_{Tx}, g^1_{Tx}, and w^1_{Tx} are optimized. The Tx Coil-1 parameters which achieve objective (4.9) with H_z formed within 1% of $H_x = H_y = 11.46$ A/m are selected as optimal solution. For this, Figure 4.4 presents a parametric study of $S21$ within time-slot T_3 for optimizing the parameters of the Tx Coil-1. Figure 4.4(a) is plotted for $S21$ versus g^1_{Tx} for various N^1_{Tx} and $r^1_{Tx} = 46$

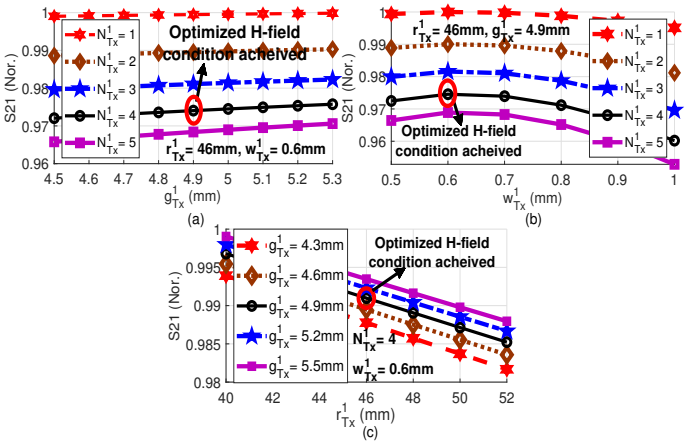

Figure 4.4: Parametric study of the axial Coil-1 of the proposed antenna.

mm and $w^1_{Tx} = 0.6$ mm. The figure is maximized where the equal field constraint is satisfied at $g^1_{Tx} = 4.9$ mm and $N^1_{Tx} = 4$. Figure 4.4(b) shows the variation of $S21$ with w^1_{Tx} for various N^1_{Tx} values and by setting $r^1_{Tx} = 46$ mm and $g^1_{Tx} = 4.9$ mm. The plot indicates that the equal H-field constraint is achieved for $w^1_{Tx} = 0.6$ mm and $N^1_{Tx} = 4$. Similarly, Figure 4.4(c) presents the variation of $S21$ versus r^1_{Tx} for various g^1_{Tx}, where $N^1_{Tx} = 4$ and $w^1_{Tx} = 0.6$ mm. It is concluded from the plots that the H-field criteria is satisfied for the optimized parameter values as $r^1_{Tx} = 46$ mm, $N^1_{Tx} = 4$, $g^1_{Tx} = 4.9$ mm, and $w^1_{Tx} = 0.6$ mm and correspondingly the achieved $H_z = 11.37$ A/m is calculated using

(2.3). The final optimized parameters of the proposed Tx antenna are listed in Table 4.1. Subsequently, the analytically evaluated performance of proposed antenna is presented for

Table 4.1: Optimized coil parameters for the proposed Tx antenna

Coil$-i$	r^i_{Tx} (mm)	N^i_{Tx}	g^i_{Tx} (mm)	w^i_{Tx} (mm)
Coil-1	46	4	4.9	0.6
Coils $2-5$	29	11	1.5	0.5

angular misalignment tolerance.

Analytical Results of the Switched Polarized Field Forming and V_r Variation

The proposed optimized Tx antenna is analyzed to verify the production of three orthogonal H-field components with equal magnitude at the Rx location. The H-field distributions evaluated using (2.3) for the three coil sets, which are activated in three different time slots, are demonstrated in Figure 4.5 and respectively generated by Coils $2-3$, Coils $4-5$, and Coil-1 in the Rx plane $h = 50$ mm. For analysis, these orthogonal

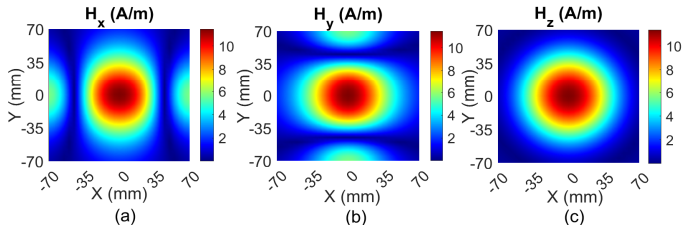

Figure 4.5: The H-field distributions produced by the proposed switched Tx antenna in the Rx plane when (a) Coils $2-3$ is ON, (b) Coils $4-5$ is ON, (c) Coil-1 is ON.

H-field distributions are used in (2.9) to illustrate the individual contribution V_{ind} of the three coil sets to power the Rx in different orientations. Figure 4.6 shows the $V_{ind}(\theta_r, \phi_r)$ contributed at various Rx coil orientations when the three coil sets, Coil -1, Coils $2-3$, and Coils $4-5$, are excited exclusively. From Figure 4.6, it is clear that when the three coil

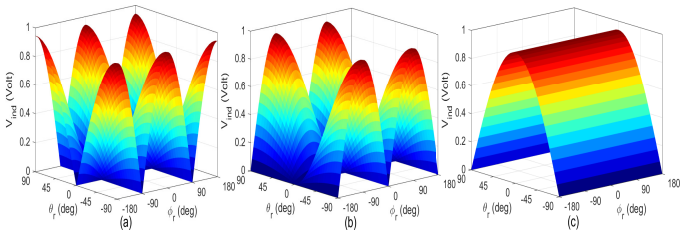

Figure 4.6: $V_{ind}(\theta_r, \phi_r)$ for independently working coil sets (a) Coils $2-3$ is ON for T_1, (b) Coils $4-5$ is ON for T_2, (c) Coil-1 is ON for T_3 duration.

sets are excited individually, a high degree of angular misalignment problem persists in all the cases. In contrast, when the proposed scheme is implemented by switching control of the coils according to Figure 4.2, the Rx coil experiences the proposed switched polarized H-field, as depicted in Figure 4.7(a), formed by the combination of the three orthogonal fields which together mitigate the angular misalignment problem such that the V_r remains

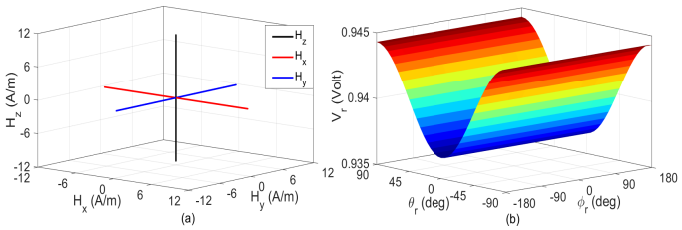

Figure 4.7: (a) The proposed switched polarized H-field forming and (b) resulting $V_r(\theta_r, \phi_r)$ variation.

constant. This is proved by plotting the net $V_r(\theta_r, \phi_r)$ variation in Figure 4.7(b) calculated using (4.4) for different orientations of the Rx coil, which shows that the V_r, almost independent from θ_r and ϕ_r, is obtained by employing the proposed switched polarized H-field. To generate this H-field, the proposed Tx antenna is realized and simulated next.

4.1.3 Realization of the Proposed Tx and Simulations

The proposed planar Tx antenna is realized with the design parameters listed in Table 4.1 by adopting low cost PCB technology. A double-sided PCB of FR4 substrate is utilized having a thickness of 1.575 mm, dielectric constant $\epsilon_r = 4.4$, loss tangent $\tan\delta = 0.02$, and 35 μm of copper deposition. The layout of the proposed optimized Tx is shown in Figure 4.8 where Coil−1 is printed at the bottom layer, as depicted in Figure 4.8(a), and

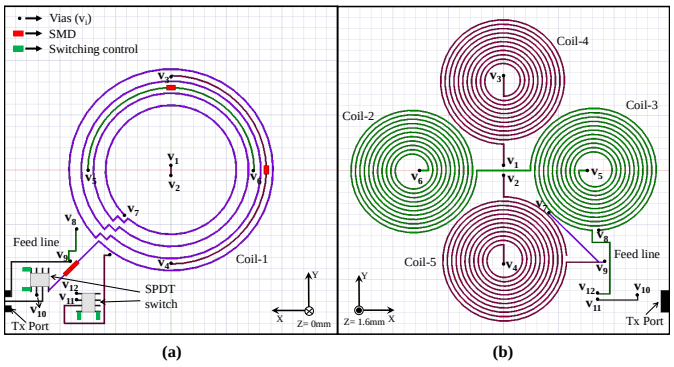

Figure 4.8: PCB layout of the proposed antenna (a) bottom and (b) top layers.

the double dumbbell coils are on the top layer of the PCB, as shown in Figure 4.8(b). The Coils 2−3 (similarly Coils 4−5) are connected in series through via with opposite windings to achieve opposite current circulations. For interconnecting the two coils of a dumbbell, semicircular tracks (printed jumpers) are etched at the bottom layer judiciously to avoid short-circuiting with the Coil−1 tracks. All the coils are excited through a single Tx port, as indicated in Figure 4.8, with a controlled sinusoidal source. The switching circuit with two SPDT switches is implemented and fed to the three coil sets. The design is simulated using commercial software Ansys EM Suite 20.2 to verify the analytically obtained results of the proposed H-field forming in the Rx plane. The simulated H-field results (by exciting individual coil set) are included in Figure 4.9 showing a good agreement with the analytically obtained results. The result also indicates that the H-field components

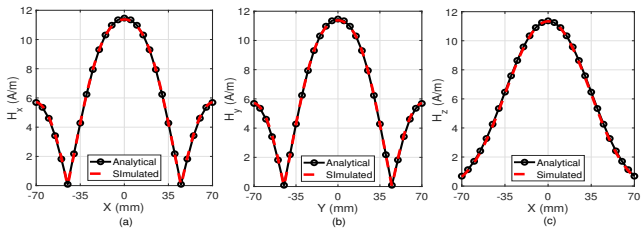

Figure 4.9: Simulated and analytical results of H-field components generated by the proposed antenna in the Rx plane.

produced by the proposed antenna at the Rx location satisfy the criteria given in (4.7).

4.1.4 Fabrication and Measurements

The proposed Tx antenna along with the Rx coil is fabricated using MITS PCB prototyping machine as shown in Figure 4.10 and measurements are performed to validate the design. To resonate the proposed Tx at operating frequency, the unloaded impedance

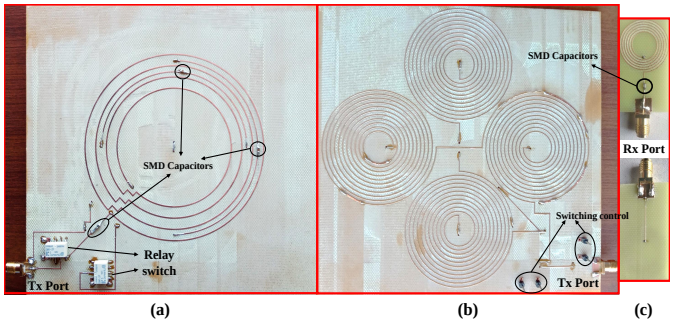

Figure 4.10: Realized prototypes, (a) bottom and (b) front view of the Tx antenna, and (c) the Rx antenna.

of Coil-1, Coils $2-3$, and Coils $4-5$ are measured using Agilent VNA (PNA-L N5230C). The measured impedences (in Ω) are respectively $(0.96 + j12.85)$, $(4.92 + j57.10)$, and $(4.94 + j57.32)$. The corresponding capacitors to resonate these coils at the operating frequency are 9.12 nF, 2.05 nF, and 2.04 nF, respectively, and the closest available SMDs are inserted in series with the coils. To realize the SPDT switches, two PCB mounted DPDT relays (G6K-2F) are employed since their readily availability in the laboratory. The placement of these relays with the proposed Tx structure is depicted in Figure 4.10. The experimental setup used to validate the design is shown in Figure 4.11. To excite the Tx antenna with a single sinusoidal signal, a Tektronix function generator (AFG1062) is utilized. Arduino Uno controller is used to operate the integrated switching circuit with the Tx antenna. The pulse provided by the controller board for switching durations T_1 and T_2 of 100 msec and corresponding relay output is provided in the bottom inset of Figure 4.11. The response at the rotating Rx coil is measured using a Keysight Digital Storage Oscilloscope (DSOX2022A) and the observed V_r variation results for different orientations of the Rx coil are presented in Figure 4.12. To compare the proposed switched polarized H-field forming and the proposed antenna performance, the

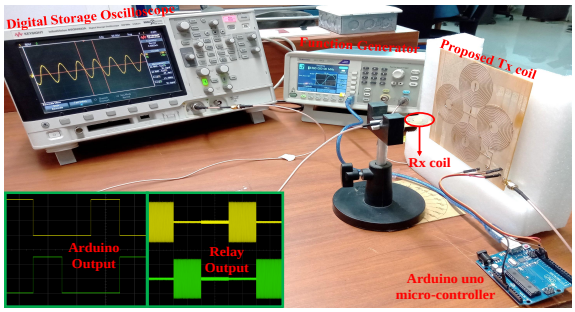

Figure 4.11: Hardware setup to validate the proposed antenna and WPT method.

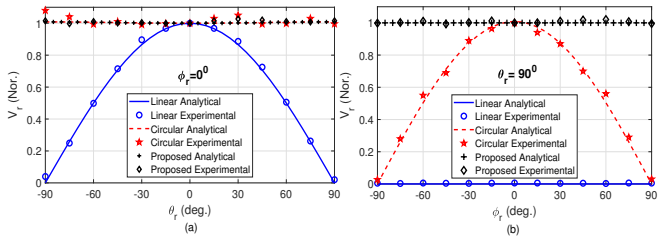

Figure 4.12: Measured V_r obtained for Rx orientation (a) $\phi_r = 0°$ (b) $\phi_r = 90°$.

V_r variations of linearly polarized and circularly polarized H-fields are also included in Figure 4.12. The results indicate that the linearly polarized H-field worsens the angular misalignment problem and is unable to support constant power transfer when the Rx is misaligned from its intended orientation. Whereas, the circularly polarized H-field is able to mitigate the angular misalignment problem, however, only in one orientation plane $\phi_r = 0°$ of the Rx. In contrast, the proposed antenna generating switched polarized H-field completely mitigates the angular misalignment problem and turns the WPT into an orientation-oblivion process. To quantify the performance in terms of misalignment tolerance, standard deviation σ_{V_r} in the measured $V_r(\theta_r, \phi_r)$ is evaluated from the observed data. The values of σ_{V_r} as 0.3011 V, 0.2247 V, and 0.0028 V are observed respectively for the linear, circular, and the proposed switched polarized H-field. Hence, the proposed Tx antenna designed to produce the switched polarized H-field demonstrates its capability to completely address the angular misalignment problem, which results in a constant power delivery to the Rx coil independent of its orientation. However, Design$-2A$ only focuses on mitigating angular misalignment at a fixed Rx location and is not suitable for applications where lateral misalignment is evident. Therefore, a newly designed Tx is needed to address both misalignment problems simultaneously, as presented subsequently.

4.2 Quadrant Coil Transmitter Antenna (Design$-2B$)

The WPT system comprises two magnetically coupled coil antennas, a planar Rx coil antenna and the proposed Tx antenna, as depicted in Figure 4.13(a). Here, the Tx is located at the origin of the coordinate system, whereas the Rx in perfect alignment is positioned at (0, 0, h) co-axial to the Tx. Due to misalignment, the position and orientation of the moving Rx changes to (x_r, y_r, z_r, θ_r, ϕ_r). To counter the misalignment

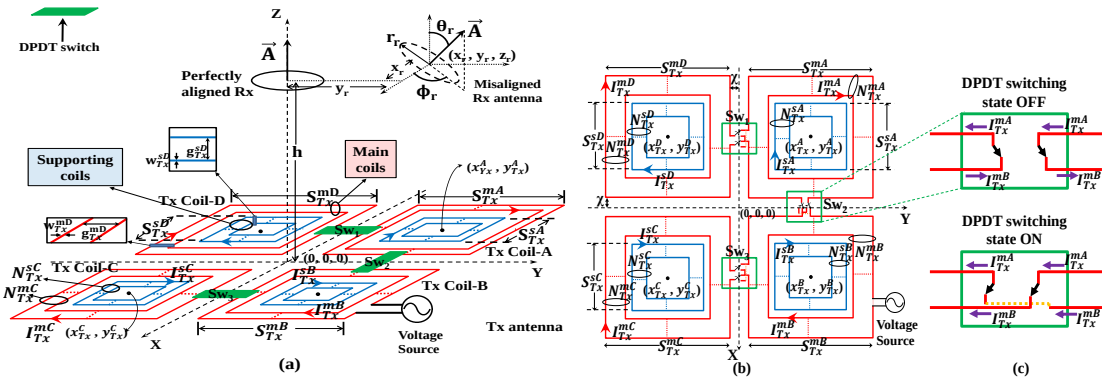

Figure 4.13: Proposed planar switchable transmitter antenna (a) 3−D view, (b) 2−D view, (c) Switching states of a DPDT switch.

effects, the proposed Tx antenna consists of four spatially distributed series-connected quadrant coils designated as Tx Coil-n, where $n \in \{\text{A, B, C, D}\}$, as shown in Figure 4.13(a). By using the four quadrant coils composing the proposed antenna, the three orthogonal H-field components (H_x, H_y, and H_z) are effectively generated. This is achieved by adequately switching the current circulations in the coils to form a particular field component. This field formations and working principle are detailed later in Chapter 4.2.1. Though all the coils are series connected to a single Tx input port, to facilitate the control over current circulations, three double pole double throw (DPDT) switches (Sw_1, Sw_2, and Sw_3) are employed in the proposed design schematic as depicted in Figure 4.13(b). A DPDT switch can reverse the connection between the adjacent coils based on its switching states illustrated in Figure 4.13(c), which reverses the current flow direction from common to opposite circulation and vice versa. For instance, when the Sw_2 is OFF, the coil-A and the coil-B both carry currents in the same circulation, however, when the Sw_2 switches to ON state, the current in Tx coil-B flows in the reverse circulation. Hence, the current reversal is achieved by employing a DPDT switch across the two adjacent coils. As shown in Figure 4.13(b), each quadrant Coil-n is composed of a supporting coil circumscribed by a main coil. The supporting coil assists the main coil in optimization to achieve widespread uniformity in the H_z distribution in the Rx plane. To excite the main and the supporting coils together using a single source, both the coils are connected in series, i.e., $I_{Tx}^{mn} = I_{Tx}^{sn}$, where I_{Tx}^{mn} and I_{Tx}^{sn} are the currents flowing through the two coils respectively. All the design parameters of the proposed antenna are described and formulated subsequently in Chapter 4.2.2.

4.2.1 Evolution and Working Principle of the Proposed Design

The proposed design is evolved by using field-forming technique to obtain the desired orthogonal H-field distributions in the Rx plane. The field-forming is accomplished by analyzing combinations of the current circulations in the four quadrant coils, which is defined by the parameter α_n. For instance, $\alpha_n = 1$ signifies clockwise current circulation in the coil-n , whereas, $\alpha_n = -1$ indicates counterclockwise current circulation. Figure 4.14 illustrates the proposed current control scheme to produce H_x, H_y, and H_z distributions

in the Rx plane $z_r = h$. Here, Figure 4.14(a) exhibits that, when all the four quadrant coils

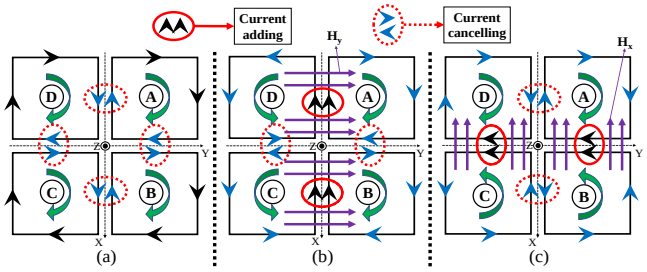

Figure 4.14: Current control scheme for the proposed Tx antenna to produce the H-field components (a) H_z, (b) H_y, (c) H_x.

have identical current circulations i.e. $\alpha_n = 1$, the currents flowing through the adjoining turns of the neighbouring coils cancel each other. Thus, the resultant current circulates on the outer periphery of the antenna to predominantly generate the H_z component in the Rx plane. In contrast, when the currents in coil-C and -D are switched to opposite circulation ($\alpha_A = \alpha_B = 1$, $\alpha_C = \alpha_D = -1$) shown in Figure 4.14(b), the currents flowing in adjoining turns of the coil pairs A-D and B-C add and the those flowing in A-B and C-D cancel. This produces an effective current flowing along the X-axis which dominantly generates the H_y component from the right-hand thumb rule. Similarly, when the currents in coil-B and -C are reversed ($\alpha_A = \alpha_D = 1$, $\alpha_B = \alpha_C = -1$), the net current flows along Y-axis resulting in the dominant H_x component generation. The switching circuit employed to realize the proposed current control scheme is integrated within the antenna structure itself to obtain a cost-effective and compact antenna design as demonstrated in Figure 4.13(b). Moreover, this integrated design has a single feeding port and requires only one excitation source. The number of switches employed and their placements are chosen judiciously to minimize complexity and switching losses. Only three switches are sufficient to control the current circulations properly. The switching modes correspondingly generating H_x, H_y, and H_z components are defined in Table 4.2 which lists the states of the three switches to implement the proposed current control scheme.

Table 4.2: Switching states to generate orthogonal H-field components.

Switching mode	Generated component	Sw_1	Sw_2	Sw_3
SM-1	H_x	OFF	ON	OFF
SM-2	H_y	ON	OFF	ON
SM-3	H_z	OFF	OFF	OFF

4.2.2 Antenna Parameters for Optimization and Field Formulation

The geometric parameters of the proposed antenna are the maximum side length S_{Tx}^{mn}, available number of turns N_{Tx}^{mn}, track width w_{Tx}^{mn}, and spacing between the turns g_{Tx}^{mn} for the main coils, and the same for the supporting coils are denoted as S_{Tx}^{sn}, N_{Tx}^{sn}, w_{Tx}^{sn}, and g_{Tx}^{sn}, respectively, for each quadrant coil$-n \in$ {A, B, C, D} as defined in Figure 4.13. The side length of j^{th} turn of the main coil is obtained as $S_{Tx}^{mnj} = S_{Tx}^{mn}$ - 2(j - 1)($w_{Tx}^{mn} + g_{Tx}^{mn}$) $\forall$

$j \in \{1, N_{Tx}^{mn}\}$, and that for the supporting coil is $S_{Tx}^{snj} = S_{Tx}^{sn}$ - 2(j - 1)($w_{Tx}^{sn} + g_{Tx}^{sn}$) $\forall\ j \in \{1, N_{Tx}^{sn}\}$. In the optimization process, the independent design variables are, S_{Tx}^{mn}, N_{Tx}^{mn}, and g_{Tx}^{mn} corresponding to the main coils and S_{Tx}^{sn}, N_{Tx}^{sn}, and g_{Tx}^{sn} for the supporting coil. These design variables are optimized and the other dependent parameters are evaluated using the following relations. For instance, the positions of Tx coil$-n$ centered at (x_{Tx}^{n}, y_{Tx}^{n}, 0) is determined by

$$x_{Tx}^{n} = \pm\left(\frac{S_{Tx}^{mn}}{2} + \chi\right), \quad y_{Tx}^{n} = \pm\left(\frac{S_{Tx}^{mn}}{2} + \chi\right), \tag{4.10}$$

where, χ is a positive offset to avoid overlapping between the coils as marked in Figure 4.13(b). A minimum limit S_{fab} on the side length of the coils is applied under fabrication limitations. Thus, for given S_{Tx}^{mn} and g_{Tx}^{mn} values, the maximum turns possible in the main coil is

$$N_{Tx}^{mn,max} = \left\lfloor \frac{S_{Tx}^{mn} - S_{fab}}{2(w_{Tx}^{mn} + g_{Tx}^{mn})} \right\rfloor. \tag{4.11}$$

Since the supporting coil dimension is limited by inner turn size of the main coil for a given $N_{Tx}^{mn} \leq N_{Tx}^{mn,max}$, the maximum side length of the supporting coil is evaluated as

$$S_{Tx}^{sn,max} = S_{Tx}^{mn} - 2N_{Tx}^{mn} \times (w_{Tx}^{mn} + g_{Tx}^{mn}). \tag{4.12}$$

Similarly, the maximum number of turns that the supporting coils can accommodate for a given S_{Tx}^{sn} is found as

$$N_{Tx}^{sn,max} = \left\lfloor \frac{S_{Tx}^{sn} - S_{fab}}{2(w_{Tx}^{sn} + g_{Tx}^{sn})} \right\rfloor. \tag{4.13}$$

These relations between various design parameters are used for antenna optimization. The total length of conductive tracks l_c of all the coils is also constrained during optimization for electrically small antenna condition. This is to ensure a uniform current distribution in each turn of the series-connected coils composing the antenna and given by

$$l_c = 16 \times \left(\sum_{j=1}^{N_{Tx}^{mn}} S_{Tx}^{mnj} + \sum_{j=1}^{N_{Tx}^{sn}} S_{Tx}^{snj} \right). \tag{4.14}$$

For analytical evaluation of the H-field distribution from the proposed Tx, the field expression corresponding to a single turn square coil as presented in (2.5) – (2.6) has been utilized. Thus, the total H-field generated from the proposed Tx is the summation of the H-field generated by four quadrant coils individually, and the corresponding orthogonal components are given as H_x, H_y, and H_z, respectively. The H-field forming criteria to address the misalignment problem of the WPT system is presented next.

4.2.3 Field-forming Condition to Address Angular and Lateral Misalignment Problems

As the proposed antenna is designed to generate a widespread distribution of the switched orthogonal H-field components to mitigate the misalignment issues. Particularly the angular misalignment problem is addressed by field-forming of switched polarized H-field, which can couple with the Rx coil in any orientation. The switched polarized H-field is realized using time switched excitation of H_x, H_y, and H_z components by optimally controlling their magnitudes and the switching duration of the three switches as presented

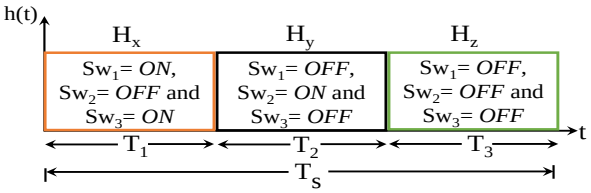

Figure 4.15: Switching duration and state of switches for generating a switched polarized H-field.

previously in Chapter 4.1.1. For the proposed Tx, to realize the switched polarization the switching sequence and period of the DPDT switches for one complete switching duration T_s is presented in Figure 4.15. The three switching modes SM-1, -2, and -3 are sequentially operated for T_1, T_2, and T_3 duration, respectively to generate H_x, H_y, and H_z components. Thus, the resultant switched polarized H-field $\vec{h}$ at the Rx location for the T_s duration is formulated in terms of unit step function $u(.)$ as

$$\begin{aligned}\vec{h}(x_r, y_r, t) = H_x(x_r, y_r)[u(t) - u(t - T_1)]\hat{x} + H_y(x_r, y_r)[u(t - T_1) - u(t - (T_1 + T_2))]\hat{y} \\ + H_z(x_r, y_r)[u(t - (T_1 + T_2)) - u(t - (T_1 + T_2 + T_3))]\hat{z}.\end{aligned} \tag{4.15}$$

To eliminate solely the angular misalignment problem, the required switching duration along with the optimal H-field condition is previously presented in (4.7) and given as

$$H_x = H_y = H_z \quad \text{and} \quad T_1 = T_2 = T_3 = \frac{T_s}{3}, \tag{4.16}$$

which is defined by considering a perfect lateral alignment of the Rx antenna. However, when the lateral misalignment of the Rx is obvious, satisfying the equality condition (4.16) at all the lateral positions (x_r, y_r) of the Rx is intractable. Therefore, the optimal switched polarized H-field condition for an angular misalignment tolerant system that allows the Rx lateral movements is modified to

$$H_x(x_r, y_r) \approx H_y(x_r, y_r) \approx H_z(x_r, y_r) \quad \text{and} \quad T_1 = T_2 = T_3 = \frac{T_s}{3}. \tag{4.17}$$

Here, $\approx$ represents a allowed deviation between the H_x, H_y, and H_z values observed at various Rx locations (x_r, y_r) and considered as 10% limit as an acceptable maximum variation. Furthermore, particularly for the lateral misalignment mitigation, a widespread H_z distribution is desired. To analytically quantify this, standard deviation σ_{H_z} of the H_z distribution in the Rx plane, evaluated with respect to the value $H_z(0, 0)$ at the aligned Rx location, can be defined

$$\sigma_{H_z} = \sum |H_z(x_r, y_r) - H_z(0, 0)| \Longrightarrow 0. \tag{4.18}$$

The σ_{H_z} in (4.18) should ideally be zero to mitigate lateral misalignment problem, however, for a feasible field-forming solution, its minimization is aimed to achieve a widespread H_z distribution.

Hence, the constraints in (4.17) and (4.18) indicate the field-forming conditions to address both the misalignment problems together. Once the optimal fields are generated, the induced voltage (V_{ind}) in the misaligned Rx antenna can be evaluated from the Faraday's law of electromagnetic induction using (2.9) as

$$V_{ind}(x_r, y_r, \theta_r, \phi_r, t) = -N_r \mu_o \frac{d}{dt} \vec{h}(x_r, y_r, t) \cdot \vec{A}(\theta_r, \phi_r), \tag{4.19}$$

Next, the optimization and the design of the proposed Tx antenna for achieving widespread switched H-field components is presented in Section 4.2.4.

4.2.4 Analytical Optimization of the Proposed Antenna Design

The proposed antenna is analytically optimized to target the conditions (4.17) and (4.18) for addressing the misalignment problems. Moreover, the generated field intensity is also maximized to deliver sufficient power to the Rx for which a maximum $H_z(0,0)$ is targeted at the Rx location $(0,0,h)$. Hence, the multi-objective function for the proposed antenna optimization is defined as

$$\begin{aligned} &\underset{S_{Tx}^{mn},N_{Tx}^{mn},g_{Tx}^{mn},S_{Tx}^{sn},N_{Tx}^{sn},g_{Tx}^{sn}}{\text{Minimize}} \quad [\eta_1 \sigma_{H_z} - (1-\eta_1) H_z(0,0)] \\ &\text{subject to} \\ &H_x(x_r,y_r) \approx H_y(x_r,y_r) \approx H_z(x_r,y_r),\ S_{Tx}^{mn} \leq 70 \text{ mm}, \\ &S_{fab} = 10 \text{ mm},\ w_{Tx}^{mn} = 0.5 \text{ mm},\ w_{Tx}^{sn} = 0.5 \text{ mm},\ \text{and } l_c < \frac{\lambda_o}{10}. \end{aligned} \tag{4.20}$$

To note that, incorporating negative sign with $(1-\eta_1)H_z(0,0)$ indicates maximizing the $H_z(0,0)$. Here, η_1 is the weight of the objective function to simultaneously minimize σ_{H_z} and maximize $H_z(0,0)$, where both are optimized with a same rate by assuming $\eta_1 = 0.5$. The design constraint $S_{Tx}^{mn} \leq 70$ mm is applied to limit the maximum dimension of the proposed Tx antenna to 140 mm. The $S_{fab} = 10$ mm and $\chi = 0.5$ mm are initialized and $w_{Tx}^{mn} = w_{Tx}^{sn} = 0.5$ mm is set according to the minimum fabrication limit of the PCB prototyping machine available in the laboratory. Also, the last constraint $l_c < \frac{\lambda_o}{10}$ is enforced to ensure that the optimized Tx antenna remains electrically small at the operating frequency of 6.78 MHz where l_c is evaluated using (4.14).

Design Procedure to Optimize the Proposed Transmitter Antenna

To solve the optimization problem formulated in (4.20), a flowchart of the proposed design procedure is provided in Figure 4.16. The steps involved in the optimization process are detailed.

Step-1: Initialize all the design parameters involved in the optimization process.

Step-2: Sweep the design parameters of the main coil S_{Tx}^{mn} and g_{Tx}^{mn}. Corresponding to each sweeping variable, determine the maximum turns $N_{Tx}^{mn,max}$ possible in the main coil using (4.11), then sweep N_{Tx}^{mn} for the range $1 \leq N_{Tx}^{mn} \leq N_{Tx}^{mn,max}$.

Step-3: For each sweeping cycle of the main coil parameters, evaluate the maximum side length $S_{Tx}^{sn,max}$ of the supporting coil using (4.12).

Step-4: Sweep the supporting coil design parameters, S_{Tx}^{sn} and g_{Tx}^{sn}, and determine the maximum turns $N_{Tx}^{sn,max}$ possible in the supporting coil using (4.13). Then sweep N_{Tx}^{sn} for the range $1 \leq N_{Tx}^{sn} \leq N_{Tx}^{sn,max}$.

Step-5: Calculate l_c from (4.14) and verify the electrically small design condition. If the condition fails, jump to the next sweeping combination in Step-4, otherwise, proceed to the next step.

Step-6: Determine the generated H-field components using (2.5) – (2.6) by the antenna design corresponding to the current status of the sweeping parameters.

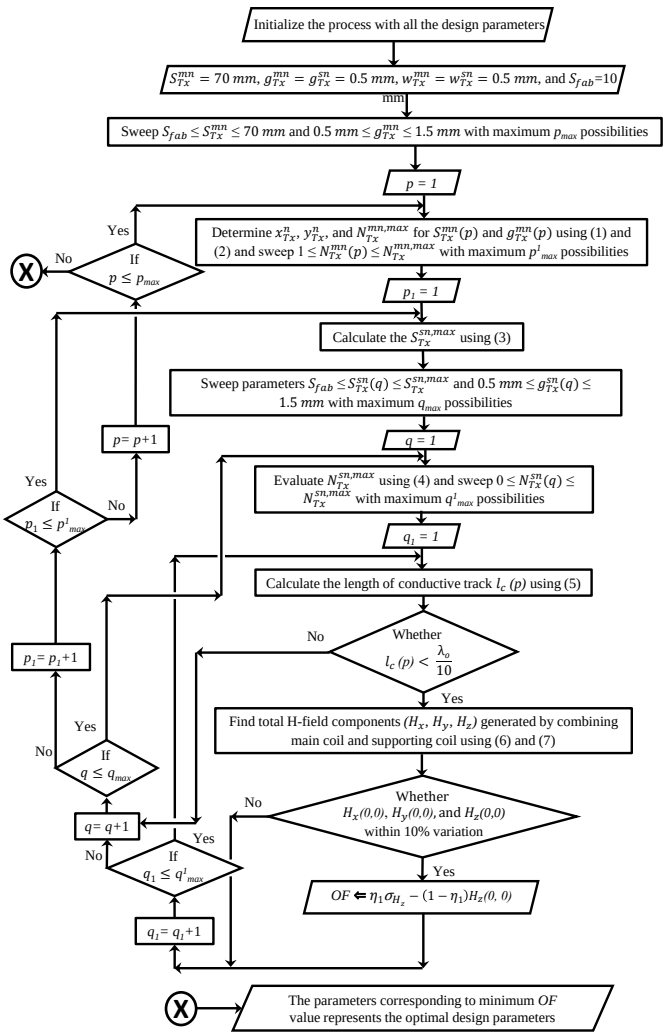

Figure 4.16: Flowchart for optimizing the proposed antenna.

Step-7: Check for the optimal H-field condition defined in (4.17). If satisfied, then determine the objective function value of (4.20) and store in a vector OF for all sweeping iterations. Repeat Step-2 to Step-7 for all possible sweeping values of optimization variables corresponding to the main coil.

Step-8: The iteration corresponding to the minimum value of OF reveals the final optimized design parameters as a solution to the problem defined in (4.20).

Parametric Study of the Design Variables

While the procedure shown in Figure 4.16 is executed, the design variables of the main coil and the supporting coils are varied and the generated H-field components are observed at the Rx region $h = 50$ mm. Since the proposed design is symmetrical, the current distributions which are responsible for generating H_x and H_y are identical. Therefore, these two lateral field components are identical and only H_x and H_z variations are shown under analytical parametric study of the optimization process. Though all the design variables are rigorously swept within their entire ranges, only a subset of the parametric

variation results are discussed here for brevity. Figure 4.17(a) presents the variation of

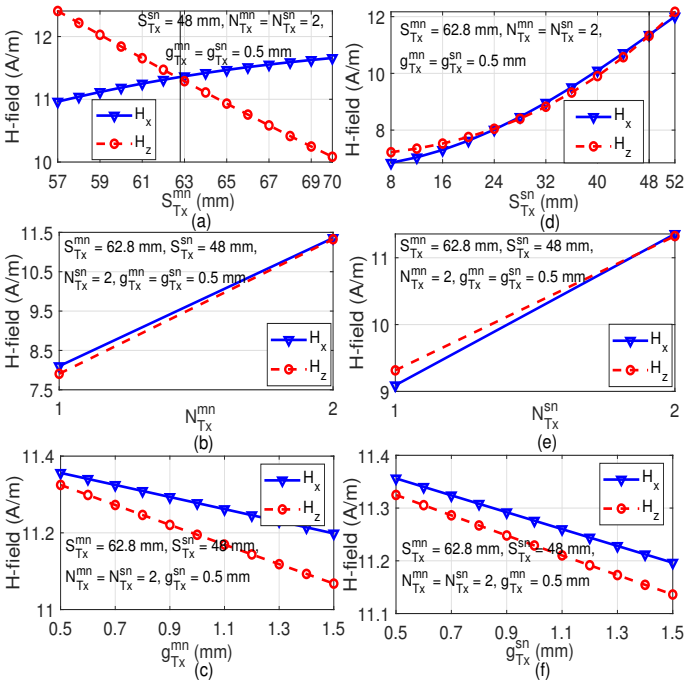

Figure 4.17: Parametric study of the design variables (a) S^{mn}_{Tx}, (b) N^{mn}_{Tx}, (c) g^{mn}_{Tx}, (d) S^{sn}_{Tx}, (e) N^{sn}_{Tx}, (f) g^{sn}_{Tx}.

H-field components versus S^{mn}_{Tx} for other parameter values set to $S^{sn}_{Tx} = 48$ mm, $N^{mn}_{Tx} = N^{sn}_{Tx} = 2$, and $g^{mn}_{Tx} = g^{sn}_{Tx} = 0.5$ mm. The plot indicates that an increase in S^{mn}_{Tx} enhances the H_x at the center because the length of current-carrying element increases along X and Y-axis. However, a reduction in H_z component with increasing S^{mn}_{Tx} is resulted from the change in the center position of the coils as given in (4.10). An approximately equal H_x and H_z are achieved for $S^{mn}_{Tx} = 62.8$ mm. Similarly, the H-field variation with S^{sn}_{Tx} is presented in Figure 4.17(d) showing the optimized value $S^{sn}_{Tx} = 48$ mm for which the fields $H_x \approx H_z$ and also maximized. The variation of H-field components with N^{mn}_{Tx} is plotted in Figure 4.17(b) where the main coil can contain maximum 2 turns due to the imposed electrical length criteria, hence, $N^{mn}_{Tx} = 2$ is optimized. For the same reason, the variation with N^{sn}_{Tx} plotted in Figure 4.17(e) shows optimal $N^{sn}_{Tx} = 2$. Figure 4.17(c) exhibits a decaying H-field variation with g^{mn}_{Tx} indicating that a minimum possible value of the g^{mn}_{Tx} should be chosen to maximize the generated fields. Hence, $g^{mn}_{Tx} = 0.5$ mm is dictated by the minimum fabrication limit of the PCB prototyping machine available in the laboratory. Similarly, $g^{sn}_{Tx} = 0.5$ mm is obtained from the parametric variation plot of Figure 4.17(f).

To demonstrate the necessity of the supporting coil, the H_z distributions generated by the main coil ($N^{mn}_{Tx} = 2$), in presence ($N^{sn}_{Tx} = 2$) and in absence ($N^{sn}_{Tx} = 0$) of the supporting coil, are compared in Figure 4.18. The plots prove that the incorporation of a supporting coil along with the main coil achieves a wider uniformity in H_z distribution obtained in the Rx plane.

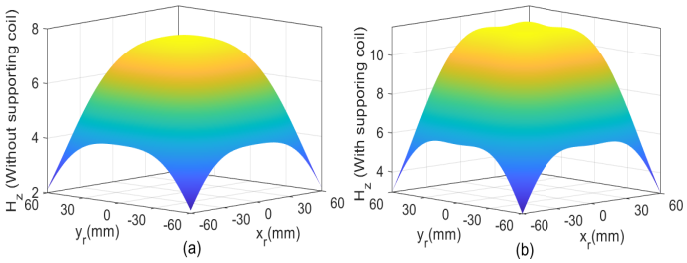

Figure 4.18: H_z distribution for $N_{Tx}^{mn} = 2$ (a) without supporting $N_{Tx}^{sn} = 0$, (b) with supporting $N_{Tx}^{sn} = 2$ coils.

Analytical Optimization Results

The optimization process on completion reveals the design parameter values. The four quadrant coil centers (x_{Tx}^{n}, y_{Tx}^{n}) are obtained as $(\pm 31.9, \pm 31.9)$, the main coil parameters as $S_{Tx}^{mn} = 62.8$ mm, $N_{Tx}^{mn} = 2$, $w_{Tx}^{mn} = 0.5$ mm, $g_{Tx}^{mn} = 0.5$ mm, and the supporting coil parameters as $S_{Tx}^{sn} = 48$ mm, $N_{Tx}^{sn} = 2$, $w_{Tx}^{sn} = 0.5$ mm, and $g_{Tx}^{sn} = 0.5$ mm. The optimized field-forming achieved by the proposed antenna for the optimal transfer distance $h = 50$ mm is analytically obtained and presented in Figure 4.19 for the three switching modes SM-1, -2, and -3. The distribution results exemplify the widespread formation

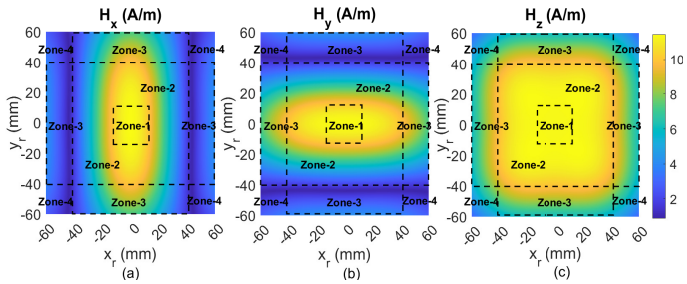

Figure 4.19: Widespread orthogonal H-field components formed by the proposed antenna (a) H_x, (b) H_y, (c) H_z distributions in $h = 50$ mm plane.

of orthogonal H-field components in the Rx plane by the proposed Tx antenna. A peak H_x and H_y of 11.35 A/m and a peak H_z of 11.32 A/m at (0,0) are obtained in the Rx plane.

Due to the involvement of multiple objectives and constraints in the optimization problem of (4.20), achieving a complete uniformity for each of the H-field components throughout the Rx region is not possible. Therefore, the total Rx working region is categorized into four different zones as depicted in Figure 4.19 on the basis of field variations. The Zone-1 covers the region where the three H-field components are similar and have a maximum deviation of $\pm 10\%$ from the value at the center. The extension of the Zone-1 is $-10\text{mm} \leq x_r, y_r < 10\text{mm}$, with H_x and H_y vary to 10.43 A/m along X-axis and Y-axis and H_z varies to 11.3 A/m. Hence, a robust switched polarized H-field is generated throughout the Zone-1 to completely mitigate the lateral and angular misalignment problems. The Zone-2 with the boundary range $10\text{mm} \leq |x_r|, |y_r| < 38\text{mm}$ comprises deviations beyond 10% limit in the H-fields as shown in Figure 4.19(a). In this region, the H_x drops to 9.96

A/m for the Rx moving along $x_r = 0$ mm and 1.84 A/m along $y_r = 0$ mm, whereas the H_z component varies to 10.15 A/m maximum in both the directions. Hence, widespread uniformity in H_z is still present in Zone-2 to completely mitigate lateral misalignment for the co-planar Rx movements. In some Rx locations, one of the lateral fields (H_x and H_y) decreases along one of the axis, thus, both the misalignment problems are not completely mitigated simultaneously, however, they are addressed for a moderately high range of the misalignment positions and orientations in Zone-2. Similarly, Zone-3 is dominated by only two H-field components, i.e. either H_x and H_z or H_y and H_z, with the maximum deviation observed in H_x or H_y field as 6.83 A/m and in H_z as 5.97 A/m within the boundary range of 38mm $\leq |x_r|, |y_r| <$ 60mm. Thus, for the Rx located in Zone-3, a relatively low tolerance for the misalignment is provided. Lastly, the Zone-4 contains only the H_z component with high variation and is unsuitable for misalignment mitigation.
The WPT performance of the proposed antenna is analyzed in terms of the variation present in V_r at the Rx antenna, owing the fact that the average power P_{avg} delivered to the load solely depends on V_r variation. Figure 4.20(a) depicts the V_r variation when

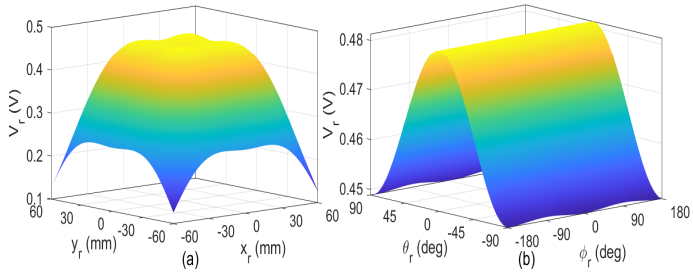

Figure 4.20: Analytically obtained V_r variation for the Rx antenna in (a) lateral (b) angular misalignment.

the Rx moves laterally and co-planar to the Tx antenna i.e. $\theta_r = 0°$ and $\phi_r = 0°$. For this movement, only H_z can couple with the Rx coil. The flatness present in V_r distribution indicates mitigation of lateral misalignment problem for the Rx movement range -38 mm $\leq x_r, y_r \leq 38$ mm considering 10% tolerance in V_r variation. Figure 4.20(b) shows V_r variation for the Rx fixed at (0, 0, 50) mm but rotating. For this angular movement, the Rx experiences highly consistent V_r with a standard deviation $\sigma_{V_r} = 3$ mV and mean $\bar{V_r} = 0.46$ V. This shows that WPT to the Rx is completely independent of its orientation. Thus, for the Rx which is perfectly aligned in one posture (either lateral or angular), its misalignment problem in other posture is completely mitigated. The performance of the proposed antenna is also evaluated relative to the single coil Tx of same dimension and demonstrated in Figure 4.21. The plot indicates that the proposed antenna outperforms relative to the single coil Tx in both lateral and angular misalignments cases due to the presence of wider H_z distribution and lateral H-field components, respectively. The other Rx movements for which both the lateral and the angular misalignment occur can be analyzed in terms of $\bar{V_r}$ and σ_{V_r}. Since the antenna is symmetrical in all the four quadrants, the misalignment results in one quadrant of the Rx plane is presented in Table 4.3. Here, at a particular lateral misalignment, all the orientations of the Rx are

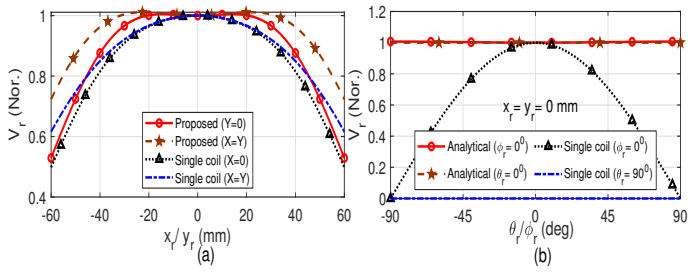

Figure 4.21: Performance comparison of proposed antenna relative to single coil Tx in (a) lateral (b) angular misalignment.

evaluated for V_r. The data indicates that, for Rx movement along X-axis, Y-axis, and

Table 4.3: Misalignment performance of the proposed antenna at various Rx positions

Position	$\sigma_{V_r}(V)$	$V_r(V)$
(0, 0)	0.003	0.46
(10, 0)	0.035	0.46
(20, 0)	0.069	0.47
(30, 0)	0.094	0.47
(38, 0)	0.105	0.46
(50, 0)	0.102	0.40
(60, 0)	0.093	0.33

Position	$\sigma_{V_r}(V)$	$V_r(V)$
(0, 10)	0.035	0.46
(0, 20)	0.070	0.47
(0, 30)	0.095	0.47
(0, 38)	0.106	0.46
(0, 50)	0.103	0.35
(0, 60)	0.094	0.33

Position	$\sigma_{V_r}(V)$	$V_r(V)$
(10, 10)	0.035	0.46
(20, 20)	0.070	0.47
(30, 30)	0.166	0.47
(38, 38)	0.172	0.45
(50, 50)	0.140	0.40
(60, 60)	0.102	0.23

diagonally in the range -38 mm $\leq x_r, y_r \leq 38$ mm, the evaluated $\bar{V_r}$ for all orientations is invariant implying a constant P_{avg}. However, the σ_{V_r} increases due to reduction in H_x or H_y away from the center as depicted in Figure 4.19(a) and (b). Beyond $|x_r|$, $|y_r| > 38$ mm, the diminishing field components lead to reduction in both, $\bar{V_r}$ and σ_{V_r}. The analytically optimized antenna is realized and further the results are verified by simulations and measurements.

4.2.5 Antenna Realization and Simulation Results

To realize the proposed Tx antenna, a low cost planar PCB technology is adopted. The final layout of the proposed optimized Tx antenna is shown in Figure 4.22 depicting the front and the back views of the PCB. The connections between the two layers are made through vias exhibited by red dots. The switches, Sw_1, Sw_2, and Sw_3, are inserted and connections are shown in Figure 4.22(b). Since the switching is integrated within the antenna structure, the impedance at the Tx port changes for the three switching modes (SM−1, SM−2, and SM−3) listed in Table 4.2. Two incremental capacitance (C_{reso}^{SM-1} and C_{reso}^{SM-2}) along with one port capacitance (C_{reso}^{SM-3}) are inserted in series with the coils corresponding to the three different switching modes as indicated in Figure 4.22. The incremental capacitance of a mode is selected such that its series combination with the C_{reso}^{SM-3} leads to the actual resonating capacitance of the port required in that mode.
The design layout is simulated using ANSYS EM Suite 20.2 and the simulated field

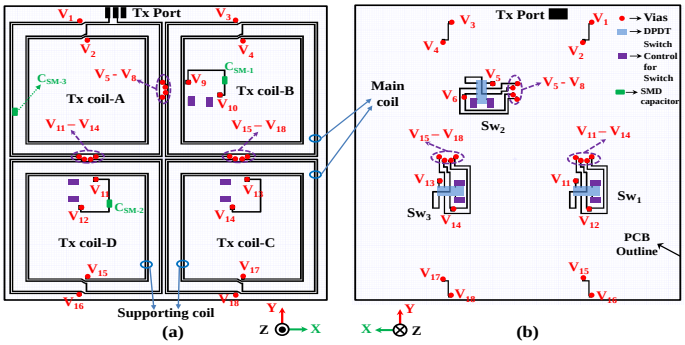

Figure 4.22: Layout of the proposed Tx antenna (a) front view, (b) back view.

distributions in $h = 50$ mm plane are compared in Figure 4.23 with the analytical results. The simulation results verify the orthogonal field forming achieved by the proposed Tx antenna for generating the switched polarized H-field distribution in the Rx plane. Experimental validation of the proposed design and results are presented subsequently.

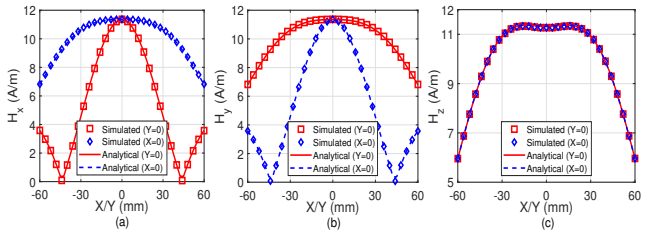

Figure 4.23: Simulated H-field distributions (a) H_x, (b) H_y, (c) H_z.

4.2.6 Experimental Verification

To validate the proposed design, the antenna is fabricated using a MITS PCB prototyping machine and the developed prototype is shown in Figure 4.24 depicting the front and back sides of the antenna. For three switches, PCB mountable DPDT relays (G6K-2F)

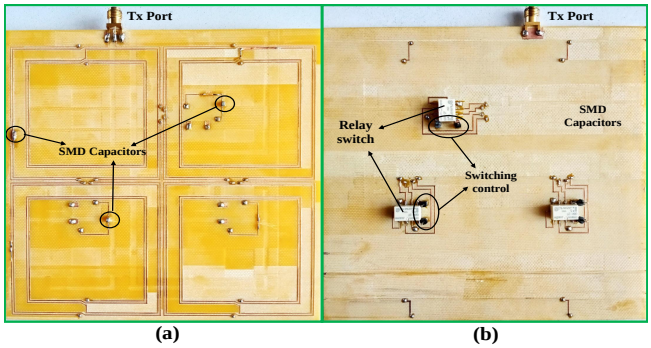

Figure 4.24: Fabricated prototype of the proposed antenna (a) front (b) back view.

are integrated at their designated places on the prototype as shown in Figure 4.24(b). To validate the misalignment performance by measuring V_r variation, a six turn Rx coil antenna is used having a maximum diameter of 20 mm, track width and adjacent turn spacing as 0.5 mm. To resonate the fabricated Tx and Rx antennas at the working

frequency (6.78 MHz), the unloaded impedance of the antenna port is measured in three switching modes using an Agilent VNA (PNA-L N5230C). The measured values (in Ω) are $15.52 + j439.12$, $15.95 + j443.17$, and $15.30 + j343.94$, respectively for SM−1, SM−2, and SM−3 modes. For the Rx port, the measured impedance is $1.86 + j33.27$ Ω. The required capacitance values to resonate the Tx coil in three different switching modes are 52.97 pF, 53.457 pF, and 68.45 pF and for the Rx coil $C_{Rx} = 705.54$ pF. Therefore, the incremental capacitance of $C_{reso}^{SM-1} = C_{reso}^{SM-2} = 236.78$ pF are chosen along with $C_{reso}^{SM-3} = 68.45$ pF and the SMD capacitors with closest commercially available values are used.

The misalignment performance of the proposed antenna is measured using the experimental setup shown in Figure 4.25. The Tx port is excited using an RF signal

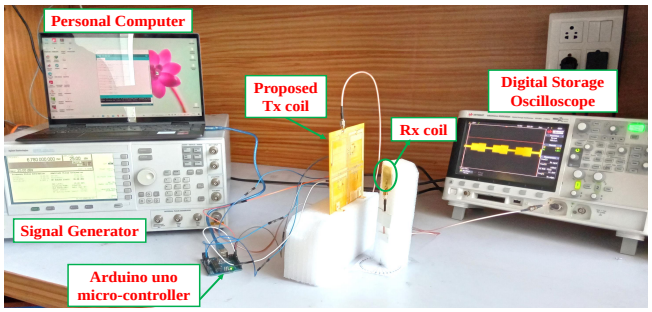

Figure 4.25: Experimental setup for the misalignment performance measurements.

generator (Agilent Technologies E8257D) and the Rx output response (V_r) is measured using Keysight Digital Storage Oscilloscope (DSOX2022A). The switching control is performed through the relay control terminals by using an Arduino uno micro-controller. Figure 4.26 shows the measured results of the V_r variation for the moving Rx misaligned in either lateral or angular domain. Here, Figure 4.26(a) shows the measured V_r variation

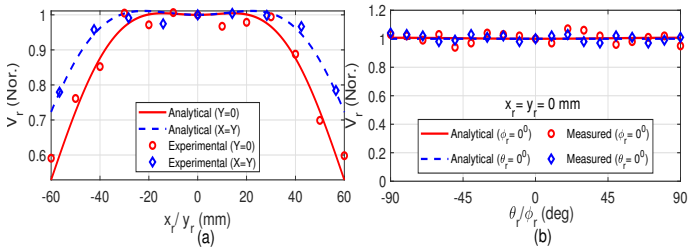

Figure 4.26: Measured V_r in the Rx for angular misalignment (a) ϕ_r= 0° (b) ϕ_r= 90°.

when the Rx is co-planar to the Tx and displaced laterally in step of 10 mm along $Y = 0$ (i.e. horizontal cut) and $X = Y$ (i.e. diagonal cut). Figure 4.26(b) shows the measured V_r variation with angular misalignment when Rx is located at (0, 0, 50) mm and free to rotate in both θ_r and ϕ_r dimensions. The analytical results are also included for comparison and the measured results are found well corroborating.

The measurements are also performed when the Rx is misaligned in both the lateral and the angular domains simultaneously and the results are presented in Figure 4.27. In Figure 4.27(a), with increase in lateral misalignment x_r, an increasing V_r variation with θ_r misalignment is observed whereas a stable V_r is obtained in ϕ_r domain for a

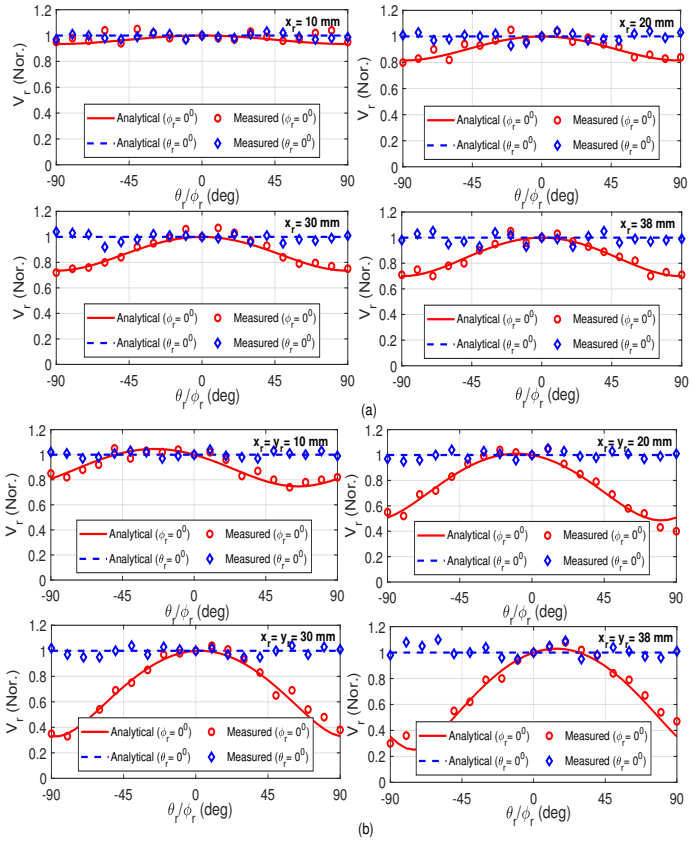

Figure 4.27: Measured V_r when Rx is misaligned (a) horizontally (b) diagonally.

complete mitigation of misalignment. As stated earlier, this occurs due to the drop of H_x component in Zone-2 shown in Figure 4.19(a). In contrast, when the Rx moves diagonally, the drop in H_x and H_y components results in a higher variation of V_r in the θ_r domain, Figure 4.27(b), whereas a good tolerance for misalignment problem is achieved in the ϕ_r domain. The measured results are corroborated with the analytical results. Hence, the proposed Tx antenna is able to completely address the misalignment problem within the Rx region Zone-1 with range -10 mm $\leq x_r, y_r \leq 10$ mm. Moreover, the working region of the proposed Tx is increased to Zone-2 having range -38 mm $\leq x_r, y_r \leq 38$ mm with a little compromised tolerance for the angular misalignment. The results demonstrate that the proposed antenna has the potential to generate a widespread distribution of the switched orthogonal H-field components at the Rx location to enhance the misalignment tolerance. It must be noted here that the power delivery to the load is affected by the mutual coupling between individual Tx-Rx antennas in individual switching mode. In spite of this, the average power delivered to the load remains constant due to cumulative effect of V_{ind} obtained from three distinct switching modes. As a result, the power transfer performance of a near field WPT system under misalignment can be improved to a large extent using the proposed antenna. Besides, employing switches in the proposed antenna may slightly degrade the PTE of the WPT system due to the switching and ohmic losses. Nevertheless, the advantages such as reduced circuit complexity and liberty to produce the desired flux for a higher misalignment tolerance range make the switches a promising

solution. This proves the proposed design to be a potential antenna candidate for a misalignment resilient WPT application.

4.3 Summary

This chapter investigates an alternate method for mitigation of angular misalignment problem in the near-field WPT applications. As a solution, a new methodology of integrating field-forming approach with switching control is presented in Design−2A. The switched polarized H-field is demonstrated to completely mitigate the angular misalignment problem and requires only a single source of single-tone signal in contrast to the multi-tone multiple-sources required by the previous methods of 3−D rotating H-field forming. The optimal constraint on the H-field components related to their respective excitation duration is analytically derived. To generate the switched polarized H-field, a planar Tx antenna consisting of an axial and two dumbbell shape coils is proposed and optimized for a maximum $S21$ between the Tx and the Rx coils. The switching is integrated within the design using two SPDT switches to realize three states. The effectiveness of the proposed method and antenna design to mitigate angular misalignment problem is proved by demonstrating an invariant induced voltage in the rotating receiver coil. The design is experimentally validated and a comparison with linear and circular polarization is performed. The results indicate that the standard deviations in RMS induced voltages in the rotating Rx for the linearly and the circularly polarized H-fields are 0.3011 V and 0.2247 V, respectively, which is reduced to 0.0028 V by the proposed switched antenna. Hence, the proposed antenna is proved to be a potential solution for orientation-oblivion wireless charging of small devices, however, mitigation of lateral misalignment still persists.

Aiming both angular and lateral misalignment simultaneously, a planar switching integrated quadrant coil antenna is proposed in Design−2B. For this purpose, an optimization of the proposed antenna is optimized by field-forming approach to generate a widespread switched orthogonal H-field components for producing a switched polarized H-field distribution. Furthermore, a time switching is employed to control the current circulations within the four quadrant coils composing the antenna. The three DPDT switches are judiciously integrated within antenna structure itself resulting in a single port antenna as a low-cost solution. The different constraints encapsulated within the optimization objective function reveal the antenna design with four quadrant coils each consisting of a main and a supporting coil to achieve a widespread distribution of three orthogonal H-field components. The performance analyzed in terms of RMS value of induced voltage shows that the proposed antenna eliminates both the misalignment problems completely in the Rx lateral movement region in Zone-1 of 20×20 mm^2 for all the angular movements. For the Rx lateral movement in the Zone-2 range $10\text{mm} \leq |X_r|, |Y_r| < 38\text{mm}$, the lateral misalignment problem is completely mitigated whereas the angular misalignment is moderately addressed. Thus, the results proved the

importance of Design−2B to simultaneously address lateral and angular misalignment problems for a wider range. This concludes that the proposed antenna has a high misalignment tolerance with a simple efficient design suitable for low-cost manufacturing. However, once the Rx settled down, generating widespread distribution of H-field resulted in a flux leakage problem and necessitated a magnetic beam formation towards the Rx. Nonetheless, the efficient charging of the Rx through magnetic beam formation relies on knowing its position and orientation. Consequently, addressing the primary challenge of localizing the Rx is targeted and presented next.

[0]**CHAPTER OUTCOMES:**

[1]. **V. K. Srivastava** and A. Sharma, "Switched Polarized H-Field Forming Using a Planar Switchable Double-Dumbbell Coil Antenna for Orientation-Oblivion Wireless Power Transfer," in *IEEE Transactions on Antennas and Propagation*, vol. 70, no. 6, pp. 4234-4242, June 2022, doi: 10.1109/TAP.2022.3140499.
[2]. **V. K. Srivastava** and A. Sharma, "A Planar Switching Integrated Quadrant Coil Antenna to Form Widespread Switched Polarized H-Field for Misalignment Resilient WPT System," in *IEEE Transactions on Antennas and Propagation*, vol. 70, no. 11, pp. 10294-10303, Nov. 2022, doi: 10.1109/TAP.2022.3195554.

Chapter 5

Non-uniform Magnetic Field Forming Transmitter

SO−3: *Inspect a planar Tx that localizes the position and orientation of an arbitrarily placed Rx.*

This chapter addresses a critical aspect of localization, particularly in the context of biomedical implants. In order to power up these devices effectively, it is crucial to accurately determine both the position and orientation of a small implanted device. To achieve this, the chapter focuses on creating a highly non-uniform H-field, unlike the uniform H-field targeted in the preceding chapter. The reason for choosing a non-uniform H-field is that it provides a distinct voltage sample at the Rx, which is later used to accurately determine the location of moving receiver. Additionally, this chapter discusses the design and development of three different Tx coil designs, known as Design−3A, Design−3B, and Design−3C, all aimed at achieving the objectives outlined in SO−3 as provided in Section 1.7. Here, Design−3A focuses explicitly on localizing the position of a moving object, while Design−3B and Design−3C elaborate on the methodology used to determine both position and orientation.

5.1 System Design of Transceiver Antenna (Design−3A)

The proposed MRC-based interface system to localize the position of a human's fingertip is depicted in Figure 5.1 showing potential applications of the proposed transceiver antenna

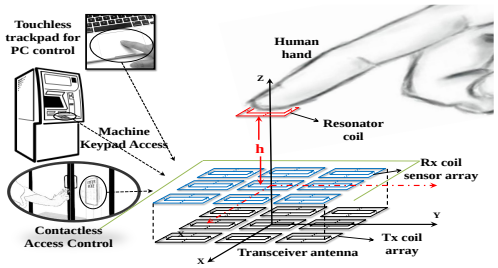

Figure 5.1: Application scenarios of the proposed MRC-based transceiver antenna.

platform such as contact-less keypad for ATMs, AHI-based computer trackpad, contactless access control, etc. The proposed interface system comprises of a transceiver antenna platform and a wearable resonator coil attached to the fingertip at a height h as shown in

Figure 5.1. The transceiver antenna consists of a Tx coil array and a Rx coil sensor array co-located within the same platform. This arrangement greatly simplifies the wearable device design providing a user friendly solution. Moreover, inclusion of the Tx array and the Rx sensor array together within the transceiver antenna platform makes the proposed system cost effective and low in latency for localization.

The transceiver antenna is designed in low-cost PCB technology, and the Tx coil array and the Rx coil sensor array are printed at the front and back layers of the same PCB, respectively. For PCB realization, a double-sided FR4 substrate of thickness, $t = 1.6$mm, relative dielectric constant $\epsilon_r = 4.4$, loss tangent $\tan\delta = 0.02$, and 0.017mm of copper deposition is used. The schematic model of the proposed system compatible with PCB technology is shown in Figure 5.2. The Tx comprises of a $n \times n$ array of K number

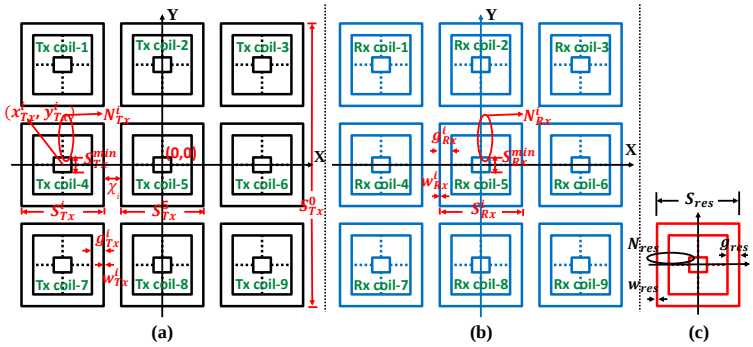

Figure 5.2: Schematic view of the proposed system for $n = 3$ (a) Tx coil array (b) Rx coil sensor array (c) Resonator coil.

of spatially distributed planar elements where each element is a multi-turn coil antenna denoted as Tx coil-i $\forall$ $i \in [1, \text{K}]$. Here, K$= n^2$ is the total coils present in the $n \times n$ array (n is an odd integer), e.g., for an array shown in Figure 5.2(a), $n = 3$ and K$= 3^2 = 9$. Similarly, the Rx is a $n \times n$ array of K sensor elements realized as planar multi-turn coil antennas denoted as Rx coil-i $\forall$ $i \in [1, \text{K}]$ as shown in Figure 5.2(b). The resonator is a multi-turn single coil of a size equivalent to a single coil of the Tx array and modeled in Figure 5.2(c). When the Tx array is excited with an AC source, voltages are induced in the Rx sensor coils due to magnetic coupling and voltage readings are used to track the position of the resonator coil (fingertip).

5.1.1 Working Principle of the Proposed System

The proposed transceiver antenna works on the principle of 2-coil and 3-coil MRC-based WPT techniques. In a 2-coil MRC system, two spatially separated coils, a Tx coil and a Rx coil, are tuned by external capacitors to resonate at a common operating frequency and maximize voltage gain of the Rx with respect to the Tx. Whereas, an additional resonator coil is inserted between the Tx and the Rx coils in the 3-coil MRC system to achieve a higher WPT range. The presence of the resonating coil between the Tx-Rx coil pair shifts the resonance frequency of the system, which is re-tuned to the operating frequency by tuning the matching capacitors. However, without re-tuning, if a resonator coil is brought closer to the originally tuned Tx-Rx pair of a 2-coil MRC system, the resulting detuned

3-coil system encounters a reduction in voltage gain. Thus, the two states, the presence and the absence of the resonator coil, can be distinguished by comparing the change in the Rx coil voltages.

Utilizing this principle in the proposed design, the Tx coil array and the Rx coil array are tuned to resonate at the operating frequency in the absence of the resonator coil, therefore, forming a 2-coil MRC WPT system locally per array element. The Tx is designed to generate a robust H-field distribution in the plane of the Rx. This H-field distribution drives the voltage outputs of the Rx sensor coils at the operating frequency. However, if a single large Tx coil is used to generate a uniform H-field distribution, the presence of a tuned resonator in the vicinity of any of the Rx sensor coils can also disturb the readings in the neighboring sensor coils. To demonstrate the disturbance caused by the resonator coil, a single large Tx coil is simulated in commercial EM software both in the absence and presence of a tuned resonator coil above Rx coil-5. The corresponding H-field distribution for $Y = 0$ cut is presented in Figure 5.3 and exemplifies the presence of disturbance caused by the resonator coil to the nearby placed Rx coils. Therefore, the system does not provide

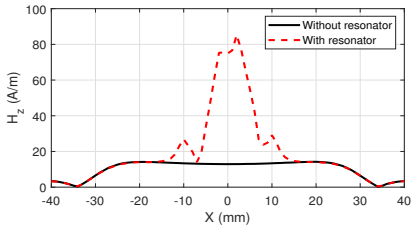

Figure 5.3: Impact of resonator on H-field distribution produced by a single turn Tx coil presented in.

an optimal localization accuracy. This problem is avoided by the use of the Tx with an $n \times n$ array of coil elements that can power each Rx coil sensor individually as depicted in Figure 5.1 and Figure 5.2. Moreover, this provides an opportunity to exploit non-uniform H-field forming to enhance localization accuracy.

For analysis, let $V_{Rx}^{i}(x, y)$ denote the voltage gain of the Rx coil-i matched output with respect to the Tx coil matched input when the resonator is placed at coordinate (x, y). The $V_{Rx}^{i}(x, y)$ denotes the $S21$-parameter measured between the antenna ports of the Rx coil-i and the Tx. Thus, in the absence of the resonator coil, the voltage gain of the Rx coil-i is $V_{Rx}^{i}(\infty, \infty)$ corresponding to the 2-coil MRC system. The system is designed to maximize $V_{Rx}^{i}(\infty, \infty)$ and obtain similar values for each Rx coil-i $\forall$ $i \in$ [1, K]. However, in the presence of the resonator coil near to the Rx coil-i, the corresponding $V_{Rx}^{i}(x, y)$ deteriorates and the difference in the Rx sensor voltage gain is registered for the localization process. Using the comparison of the Rx sensor voltage with predefined threshold levels, the position of the resonator coil can be estimated. Therefore, the farther the separation of the voltage gains from the decision threshold in the two cases, the better the accuracy obtained in positioning. Therefore, in addition to the maximum $V_{Rx}^{i}(\infty, \infty)$ obtained in the absence of the resonator coil, the optimization of the proposed system also targets to minimize the $V_{Rx}^{i}(x, y)$ in the presence of the resonator coil to maximize the

accuracy. This forms the objective of the optimization problem defined for the proposed antenna system.

5.1.2 Design Parameters of the System for Optimization

The geometric parameters of the Tx coil array are maximum side dimension of the pad (S^0_{Tx}), maximum side length (S^i_{Tx}), conductive strip width (w^i_{Tx}), and inter-turn spacing (g^i_{Tx}) of the Tx coil-i $\forall$ $i \in [1, 9]$, and minimum side length (S^{min}_{Tx}) as denoted in Figure 5.2(a). For the design with $n = 3$, the number of turns in the Tx coil-i, N^i_{Tx}, for a given side length S^i_{Tx} is calculated as

$$N^i_{Tx} = \left\lfloor \frac{S^i_{Tx} - S^{min}_{Tx}}{2(w^i_{Tx} + g^i_{Tx})} + 1 \right\rfloor. \tag{5.1}$$

The coordinates of the Tx coil-i center is $(x^i_{Tx}, y^i_{Tx}, 0)$, and evaluated as

$$\chi_i = \frac{S^0_{Tx}}{2} - \left(\frac{S^5_{Tx}}{2} + S^i_{Tx}\right), \quad x^i_{Tx} = \pm\left(\frac{S^5_{Tx}}{2} + \frac{S^i_{Tx}}{2} + \chi_i\right), \quad y^i_{Tx} = \pm\left(\frac{S^5_{Tx}}{2} + \frac{S^i_{Tx}}{2} + \chi_i\right). \tag{5.2}$$

Here, χ_i is the separation between the adjacent coils. Particularly for coil-5, the center coincides with the origin. Similarly, the design parameters for the Rx coil sensor array are the maximum side length (S^i_{Rx}), minimum side length (S^{min}_{Rx}), number of turns (N^i_{Rx}), conductive track width (w^i_{Rx}), and inter-turn spacing (g^i_{Rx}) corresponding to each coil in the Rx array as denoted in Figure 5.2(b). The maximum number of turns in the Rx coil, N^0_{Rx}, for a given S_{Rx} is found by

$$N^0_{Rx} = \left\lfloor \frac{S_{Rx} - S^{min}_{Rx}}{2(w_{Rx} + g_{Rx})} + 1 \right\rfloor. \tag{5.3}$$

In the design, the center, (x^i_r, y^i_r, z^i_r), of the Rx coil-i is assumed coinciding with the Tx coil-i but $z^i_r = 1.6$mm representing the top layer of PCB. For optimization of resonator coil, the design parameters are maximum side length (S_{res}) and the number of turns (N_{res}), the track width, (w_{res}), and the inter-turn spacing, (g_{res}), which are optimized to maximize the effect of its presence on the Rx coils.

Once the design parameters of the proposed system are defined, further optimization adopts non-uniform H-field forming. To analyze the field generated by the Tx coil array, the H-field formulation for a square coil is utilized as presented in (2.5). The z-component of the H-field at any observation point (x, y, h) in space generated by the Tx coil-i is defined as $H^i_z(x, y)$. Thus, the total H-field distribution originated by the Tx coil array can be evaluated by the superposition of the individual H-field of each coil element of the array as $\sum_i H^i_z(x, y)$. The optimal design of the proposed system is presented subsequently.

5.1.3 Optimization and Design

The optimization of the proposed system is performed jointly for the Tx and Rx coil arrays, and the resonator coil to attain the global design objective as discussed in Section 5.1.1. The global objective is now stated as; to form optimal non-uniform H_z in the absence of the resonator coil such that the $V^i_{Rx}(\infty, \infty)$ is maximized and to minimize the $V^i_{Rx}(x, y)$ in the presence of the resonator coil. Since the design problem is very complex, it is divided into sub-objectives that are interdependent and jointly achieves the global objective.

Optimization Problem Formulation

The Tx coil array design is optimized in absence of the resonator coil to generate non-uniform H_z distribution so that $V_{Rx}^{i}(\infty,\infty)\ \forall\ i \in [1,\ \mathrm{K}]$ are maximized and achieve similar values. For this, initially the coil-$\lceil \mathrm{K}/2 \rceil$ located at the center of the Tx array (e.g. coil-5 as presented in Figure 5.2) is optimized to achieve maximum field $\sum_i H_z^i(0,0)$ at the origin. Here, $\lceil . \rceil$ denotes the ceiling function. Let $\triangle_V^i$ is defined as the percentage deviation of the voltage gain of the other Tx coil-i from the voltage gain $V_{Rx}^{\lceil \mathrm{K}/2 \rceil}(\infty,\infty)$ of the coil-$\lceil \mathrm{K}/2 \rceil$. Subsequently, for a given Rx coil array, the $\triangle_V^i$ is minimized to achieve similar voltage gains in absence of the resonator coil. To accomplish this sub-objective, the optimization problem is formulated as

- **Sub-objective-1**

$$
\begin{aligned}
&\underset{S_{Tx}^i, w_{Tx}^i, g_{Tx}^i}{\text{Minimize}}\ \triangle_V^i = \left| \frac{V_{Rx}^i(\infty,\infty) - V_{Rx}^{\lceil \mathrm{K}/2 \rceil}(\infty,\infty)}{V_{Rx}^{\lceil \mathrm{K}/2 \rceil}(\infty,\infty)} \right| \\
&\qquad\qquad \forall\ i \in [1, \mathrm{K}] \quad i \neq \lceil \mathrm{K}/2 \rceil \\
&\text{preceded by} \quad \underset{S_{Tx}^{\lceil \mathrm{K}/2 \rceil}, w_{Tx}^{\lceil \mathrm{K}/2 \rceil}, g_{Tx}^{\lceil \mathrm{K}/2 \rceil}}{\text{Maximize}} \sum_i H_z^i(0,0) \\
&\text{Subject to} \quad S_{Tx}^0 \leq 62\text{mm}, \quad 10\text{mm} \leq S_{Tx}^i \leq 21\text{mm}, \\
&w_{Tx}^i \geq 0.5\text{mm}, \quad g_{Tx}^i \geq 0.5\text{mm}, \quad \text{and} \quad S_{Tx}^{min} = 8\text{mm}.
\end{aligned}
\tag{5.4}
$$

Following the Tx coil array design, the resonator coil and the Rx coil array are jointly optimized. This is performed by placing the resonator coil at certain location, P_n, with coordinate (x_{P_n}, y_{P_n}) at a height h above the transceiver antenna. The P_n location in the design process begins with coordinate $(0,0)$ and assumes perfect alignment with the Rx coil-$\lceil \mathrm{K}/2 \rceil$. For this arrangement, the resonator coil is optimized to have a maximum effect on deteriorating the voltage gain $V_{Rx}^{\lceil \mathrm{K}/2 \rceil}(x_{Tx}^{\lceil \mathrm{K}/2 \rceil}, y_{Tx}^{\lceil \mathrm{K}/2 \rceil})$ of the Rx coil-$\lceil \mathrm{K}/2 \rceil$. Hence, to design the resonator coil, the optimization problem is formulated as

- **Sub-objective-2**

$$
\begin{aligned}
&\underset{S_{res}, N_{res}}{\text{Minimize}} \quad V_{Rx}^{\lceil \mathrm{K}/2 \rceil}(x_{Tx}^{\lceil \mathrm{K}/2 \rceil}, y_{Tx}^{\lceil \mathrm{K}/2 \rceil}) \\
&\qquad\qquad \text{when resonator aligned with Rx coil-} \lceil \mathrm{K}/2 \rceil \\
&\text{subject to} \quad 18\text{mm} \leq S_{res} \leq 22\text{mm}, \ N_{res} \geq 1 \\
&S_{Tx}^i = S_{Tx}^{opti}, \quad N_{Tx}^i = N_{Tx}^{opti}, \quad w_{Tx}^i = w_{Tx}^{opti}, \quad g_{Tx}^i = g_{Tx}^{opti}.
\end{aligned}
\tag{5.5}
$$

where S_{Tx}^{opti}, N_{Tx}^{opti}, w_{Tx}^{opti}, and g_{Tx}^{opti} represent the optimized Tx parameters obtained as solution of the sub-objective-1. Succeeding (5.5), the Rx coil array is optimized considering various positions, P_n, of the resonator coil. Since the resonator coil attached to the fingertip can be present anywhere on the platform, there are various alignments possible with the Rx coil array. For instance, P_n locations in the second quadrant of the transceiver antenna are shown in Figure 5.4, where following three cases of alignments are possible; perfectly aligned to one single Rx coil ($P_1, P_3, P_7,\ P_9$), aligned with two adjacent coils ($P_2, P_4, P_6,\ P_8$), and aligned with four adjacent coils (P_5) denoted as ζ_1, ζ_2, and ζ_3, respectively. To distinguish these cases for better positioning of the resonator coil, the voltage gain values of a particular Rx coil-i for these cases should be appreciably separated

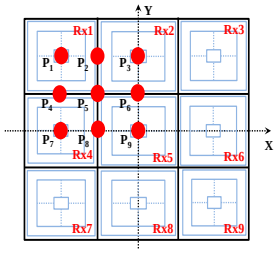

Figure 5.4: Resonator coil position for optimizing Rx coil sensor array.

away from the decision thresholds. For example, let the resonator is placed at P_9, P_6, and P_5, representing the three cases of alignments, then, particularly for the Rx coil-5, the corresponding voltage gain levels $V^5_{Rx}(x_{P_9}, y_{P_9})$, $V^5_{Rx}(x_{P_6}, y_{P_6})$, and $V^5_{Rx}(x_{P_5}, y_{P_5})$ should be unequal and their difference is maximized. Similarly, the voltage gains for one particular case of alignment should be equal for all the Rx coils laying under the resonator coil. For instance, if the resonator is placed at P_6, then the voltage gain levels of the Rx coils laying under the resonator, $V^5_{Rx}(x_{P_6}, y_{P_6})$ and $V^2_{Rx}(x_{P_6}, y_{P_6})$, should ideally be equal.
This is achieved by defining the decision threshold limits, γ_1, γ_2, and γ_3 for the three different cases of the P_n alignments, respectively. The Rx coil parameters S^i_{Rx}, N^i_{Rx}, w^i_{Rx}, and g^i_{Rx} are optimized to attain farthest possible V^i_{Rx} solutions from the decision thresholds γ for various P_n. For this, the difference function defined as $\delta_{Rx} = |V^i_{Rx}(x_{P_n}, y_{P_n}) - \gamma|$ is maximized for each Rx coil-i. Hence, the optimization problem to design Rx coil sensor array is defined as

- **Sub-objective-3**

$$\begin{aligned}
&\underset{(S_{Rx}, N_{Rx}, w_{Rx}, g_{Rx})}{\text{Maximize}} \quad \delta_{Rx} = |V^i_{Rx}(x_{P_n}, y_{P_n}) - \gamma|, \\
&\text{subject to} \quad S_{Rx} = 18\text{mm}, \; S^{min}_{Rx} = 8\text{mm}. \\
&w_{Rx} \geq 0.5\text{mm}, \; g_{Rx} \geq 0.5\text{mm}, \\
&S^i_{Tx} = S^{opti}_{Tx}, \quad N^i_{Tx} = N^{opti}_{Tx}, \quad w^i_{Tx} = w^{opti}_{Tx}, \quad g^i_{Tx} = g^{opti}_{Tx}, \\
&S_{res} = S^{opti}_{res}, \quad N_{res} = N^{opti}_{res}, \quad w_{res} = w^{opti}_{res}, \quad g_{res} = g^{opti}_{res},
\end{aligned} \tag{5.6}$$

where, S^{opti}_{res}, N^{opti}_{res}, w^{opti}_{res}, and g^{opti}_{res} are the optimal resonator coil parameters. The optimization problem defined in (5.4)-(5.6) is solved by an algorithm adopting hybrid approach of analytical modelling of $H_z(x, y)$ and simulation based parametric optimization of $V^i_{Rx}(x, y)$ in Section-5.1.3.

Design Procedure to Optimize the Proposed Transceiver Antenna System

The flow chart of the design algorithm to solve optimization problem (5.4)-(5.6) is presented in Figure 5.5. A detailed description of the steps involved in the design process is now provided.

Step-1: All the design parameters are initialized.

Step-2: The Tx coil optimization process begins with the initial iteration to first achieve the objective function defined in (5.4) to maximize $\sum_i H^i_z(0, 0)$, by sweeping design variables $S^{[K/2]}_{Tx}$, $w^{[K/2]}_{Tx}$, and $g^{[K/2]}_{Tx}$.

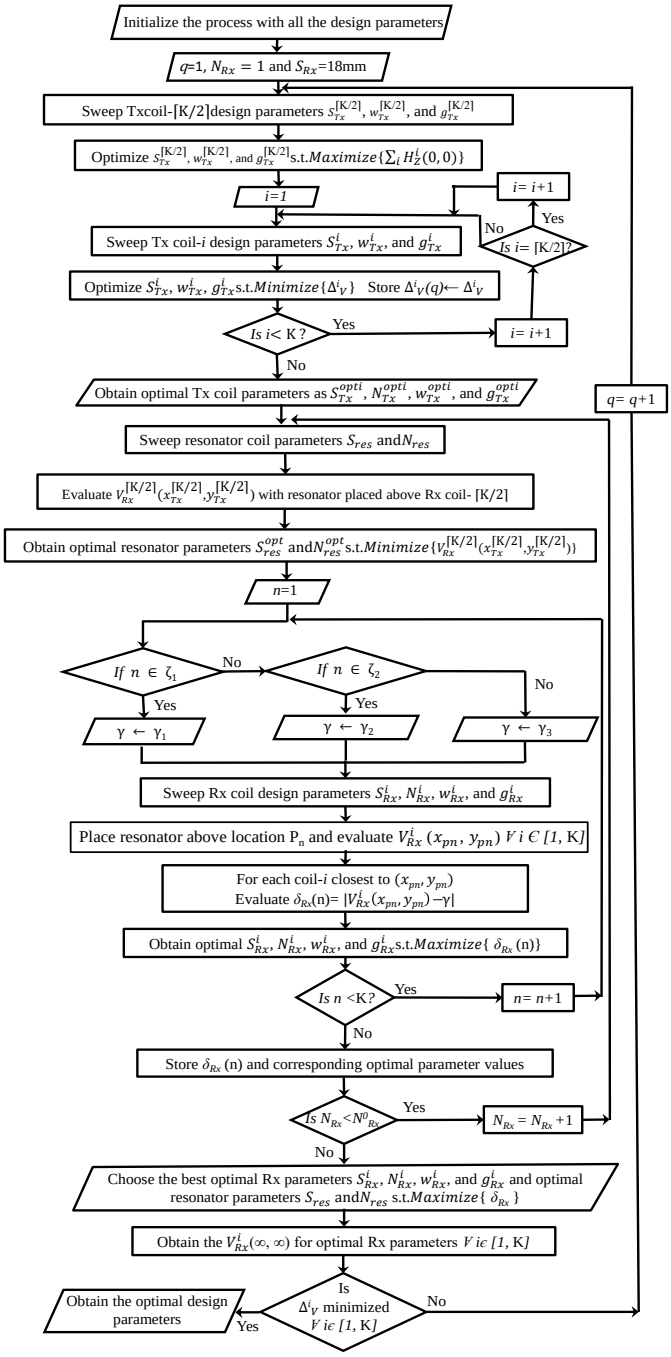

Figure 5.5: Flowchart for optimizing the proposed transceiver antenna system.

Step-3: Subsequent to Step-2, other Tx coil-i are optimized to achieve the objective (5.4) as minimize $\triangle_V^i$ by sweeping design variables S_{Tx}^i, w_{Tx}^i, and g_{Tx}^i and initializing the N_{Rx}= 1 and S_{Rx}= 18mm for initial iteration. The design parameters corresponding to minimum $\triangle_V^i$ are stored for each Tx coil-i $\forall$ $i \in$ [1, K].

Step-4: The obtained parameters corresponding to minimum $\triangle_V^i$ are consider as the optimal Tx coil parameters as S_{Tx}^{opti}, N_{Tx}^{opti}, w_{Tx}^{opti}, and g_{Tx}^{opti}.

Step-5: The problem defined in (5.5) is now targeted in the presence of the resonator coil, which is aligned with the Rx coil-⌈K/2⌉ in the beginning.

Step-6: Sweep the design variables of the resonator coil and evaluate $V_{Rx}^{\lceil K/2 \rceil}(x_{Tx}^{\lceil K/2 \rceil}, y_{Tx}^{\lceil K/2 \rceil})$. Select the optimal resonator coil parameters S_{res}^{opt} and N_{res}^{opt} corresponding to minimum $V_{Rx}^{\lceil K/2 \rceil}(x_{Tx}^{\lceil K/2 \rceil}, y_{Tx}^{\lceil K/2 \rceil})$ to achieve the objective (5.5).

Step-7: Place the resonator coil optimized in previous step at other location P_n and assign the corresponding threshold values as γ_1, γ_2, and γ_3, respectively for the three cases of alignment; with one (P_1, P_3, P_7, and P_9), two (P_2, P_4, P_6, and P_8), and four (P_5) Rx coils as defined in Figure 5.4.

Step-8: Determine $V_{Rx}^{i}(x_{P_n}, y_{P_n})$ $\forall$ $i \in$ [1,K] for various parametric sweep of Rx coil parameters and evaluate the difference function δ_{Rx} defined in (5.6) for each Rx coil-i affected by the resonator coil.

Step-9: The Rx coil design variables S_{Rx}^{i}, N_{Rx}^{i}, w_{Rx}^{i}, and g_{Rx}^{i} are selected to achieve the objective function defined in (5.6) to maximize δ_{Rx}.

Step-10: Repeat Step$-$7 to Step$-$9 for all the defined positions P_n and store the various maximum δ_{Rx} and corresponding optimal Rx coil parameters.

Step-11: Repeat Step$-$6 to $-$10 by increasing N_{Rx} of coil-i by one for maximum N_{Rx}^{0} and store the result in $\delta_{Rx}(n)$ vector. Choose the best result corresponding to the minimum value in the vector $\delta_{Rx}(n)$ and obtain the optimal Rx and resonator coil parameters as S_{Rx}^{opti}, N_{Rx}^{opti}, w_{Rx}^{opti}, g_{Rx}^{opti}, S_{res}^{opti}, and N_{res}^{opti}.

Step-12: Determine the $V_{Rx}^{i}(\infty, \infty)$ for the optimal Rx coil array parameters and check for $\triangle_V^i$ $\forall$ $i \in$ [1, K]. Repeat all the steps until $\triangle_V^i$ obtained for all Rx coils is minimized.

Result of the Optimization Process

The parameters of the proposed system are optimized using algorithm presented in Figure 5.5 for K= 9 design. The PCB layout of the resulting optimized design is shown in Figure 5.6 depicting the Tx coil array at the bottom layer and the Rx coil sensor

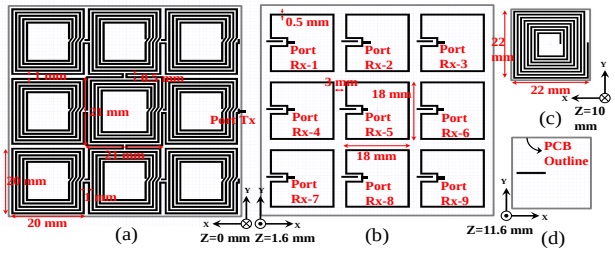

Figure 5.6: Transceiver antenna system (a) bottom view, (b) top view, (c) resonator coil bottom view, (d) resonator coil top view.

array at the top layer of the PCB, respectively. Figure 5.6(c) and Figure 5.6(d) show the bottom and the top view of the resonator coil layout. The connections across the two PCB layers are made through vias. The coil elements of the Tx array are connected in series to minimize number of ports required in the Tx and avoid additional jumper inter-connects. The system has in total ten ports out of which the Tx coil array has one port denoted by Port-Tx, the rest nine ports are attached to the nine sensor coils of the Rx array and denoted as Port Rx-i $\forall$ $i \in$ [1, 9] in Figure 5.6. The optimal Tx coil parameters are listed in Table 5.1 and $N_{Tx}^{i} = 5$, $w_{Tx}^{i} = 0.5$ mm, and $g_{Tx}^{i} = 0.5$ mm are obtained and $h = 10$ mm is considered in this study.

Table 5.1: Optimized coil parameters of the proposed antenna

Tx Coil-i	Position (mm)	S^i_{Tx} (mm)	$V^i_{Rx}(\infty,\infty)$ (dB)
1	(-21,-21,0)	20	-26.46
2	(-21,0,0)	20	-26.90
3	(-21,21,0)	20	-26.35
4	(0,-21,0)	20	-26.89
5	(0,0,0)	21	-27.10
6	(0,21,0)	20	-26.90
7	(21,-21,0)	20	-26.26
8	(21,0,0)	20	-26.85
9	(21,21,0)	20	-26.31

The analytically optimized H-field distribution generated by the Tx coil array in absence of the resonator coil is demonstrated in Figure 5.7(a). The analytical results are verified

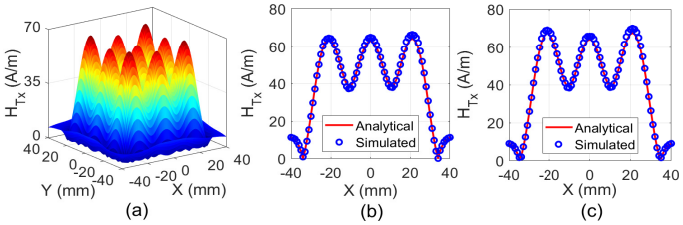

Figure 5.7: Optimized H-field generated by the Tx coil array (a) analytical distribution, (b) simulated for cut $Y = 0$ mm, (c) simulated for cut $Y = 21$ mm.

using an EM simulator. The 2D plots of the H-field generated from the optimized Tx coil array are compared in Figure 5.7(b) and Figure 5.7(c) for $Y = 0$ mm and $Y = 21$ mm cuts, respectively, and the results are found corroborating. The $V^i_{Rx}(\infty,\infty)$ values observed in Rx coil-i $\forall\ i \in [1, 9]$ is included in Table 5.1.

The parametric variation of S_{res} and N_{res} for optimization of the resonator coil as formulated in (5.5) is shown in Figure 5.8(a). The optimal parameters for the resonator coil are S^{opt}_{res}= 22 mm and N^{opt}_{res}= 8 to minimize $V^5_{Rx}(x^5_{Tx}, y^5_{Tx})$ from Figure 5.8(a).

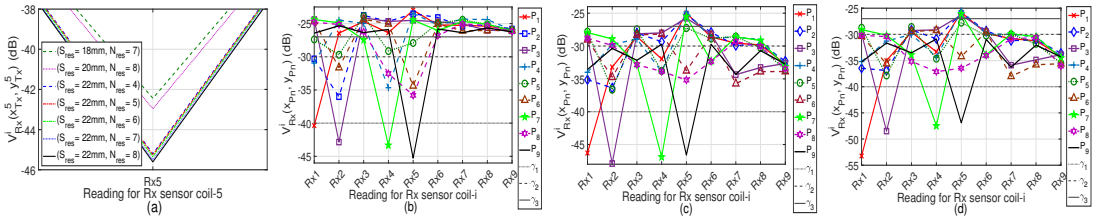

Figure 5.8: Optimization of (a) resonator coil, (b) Rx coil sensor array $N^i_{Rx} = 1$, (c) Rx coil sensor array $N^i_{Rx} = 3$, (d) Rx coil sensor array $N^i_{Rx} = 5$.

The parametric study for optimizing the Rx coil sensor array in presence of the optimized Tx and the resonator coil located at various positions (P_1 - P_9 defined in Figure 5.4) is presented in Figure 5.8(b)-(d). The plots are shown for various N^i_{Rx} and $w^i_{Rx} = g^i_{Rx} = 0.5$mm and for the proposed design K= 9, the threshold values accounted in the algorithm are $\gamma_1 = -40$dB, $\gamma_2 = -30$dB, and $\gamma_3 = -27$dB. To observe the effect of N^i_{Rx} on voltage gain, consider that the resonator is first placed at P_1. In this case, only the $V^1_{Rx}(x_{P_1}, y_{P_1})$ for the Rx coil-1 is below the threshold defined as $\gamma_1 = -40$dB for various

N^i_{Rx} in Figure 5.8(b)-(d), whereas, the $V^i_{Rx}(x_{P_1}, y_{P_1})$ for the other Rx coils are above the threshold $\gamma_1 = -40$dB and most uniform (~ -26dB) for $N^i_{Rx} = 1$. Similarly, when the resonator is shifted to position P_2, the voltage gains for the Rx coil-1 and Rx coil-2 are below the set threshold $\gamma_2 = -30$dB and above $\gamma_1 = -40$dB. Whereas, for other Rx coils, the voltage gains are above γ_2 and observed as more consistent for N^i_{Rx}= 1. Likewise, the other positions can also be verified. This concludes that the $N^i_{Rx} = 1$ has least effect on the V^i_{Rx} of other Rx coils which are not in close proximity of the resonator suggesting $N_{Rx} = 1$ as the optimal Rx coil array parameter. The algorithm reveals the optimal Rx coil array parameters are $S_{Rx} = 18$mm, $N_{Rx} = 1$, and $w_{Rx} = 0.5$mm. The performance of the proposed transceiver antenna system is evaluated subsequently.

5.1.4 Simulation and Results

The performance of the optimized system is evaluated in the two states, with and without the resonator coil. In absence of the resonator coil, the input reflection coefficient (port matching) of various ports of the Rx coil sensor array and corresponding $V^i_{Rx}(\infty, \infty)$ versus frequency are shown in Figure 5.9(a) and Figure 5.9(b). The results indicate that

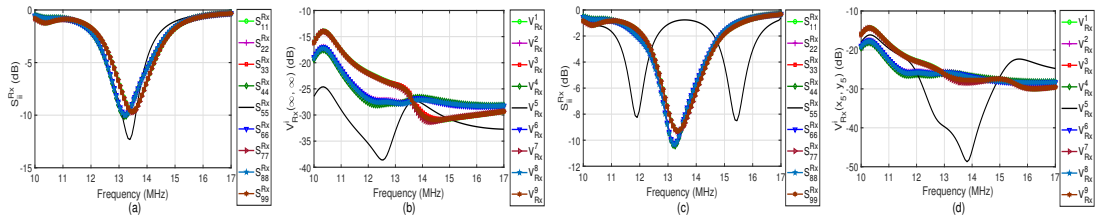

Figure 5.9: Frequency response of the proposed system (a) reflection coefficient of the Rx port-i in absence of the resonator coil, (b) $V^i_{Rx}(\infty, \infty)$ variation, (c) reflection coefficient of the Rx port-i in presence of the resonator coil above Rx coil-5, (d) $V^i_{Rx}(x, y)$ of the Rx port-i.

the $V^i_{Rx}(\infty, \infty)$ of different Rx sensor coils are ~ -26dB at operating frequency 13.56MHz. However, once the resonator coil is placed in the vicinity of any Rx coil, the voltage gain of that coil is drastically reduced due to detuning of the input matching. To demonstrate this, the detuning of the Rx coil-5 is demonstrated by plotting all S_{ii} in Figure 5.9(c) when the resonator is placed above the Rx coil-5 at position P_9. The corresponding change in the V^i_{Rx} is plotted in Figure 5.9(d). The comparison of Figure 5.9(b) and 5.9(d) indicates that the presence of the resonator coil above Rx coil-5 reduces V^5_{Rx} while the other Rx coils are not much affected because of the proposed non-uniform field forming and the use of coil array at the Tx which allows individual coupling with each Rx sensor coil.

To exemplify further the tracking of fingertip, various movements of the resonator coil are analyzed as shown in Figure 5.10. For instance, consider the tracking process for horizontal movement of the resonator as defined in Figure 5.10(a) with marked positions and their corresponding $V^i_{Rx}(x, y)$ values are plotted in Figure 5.10(b). The resonator begins from position H_1 where it is aligned with Rx4. In this case, the voltage gain of Rx coil-4 is $V^4_{Rx}(H_1) = -43.33$dB, which is well below the set threshold value ($\gamma_1 = -40$dB),

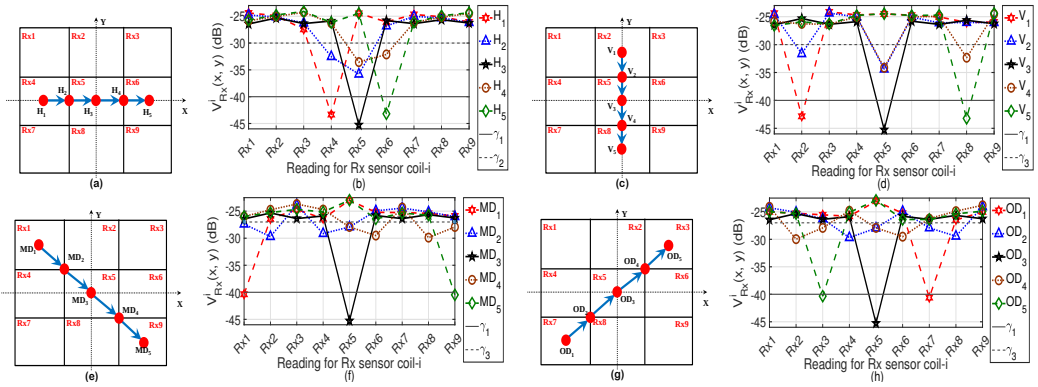

Figure 5.10: Simulated $V_{Rx}^{i}(x, y)$ variation for various movements of resonator coil in (a, b) horizontal, (c, d) vertical, (e, f) main diagonal, (g, h) off-diagonal directions.

whereas, all the other Rx sensor coils show voltage gain of ~ -26dB. As the resonator coil shifts to H_2 where it is aligned between Rx4 and Rx5, the $V_{Rx}^{4}(H_2)$ and $V_{Rx}^{5}(H_2)$ values for the Rx coil-4 and coil-5 are -32.53dB and -35.8dB, respectively; both are below the predefined threshold $\gamma_2 = -30$dB. Further movement of the resonator coil to H_3 aligns it perfectly with Rx5 and the $V_{Rx}^{5}(H_3) = -45.26$dB is observed below the decision threshold $\gamma_1 = -40$dB. Similarly, the remaining positions H_4 and H_5 can be verified from values shown in Figure 5.10(b) for horizontal movement. The other movements can also be verified similarly by comparing the $V_{Rx}^{i}(x, y)$ values of Rx coils with decision thresholds. To note that setting the decision threshold values is critical for the localization performance of the system, therefore, for practical purposes, any variations due to imperfections in hardware realization can be incorporated by calibration and using normalized decision thresholds (γ_{th}). Moreover, to distinguish the voltage gain values for tracking the fingertip movement, the normalized decision thresholds $\gamma_{th}^{1} = 0.25$, $\gamma_{th}^{2} = 0.5$, and $\gamma_{th}^{3} = 0.65$ are set for the resonator coil positioned respectively over a single Rx coil, two adjacent Rx coils, and four adjacent Rx coils. The influence of distance is presented by plotting the normalized voltage gains of the system simulated for varying distances (h = 5 mm, 10 mm, and 15 mm) in Figure 5.11 with corresponding γ_{th} marked. Here, Figure 5.11(a),

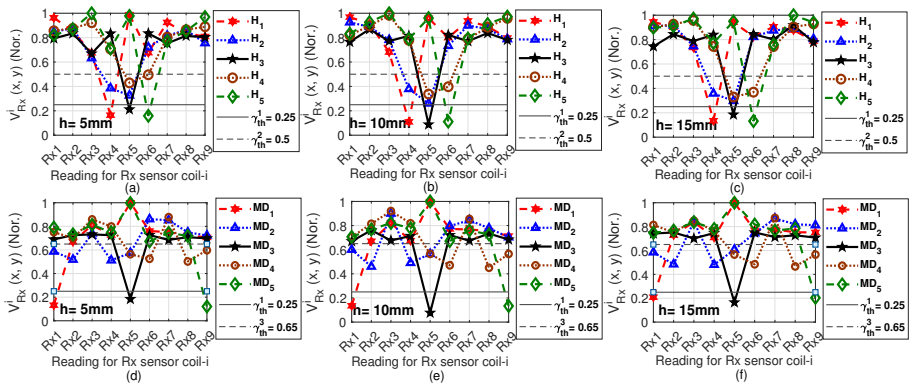

Figure 5.11: Simulated $V_{Rx}^{i}(x, y)$ variation under varying distance of resonator coil in (a, b, c) horizontal movement, (d, e, f) main diagonal movement.

(b), and (c) correspond to the horizontal movement, whereas, Figure 5.11(d), (e), and (f)

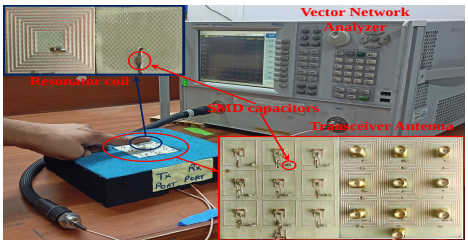

Figure 5.12: Experimental setup and fabricated prototype.

Table 5.2: Measured Z_i and corresponding C^i_{reso} values for various coils.

Coil-i	$Z_i(\Omega)$	C^i_{reso}(F)
Tx	22.07+j440.12	26.67p
Rx1	0.72+j9.42	1.24n
Rx2	0.69+j9.47	1.24n
Rx3	0.71+j9.43	1.24n
Rx4	0.69+j9.61	1.22n
Rx5	0.71+j9.53	1.23n
Rx6	0.69+j9.59	1.22n
Rx7	0.71+j9.48	1.24n
Rx8	0.67+j9.47	1.24n
Rx9	0.70+j9.53	1.23n
Resonator	1.94+j81.56	143.91p

are plotted for the main diagonal movement. The plots indicate that a slight variation in the resonator coil separation from the transceiver antenna does not much affect the pattern of the normalized $V^i_{Rx}(x, y)$ in the range of 5mm to 15mm.
Thus, the results of Figure 5.10 and Figure 5.11 together prove that the voltage gains of the Rx coils change insignificantly with the vertical moving resonator coil in the vicinity and are easily detectable with appreciable differences from the decision thresholds to implement the position tracking of the resonator coil. Further experimental verification of the proposed system is presented in the next section.

5.1.5 Experimental Verification

To validate the proposed design, the coils are fabricated using a PCB prototyping machine in the laboratory. The fabricated prototypes are shown in the inset demonstrating the experimental setup to measure S-parameters in Figure 5.12. An Agilent VNA (PNA-L N5230C) is used to measure the impedances of the unloaded coil input ports. The impedances (Z_i) of various coils measured at the operating frequency of 13.56MHz are shown in Table 5.2 including the corresponding capacitance (C^i_{reso}) value required to resonate each coil at 13.56MHz. The SMD capacitors of the closest available values are inserted in series with the coils as shown in the inset of Figure 5.12. The final prototype is tested and the $V^i_{Rx}(x, y)$ values are recorded from the Rx coil sensor array using the network analyzer. Further, the effect of random errors on the verge of external noise is addressed by converging 1000 samples of data using an inbuilt averaging factor function available in network analyzer. The data is then collected in the absence of resonator coil and the measured normalized $V^i_{Rx}(\infty, \infty)$ for each Rx sensor coil is shown in Figure 5.13 including simulation results for a proper comparison. In the absence of the resonating

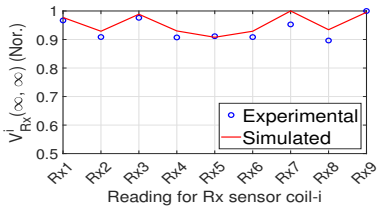

Figure 5.13: Normalized $V^i_{Rx}(\infty, \infty)$ values measured without resonator coil.

coil, the measured voltage gain values of the Rx sensor coils show slight variation and the measured data corroborates with the simulation result.

Now the resonating coil is moved in the vicinity of the transceiver antenna by following the paths defined previously in Figure 5.10 (left column), and measured $V^i_{Rx}(x, y)$ values are recorded. The variation in the normalized voltage gains of the Rx sensor coils for these movements is plotted in Figure 5.14 also indicating the γ_{th} set by measurements. The

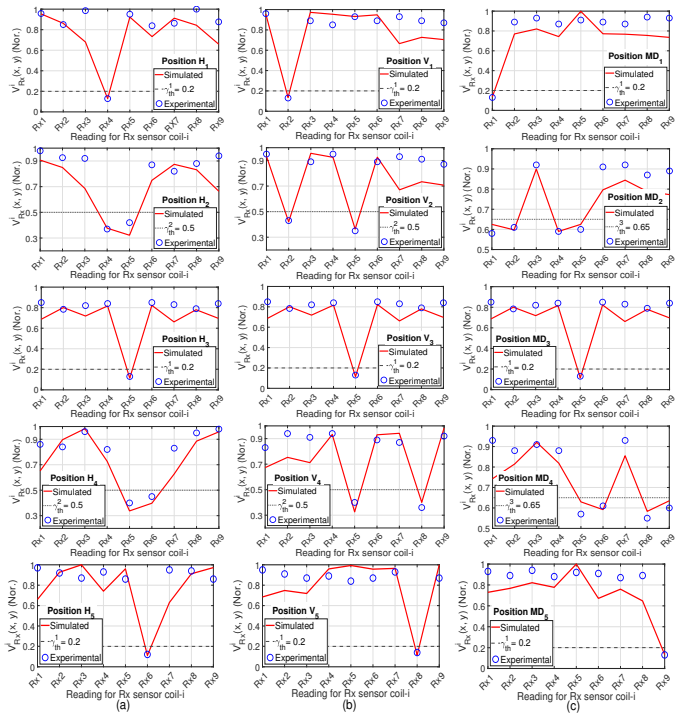

Figure 5.14: Normalized V^i_{Rx} measured for (a) horizontal movement, (b) vertical movement, (c) main diagonal movement.

experimental results obtained are found in good agreement with the simulation results for various resonator coil positions, as shown in Figure 5.14. For all the movements of the resonator coil, the voltage gain patterns of the Rx sensor array are shown to follow the desired trend with respect to the set threshold value, therefore, can be distinguished. Further experiments conducted in presence of metallic objects, e.g., keychain, ring, and metal sheet in the vicinity of the proposed antenna, when the resonator is placed above Rx coil−5 as depicted in Figure 5.15. The corresponding voltage gain obtained at the Rx coil−5 is illustrated in Table 5.3 and Table 5.4, which exhibited an insignificant effect and can be tolerated.

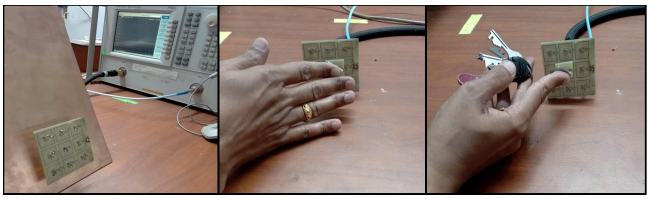

Figure 5.15: Experimental setup with different metallic objects (a) Conducting sheet, (b) Ring, (c) Keychain.

Table 5.3: Effect of the metallic sheet behind the transceiver antenna.

S.No.	Experiment	$V_{Rx}^{5}(\infty,\infty)$
1	Placing only finger near the transceiver	-19.64dB
2	Placing conducting sheet at 1cm behind the antenna	-19.91dB
3	Placing conducting sheet at 2cm behind the antenna	-19.87dB
4	Placing conducting sheet at 3cm behind the antenna	-19.80dB
5	Placing conducting sheet at 4cm behind the antenna	-19.78dB

Table 5.4: Effect of ring and keychain in hand placed above the transceiver antenna.

S.No.	Experiment	$V_{Rx}^{5}(0,0)$
1	Placing only finger without resonator at Rx coil-5	-19.64dB
2	Placing finger attached with resonator at Rx coil-5	-28.10dB
3	Finger attached with resonator and ring	-28.22dB
4	Finger attached with resonator, ring, and keychain	-28.46dB

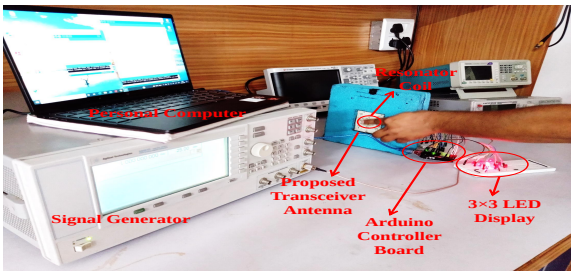

Figure 5.16: Real-life demonstration to trace the position of the moving fingertip.

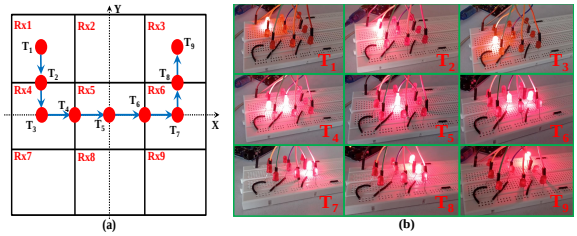

Figure 5.17: Real-life tracing (a) path followed, (b) acquire LED response for traced points.

Figure 5.16 demonstrates a real-life application of the proposed antenna utilized for tracing the moving fingertip. The proposed transceiver antenna is excited by Agilent Signal Generator (E8257D) and the responses obtained from the Rx sensor coils are processed using Arduino Uno controller board. A 3×3 LED array is employed to visually display the position tracing. The fingertip with resonator coil follows the path defined in Figure 5.17(a) and the acquired responses from the LED array at various time instants are shown in Figure 5.17(b). The demonstration depicts the glowing LED corresponding to the resonator position aligned with the particular Rx coil. When the resonator comes

between the two Rx coils, both the corresponding LEDs glow. The complete path tracing is verified in Figure 5.17. This demonstrates the effectiveness of the proposed localization system. Nevertheless, the suggested transceiver antenna solely identifies the position of a moving object and does not anticipate its orientation. This necessitates the development of a new Tx capable of predicting both the position and orientation simultaneously presented next.

5.2 Switchable Multicoil Transmitter (Design−3B)

The system configuration of a localization system containing a multicoil Tx and a planar Rx whose position and orientation OP (x_r, y_r, z_r, θ_r, ϕ_r) need to be determined is shown in Figure 5.18. The planar multicoil Tx antenna of size $S^0_{Tx} \times S^0_{Tx}$ is located in x-y plane

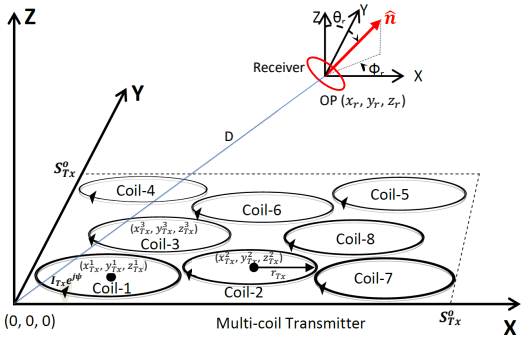

Figure 5.18: The planar receiver coil and the multicoil transmitter coordinates.

with dimension $S^0_{Tx} = 30$cm and comprises of $n = 8$ identical electrically small coils (coil-i, $\forall i \in [1, n]$) of outer turn radius $r_{Tx} = 50$mm arranged as shown in Figure 5.18 same as presented in [76, 77, 78, 79]. Each Tx coil-i centered at (x^i_{Tx}, y^i_{Tx}, z^i_{Tx}) has uniform total current $I_{Tx}e^{j\psi}e^{j2\pi f_i t}$ whose excitation source frequency f_i is set based on the feeding method adopted at the Tx as discussed later in this section. The current excitation in the Tx coils forms oscillating H-field distribution in the Rx region. The total H-field $\vec{H}$ generated at OP is contributed by individual coil-i with the three orthogonal components defined as H_x, H_y, and H_z at the observation point OP and calculated using (2.3). Thus, the RMS value induced voltage V_{ind} in the Rx coil having orientation (θ_r, ϕ_r) are evaluated using (2.10) and re-written as

$$\begin{aligned} V_{ind}(x_r, y_r, z_r, \theta_r, \phi_r) &= -N_r \mu_o \frac{d}{dt} \left[H_x A_x + H_y A_y + H_z A_z\right] \\ &\implies f(x_r, y_r, z_r, \theta_r, \phi_r) \end{aligned} \tag{5.7}$$

where function f denotes the analytical expression of ideal induced voltage for a given Rx location $(x_r, y_r, z_r, \theta_r, \phi_r)$ as

$$f(x_r, y_r, z_r, \theta_r, \phi_r) = -N_r \mu_o \frac{d}{dt} \left[H_x A_x + H_y A_y + H_z A_z\right] \tag{5.8}$$

and analytically evaluated by substituting (2.2-2.4) in (5.8). The actual location vector OP ={x_r, y_r, z_r, θ_r, ϕ_r} of the Rx is noted and actual distance D of the Rx from origin is calculated as $D = \sqrt{x_r^2 + y_r^2 + z_r^2}$. The induced voltage can be sensed and processed to

completely localize the Rx coil. Let the sensed output samples from the Rx having actual location $(x_r, y_r, z_r, \theta_r, \phi_r)$ is V' which can be expressed as

$$V' = f(x_r, y_r, z_r, \theta_r, \phi_r) + N_0, \tag{5.9}$$

where the effect of noise is accounted in the analysis to imitate realistic scenario and the V' samples are assumed corrupted by random white Gaussian noise N_0 with variance σ_N^2. For the given V' samples the predicted position and orientation vector OP' ={x'_r, y'_r, z'_r, θ'_r, ϕ'_r} of the Rx can be found by solving the following reverse expression

$$(x'_r, y'_r, z'_r, \theta'_r, \phi'_r) = f^{-1}(V') \tag{5.10}$$

where, f^{-1} is the inverse function of f in (5.8) and having a non-linear relation with $(x_r, y_r, z_r, \theta_r, \phi_r)$. Here, (5.9) and (5.10) are valid for electrically small Tx and Rx coil antennas which are assumed separated by the free space and laid within the near-field range. The non-linear equation (5.10) can be solved using the Levenberg–Marquardt (LM) method, which is a non-linear least-square algorithm and implemented using MATLAB [76, 77, 78, 79]. In this method, several distinct V' samples are sensed for a given Rx location to predict five unknown variables consisted in location vector OP'. The accuracy of the localization method is analyzed by evaluating errors (E_d and E_a) between actual and predicted location (position and orientation respectively) using the following expressions

$$\begin{aligned} E_d &= \sqrt{(x_r - x'_r)^2 + (y_r - y'_r)^2 + (z_r - z'_r)^2}, \\ E_a &= |\theta_r - \theta'_r| + |\phi_r - \phi'_r|. \end{aligned} \tag{5.11}$$

The localization accuracy depends on the H-field distribution and correspondingly induced V' samples in the Rx coil which are governed by the excitation of individual coil-i and its feeding method deployed at the Tx antenna. In general, the conventional feeding approach adopted previously [75, 76, 77, 78, 79] corresponds to the frequency-divisional tracking method described in Section 5.2.1 which is followed by the proposed approach of time-divisional tracking method in Section 5.2.2.

5.2.1 Conventional Frequency-divisional Tracking Method with Multi-frequency Tx Antenna

In this approach, all the eight coils of the Tx shown in Figure 5.18 are driven simultaneously and each coil-i is excited with a signal of different frequency f_i $\forall i \in [1, 8]$ ranging from 20 KHz to 30 KHz but of identical amplitude and phase. At the Rx, these frequency channels are sensed, demodulated, and eight frequency components of V' are extracted each corresponding to the H-field at OP due to coil-i of the Tx. These V' samples satisfy (5.10) which results in a set of eight non-linear equations and the solution of which determines the position and orientation vector OP'. The set of non-linear equations are solved using the LM method as mentioned earlier. To overcome the aforementioned drawbacks of the frequency-divisional tracking method as discussed in Section 1.6.2, a new Tx antenna design with proposed time-divisional tracking is presented next.

5.2.2 Proposed Time-divisional Approach with Optimized Multicoil Grouping and Minimized Feeding Complexity

In this section, the evolution of the proposed switched multicoil Tx antenna for time-divisional tracking method is presented. Initiating with the same Tx as depicted in Figure 5.18 with integrated time-divisional approach, all the coils are excited with a signal source of one frequency signal, but at various time-slots in a sequence by using a switching circuit. By using a number of switches (Sw) equal to number of feeding ports (n_p), the excitation can be switched ON-OFF for certain groups of the coils, simultaneously. However, to minimize the n_p for reducing the complexity, an optimal grouping of the coils (represented by grouping function G_{n_p}) is required. Since the localization accuracy depends on the H-field distributions that are generated by various coil groups in different time slots, the G_{n_p} is optimized to form a non-uniform field distribution such that the average errors in position ($\hat{E}_d$) and orientation ($\hat{E}_a$) of the localized Rx is minimized. The design parameter G_{n_p} with minimum possible n_p is selected to minimize $\hat{E}_d$ and $\hat{E}_a$, therefore, the formulated objective function of the design is defined as

$$\begin{aligned} &\text{Forming a non-uniform H-field distribution to achieve} \\ &\min_{G_{n_p}, n_p} \quad \left(\hat{E}_d \quad \text{and} \quad \hat{E}_a\right) \\ &\qquad s.t. \quad \min(n_p), \quad n_p \in [1, N] \end{aligned} \tag{5.12}$$

To understand the effect of the parameters on the solution of (5.12), initially consider that eight Sw ($n_p = 8$) are used to switch each coil ON-OFF individually in a sequence; this will result in formation of eight groups comprised in G_8 where each group is containing one coil member. In this case, 2^8 combinations of Sw states (ON or OFF) will excite $2^8 - 1$ different combinations of the coils (excluding the state in which all Sw are OFF) and hence generate $2^8 - 1$ distinct H-field distributions around the Rx. However, it requires $2^8 - 1$ number of time-slots, hence, not applicable for real-time localization of mobile Rx due to latency issue. Since, in frequency-divisional tracking, only eight distinct H-field distributions (because each coil is excited at different frequency) are suggested sufficient to localize the Rx, the same is assumed as sufficient condition for the time-divisional method to upper bound the complexity. For time-divisional tracking using $n_p = 8$ Sw, any eight states out of $2^8 - 1$ can be chosen to generate eight distinct H-field distributions, thereby reducing the required number of time-slots to eight hence improving the latency significantly. However, the system still remains complex due to the use of several Sw and complex feeding network.

In contrast to the eight Sw case, if just one Sw ($n_p = 1$) is used then only a single group is formed in G_1, hence, all the coils can be switched ON or OFF simultaneously providing only one distinct H-field distribution which is not sufficient to find five variables (x_r, y_r, z_r, θ_r, ϕ_r) of the location vector OP. Essentially, atleast five distinct H-field distributions to solve five relations are required to evaluate the OP. Therefore, a minimum of three SWs

($n_p \geq 3$) are required that can generate seven ($2^3 - 1$) distinct H-field distributions. Thus, the minimum possible $n_p = 3$ is proposed which divides the Tx coils into three groups contained in G_3 and only seven time-slots are required to estimate the OP. This highly reduces the system complexity and localization time. To form three groups in G_3, several possible combinations of the coils are studied and realizable arrangements (the ways of grouping in G_3) are listed in Table 5.5. Out of these possible arrangements where each

Table 5.5: Various coil arrangements to form three groups.

Coil arrangement	Group-1	Group-2	Group-3
1	Coil-1	Coil-2	Coil-3-4-5-6-7-8
2	Coil-1	Coil-4	Coil-2-3-5-6-7-8
3	Coil-1	Coil-5	Coil-2-3-4-6-7-8
4	Coil-1	Coil-6	Coil-2-3-4-5-7-8
5	Coil-1	Coil-2-3	Coil-4-5-6-7-8
6	Coil-1	Coil-2-7	Coil-3-4-5-6-8
7	Coil-1	Coil-4-6	Coil-2-3-5-7-8
8	Coil-1	Coil-5-6	Coil-2-3-4-7-8
9	Coil-2	Coil-1-3	Coil-4-5-6-7-8
10	Coil-1-2	Coil-3-4	Coil-5-6-7-8
11	Coil-1-2	Coil-3-4-6	Coil-5-7-8

can generate a different H-field distribution, an optimal grouping is found to generate the optimal non-uniform field distribution such that the design objective of (5.12) is achieved. To accomplish that, the effect of coil grouping on localization performance is analyzed and accuracy results for comparison of the possible grouping G_3 listed in Table 5.5 are shown in Figure 5.19. It is revealed that the arrangement-11 has best localization accuracy in

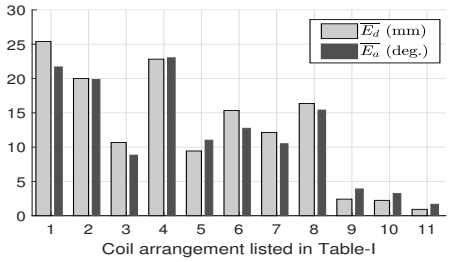

Figure 5.19: Localization performance of various coil arrangements in G_3 ($\sigma_N^2 = -90$dB).

terms of minimum average localization errors among the various coil arrangements listed in Table 5.5, hence, correspondingly chosen as the proposed design. The non-uniform H-field distribution result formed by the arrangement-11 is demonstrated later in Section 5.2.4. The proposed design (arrangement-11) which also has better localization accuracy as compared to the multi-frequency Tx is detailed subsequently.

5.2.3 Proposed Antenna for Time-divisional Tracking Approach

In this section, the multicoil Tx antenna conceptualized for time-divisional tracking method in Section 5.2.2 is realized into a practical design. For a cost effective planar solution, the antenna is realized on a single-sided PCB (Printed Circuit Board) made of FR4 substrate of thickness, $h = 1.575$ mm, relative dielectric constant $\epsilon_r = 4.4$, loss tangent $\tan\delta = 0.02$, and 0.02 mm of copper deposition. The proposed switched multicoil

antenna is presented in Figure 5.20 consisting of coil-i $\forall i \in [1, 8]$ each with a coil radius $r_{Tx} = 5$ cm, available turns $N_{Tx} = 25$, width of conductive track $w_{Tx} = 0.5$ mm and spacing between the adjacent tracks $g_{Tx} = 0.5$ mm, respectively, moreover, a small Rx having dimensions coil radius $r_r = 1$ cm, turns $N_r = 3$, track width $w_r = 0.5$ mm and spacing between the tracks $g_r = 0.5$ mm, respectively, is employed to not perturb the H-field distribution generated by the Tx antenna. The identical dimensions of each coil present in Tx antenna is used also for the multi-frequency antenna to fairly compare the performance with the proposed design. Moreover, the maximum N_{Tx} present in the Tx coil-i is chosen to enhance the localization accuracy, and w_{Tx}, g_{Tx}, w_r, and g_r values are selected in accordance to the minimum fabrication limit of the PCB prototyping machine available in the laboratory. As discussed in Section 5.2.2, three switches Sw_1,

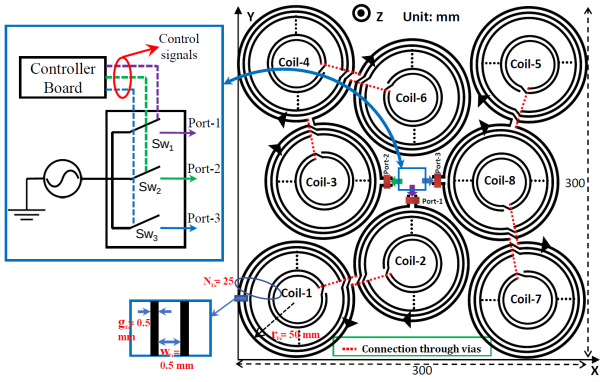

Figure 5.20: The proposed switched multicoil antenna realization.

Sw_2, and Sw_3 are used to divide the coils into three groups Coil$-1-2$, Coil$-3-4-6$, and Coil$-5-7-8$, respectively fed by Port-1, -2, and -3, where all the coils of a group are excited simultaneously to implement the proposed time-divisional tracking method. The complex feeding network is avoided by judiciously connecting all the member coils of every group in series such that they are excited through a common input port with a same signal of frequency 10 KHz excited from a single source as depicted in the inset of Figure 5.20. Here, the states of the switches are controlled by a controller board and L-section matching networks are inserted for impedance matching at the individual ports. The current circulation is same for all the coils of a group to achieve constructive addition of the fields. The proposed antenna is fed by three input ports compared to eight ports required for multi-frequency Tx presented in Section 5.2.1.

As discussed in Section 5.2.2, the proposed localization method requires seven time-slots t_i $\forall i \in [1, 7]$ to sense and localize the Rx. This is performed by switching ON or OFF the three coil groups using Sw_1, Sw_2, and Sw_3 in each t_i. The state of Sw during t_i times are shown in Table 5.6 and the correspondingly excited coils are listed. This arrangement generates seven distinct H-field distributions (one per time-slot) at the Rx location. The channel at the Rx is sensed, demodulated, and extracted voltage samples provide seven V' values at Rx each corresponding to one t_i. The sensed V' values and the corresponding H-field satisfy (5.10) for a combination of excited coils as per Table 5.6. This gives seven

Table 5.6: Switching states and excited coils for the proposed design

Time-slot	Sw_1	Sw_2	Sw_3	Excited coils
t_1	ON	OFF	OFF	Coil-1-2
t_2	OFF	ON	OFF	Coil-3-4-6
t_3	OFF	OFF	ON	Coil-5-7-8
t_4	ON	ON	OFF	Coil-1-2-3-4-6
t_5	ON	OFF	ON	Coil-1-2-5-7-8
t_6	OFF	ON	ON	Coil-3-4-5-6-7-8
t_7	ON	ON	ON	Coil-1-2-3-4-5-6-7-8

non-linear equations involving variables of the location vector OP of the Rx and solved by using the same algorithm (based on LM method) as adopted for multi-frequency design presented in Section 5.2.1.

5.2.4 Performance evaluation and results

In this section, the performance of the proposed switched multicoil Tx antenna presented in Section 5.2.3 is evaluated and compared with the equivalent multi-frequency Tx antenna discussed in Section 5.2.1.

Analyzed H-field distributions of the two designs

The resulting H-field distributions for both the designs are computed using (2.2)−(2.4) for $z_r = 10$ cm plane. The calculated normalized 2−D field-distributions of H_x, H_y and H_z originating from the multi-frequency Tx antenna is shown in Figure 5.21 for all the frequencies f_i $\forall i \in [1, 8]$ transmitted by the antenna. The plots indicate that the H-field

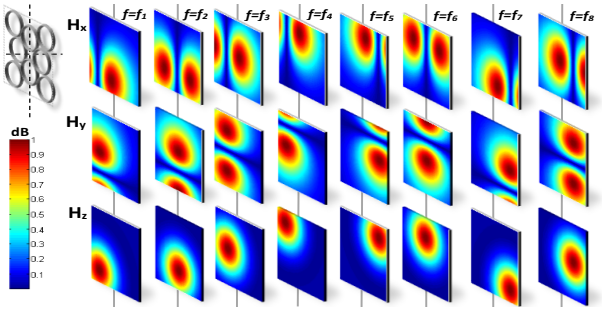

Figure 5.21: H-field distributions of multi-frequency Tx antenna for all f_i.

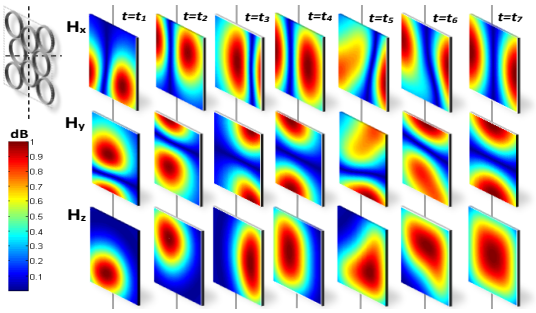

Figure 5.22: H-field distributions of proposed switched multicoil antenna at all t_i.

patterns at various f_i are the same but spatially shifted versions according to the spacial location of the corresponding coil$-i$ excited by f_i. At a particular Rx location, diverse H-field components are produced at various f_i implying diverse values of induced voltages in the Rx coil, hence eight distinct H-field distributions are obtained. However, there exist a large area where the H-field strength is very low resulting in low noise immunity of several V' samples in the previous approach of frequency divisional tracking with multi-frequency antenna. In contrast, the normalized 2$-$D field distributions for the proposed switched multicoil Tx antenna are shown in Figure 5.22 for various time slots t_i. According to the excited coil groups for each time-slot t_i given in Table 5.6, the H_x, H_y and H_z distributions are plotted. The patterns demonstrate that, at a particular Rx location, seven distinct H-field distributions are obtained at various t_i by using the proposed antenna. Moreover, the field strength is improved over a wider Rx area compared to the multi-frequency antenna so as to achieve enhanced noise immunity by the proposed switched antenna. Hence, the field pattern results validate the discussion presented in Section 5.2.2 regarding generation of non-uniform H-field distributions.

Localization performance evaluation and comparison

In this section, performance of the proposed localization method is evaluated through analysis and the results are validated using simulations. The proposed switched Tx antenna of Figure 5.20 and its equivalent multi-frequency Tx antenna were analyzed using Mathworks MATLAB and simulated using commercially available electromagnetic solver HFSS. The Rx coil having sensitivity ~0.1 V/Hz/T and an effective coil area (summation of individual turn area) of 0.1m^2 was used [78]. The procedure to evaluate localization performance is now described.

The planar Rx coil is randomly placed at several test positions and orientations in a volume of 300×300×300 mm^3 above the planar Tx. The actual location vector OP=$\{x_r,\ y_r,\ z_r,\ \theta_r,\ \phi_r\}$ of the Rx is noted and actual distance D of the Rx from origin is calculated as $D = \sqrt{x_r^2 + y_r^2 + z_r^2}$. For each case, the Rx is localized using the methods presented in Section 5.2, and the predicted position and orientation vector $OP' = \{x'_r,\ y'_r,\ z'_r,\ \theta'_r,\ \phi'_r\}$ is found. To imitate realistic scenario, the effect of noise is accounted and the induced EMF samples at the Rx are corrupted by random white Gaussian noise with variance σ_N^2. Then the accuracy of the localization method is given by evaluating errors (E_d and E_a) between actual and determined location (position and orientation) using (5.11).

Next, to evaluate terminal characteristics, the unloaded antenna is simulated to evaluate input impedances of the three ports and corresponding L-section matching network parameters are calculated as $C = 53$ nF and $L = 9$ mH for Port-1, and $C = 40$ nF and $L = 12$ mH for Port-2 and Port-3 for a 50 Ω impedance matching. The matched antenna was simulated and the results indicate a high isolation of 40 dB existing between the ports. This shows that a low coupling between the various ports exists due to the formation of a highly non-uniform concentrated H-field by the coil groups of the proposed antenna which are distributed in a same plane for lower mutual coupling, hence, not affecting the

localization accuracy. Moreover, the performance of the proposed Tx antenna is evaluated in terms of signal-to-noise ratio (SNR) obtained at the Rx coil [106]. The achieved SNR values (in dB) by placing the Rx at (0, 0, 50) mm and exciting Tx Port-1, -2, and -3 are obtained as 33.58, 38.40, and 16.30, respectively.

The localization performances of the proposed switched multicoil and the multi-frequency Tx antennas are now compared. The effect of noise and Rx-Tx distance (Rx z-coordinate z_r) on position and orientation errors (E_d and E_a) is shown in Figure 5.23. The

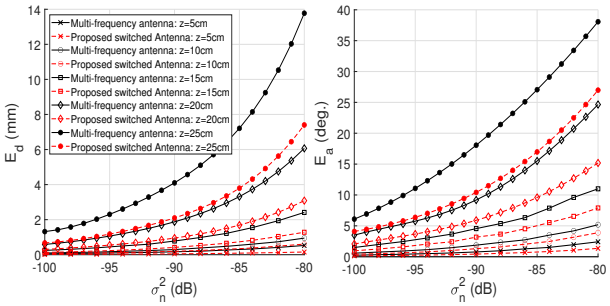

Figure 5.23: Effect of noise on localization error for various Rx-Tx distances $z_r = z$.

results demonstrate that the proposed design with localization approach is more noise resilient compared to the multi-frequency design. Moreover, though both the designs show degraded localization performance for higher Rx-Tx distances, the errors are comparatively much lower for the proposed antenna. The enhanced performance can be attributed to the better non-uniform field-forming and a strong H-field distribution obtained in Figure 5.22 by the proposed switched antenna.

Evaluated for several random test points, Figure 5.24 presents the location errors with respect to the Rx distance D from the origin and the proposed design shows better localization accuracy in both, the position as well as the orientation. A general workstation having a 3.6 GHz Intel Xeon processor with 64 GB RAM is employed for this purpose. The convergence performance of the LM method is found similar for both the designs and required $4-15$ iterations and $17-40$ msec tracking time on average to converge. Considering all the test point results, the average, $\hat{E}_d$, $\hat{E}_a$, and standard deviation σ_d, σ_a, of

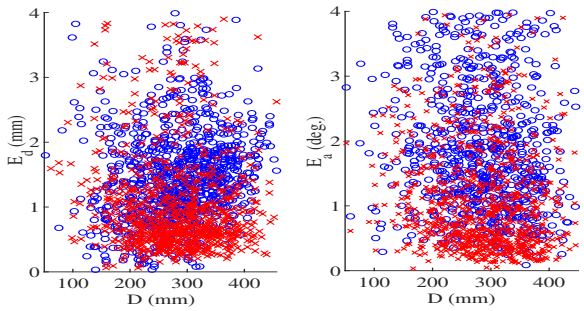

Figure 5.24: Position and orientation errors E_d and E_a for several test locations ($\circ$ using multi-frequency antenna, $\times$ using proposed switched antenna).

the position and orientation errors, respectively, are listed in Table 5.7. Both the analytical and simulated results are included for comparison. The analytical results reveal that localization performed using multi-frequency Tx antenna shows mean position error (mean

Table 5.7: Localization accuracy comparison between proposed and previous design

	Multi-frequency antenna		Proposed switched antenna	
	Analysis	Simulation	Analysis	Simulation
$\hat{E}_d$ (mm)	1.5190	1.8404	1.2211	1.4292
σ_d (mm)	0.9817	0.8374	0.8312	0.8093
$\hat{E}_a$ (deg)	2.7136	2.5081	1.1835	1.7140
σ_a (deg)	0.8158	0.9977	0.8919	0.6896

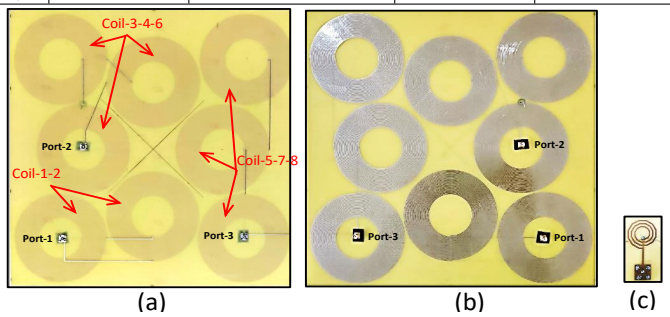

Figure 5.25: Fabricated prototypes of the proposed switched antenna (a) bottom view (b) front view (c) the Rx coil.

orientation error) as 1.52 mm (2.71°) with standard deviation 0.98 mm (0.82°), whereas, the proposed switched Tx antenna has reduced mean position error (mean orientation error) to 1.22 mm (1.18 °) with standard deviation 0.83 mm (0.89°). The superiority of the proposed antenna is corroborated by simulation results in Table 5.7 showing mean position and orientation errors to be 1.43 mm and 1.71° with standard deviation of 0.81 mm and 0.69° for the proposed design as compare to 1.84 mm and 2.51° with standard deviation of 1.84 mm and 2.51° for the previous design, respectively. Hence, the proposed antenna is shown to have a better localization accuracy, in addition, having a lower complexity and simplified feeding network as compared to the previous multi-frequency design. Further, the proposed antenna performance is validated experimentally in the subsequent section.

5.2.5 Experimental verification and Results

To experimentally validate the proposed design and the performance of the proposed localization approach, the antenna is fabricated using a PCB prototyping machine available in the laboratory and prototype of the proposed switched antenna is shown in Figure 5.25 which also shows the fabricated planar Rx coil to be localized. The dimensions of the fabricated Tx and Rx designs are the same as those mentioned in Section 5.2.3. Figure 5.26 demonstrates the measurement setup employed to verify performance of the proposed system. For that, a robotic arm (DRS60L) is deployed to precisely move the Rx coil in various orientations at different positions over the transmitter antenna. To excite the proposed Tx antenna with sinusoidal signal of frequency 10 KHz, a Tektronix function generator (AFG1062) is utilized. To implement the switching control, a relay based switching circuitry is designed which is triggered with a micro-controller as depicted in the Figure 5.26. A Keysight DSO (DSOX2022A) is employed at the Rx coil for reading

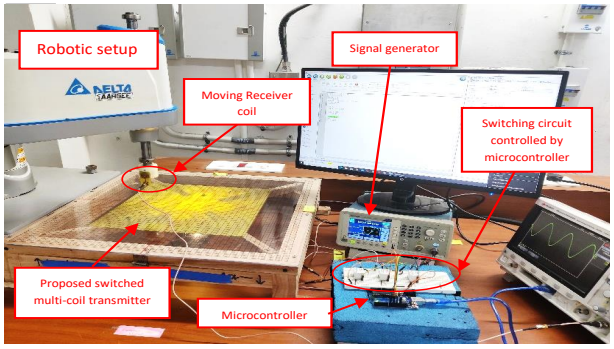

Figure 5.26: Hardware setup for experimentation.

the signal received from the Rx coil. First, to verify the claim of the robust non-uniform H-field forming by the proposed antenna, the Rx coil is moved by 10 mm steps to scan the entire parallel plane at 50 mm above the Tx antenna. The scan is performed thrice each for an orthogonal orientation of the Rx to read H_x,H_y, and H_z distributions. The normalized H_z distributions measured corresponding to the different switching states (time slots t_i) of Table 5.6 are shown in Figure 5.27 where only H_z field distributions are shown for brevity. The left column of Figure 5.27 includes analytically obtained H_z distributions for comparison which shows a good agreement with the measured field distributions shown in the right column of the figure. For instance, in the switching state t_1 in which Coil-1-2 are ON and others are OFF, the H_z distributions are given in Figure 5.27(a) and (b), respectively obtained from analysis and measurement. Similarly, the H_z distributions for other switching states can be verified. To further validate the H_x and H_y along with H_z, the measured results in 2−D cuts of the Rx movements are shown in Figure 5.28. Here, Figure 5.28(a, b) are plotted for $X = 0$ and $Y = 0$ cuts, respectively, for the switching state t_1. Similarly, Figure 5.28(c, d) framed the t_2 switching state results and Figure 5.28(e, f) plots the results of the switching state t_3. The plots conclude that the measured H-field distributions validate the non-uniform field forming by the proposed switched antenna. Some deviation present in the measured results can be attributed to fabrication and measurement tolerances and the presence of noise.

The localization precision in terms of position and orientation measurement is evaluated by tracing the moving Rx along a line for various orientations of the Rx coil. The measured localization results are presented in Figure 5.29. Here, Figure 5.29(a) and (b) demonstrate the tracking by the algorithm and the disparity between the actual (x_r and y_r) and the predicted (x'_r and y'_r) position values for three different orientations of the Rx coil. Similarly, the actual and predicted orientations θ_r and ϕ_r for various positions of the Rx coil is demonstrated in Figure 5.29(c) and Figure 5.29(d), respectively. For all the testing samples, the localization errors E_d and E_a are measured and shown in Figure 5.29(e) and Figure 5.29(f), respectively. The experimental results reveal that the localization error distributions and limits are similar to what have been observed through analysis in Figure 5.24. The measured $\hat{E}_d$ and $\hat{E}_a$ along with analytically obtained $\hat{E}_d$ and $\hat{E}_a$ are presented in Table 5.8 and the values are well corroborating. A small deviation present between the measured and analytical values is attributed to fabrication and measurement

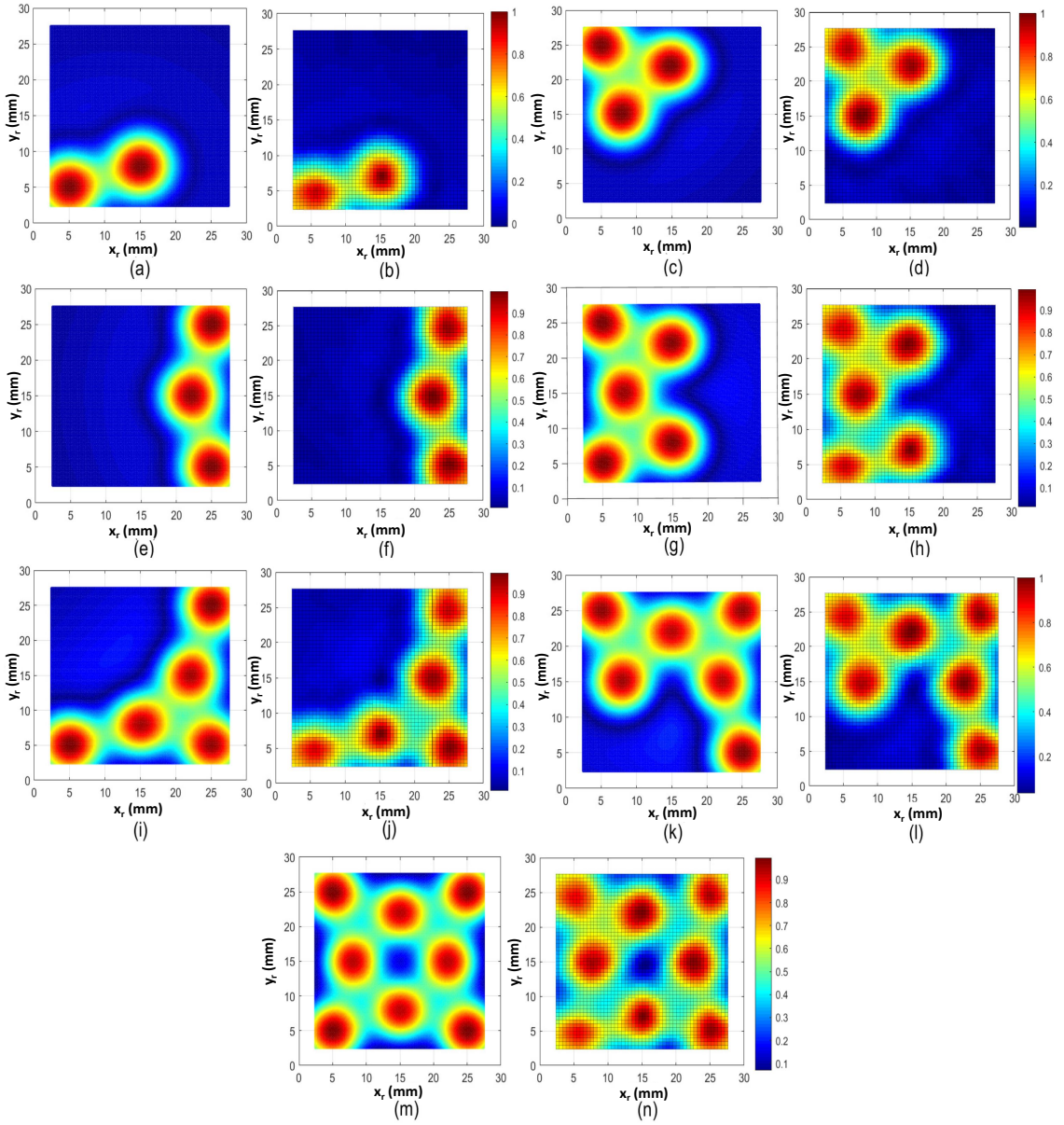

Figure 5.27: Normalized H_z distributions at $z_r = 50$ mm. Results for various switching states (a, c, e, g, i, k) analytical $t_1 - t_7$, (b, d, f, h, j, l) measured $t_1 - t_7$.

Table 5.8: Comparison between analytical and measured error values

Average position and orientation error	Analysis	Measured
$\hat{E}_d$ (mm)	1.22	1.67
$\hat{E}_a$ (deg)	1.18	1.60

errors. This exemplifies that the proposed Tx antenna designed using planar technology has the potential to track the position and orientation of a planar Rx coil accurately compared to the similar conventional tracking scheme. Therefore, the exploitation of non-uniform H-field forming for the proposed time divisional tracking approach is proved beneficial to enhance localization accuracy along with reduced complexity. Nevertheless, the design parameters of the selected transmitter are unoptimized, leading to a larger size. This necessitates the introduction of an optimized transmitter to further minimize its overall size, which is presented subsequently.

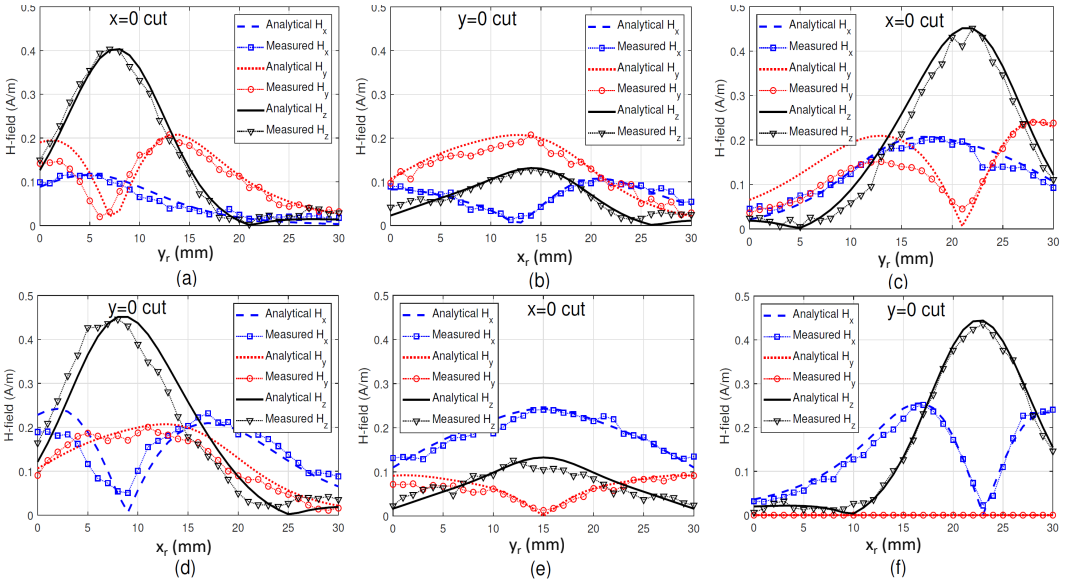

Figure 5.28: 2-D H-field plots in switching states (a, b) t_1, (c, d) t_2, (e, f) t_3, for $z_r = z$.

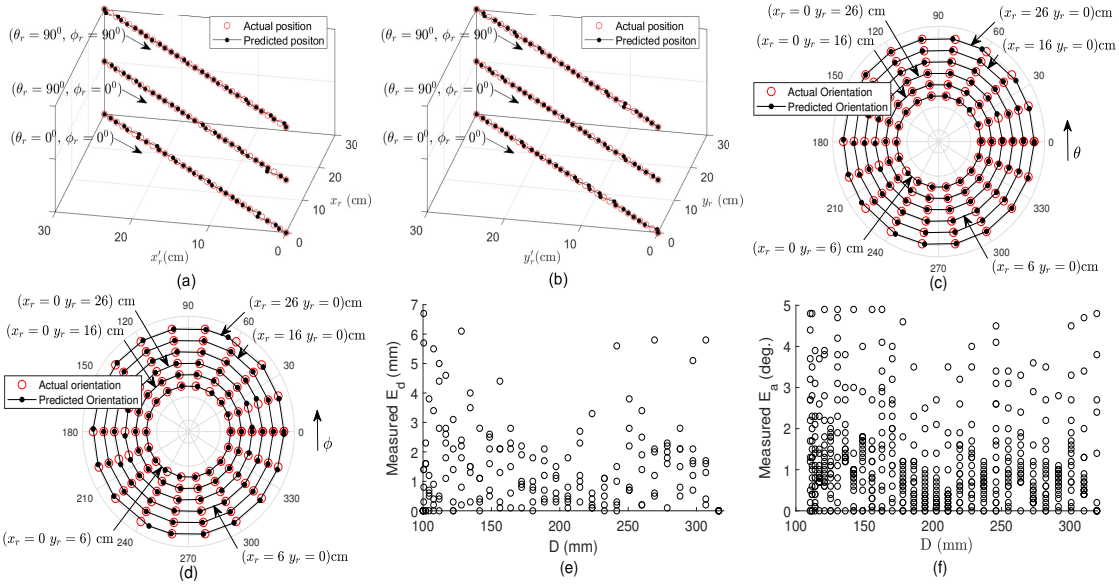

Figure 5.29: Measured tracking and localization in (a) position x_r, (b) position y_r, (c) orientation θ_r, (d) orientation ϕ_r, (e) position error E_d , (f) orientation error E_a.

5.3 Switching Integrated Overlapping Transmitter (Design−3C)

The proposed localization system contains a Tx pad and a Rx coil to effectively localize the position and orientation (x_r, y_r, z_r, θ_r, ϕ_r) of an implanted device. For this purpose, the Rx is equipped within the implanted device and captures the H-field generated by the proposed Tx. Whereas, for generating the sufficient amount of H-field from the proposed Tx, an array of eight overlapping square coils (Coil$-i$, $\forall\, i \in [1, 8]$ as shown in Figure 5.30(a) is employed. Here, the coils present in the proposed Tx are judiciously located in different layers to avoid any shorting between the adjacent coils. For instance, Coil-1 to Coil-4 are located at Layer-1 with a small spacing between them defined as $\chi = 1$ mm to avoid

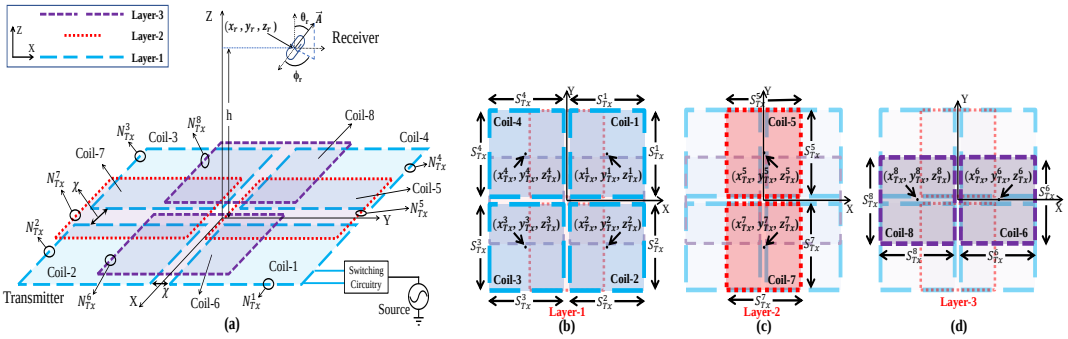

Figure 5.30: Configuration of proposed localization system (a) 3−D view, (b) Layer-1, (c) Layer-2, (d) Layer-3 of the proposed Tx.

superimposing between the coils as depicted in Figure 5.30(b). Whereas, Coil−5 and Coil−7 are positioned at Layer−2. Similarly, Coil−6 and Coil−8 are placed on Layer−3 as demonstrated in Figure 5.30(c) and (d), respectively. The side length and positioning of the individual coil are symbolized as S^i_{Tx} and $(x^i_{Tx}, y^i_{Tx}, z^i_{Tx})$, respectively, $\forall\ i \in [1, 8]$. To make the system cost-effective, a single sinusoidal excitation with a switching circuitry has been utilized to feed these coils. The switching circuitry consists of three Single Pole Double Throw (SPDT) switches to connect the desired set of parallel connected coils to the source, along with eight Single Pole Single Throw (SPST) switches symbolized as $(Sw_1 - Sw_8)$ to operate a particular set of coils and depicted in Figure 5.31. Moreover, four capacitors $(C^1_{reso} - C^4_{reso})$ are inserted in series with each terminal to resonate the system at working frequency. Once the source is connected to the parallel Tx coils for

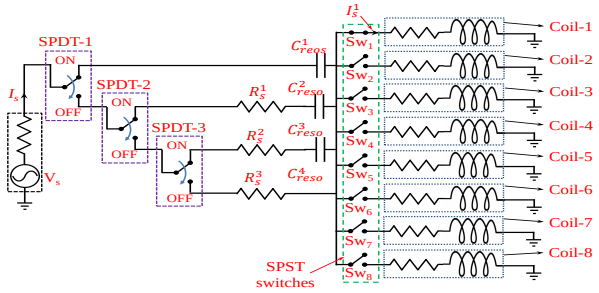

Figure 5.31: Switching circuitry to excite the coils present in the proposed Tx.

a particular switching duration, it fetches current from the source symbolized as I_s and distributes this current to the parallel connected coils denoted as I^i_s. This flow of current through the coils is responsible for generating H-field at the Rx location, which can be exploited to localize the position and orientation of any implanted Rx.

To analytically evaluate the H-field generated from Coil$-i$ of the proposed Tx at the Rx location (x_r, y_r, z_r), the H-field formulation corresponds to a single turn square coil is utilized as presented in (2.5)-(2.6). Thus, the total H-field at the Rx location is the summation of the H-field generated from individual Tx coils and the resultant H-field is the vector summation of all the three H-field components calculated using (2.6) and defined as $\vec{H} = H_x\hat{x} + H_y\hat{y} + H_z\hat{z}$. This generated H-field induces a voltage V_{ind} at the Rx location and is evaluated as (2.9).

A previous study found that at least five different voltage samples are required for

effectively estimating the position and orientation of a moving Rx. Moreover, in the presented design, the required voltage sample can be obtained by exciting a particular dominant coil group and their combination to predict the location of Rx placed in any quadrant. This is because only the dominant coil will provide ample strength of the H-field at the Rx location. For instance, Coil−1, Coil−5, and Coil−6 are the dominant coil groups in the first quadrant with $x_r > 0$, $y_r > 0$. Similarly, the dominant coil group for the remaining quadrants is provided in Table 5.9. As the proposed structure is

Table 5.9: Dominant coil groups in a specific quadrant of Rx region.

Quadrant	x_r range	y_r range	Dominant coil group
First	[0, 150] mm	[0, 150] mm	Coil−1, Coil−5, and Coil−6
Second	[−150, 0] mm	[0, 150] mm	Coil−4, Coil−5, and Coil−8
Third	[−150, 0] mm	[−150, 0] mm	Coil−3, Coil−7, and Coil−8
Fourth	[0, 150] mm	[−150, 0] mm	Coil−2, Coil−6, and Coil−7

symmetric along the X and Y axes, the performance is analyzed only in the first quadrant of the proposed Tx. The circuit schematic for acquiring the voltage samples in the first quadrant by only exciting the dominant coil group of the first quadrant is presented in Figure 5.32. Besides, the possible switching state, along with the switching sequence of the

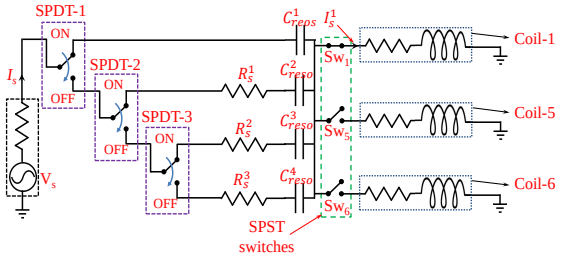

Figure 5.32: Circuit schematic for exciting dominant coil group of the first quadrant of proposed Tx.

dominant coils of the first quadrant to acquire the required voltage samples, are provided in Table 5.10. Further optimization of the proposed Tx for achieving a highly non-uniform

Table 5.10: Switching sates and switching sequence when exciting dominant coils in the first quadrant.

Switching states	ST−1	ST−2	ST−3	ST−4	ST−5	ST−6	ST−7
SPDT−1	OFF	OFF	OFF	ON	ON	ON	ON
SPDT−2	OFF	OFF	OFF	OFF	OFF	ON	ON
SPDT−3	OFF	OFF	OFF	OFF	OFF	OFF	ON
Sw_1	ON	OFF	OFF	ON	ON	OFF	ON
Sw_5	OFF	ON	OFF	ON	OFF	ON	ON
Sw_6	OFF	OFF	ON	OFF	ON	ON	ON
Coil−1	ON	OFF	OFF	ON	ON	OFF	ON
Coil−5	OFF	ON	OFF	ON	OFF	ON	ON
Coil−6	OFF	OFF	ON	OFF	ON	ON	ON

H-field distribution at the Rx region to improve the localization accuracy is demonstrated in the subsequent section.

5.3.1 Analytical Optimization and Performance Evaluation

Proposed transmitter optimization

The proposed Tx needs to be optimized analytically to increase the accuracy for a larger localization range. This demands a highly nonuniform distribution of H-field components throughout the Rx region for various switching intervals because a nonuniform H-field improves spatial resolution and precision compared to the uniform H-field distribution in localizing implanted devices during dynamic movements. Therefore, the coil design parameters of the proposed Tx, such as side length and the number of turns, must be appropriately selected. As the coils in the proposed Tx are identical, optimizing a single coil and replicating the same optimized coil with other coils resulted in an optimized Tx structure. To attain this objective, initially, the design variables of Coil−1 present in the proposed Tx and positioned at (x^1_{Tx}, y^1_{Tx})= (75, 75) mm are made variable, and the generated H-field components are observed at the Rx plane $z_r = 50$ mm. Since the Coil−1 is square, the generated lateral fields (H_x and H_y) must be identical. Therefore, only H_x and H_z variations are shown in the analytical parametric study of the optimization process as illustrated in Figure 5.33. Here, Figure 5.33(a) shows the variations of H_x

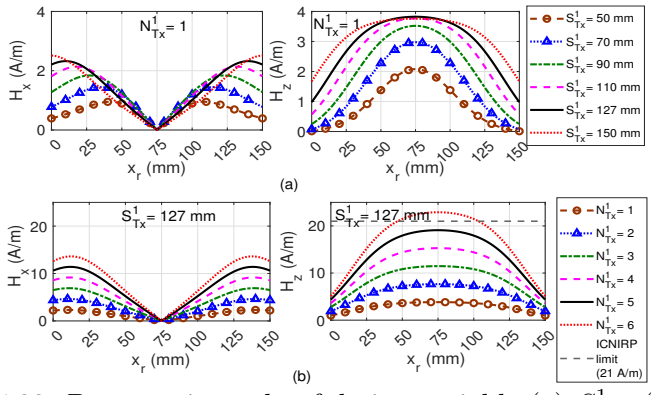

Figure 5.33: Parametric study of design variable (a) S^1_{Tx}, (b) N^1_{Tx}.

and H_z components versus x_r for different S^1_{Tx} values, with $N^1_{Tx} = 1$. The plot reveals that the maximum H_x component occurs at the edges of the coil, while the maximum H_z value is attained at the coil's center. Additionally, the plot illustrates that both H_x and H_z components increase with the increment of S^1_{Tx} for a single-turn Tx coil, as depicted in Figure 5.33(a). However, beyond a certain value of S^1_{Tx}, the H_x component continues to increase at the edges, whereas the H_z component starts decreasing at the coil's center. Therefore, a trade-off between these values is chosen as the optimal value and given as $S^1_{Tx} = 127$ mm. On the other hand, the optimization of N^1_{Tx} adheres to the ICNIRP guidelines, wherein the maximum field should not exceed 21 A/m. Figure 5.33(b) demonstrates the variation of the H-field against x_r for various N^1_{Tx} values, plotted with the optimal $S^1_{Tx} = 127$ mm. The plot illustrates that both H_x and H_z components are within the ICNIRP limit for $N^1_{Tx} = 5$, thereby confirming the optimized parameters for Coil-i, $\forall i \in [1, 8]$, as $S^i_{Tx} = 127$ mm and $N^i_{Tx} = 5$, respectively.

Transmitter structure miniaturization and magnetic field variation from the optimized coil

To further miniaturize the size of the proposed Tx, the central position (x^i_{Tx}, y^i_{Tx}, z^i_{Tx}) of the various coils present in the proposed Tx are made closer to the central region of the Tx as shown in Figure 5.30(a) without altering the optimized S^i_{Tx}. Moreover, the coils' centers are adjusted judiciously such that the adjacent coils present in a specific layer do not intersect with each other and result in reduced deformation in the H-field non-uniformity. For this purpose, the lower limit of the center is taken as 64 mm because, beyond this range, adjacent turns will coincide with each other. The impact on H-field variation by shifting the center of Tx Coil−1 from (75, 75) mm to (64, 64) mm are plotted in Figure 5.34. The plot signifies that the H-field variation is not significantly

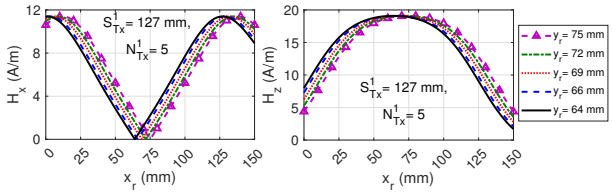

Figure 5.34: Impact on H-field by varying the center of Tx Coil−1.

disturbed, even by shifting the Tx coil position to the minimum possible value. Thus, the final optimal parameters and corresponding positions of the various coils present in the proposed Tx are listed in Table 5.11. This results in the proposed Tx's overall size

Table 5.11: Final optimized parameters (in mm) of the various coils present in the Tx.

Tx Coil−i	S^i_{Tx}	N^i_{Tx}	(x^i_{Tx}, y^i_{Tx})
Coil−1 to Coil−4	127	5	(±64, ±64)
Coil−5 and Coil−7	127	5	(0, ±64)
Coil−6 and Coil−8	127	5	(±64, 0)

to be 255×255 mm^2. Hence, the reduction in overall Tx size compared to the previous design presented in Section 5.2.3 will be 27.75%. Once the optimal coil parameters of the various coils are known, placing them to their respective optimal positions and exciting for a specified switching duration resulted in H-field distribution as shown in Figure 5.35. This demonstrates the non-uniformity present in the H-field component's distribution at the Rx position $z_r = 50$ mm.

5.3.2 Performance evaluation of the optimized Tx structure

Once the optimization of the proposed Tx is completed, its localization performance in the first quadrant of the Tx structure is examined using Mathworks software. For this purpose, the dominant coil group of the first quadrant, present in the proposed Tx structure, as listed in Table 5.9, is modelled analytically and excited sequentially as presented in Table 5.10. The voltage samples collected from the Rx for various switching states are employed to predict the position and orientation of a moving Rx. Here, a Rx coil with a radius of 10 mm, six turns, track width, and spacing between the tracks of 0.5 mm

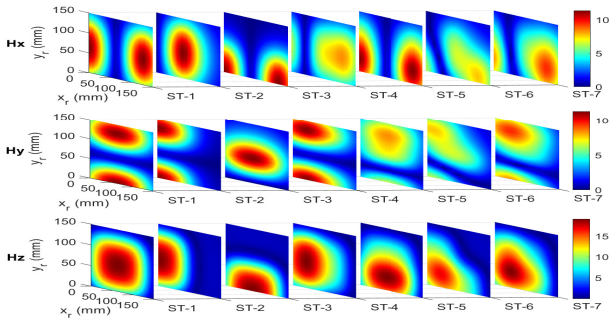

Figure 5.35: Optimized H-field distribution in the Rx plane $z_r = 50$ mm generated by the proposed Tx when excited for a specified switching duration

.

is adopted as a voltage probe for obtaining the voltage samples for various switching instants. To resemble the practical scenario, a measured random white Gaussian noise (N_o) of -53.98 dB has been included together with the voltage samples collected from various switching instants. The final voltage sample (V') available to decide the position and orientation of the Rx coil is defined as (5.9).

To evaluate localization performance, the Rx is randomly positioned at several test positions and orientations (x_r, y_r, z_r, θ_r, ϕ_r) within a test volume ranging from $0 \leq x_r, y_r \leq 150$ mm, $50 \leq z_r \leq 300$ mm, $0 \leq \theta_r \leq 180°$, and $0 \leq \phi_r \leq 360°$ above the proposed Tx structure. Consequently, the predicted position and orientation $(x'_r, y'_r, z'_r, \theta'_r, \phi'_r)$ corresponding to voltage sample V' obtained at the Rx coil using as (5.10) and a non-linear least-square algorithm, Levenberg–Marquardt (LM) is adopted and implemented using MATLAB. A workstation with a 3.6 GHz Intel Xeon processor and 64 GB RAM is employed. Additionally, to quantify the localization accuracy, an error is estimated between actual and predicted positions and orientations (E_d and E_a) as given in (5.11).

The analytically estimated localization errors for various random test positions and orientations are plotted in Fig. 5.36(a-d). Moreover, the E_d and E_a variation with the Rx transfer distance h are illustrated in Fig. 5.36(e,f) to visualize the proposed Tx localization accuracy. The plot signifies that higher h results in a drastic increase in E_d and E_a because

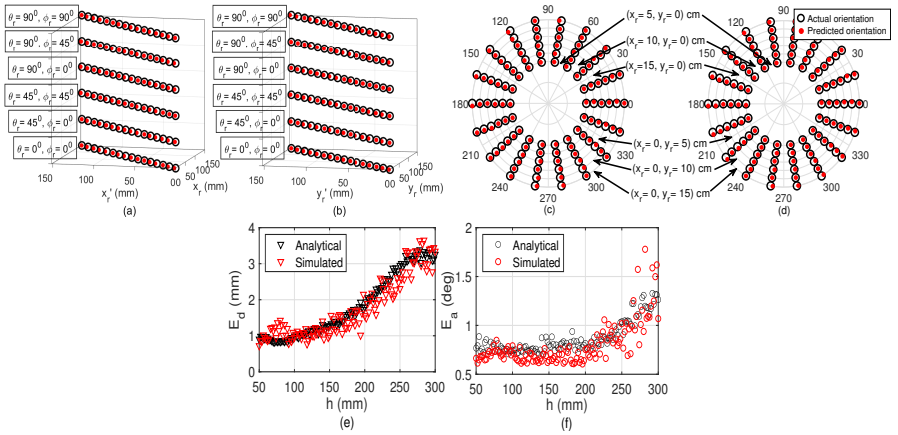

Figure 5.36: Analytically estimated localization error with (a,b) positions (x_r, y_r), (c,d) orientations (θ_r, ϕ_r), (e,f) E_d and E_a versus transfer distance h.

Table 5.12: Properties of human tissues inserted between the Tx and Rx coils.

	Skin	Fat	Muscle	Soft Tissue
Density (Kg/m^3)	1109	911	1090	1008
Relative permittivity	1.09×10^3	6.25×10^{-1}	4.94×10^3	2.24×10^3
Electric conductivity (S/m)	2.25×10^{-3}	4.63×10^{-2}	4.13×10^{-1}	5.46×10^{-1}

of a reduced signal-to-noise ratio (SNR).

To further verify the analytical results, the same Tx design and Rx coil are modelled in the ANSYS EM suite 20.2 as demonstrated in Fig. 5.37(a). A current excitation is employed at the port to excite the coils, and an air region is created around the design, as shown in Fig. 5.37(a). An appropriate meshing is selected for both the coils and the surrounding region to enhance result accuracy. Furthermore, a magnetostatic solver is employed to analyze the design. The simulated design is later imported in ANSYS Simplorer as depicted in Fig. 5.37(b) to perform circuit simulation. Each Tx and Rx coil is paired with a series-connected capacitor to achieve coil resonance at the operational frequency. Additionally, excitation is governed by source amplitudes and relay states. The voltage samples for all seven switching instants (ST$-$1 to ST$-$2), as mentioned in Table 5.10, are collected and later utilized to predict the position and orientation for the same test positions. The presence of human tissue between the proposed Tx and Rx coil

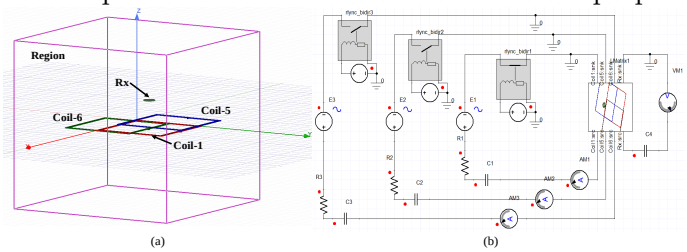

Figure 5.37: Simulated model designed in ANSYS EM suite 20.2.

is also analyzed to inspect the impact of the human body on localization performance. For this purpose, various human tissues present in the human body are inserted between the Tx and Rx coil, as illustrated in Fig. 5.38, and the corresponding tissue properties are listed in Table 5.12 [107]. The response at the Rx coil is then examined both with and without the presence of human tissues, and it remains consistent. This indicates that the performance of the proposed localization scheme remains unaffected by the presence of the human body.

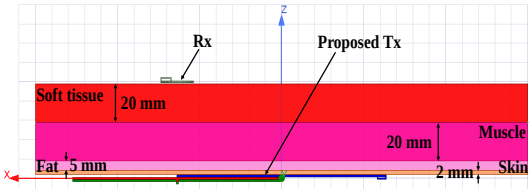

Figure 5.38: Simulated model of Tx and Rx coils with human tissue.

The simulated errors for the tested positions and orientations are plotted in conjunction with the analytically obtained errors in Figure 5.36 to compare the results and demonstrate that both the simulation and analytical results are in good agreement. For a deeper examination of the potential risks to the human body, A simulation is conducted by

positioning the same Tx behind a human body phantom within ANSYS HFSS, as illustrated in Fig. 5.39, indicating that the maximum specific absorption rate (SAR) value experienced by the back part of the human body does not surpass 0.004W/kg and remain within the safety guidelines set by ICNIRP [108].

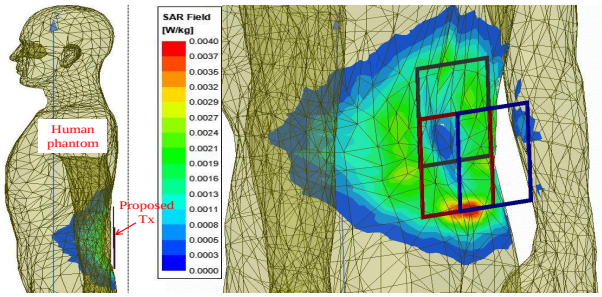

Figure 5.39: Assessment of electromagnetic absorption within the human body.

Moreover, an average position and orientation error ($\hat{E}_d$ and $\hat{E}_a$), defined as the mean value of E_d and E_a, shown in Figure 5.36, along with the standard deviations (σ_d and σ_a) is evaluated as a performance metric and listed in Table 5.13. Here, the calculated $\hat{E}_d$ and $\hat{E}_a$ are 1.9971 mm and 0.9429° for analytically obtained results, whereas, for the simulated results, the same is defined as 1.8271 mm and 0.8805°, respectively. The

Table 5.13: Calculated $\hat{E}_d$ and $\hat{E}_a$ for analytical and simulation case

	$\hat{E}_d$ (mm)	σ_d (mm)	$\hat{E}_a$ (deg)	σ_a (deg)
Analysis	1.9971	1.4408	0.9429	0.7870
Simulation	1.8271	1.4751	0.8805	0.9376

results show good corroboration between the analytical and simulated results. To further compare the performance of the proposed Tx over the design presented in Section 5.2.3, the same noise level $N_0 = -80$ dB is considered in the analysis. The analytically calculated $\hat{E}_d$ and $\hat{E}_a$ for the proposed design are 1.22 mm and 0.87°, whereas the same parameters listed by the literature design are 1.22 mm and 1.18°, respectively. Therefore, the percentage improvement in the average position and orientation errors are 3.63% and 26.25%, respectively. Moreover, the localization success rate is also evaluated as a figure of merit by randomly placing the Rx coil to 324 arbitrarily positions. Here, out of 324 samples, the design presented in Section 5.2.3 converges for 188 positions, whereas the proposed design converges to 322 positions. Thus, the percentage improvement in the success rate defined as a ratio of converge samples to the total samples is 71.29%. This proves that the proposed Tx outperforms the previously designed Tx for the same noise level because of highly distributed H-field components throughout the Rx region. Further verification of the proposed Tx with the experimental setup is presented in the subsequent section.

5.3.3 Experimental Validation and Result Discussion

Fabricated prototype and experimental setup

Initially, the dominant coil group of the first quadrant (Coil−1, Coil−5, and Coil−6) is engraved on a cardboard sheet, whereas, for measuring the voltage samples at the Rx end, a

low-cost PCB technology is adopted for fabricating the Rx coil. The fabricated prototypes of the proposed Tx and Rx are shown in Figure 5.40. Here, a high-frequency Litz wire

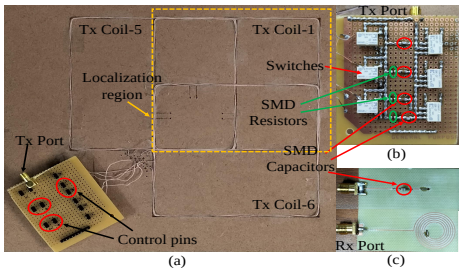

Figure 5.40: (a) Fabricated Tx (b) Switching circuitry (c) Rx coil.

containing 47 strands is utilized to realize the proposed Tx, as depicted in Figure 5.40(a). For exciting the fabricated coils using a single sinusoidal excitation and acquiring voltage samples for various switching instants as presented in Table 5.10, a switching circuitry containing six DPDT switches (G6K-2F) is employed as shown in Figure 5.40(b). The Rx coil is realized using a PCB prototyping machine available in the laboratory, and the fabricated design is presented in Figure 5.40(c). Here, the dimensions of the fabricated Tx and Rx coils are same, as discussed in Section 5.3.1. The measured unloaded impedance of the Tx coil combinations, when coils are excited sequentially for various switching instants as given in Table 5.10, along with a Rx coil, are tabulated in Table 5.14. Here, Table 5.14

Table 5.14: Measured impedance and corresponding resonating capacitance.

Switching states	Z (Ω)	C_{reso} (pF)
ST−1	(79.64 + j1464.42)	16.03
ST−2	(79.82 + j1464.53)	16.03
ST−3	(79.76 + j1464.35)	16.03
ST−4	(35.70 + j796.32)	29.48
ST−5	(35.64 + j796.55)	29.47
ST−6	(35.55 + j548.69)	42.78
ST−7	(19.59 + j500.02)	46.94
Rx	(1.86 + j33.27)	705.57

signifies that for switching states ST−1, ST−2, and ST−3, the measured impedances are nearly equal. Therefore, a single tuning capacitor (C^1_{reso}) is sufficient to resonate these coils at the working frequency of 6.78 MHz. Similarly, the measured impedance corresponding to switching states ST−4 and ST−5 are identical, thus requiring one tuning capacitor C^2_{reso}. In contrast, switching states ST−6 demands an additional C^3_{reso} because of the changing mutual coupling between Coil−5 and Coil−6. Similarly, ST−7 requires a single C^4_{reso} to resonate the coils combinations at the working frequency. The calculated value of C_{reso} corresponding to various switching instants of the proposed Tx along with Rx coil are listed in Table 5.14 and inserted in series with the switching circuitry as shown in Figure 5.40(b). Moreover, additional SMD resistors ($R^1_s - R^1_s$) are inserted within the switching circuitry to limit the current circulating through the coil combination (ST−4 - ST−7) within the ICINRP limit. The experimental setup employed to verify the real-time localization performance of the realized Tx is presented in Figure 5.41. For this purpose, a human phantom is employed and positioned on the proposed Tx pad. Here, a DC power supply (HMP2030) in conjunction with a high-frequency inverter (EPC9507) is utilized to excite the proposed Tx at the working frequency of 6.78 MHz. An Arduino UNO microcontroller is adapted to trigger a particular switching sequence of the Tx coil

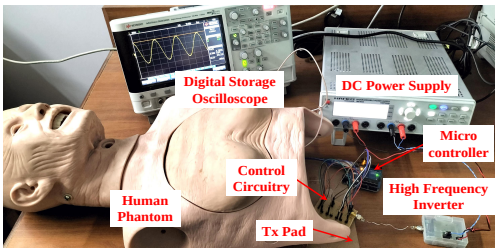

Figure 5.41: Experimental setup for localization performance measurement.

combination. Whereas, for collecting the voltage samples from the Rx coil, a Keysight Digital Storage Oscilloscope (DSOX2022A) is employed.

Experimental results

Firstly, the voltage samples in the Rx plane above 50 mm from the proposed Tx are measured to verify the claim of robust non-uniform H-field distribution obtained from the proposed Tx. For this, the Rx is moved manually by 10 mm steps to scan the entire Rx plane for all seven switching states mentioned in Table 5.10 and presented in Figure 5.42. Here, Figure 5.42(a) and Figure 5.42(b) demonstrate the normalized analytical voltage

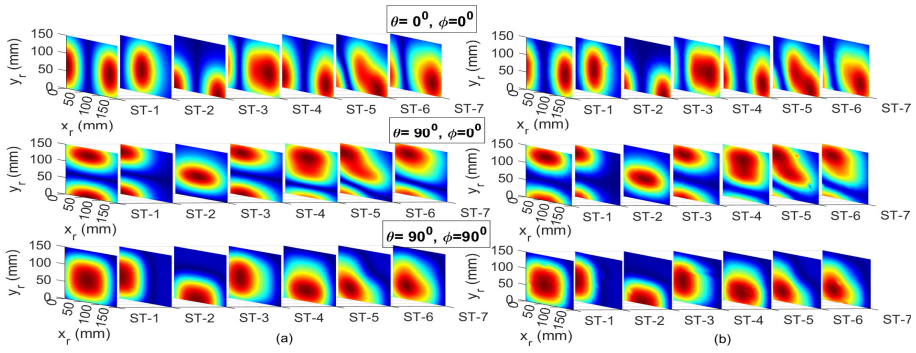

Figure 5.42: Normalized voltage distribution for various Rx orientations (a) analytical, (b) measured.

and measured voltage variation, respectively, when Rx is placed in three orthogonal orientations, i.e. $(\theta_r = 0^0, \phi_r = 0^0)$, $(\theta_r = 90^0, \phi_r = 0^0)$, and $(\theta_r = 90^0, \phi_r = 90^0)$. To examine the degree of similarity between these results, the standard deviation between the normalized analytical and measured voltage is calculated and given as 0.045, 0.056, and 0.061, respectively, in the three orthogonal orientations. This signifies that the measured results are well corroborated with analytical results. However, some deviations in the results are due to fabrication and measurement errors. To further demonstrate the localization precision of the proposed Tx, the position and orientation measurement is performed by tracing the Rx coil along a specified path and presented in Figure 5.43. Here, Figure 5.43(a) and (b) show the discrepancy obtained between the actual position values (x_r and y_r) and the predicted position values (x_r' and y_r') when Rx is oriented in different orientations. Similarly, the disparity achieved in the actual orientations values (θ and ϕ) and predicted orientations values (θ' and ϕ'), when Rx is located at $h = 50$ mm and placed randomly to different testing positions are demonstrated in Figure 5.43(c) and Figure 5.43(d), respectively. At the same time, the measured localization errors E_d and

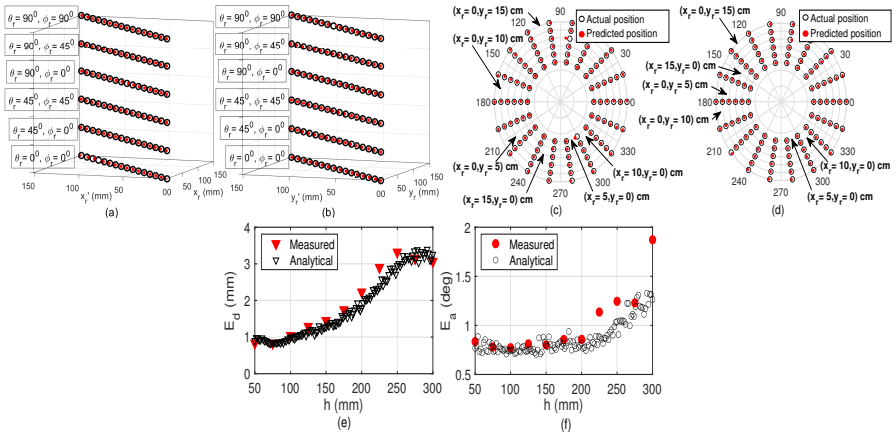

Figure 5.43: Measured localization performance with (a) position (x_r), (b) position (y_r), (c) orientation (θ_r), (d) orientation (ϕ_r), (e) position error (E_d), (f) orientation error (E_a).

E_a for these random testing positions are plotted in Figure 5.43(e) and Figure 5.43(f), respectively. The results signify that the measured results agree well with the analytical results. Moreover, the measured average position and orientation errors for the testing positions and orientations are 1.9863 mm and 1.0178° respectively. Thus, the acceptable tolerance to localize the Rx accurately is defined as $0 \leq x_r, y_r \leq 150$ mm, $50 \leq z_r \leq 275$ mm, $0 \leq \theta_r \leq 180°$, and $0 \leq \phi_r \leq 360°$. Beyond this range, a large deviation between analytical and measured results or the presence of outliers will be observed because of reduced SNR. This proves the usefulness of the proposed Tx structure, designed using planar technology, and its potential to localize the position and orientation of a planar Rx coil. Moreover, exploiting a highly non-uniform H-field distribution for the proposed Tx improves localization accuracy.

5.4 Summary

This chapter presents an optimized multi-coil array transceiver antenna system based on combined 2−coil and 3−coil MRC to localize the position of a human hand. For optimizing the proposed antenna system, a hybrid approach is adopted and demonstrated in Design−3A. The Tx coil array is optimized to generate a non-uniform H-field distribution to enhance the sensitivity of the localization system and obtain equal voltage gain from the Rx coils sensor array in the absence of a resonator coil. Whereas, the resonator and the Rx coil sensor array are optimized such that voltage gain obtained is below the set threshold for various alignments of the resonator coil. The optimized transceiver antenna is analyzed for various movements (horizontal, vertical, and diagonal movements) of the resonator coil in the vicinity of the transceiver antenna and the results show that the response obtained from Rx coil sensor arrays is below the set threshold limit and well enough to decide the position of the resonator coil. To verify the claim a prototype of transceiver antenna along with the resonator coil is fabricated. The experimental results obtained show good agreement with the simulation results. The proposed transceiver antenna platform finds its potential use in various touchless applications like keypad for ATMs, human intelligence-based computer mouse and tracking pads, gaming remotes,

etc, providing a hygienic interface for machine interaction. However, for powering up the implanted devices both the position and orientation need to be determined.

Targeting this, a novel approach is proposed and investigated for magnetic localization of the objects embedded with planar receivers and presented in Design−3B. To monitor both the position and orientation of a small Rx sensor coil, a planar multi-coil Tx antenna was previously presented in literature based on frequency-divisional tracking method implying the use of several frequency signals. The design suffered from a high complexity at the Tx and Rx and challenges of demodulation of multiple frequency signals. To address the drawbacks, a novel switched planar multi-coil Tx antenna is proposed based on time-divisional tracking method that uses only one frequency signal. The coils are optimally grouped using three switches and excited using only three input ports wisely in seven time-slots producing seven distinct H-field distributions. The design exploits non-uniform H-field forming to maximize the localization accuracy. The analytical and simulation study of tracking a Rx placed at several test positions and orientations revealed that the proposed design has better localization accuracy as compared to the previous design. The proposed switched planar multi-coil Tx antenna is fabricated to validate the claims and the experimental results are well corroborated with the analysis. Hence, the investigation demonstrates advantages of the proposed design over the previous multi-frequency design in terms of accuracy and complexity and suitability for localization of small objects with planar Rxs. Nevertheless, the presented design is not optimized to generate highly non-uniform H-field distribution.

For this purpose, a switching integrated overlapping coil Tx is proposed in Design−3C. To effectively localize the position and orientation of a small Rx, the proposed Tx is designed to generate highly non-uniform H-field components and distribute them throughout the receiver region. The design parameters of the proposed Tx are optimized to enhance the non-uniformity present in the H-field distribution. This results in a miniaturized Tx size (255×255 mm^2) compared to the literature design (300×300 mm^2) and reduces the overall Tx size by 27.75% for the same localization region as presented in Design−3C. A switching circuitry is implemented to excite various coils present in the proposed Tx to realize a particular switching instant. The voltage samples collected from Rx are later utilized to localize the random test positions and orientations. The result shows an improved average position and orientation errors of 3.63% and 26.25%, respectively, compared to the literature design. Moreover, the localization success rate for the same literary work is enhanced by 71.29%. This reveals that the localization performance of Design−3C outperforms the Design−3B and other state-of-the-art designs. A prototype of the proposed Tx is realized to determine its localization performance experimentally. The measured average position and orientation error are 1.9863 mm and 1.0178°, respectively, for a noise level of −53.98 dB. This demonstrates the potential of the proposed Tx and makes it suitable for localizing the position and orientation of biomedical implant devices. Furthermore, following the completion of Rx localization, a combination of localization

and powering the Rx is provided subsequently.

[0]**CHAPTER OUTCOMES:**

[1]. **V. K. Srivastava**, A. Bharadwaj and A. Sharma, "A Multicoil Array Transceiver Antenna Design for Touchless Hygienic Artificial Human Interfacing," in *IEEE Transactions on Antennas and Propagation*, vol. 70, no. 10, pp. 8911-8921, Oct. 2022, doi: 10.1109/TAP.2022.3177534.

[2]. A. Sharma and **V. K. Srivastava**, "A Switched Planar Multicoil Transmitter Antenna Designed With Nonuniform H-Field Forming for Small Device Localization," in *IEEE Transactions on Antennas and Propagation*, vol. 70, no. 11, pp. 10261-10269, Nov. 2022, doi: 10.1109/TAP.2022.3195449.

[3]. **V. K. Srivastava** and A. Sharma, "An Optimized Switching Integrated Transmitter Pad for Generating Orthogonal H-Field Components to Localize Implanted Devices," in *IEEE Journal of Electromagnetics, RF and Microwaves in Medicine and Biology*, doi: 10.1109/JERM.2024.3409423.

[4]. **V. K. Srivastava**, A. Sharma and A. Bharadwaj, "A Magnetic Resonance Coupling Based Touchless Pad for Human-Computer Interfacing," 2020 *IEEE 15th International Conference on Industrial and Information Systems (ICIIS)*, 2020, pp. 601-605.

Chapter 6

Magnetic Beam Forming Transmitter Antenna

SO−4: *Explore a planar Tx that simultaneously localizes and constructs a magnetic beam toward a Rx.*

This chapter presents the integration of existing localization techniques with wireless power transfer to address various misalignments and challenges encountered in existing literature. A machine-learning model is employed for localizing the Rx, whereas a particle swarm optimization is adopted to determine optimal excitations for effectively shaping the desired magnetic beam. Here, a single Tx antenna is exploited to accomplish the mentioned objectives. Thus, this chapter explores the design and development of distinct Tx coil designs, denoted as Design−4A, which meet the objectives outlined in SO−4 as given in Section 1.7 and represent the best possible solution over the existing state-of-the-art designs for efficiently charging implanted biomedical devices.

6.1 System description of proposed transmitter (Design−4A)

To examine the magnetic beam forming proficiency of the proposed Tx, the employed WPT system contains two magnetically coupled coils designated as Tx and Rx as depicted in Figure 6.1. The design parameters of the Rx coils are defined as r_r and N_r, representing

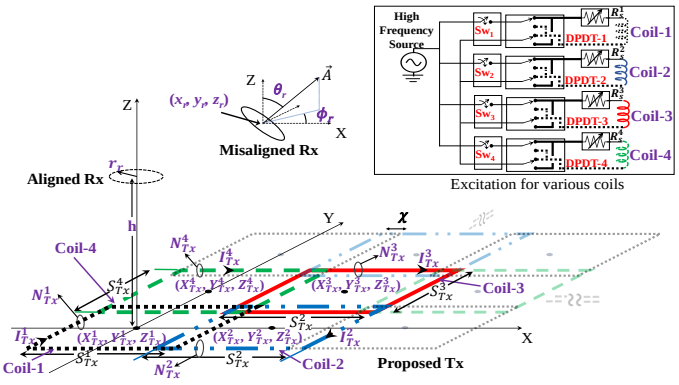

Figure 6.1: System description of the proposed WPT system.

the radius and number of turns present in the Rx coil and positioned at ($x_r = 0$ mm, $y_r = 0$ mm, $z_r = h$ mm, $\theta_r = 0°$, $\phi_r = 0°$) away from the Tx, under the perfectly aligned case. Under the presence of misalignment, the position and orientation of Rx coils are

changed to (x_r, y_r, z_r) and (θ_r, ϕ_r), respectively, which leads to altering the coupling between the Tx and Rx coil. To address the misalignment problem, a multi-coil Tx is employed that contains four spatially distributed overlapped square coils designated as Coil$-i$, where $i \in [1, 4]$ as demonstrated in Figure 6.1. However, based on the demand of the application, the number of Tx coils can be extended by inserting more coils within the Tx pad, as exhibited by transparent coils shown in Figure 6.1. Here, the individual coils present in the Tx are positioned at (x^i_{Tx}, y^i_{Tx}, z^i_{Tx}), where $z^i_{Tx} = 0$ mm and having a side length of S^i_{Tx}. The turns present in the individual coils and the current circulating through these coils are symbolized as N^i_{Tx} and $I^i_{Tx}e^{j\phi}$, respectively. A single excitation source is employed to excite the various coils present in the proposed Tx, resulting in a cost-effective solution for powering the proposed WPT system. To control the states of individual coils, four single pole single throw switches (Sw_1 to Sw_4) are employed and inserted in series with each coil to switch ON and OFF a particular coil. This enables the collection of required voltage samples at different time slots for localizing the Rx coils. Once the Rx is localized, a magnetic beam is constructed toward the localized Rx using current amplitude control. For this purpose, four variable resistors (R^1_s to R^4_s) are inserted along with the individual coil, as presented in Figure 6.1. Moreover, four double pole double throw (DPDT-1 to DPDT-4) switches are employed to control the current circulation within the coils, providing more liberty to form the magnetic beam in the desired direction.

To analytically analyze the localization and magnetic field formation potential of the proposed Tx, the H-field generated from the various Tx coils needs to be evaluated. This objective can be attained by adopting the analytical formulation of the H-field generated from a single-turn square coil as presented in (2.5). Thus, the three orthogonal H-field components produce by simultaneously exciting N^i_{Tx} turns present in the Coil$-i$ are determined using (2.6). Moreover, the RMS voltage at the Rx coil is thus evaluated using (2.10). Later on, this V_r sample is utilized to determine the localization and magnetic beam-forming capability of the Rx coil. Further optimization of the coil design parameters and its positioning in the proposed Tx antenna is discussed in Chapter 6.1.1.

6.1.1 Optimization of Proposed Antenna Structure

The optimization of the proposed Tx is required to simultaneously increase the localization sensitivity and acquire a sharp magnetic beam toward the intended Rx.

Optimizing coil design parameter of the proposed Tx

For magnetic-based localization, the accuracy primarily depends on the non-uniformity in the H-field produced by the Tx coil. This demands an optimization of individual coils present in the proposed Tx. For this purpose, highly non-uniform H-field components are targeted from the coil elements and achieved by properly selecting the design parameters. The standard deviation (σ) is adopted as a figure of merit to measure the non-uniformity present in the H-field components, and a parametric study on coil design parameters is

performed. The σ variation present in the distribution of H-field components (H_x and H_z) versus varying S^i_{Tx} is plotted in Figure 6.2(a). The reason behind considering only

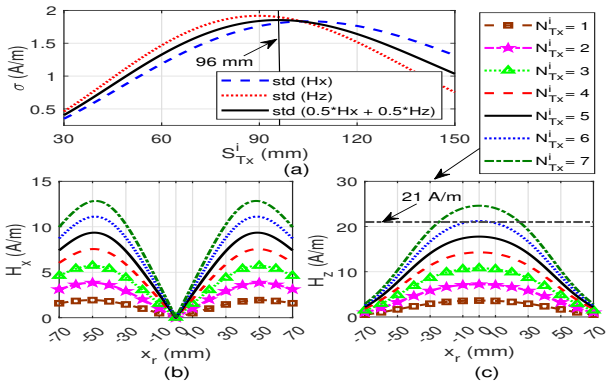

Figure 6.2: Optimization of coil design parameters (a) Non-uniformity present in the field components, (b) H_x versus N^i_{Tx}, (c) H_z versus N^i_{Tx}.

the H_x field component and ignoring the H_y component is because the distribution of both H_x and H_y components are identical. Thus, only the plot of H_x and H_z components are shown. From Figure 6.2(a), it infers that the maximum deviation for H_x and H_z are obtained corresponding to two distinct side lengths. Therefore, an average value is considered an optimal side length value and is found as 96 mm. Once the side length is optimized, further optimization of the number of turns follows ICNIRP guidelines. According to ICNIRP guidelines, the maximum value of H-field components should not exceed 21 A/m. The plot of H_x and H_z versus various N^i_{Tx} for the optimized value of S^i_{Tx} is plotted in Figure 6.2(b) and Figure 6.2(c), respectively. The graph indicates that as the value of N^i_{Tx} increases, both H_x and H_z increase at the coil's edges and center, respectively. Moreover, the maximum value of H_z exceeds the acceptable field limit for $N^i_{Tx} = 5$ considering $I^i_{Tx} = 1$ Amp, whereas the H_x value will remain in the targeted field range. This provides the optimized turn present in the individual coil should be five. Once the coil design parameters are optimized, further optimization of coil positioning is performed to minimize the cross-coupling between the coil array.

6.1.2 Coil position optimization to minimize the coupling between the adjacent coils

To determine the optimal positions of various coils present in the proposed Tx, the coupling (k) between the coils is estimated. For this purpose, the position of one coil is varied relative to the other coil, and the value of k is evaluated analytically. Here, the position of Coil-2 and Coil-3 is made to vary with reference to Coil-1, considering Coil-1 is located at the origin as demonstrated in Figure 6.1. In this scenario, the position of Coil-2 is moved horizontally along $X-$axis ($y^2_{Tx} = 0$), in contrast, the location of Coil-3 is shifted diagonally ($x^3_{Tx} = y^3_{Tx}$). The correspondingly evaluated coupling between the Coil-1 and Coil-2, and Coil-1 and Coil-3 are defined as k_{12} and k_{13}, respectively, and plotted in Figure 6.3. As the positioning of Coil-2 and Coil-3 is symmetric relative to Coil-1 within

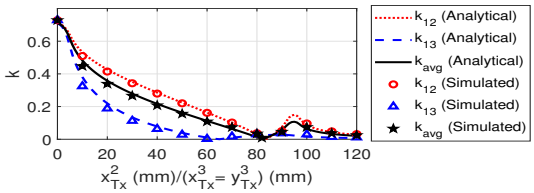

Figure 6.3: Minimization of cross-coupling between the Tx coils.

the proposed Tx, the coupling variation versus the location of Coil-4 is not presented and remains the same as Coil−2. Further, Figure 6.3 signifies that the minimum value of both k_{12} and k_{13} are obtained at different Rx positions. Therefore, an average value of coupling coefficient (k_{avg}) is determined that is defined as [38]

$$k_{avg} = \frac{2}{3}k_{12} + \frac{1}{3}k_{13}. \tag{6.1}$$

The plot indicates that the k_{avg} is minimized for the Rx position 82 mm. An EM simulator is utilized to further validate the obtained results. For this purpose, the same optimized coil parameters acquired from Figure 6.2 are designed in ANSYS MAXWELL, and the corresponding mutual inductance is plotted in Figure 6.3 for comparison purposes. This plot indicates that the analytical values are well corroborated with simulation results. Therefore, the optimized coil positions of Coil−1 to Coil−4 present in the proposed Tx are listed in Table 6.1. Once the optimized parameters and positions of the various coils

Table 6.1: Optimal coil positions for various coils present in the proposed Tx.

	Coil−1	Coil−2	Coil−3	Coil−4
x^i_{Tx} (mm)	0	82	82	0
y^i_{Tx} (mm)	0	0	82	82

present in the proposed Tx are known, further distribution of the H-field can be analyzed for different switching intervals.

6.1.3 Magnetic-field distribution from the proposed transmitter for various switching instants

The localization accuracy of a time divisional approach solely depends on the non-uniformity present in the H-field distribution. Considering this, the three orthogonal H-field components generated by the proposed Tx need to be investigated for various switching intervals. The possible coil combinations for the proposed Tx containing four coils are $2^4 - 1$. Therefore, the H-field generated by these $2^4 - 1$ coil combinations needs to be examined individually. The switching states of four single pole single throw switches as depicted in Figure 6.1 for collecting these coil combinations and corresponding switching sequences are presented in Table 6.2. The H-field distribution by exciting the coils in the specified sequence as presented in Table 6.2 at $z_r = 50$ mm is shown in Figure 6.4. The non-uniformity present in the distinct H-field distribution for different switching intervals as shown in Figure 6.4 infers that distinct V_r samples can be acquired at the Rx location, hence improving the localization accuracy to a greater extent. Further

Table 6.2: Switching sequence and corresponding switching states.

Switching states	Sw_1	Sw_2	Sw_3	Sw_4
ST−1	ON	OFF	OFF	OFF
ST−2	OFF	ON	OFF	OFF
ST−3	OFF	OFF	ON	OFF
ST−4	OFF	OFF	OFF	ON
ST−5	ON	ON	OFF	OFF
ST−6	OFF	ON	ON	OFF
ST−7	OFF	OFF	ON	ON
ST−8	ON	OFF	OFF	ON
ST−9	ON	OFF	ON	OFF
ST−10	OFF	ON	OFF	ON
ST−11	ON	ON	ON	OFF
ST−12	OFF	ON	ON	ON
ST−13	ON	OFF	ON	ON
ST−14	ON	ON	OFF	ON
ST−15	ON	ON	ON	ON

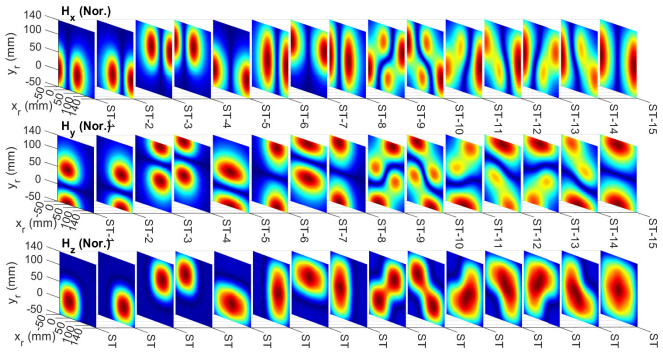

Figure 6.4: Distribution of three orthogonal H-field components from proposed Tx for possible switching instants.

performance evaluation of the proposed Tx for localization and magnetic beam forming is presented in Chapter 6.1.4.

6.1.4 Analytical Performance Evaluation of the Proposed Transmitter

The efficacy of the proposed Tx is evaluated based on its ability to localize and generate a desired magnetic beam. The working procedure of the proposed Tx is illustrated in Fig. 6.5. Initially, to assess the localization performance, the Rx is placed randomly at

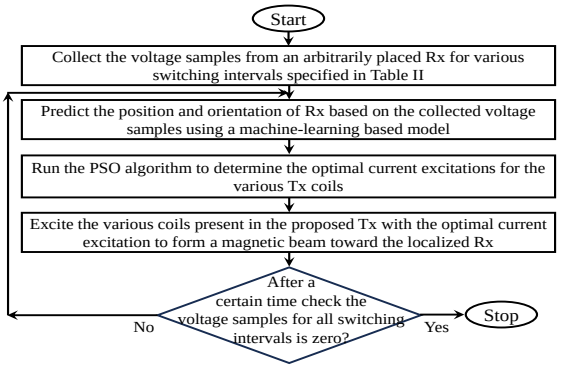

Figure 6.5: Flowchart for working of the proposed Tx mechanism.

several test positions and orientations (x_r, y_r, z_r, θ_r, ϕ_r) within a test volume spanning from $-50 \leq x_r, y_r \leq 140$ mm, $50 \leq z_r \leq 250$ mm, $0 \leq \theta_r \leq 180°$, and $0 \leq \phi_r \leq 360°$ above

the proposed Tx antenna. The V_r samples were gathered from arbitrarily placed Rx units and evaluated using (2.9) for different switching intervals, as detailed in Table 6.2. A Rx coil featuring six turns and a maximum radius of 10 mm accumulates the analytical V_r samples. Additionally, to resemble the realistic scenario, a random white Gaussian noise (N_o) is introduced alongside the gathered V_r samples from various switching instances. Subsequently, the final prediction voltage sample (V^p) is utilized to determine the position and orientation of the Rx coil and given as

$$V^p(x'_r, y'_r, z'_r, \theta'_r, \phi'_r) = V_r(x_r, y_r, z_r, \theta_r, \phi_r) + N_o. \tag{6.2}$$

Here, N_o represents the measured noise voltage at the Rx when the Tx is inactive with a variance in a measured value of 2mV. Subsequently, a machine learning algorithm is utilized to determine the predicted position and orientation $(x'_r, y'_r, z'_r, \theta'_r, \phi'_r)$ corresponding to the voltage sample V^p. After determining the position and orientation of the implanted Rx, the PSO algorithm computes the best excitation amplitudes for the multiple coils within the proposed Tx. Applying these optimized amplitudes to the coils creates a magnetic beam directed toward the predicted position and orientation of the Rx. This localization and magnetic beam-forming cycle repeats at intervals until the Rx moves out of range. Subsequently, a detailed explanation of both the machine learning-based and PSO algorithms is provided.

6.1.5 Proposed ML-based Algorithm for localization

A convolutional neural network (CNN) is employed for localizing the Rx, featuring the input, CNN model, loss function, optimization algorithm, and dataset. The architecture of the proposed CNN model is depicted in Fig. 6.6. The CNN input considers 5×3 array

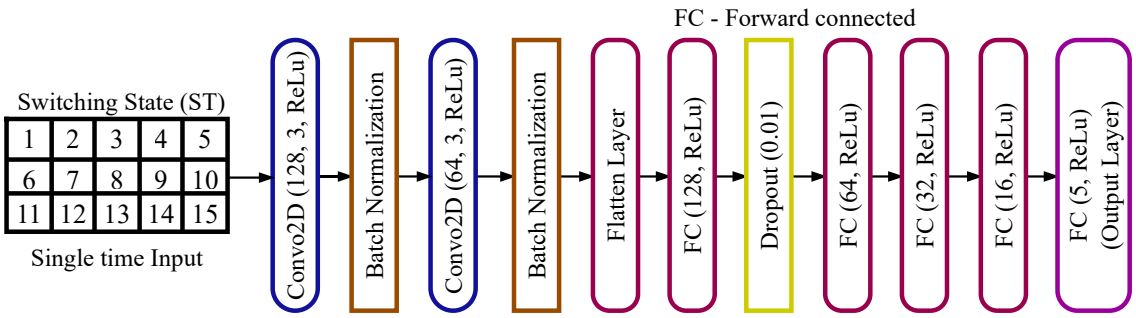

Figure 6.6: Architecture of proposed CNN model.

of switching state voltages as shown in Table 6.2. The CNN model consists of seven layers: the first two layers are 2−D CNN layers with batch normalization (with 128 and 64 kernel), and the rest four are fully connected hidden layers (with 128, 64, 32, and 16 neurons) and one output layer with five neurons. All hidden layers use the $ReLU$ activation function. The output layer utilizes the *linear* activation function. This architecture is tailored as a regression model where the response of each neuron of the output layer is for $x'_r, y'_r, z'_r, \theta'_r, \phi'_r$ respectively. The CNN model minimizes the *mean squared error* (MSE) loss during training, employing the adaptive moment estimation (ADAM) optimization algorithm. The model's accuracy and MSE while training the data are demonstrated in

Fig. 6.7, indicating that the model accuracy reaches up to 84.68, with the MSE reduced to 0.005 respectively for 5000 epoch. Finally, training on a workstation equipped with a 3.6 GHz Intel Xeon processor and 64 GB RAM, the total training time is 18504.01184 sec. This indicates the necessity for the machine learning model to predict the desired

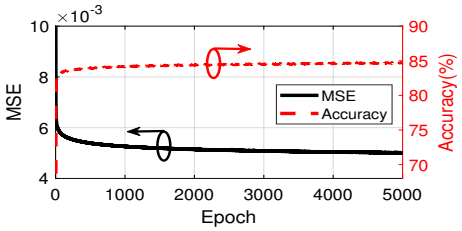

Figure 6.7: Machine learning-based CNN model accuracy and MSE.

value accurately. Furthermore, an error is calculated between the actual and predicted positions and orientations determined by the trained model to assess localization accuracy and defined in terms of position and orientation errors (E_d and E_a) given as

$$\begin{aligned} E_d &= \sqrt{(x_r - x_r')^2 + (y_r - y_r')^2 + (z_r - z_r')^2}, \\ E_a &= |\theta_r - \theta_r'| + |\phi_r - \phi_r'|. \end{aligned} \tag{6.3}$$

Results of Proposed ML-based Algorithm

For a comprehensive analytical evaluation of localization accuracy, the actual and predicted positions and orientations for different Rx configurations are examined and depicted in Figure 6.8. Here, the ML takes 731.86 μsec during the testing procedure. The plots demonstrate that the model accurately predicts both the position and

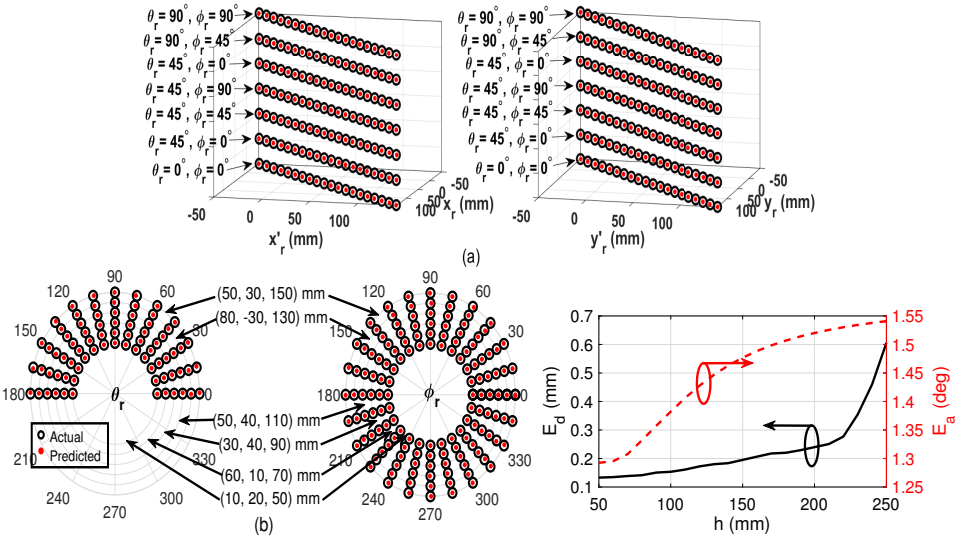

Figure 6.8: Estimated localization performance versus varying (a) positions (x_r and y_r), (b) orientations (θ_r and ϕ_r), (c) transfer distance h.

orientation values for a randomly positioned Rx, as shown in Fig.6.8(a) and Fig.6.8(b), respectively. Additionally, in Fig. 6.8(c), localization errors are plotted against h to ascertain localization accuracy across various transfer distances. It is observed that as h increases, there is a corresponding increase in E_d and E_a, attributed to a decrease in the signal-to-noise ratio (SNR), defined as the ratio of the square of V^p to N_o [106].

Consequently, the average position and orientation errors ($\bar{E}_d$ and $\bar{E}_a$) for the predicted model are calculated as 0.22 mm and 1.44°, respectively.

6.1.6 Optimal excitation evaluation for magnetic beam shaping

Once the position and orientation of an arbitrarily placed Rx are known, further magnetic beam-forming towards the localized Rx is demanded. To achieve this objective, careful control over the current amplitudes and their circulation in the individual coils (Coil$-i$, where $i \in [1, 4]$ as demonstrated in Fig. 6.1) is essential. Employing particle swarm optimization (PSO), as detailed in [109], within a MATLAB environment facilitates the determination of the optimal current distribution within the coils. PSO is chosen for beam shaping due to its high precision and the fact that it does not necessitate a precise initial guess to ensure convergence [80]. In this process, a reference voltage matrix is utilized, wherein peaks are aligned according to the predetermined position, and orientation serves as input for the PSO algorithm. The algorithm iterates and adjusts the current amplitudes and circulation of all four coils to minimize the deviation between the actual and reference voltage matrices. To demonstrate this, the algorithm is executed for randomly placed Rx units, showcasing the corresponding evaluated current amplitudes and circulation necessary to generate the desired magnetic beam at various test positions, as depicted in Fig. 6.9. This illustrates the capability of the designed algorithm to forecast the optimal

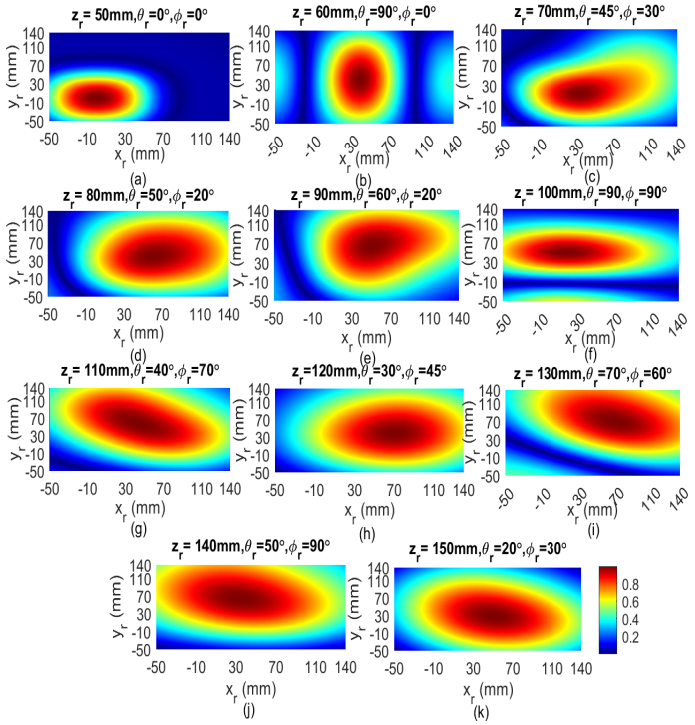

Figure 6.9: Analytically obtained V_r distribution at arbitrarily positioned Rx for Tx current vectors [I^1_{Tx}, I^2_{Tx}, I^3_{Tx}, I^4_{Tx}] (a) [0.789, 0, 0, 0], (b) [0.745, −0.806, −0.755, 0.802], (c) [1.779, 0.648, 0.632, 0], (d) [1.780, 0.937, 0.937, 1.049], (e) [2.325, 0, 1.206, 2.119], (f) [4.374, 1.988, −1.148, −1.421], (g) [1.361, 2.999, 0, 2.656], (h) [2.312, 2.759, 1.737, 0.900], (i) [3.708, 5.491, 0, 3.565], (j) [3.573, 5.291, 0, 3.436], (k) [3.139, 4.785, 0, 3.786].

excitation currents for the different coils within the proposed Tx, ensuring a focused magnetic beam towards the localized Rx regardless of its position and orientation. Here,

the designed PSO algorithm takes $10 - 15$ seconds to iterate and predict the location of the Rx. Consequently, the discussion above asserts that the proposed Tx can effectively localize and concurrently establish a magnetic beam in the desired direction. Additionally, the magnetic flux captured by the Rx serves as a figure of merit and is compared with other field-forming techniques, such as the widespread switched polarized H-field method presented previously in Design$-2B$, and shown in Figure 4.19. This comparison is facilitated because both designs consider the same Rx size. The corresponding currents in both designs are controlled by setting the input power of both Tx to 5 W. Consequently, the magnetic flux captured, i.e., the voltage received in the Rx coil, is calculated by placing the Rx at the center in both cases. Thus, the voltage obtained for widespread distribution of H-field is 0.22 V, whereas, for the proposed Design$-4A$, it is 1.13 V. This results in an increased received voltage of 413.64% and demonstrates the capability of the proposed Tx to shape the magnetic beam. Subsequent validation of the analytically obtained results is provided thereafter.

6.1.7 Results Validation

The performance of the proposed Tx is further verified using a commercially available electromagnetic simulation tool, ANSYS EM Suite 20.2, alongside an experimental setup.

Simulation Verification

To guarantee the precision of the H-field distribution acquired from the optimized Tx design, the identical Tx configuration is designed in ANSYS Maxwell as shown in Figure 6.10. To achieve this objective, a single-turn coil is modelled as an individual

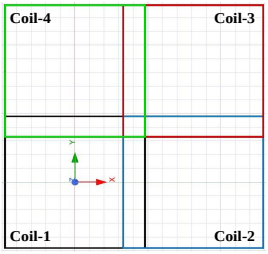

Figure 6.10: Simulated model designed in ANSYS EM suite 20.2.

Tx coil (Coil-1 to Coil-4) as provided in Chapter 6.1.1. A current excitation is employed to feed each coil with 5 Amp current to resemble individual coils with five turns. Suitable meshing is applied to both the coil conductors and the surrounding region of the Tx. The fields produced by the coils are subsequently examined at different switching intervals, as outlined in Table 6.2 and depicted in Figure 6.11. The field distributions presented in Figure 6.4 and Figure 6.11 signify that the simulated results well matched with the analytically derived field distributions. Further verification of the localization performance is carried out subsequently using an experimental setup.

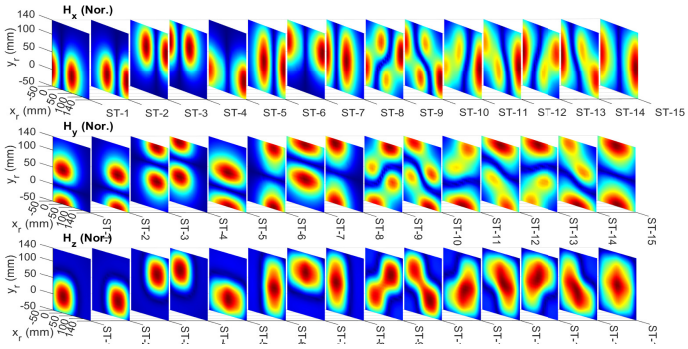

Figure 6.11: Simulated H-field components variation for various switching instants.

Experimental verification

The proposed Tx is constructed on a cardboard sheet to experimentally validate the results, with all four coils (Coil−1 to Coil−4) engraved onto it. A high-frequency Litz wire containing 47 strands is employed to realize the proposed Tx. In contrast, a low-cost PCB technology is utilized to fabricate the Rx coil, which collects the voltage samples from the Rx. The fabricated prototypes of the proposed Tx and Rx are depicted in the inset of Figure 6.12(a). A switching circuitry is employed to excite the fabricated coil with a single

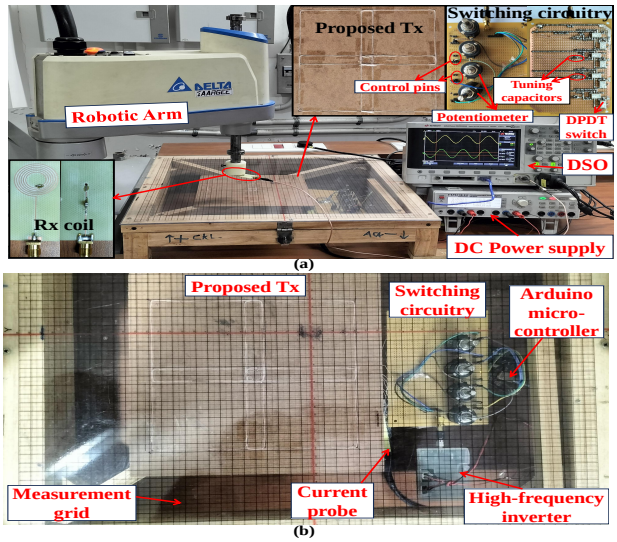

Figure 6.12: Measurement setup (a) Front view, (b) Top view.

sinusoidal excitation for various switching instants, as presented in Table 6.2. The top and bottom view of the switching circuitry is provided in the inset of Figure 6.12(a). Here, four DPDT switches (G6K-2F) control the switching states of four coils and are represented as Sw−1 to Sw−4 in Figure 6.1. Whereas the remaining four DPDT switches are engaged to control the current circulation within the coils. Moreover, four potentiometers are employed to control the amount of current flowing in the individual coils. To measure the unloaded impedance of Tx coil combinations, Agilent VNA (PNA-L N5230C) is utilized. The measured unloaded impedance of four coils by exciting the coils sequentially is listed in Table 6.3. The nearest possible value of SMD capacitors (C_{reso}) is inserted in series with the coils to resonate these coils at the working frequency of 6.78 MHz. The experimental

Table 6.3: Measured impedance and corresponding resonating capacitance.

Switching states	Z (Ω)	C_{reso} (pF)
Coil−1	(6.27 + j826.99)	28.38
Coil−2	(6.43 + j815.95)	28.76
Coil−3	(6.32 + j834.69)	28.12
Coil−4	(6.15 + j827.47)	28.36
Rx	(1.86 + j33.27)	705.57

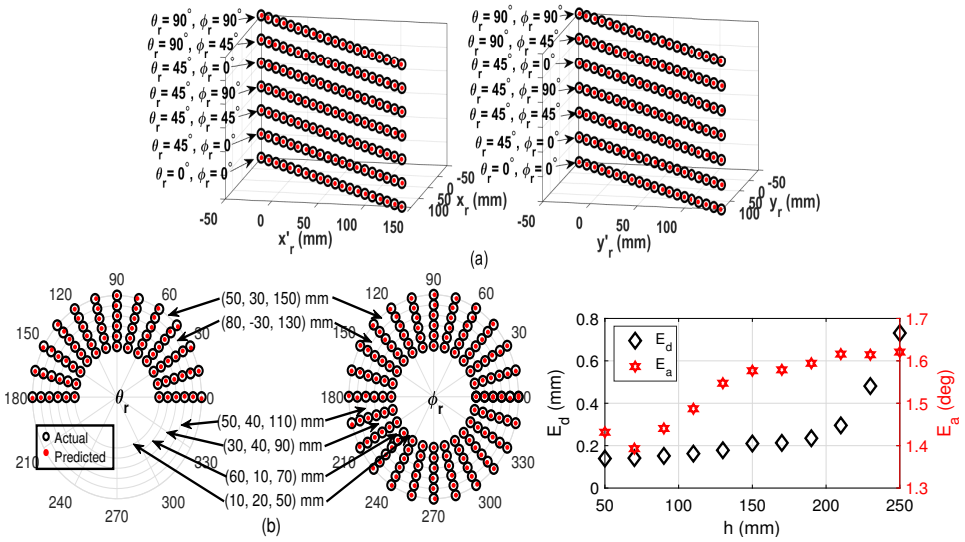

Figure 6.13: Measured localization performance with (a) position (x_r, y_r), (b) orientation (θ_r, ϕ_r), (c) transfer distance h.

setup utilized to validate the real-time performance of the implemented Tx is depicted in Figure 6.12(a) illustrates the front view, while Figure 6.12(b) displays the top view of the experimental arrangement. A high-frequency inverter (EPC9507) is employed to energize the Tx coil assembly and is powered by a DC power supply (HMP2030). An Arduino UNO microcontroller is utilized to activate the electronically controlled switches within the switching circuitry. Conversely, a Keysight Digital Storage Oscilloscope (DSOX2022A) is utilized to gather voltage samples from the Rx coil for localization purposes and later on visualize the magnetic beam shaping proficiency of the proposed Tx.

To assess localization performance, the Rx maintains the same position and orientation used during analytical performance evaluation. The errors E_d and E_a are determined by measuring voltage samples at the Rx and are presented in Figure 6.13(a) illustrates the discrepancy between actual position values (x_r and y_r) and predicted position values (x_r' and y_r') for different Rx orientations. Similarly, Figure 6.13(b) shows the disparity between actual orientation values (θ_r and ϕ_r) and predicted orientation values (θ_r' and ϕ_r'). Additionally, Figure 6.13(c) displays the measured localization errors E_d and E_a across various transfer distances. The results indicate a strong agreement between the measured and analytical results. Furthermore, the measured average position and orientation errors for the testing positions and orientations are 0.31 mm and 1.62°, respectively.

To further verify the beam-shaping proficiency of the proposed antenna, the currents provided to the coils are controlled optimally and the V_r is then collected from the Rx. For instance, the voltage and current waveform collected from DSO are shown in Figure 6.14. Here, Figure 6.14(a) and Figure 6.14(b) show the voltage and current at the Tx terminal,

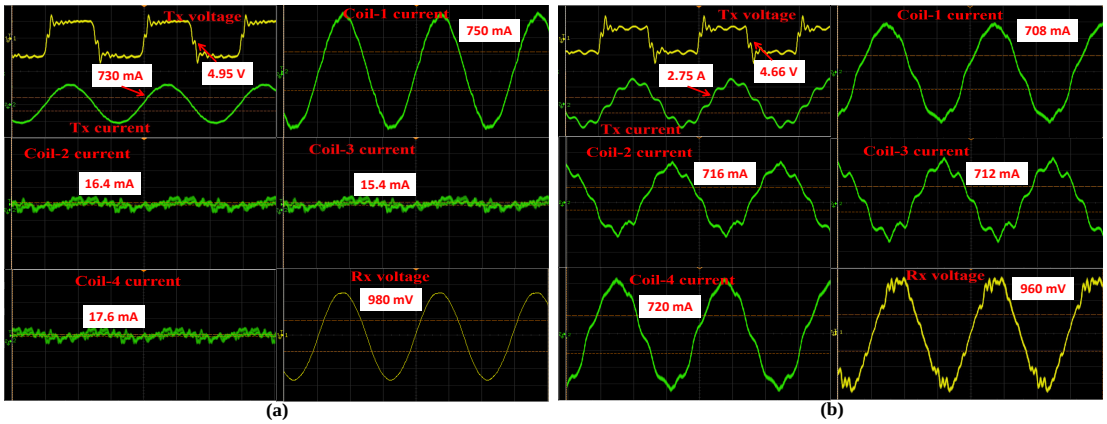

Figure 6.14: Measured current and voltage waveform in real-time beam shaping performance evaluation.

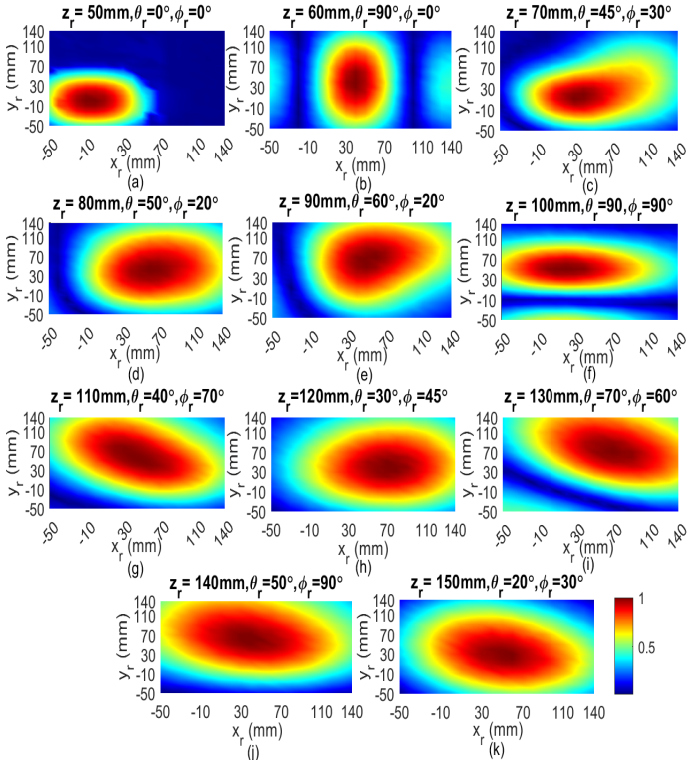

Figure 6.15: Measured normalized V_r at arbitrarily positioned Rx for Tx current vectors $[I^1_{Tx}, I^2_{Tx}, I^3_{Tx}, I^4_{Tx}]$ (a) [0.75, 0, 0, 0], (b) [0.71, −0.72, −0.71, 0.72], (c) [0.95, 0.35, 0.33, 0], (d) [0.95, 0.50, 0.50, 0.56], (e) [0.95, 0, 0.49, 0.86], (f) [0.95, 0.43, −0.25, −0.31], (g) [0.43, 0.95, 0, 0.84], (h) [0.77, 0.95, 0.6, 0.31], (i) [0.64, 0.95, 0, 0.62], (j) [0.64, 0.95, 0, 0.62], (k) [0.62, 0.95, 0, 0.75].

current circulating in individual coils, and V_r value when the Rx is placed at (0 mm, 0 mm, 50 mm, 0°, 0°) and (40 mm, 40 mm, 50 mm, 90°, 0°), respectively. The Tx voltage and current infer that the Tx is working at the unity power factor. Thus by properly controlling the current circulation within the coils a uniform voltage can be obtained at the Rx. Moreover, to make a proper comparison with the analytically obtained results, the normalized voltage distributions are plotted in Figure 6.15 for the same test positions

and orientations as presented in Figure 6.9. The plot shows the measured results are well corroborated with the analytical results. This proves the usefulness of the proposed Tx structure, designed using planar technology, and its potential to localize and construct magnetic beams to overcome the misalignment problems. Moreover, exploiting a highly non-uniform H-field distribution for the proposed Tx improves the localization accuracy and constructs a sharp magnetic beam toward the Rx.

6.2 Summary

This chapter introduces an array of overlapped coil Tx to localize and direct a magnetic beam toward a specific Rx. The Tx design is optimized to achieve a non-uniform distribution of H-field components produced by the spatially distributed coils to achieve precise localization and a sharp magnetic beam. Furthermore, optimal coil placement is determined to mitigate the impact of mutual coupling between adjacent coils. The optimized Tx is then used to assess localization accuracy and the performance of magnetic beam shaping. A time-divisional technique is employed to collect voltage samples from the Rx across various switching combinations of the Tx coils to localize the Rx. Subsequently, a machine-learning algorithm predicts the Rx's position and orientation, yielding average errors of 0.22 mm and 1.44°, respectively. Conversely, to power the localized Rx, a magnetic beam is formed towards it by controlling the current within the spatially distributed coils, determined using particle swarm optimization. Analytical results are validated using commercial EM software and an experimental setup. A prototype of the optimized Tx, along with switching circuitry, is fabricated on a cardboard sheet along with a switching circuitry. Voltage samples collected from the Rx are then utilized to localize random test positions and orientations, resulting in measured average errors of 0.31 mm and 1.62° for position and orientation, respectively. Additionally, a normalized voltage distribution is observed for various Rx positions and orientations to demonstrate the beam-shaping capability of the proposed Tx. These findings highlight the potential of the proposed antenna for efficient charging of bio-medical applications.

[0]**CHAPTER OUTCOMES:**

[1]. **V. K. Srivastava**, A. Ahmad and A. Sharma, "A Machine Learning Assisted Localization and Magnetic Field Forming for Wireless Powering of Biomedical Implant Devices," submitted in *IEEE Transactions/Journals*.

[2]. **V. K. Srivastava**, and A. Sharma, **"TITLE: STEERABLE MAGNETIC BEAM FORMING FOR BIOMEDICAL IMPLANTS."** (Patent filed with Indian patent office on 16/07/2024: Application No. 202411054346)

Chapter 7

Receiver Designs for Misalignment Insensitive WPT

SO−5: *Develop a Rx antenna design to overcome the misalignment issue.*

In the preceding sections of this thesis, we have explored the challenges associated with the design of Tx coil antennas, particularly their complexity and high maintenance costs. These challenges have motivated our investigation into Rx coil antennas. Consequently, this chapter introduces two distinct Rx antenna designs aimed at capturing both the longitudinal (H_z) and lateral (H_x and H_y) magnetic field components, primarily for pacemakers application and later suggest a use case of the H-field harvesting antenna for a wireless drone charging. These designs, referred to as Design−5A and Design−5B, respectively and aligned with the objectives outlined in SO−5 as defined in Section 1.7.

7.1 System Configuration of Rectenna Design for Pacemaker (Design−5A)

The application scenario of the proposed WPT system is illustrated in Fig. 7.1, which depicts the wireless charging of an implanted pacemaker device via the proposed rectenna array. To achieve this, a conventional circular Tx coil is situated outside the human

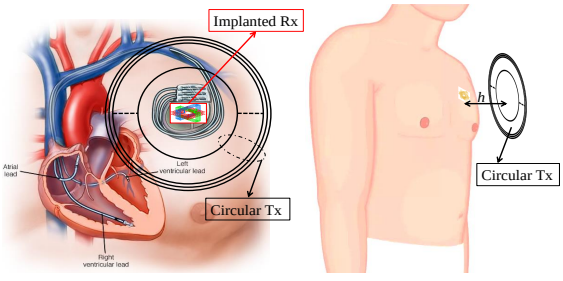

(a) (b)

Figure 7.1: Application scenario of the proposed WPT system (a) front view, (b) isometric view.

body, establishing a magnetic linkage between the Tx and the rectenna array. Here, the Tx and the proposed rectenna array are separated by a distance of h_k, where $k \in [1, n]$ for different Rx planes, and n denotes the n^{th} Rx plane, as shown in Fig. 7.2(a). The Tx is located at (x_{Tx}, y_{Tx}, z_{Tx}) with a maximum radius r_{Tx}, available turns N_{Tx}, track width w_{Tx}, and spacing between the adjacent tracks g_{Tx}. The current circulation through the Tx coil is denoted by $I_{Tx}e^{j\psi}$. The total H-field components generated by the Tx

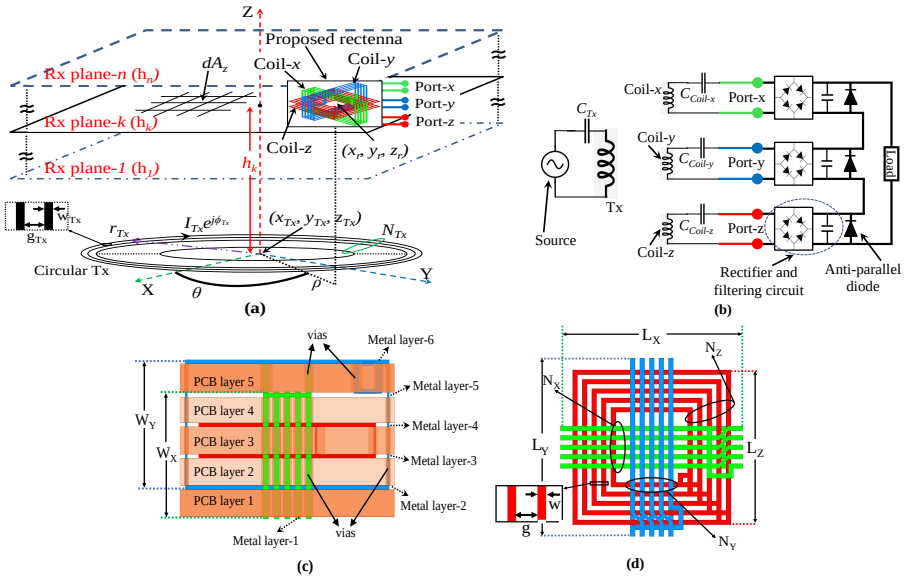

Figure 7.2: The proposed (a) WPT system with rectenna, (b) compensation topology along with smart DC series combining, (c) planar multi-layer PCB realization of the proposed Rx, (d) compact multi-coil Rx antenna.

having coil parameter values set to $r_{Tx} = 70.7$ mm, $N_{Tx} = 5$, $w_{Tx} = g_{Tx} = 0.5$ mm and $I_{Tx} = 1$ A (considering the ICNIRP guidelines, i.e., the maximum field should not exceed 21 A/m at target Rx region $h_k = 50$ mm are evaluated using (2.4) and plotted in Fig. 7.3. The purpose of adopting $r_{Tx} = 70.7$ mm is to maximize the field at the

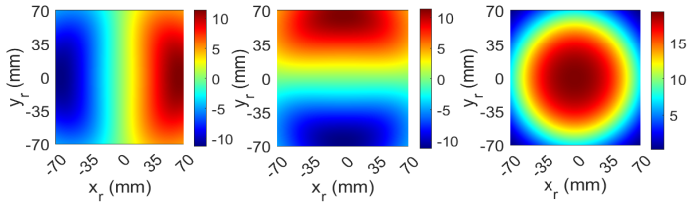

Figure 7.3: Field distribution generated from a conventional Tx antenna at the targeted Rx region ($h_k = 50$ mm) (a) H_x, (b) H_y, (c) H_z.

targeted Rx location, i.e., (0, 0, 50) mm. Similarly, w_{Tx} and g_{Tx} are chosen as 0.5 mm, which is the minimum fabrication limit of the PCB prototyping machine available in the laboratory. Here, Fig. 7.3 illustrates that the analytical distributions of the orthogonal H-field components are unevenly dispersed throughout the Rx area ($h_k = 50$ mm). It should be noted that the maximum value of 11.28 A/m for H_x and H_y components is found near the edges ($x_r = 65$ mm and $y_r = 65$ mm, respectively). In contrast, the peak value of $H_z = 19.22$ A/m occurs at the center ($x_r = y_r = 0$ mm) of the Rx area, where the Rx is accurately aligned. Additionally, the lateral components H_x and H_y are not accessible near the perfectly aligned Rx position ($x_r = y_r = 0$ mm).

To effectively harness these non-uniformly distributed H-field components, particularly by the misaligned Rx antenna, the proposed rectenna contains three orthogonal Rx coils of different dimensions, as shown in Fig. 7.2(a), along with a series-series compensation topology, rectifying and combining circuitry as demonstrated in Fig. 7.2(b). In the Rx system, two series-connected spiral coils with square geometry are utilized to capture the

H_z component of the H-field and are denoted as Coil$-z$. Whereas, to exploit the H_x and H_y components, two compact orthogonal coils designated as Coil$-x$ and Coil$-y$ are employed as shown in Fig. 7.2(a). As the coils are placed orthogonal to each other, the mutual coupling between the coils will not affect the performance of the proposed rectenna array. Moreover, the purpose of adopting a series-series topology over other compensation topologies is because series-series topology is independent of mutual coupling between the Tx and Rx antennas. The realization of the proposed Rx requires a multi-layer PCB technology with five PCB layers and six metallic layers, as depicted in the cross-section view of Fig. 7.2(c). The Coil$-x$ turns are placed at metal layer-1 and layer-5 and connected through inner layer vias. Similarly, the Coil$-y$ is printed on metal layer-2 and metal layer-6. Both the coils are placed on selected layers so that cross-section areas of Coil$-x$ and Coil$-y$ can be maximized. The Coil$z$ encompassing two planar-spiral coils are positioned at metal layer-3 and layer-4 to enhance its effective area. The connections between various layers are realized using vias, as shown in Fig. 7.2(c). The design parameters for optimization of the proposed Rx are defined in Fig. 7.2(d), where the maximum side length of the Coil$-z$ is L_Z with available turns N_r^z. Therefore, the total cross-section area of the Coil$-z$ is given as $A_Z = 2(L_Z \times L_Z)$. The Coil$-x$ contains N_r^x turns with a cross-sectional area $A_X = L_X \times W_X$, where L_X and W_X are the maximum side lengths along with horizontal and vertical directions. Similarly, the Coil$-y$ carries N_r^y turns with a cross-sectional area $A_Y = L_Y \times W_Y$. The track width and spacing between the turns in each coil of the Rx are w_r and g_r, respectively. Moreover, Fig. 7.2(a) exhibits that the Coil$-x$ and $-y$ have a different size than the Coil$-z$ to obtain the Rx profile as low as possible and compatible for biomedical implant applications. The voltage induced in the three orthogonal Rx coils is obtained from Faraday's law of electromagnetic induction. Thus, in a small differential area dA of the j^{th} turn of the Rx Coil$-i$, where $i \in \{x, y, z\}$, the differential induced voltage (dV_{ind}^i) is formulated as

$$dV_{ind}^i = j\omega_c \mu_o H_i(x_r, y_r, z_r) dA_i. \tag{7.1}$$

Here, dA_x, dA_y, and dA_z are the differential area along x, y, and z directions, respectively, for the three orthogonal coils, ω_c is the operating angular frequency in rad/sec, and μ_o is the permeability of the free space. Consequently, the net induced voltages acquired from the individual Rx coil are obtained as

$$\begin{aligned}
V_{ind}^x(x_r, y_r) &= \sum_{j=1}^{N_r^x} dV_{ind}^x = j\omega_o\mu_o \sum_{j=1}^{N_r^x} \left[\iint_{A_x} H_x(x_r, y_r) dA_x \right], \\
V_{ind}^y(x_r, y_r) &= \sum_{j=1}^{N_r^y} dV_{ind}^x = j\omega_o\mu_o \sum_{j=1}^{N_r^y} \left[\iint_{A_y} H_y(x_r, y_r) dA_y \right], \\
V_{ind}^z(x_r, y_r) &= \sum_{j=1}^{N_r^z} dV_{ind}^x = j\omega_o\mu_o \sum_{j=1}^{N_r^z} \left[\iint_{A_z} H_z(x_r, y_r) dA_z \right].
\end{aligned} \tag{7.2}$$

The total average load voltage (V_o) required to feed the charging device is obtained by combining these individual Rx voltages. Here, AC and DC combining are the two possible techniques to combine the voltages from individual Rx. The former method performs rectification followed by directly combining all the Rx coil outputs. Consequently, the V_o

post AC combining is formulated for the Rx misaligned to $(x_r,\ y_r)$ as

$$V_o^{AC}(x_r, y_r) = \frac{2}{\pi} V_{ac}(x_r, y_r) = \frac{2}{\pi}[|V_{ind}^x(x_r, y_r) + V_{ind}^y(x_r, y_r) + V_{ind}^z(x_r, y_r)|]. \tag{7.3}$$

However, the AC combining results in a large variation in the V_o as demonstrated in Fig. 7.4, where the $V_o(x_r, y_r)$ distribution is plotted against the Rx misalignment. For this

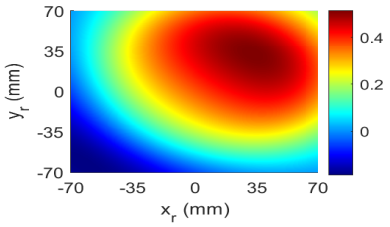

Figure 7.4: The V_o variation for the misaligned Rx by performing AC combining.

reason, the DC combining of the Rx output voltages is adopted in the proposed design as illustrated in Fig. 7.2(b). In the DC combining method, the output of each Rx coil is first rectified using a rectifier and filtering circuit. Later, a series combining of the rectified DC voltages is performed to operate the load. Thus, the V_o for this case is ideally obtained as

$$V_o^{DC}(x_r, y_r) = \frac{2}{\pi} V_{dc}(x_r, y_r) = \frac{2}{\pi}[|V_{ind}^x(x_r, y_r)| + |V_{ind}^y(x_r, y_r)| + |V_{ind}^z(x_r, y_r)|]. \tag{7.4}$$

Additionally, anti-parallel diodes are deployed in the shunt with each rectifying circuit, as depicted in Fig 7.2(b), to bypass the corresponding inactive Rx coil that is not harvesting sufficient power for the load. Because under the absence of anti-parallel diodes, the inactive Rx coil acts as a load with a substantial internal resistance due to the presence of a reverse-biased rectifying diode. Further optimization of the proposed Rx design to obtain a uniform V_o at the Rx region is presented subsequently to mitigate the lateral misalignment problem.

7.1.1 Analytical Optimization of the Proposed Rectenna Array

The enhancement of the degree of movement for a Rx coil under lateral misalignment is achieved by inducing uniform V_o throughout the Rx working region. Therefore, the objective function targets a constant voltage in the Rx region. For this, the effective area $(A_{eff}^i = A_i \times N_i)$ of the Rx coil-i $\forall\ i \in \{x, y, z\}$ needs to be controlled optimally by parametric variation of N_i and A_i of individual Rx coils. Fig. 7.3 demonstrates that the lateral field (H_x and H_y) components have similar field distributions in the Rx region. For this reason, the Rx coils (Coil$-x$ and $-y$) to capture the lateral fields are identical i.e., $A_{eff}^X = A_{eff}^Y$. Therefore, A_{eff}^X and A_{eff}^Z are adopted as optimization parameters whose ratio represents a factor $\alpha = A_{eff}^X / A_{eff}^Z$ that is used while optimization to enhance the misalignment tolerance. The case when $\alpha = 0$ indicates the absence of the vertical Rx coils, and only the conventional coil$-z$ is present at the Rx, whereas $\alpha = 1$ represents identical Rx coils by means of effective total area.

The analytical results of the V_o variations in two different misalignments of the Rx, i.e., $y_r = 0$ and $x_r = y_r$ movements, for various α values are presented in Fig. 7.5. The plots indicate that with an increase in α, a significant overshoot in V_o is observed with Rx misalignment. This is because A_{eff}^L increases with α, and the Rx harnesses more

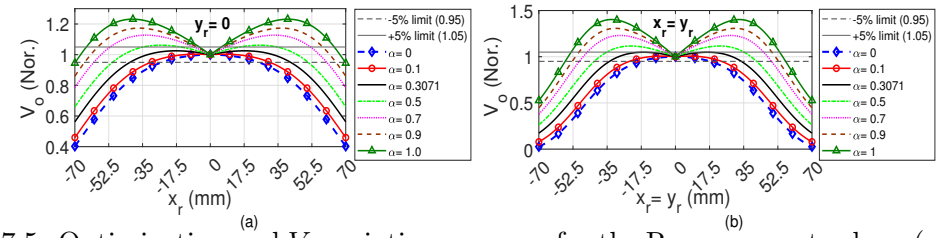

Figure 7.5: Optimization and V_o variation versus α for the Rx movements along (a) $y_r = 0$, (b) $x_r = y_r$.

lateral fields (H_x and H_y) in the Rx region than the longitudinal field component (H_z). Moreover, $\alpha = 0$ signifies the undershooting in V_o with the Rx misalignment due to the absence of harvesting capability from the H_x and H_y components. The high variation in V_o ultimately degrades the device's lifetime under charge. Due to this reason, a $\pm 5\%$ variation tolerance in the V_o value is the fluctuation limit adopted in this study as a universally accepted limit for battery charging applications. Considering this, the optimal α that retains V_o under $\pm 5\%$ limit is obtained as 0.3071 with a uniformity Rx area of 5993 mm^2. Thus, the percentage uniformity (PU), defined as the ratio of the Rx movement area with uniformity in V_o to the Tx maximum dimension area, is plotted in Fig. 7.6 for varying α. The result indicates that PU increases with increasing α for $\alpha > 0$ and reaches

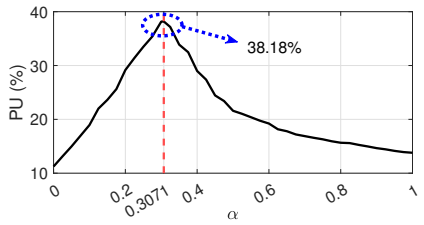

Figure 7.6: Variation of PU with α.

a maximum value of 38.18% at $\alpha = 0.3071$. Further increase in α beyond 0.3071 causes a reduction in the uniformity area because overshooting of the 5% limit. The 3−D variation plots of V_o in the misaligned Rx for various values of α (i.e. 0, 0.3071, and 1) is presented in Fig. 7.7. Fig. 7.7(a) indicates a highly varying V_o under the misaligned Rx condition

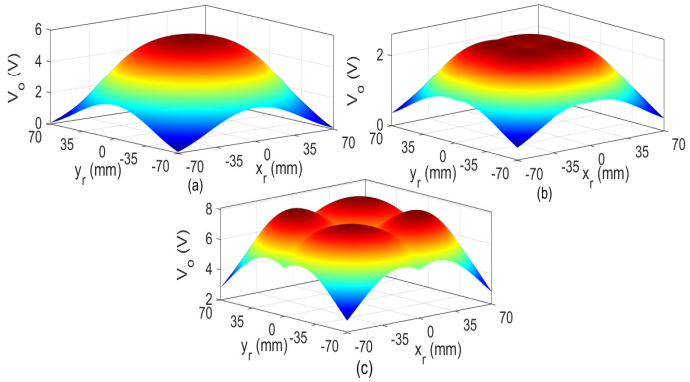

Figure 7.7: Analytical variation of the V_o under lateral misalignment (a) planar Rx ($\alpha = 0$), (b) proposed Rx ($\alpha = 0.3071$), (c) identical orthogonal Rx ($\alpha = 1$).

since it harnesses only the H_z component of the H-field, therefore causing undershoot in the V_o response. In contrast, a significant overshoot is present in the identical Rx ($\alpha = 1$)

as shown in Fig. 7.7(c), again resulting in lateral misalignment. On the contrary, the proposed Rx provides enhanced uniformity in V_o for the Rx movements. This indicates that the proposed design can mitigate lateral misalignment to a greater extent for the adopted Tx with $r_{Tx} = 70.7$ mm and a transfer distance of 50 mm. However, any change in Tx dimension or charging distance requires redesigning the rectenna array, although the optimization procedure remains the same. An EM simulator is utilized to determine the specific absorption rate (SAR) to confirm the electromagnetic absorption of the field generated by the Tx on a human body. The Tx is located at a distance of 5 mm above the chest region of a human body, as shown in Fig. 7.8. The computed SAR value is within the safety standards set by the Federal Communications Commission (FCC) [110], making it secure for charging pacemaker devices. Considering this, the final design parameters of

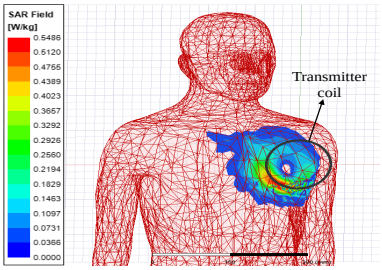

Figure 7.8: Evaluation of electromagnetic absorption by the human body.

the proposed Rx antenna corresponding to $\alpha = 0.3071$ are presented in Table 7.1. Here,

Table 7.1: Design parameters of the proposed Rx antenna

Parameters	L_X	W_X	L_Y	W_Y	L_Z	N_r^x	N_r^y	N_r^z
Values (mm)	19	6.4	19	6.4	16	5	5	5

$N_r^z = 5$ represents each spiral of the Rx coil-z containing 5 turns. The w_r^i and g_r^i are set as 0.5 mm, corresponding to the minimum fabrication limit in the laboratory. Further realization of the proposed rectenna array and experimental verification are presented subsequently.

7.1.2 Proposed Rectenna Realization using a Multi-layer PCB and Measurement Results

To realize the proposed design, a multi-layer Printed Circuit Board (PCB) technology is adopted. For this purpose, different PCB layers are fabricated individually using a PCB prototyping machine available in the laboratory, and later, stacking of these layers is performed to build the prototype. The layout of the various printed metallic layers of the proposed design, along with an isometric view of the final Rx prototype, is shown in Fig. 7.9. These metallic layers are sandwiched, as shown in Fig. 7.2(c), and the connections between various layers are realized judiciously to avoid any overlapping between the layers. The connections to the various layers are made using vias, and various SMD components are assembled with the PCB, as depicted in Fig. 7.9.

The fabricated prototype of the proposed design used for the experimental verification of analytical results is shown in Fig. 7.10. To resonate the WPT coils at the operating frequency of 6.78 MHz, the unloaded impedance of each Rx coil, i.e., Coil$-x$, $-y$, and

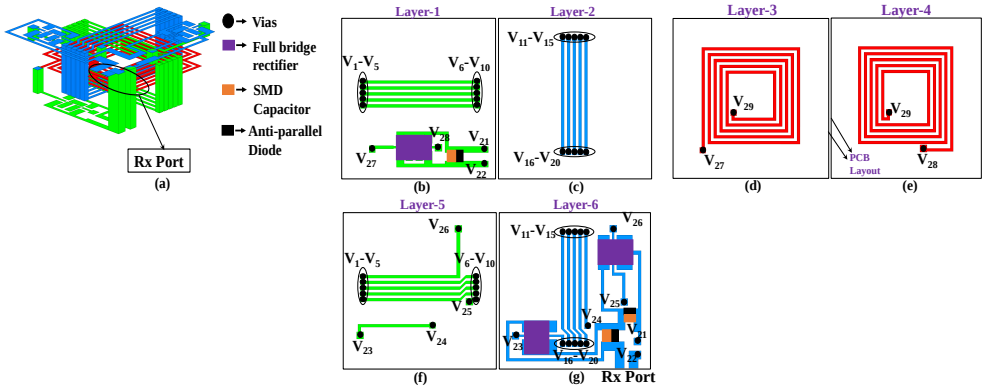

Figure 7.9: Realized layout of the proposed Rx (a) isometric view (b) metallic layer-1, (c) layer-2, (d) layer-3, (e) layer-4, (f) layer-5, (g) layer-6.

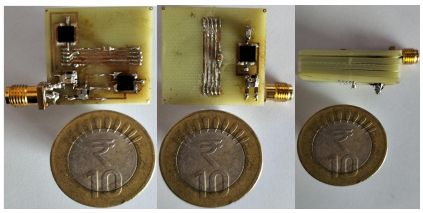

Figure 7.10: Fabricated prototype of the proposed rectenna array (a) top view, (b) bottom view, (c) side view.

$-z$ along with the Tx coil, is measured using an Agilent VNA (PNA-L N5230C). The measured impedance (in Ω) values of the Tx and individual Rx coils are listed in Table 7.2. The required matching capacitance values to resonate the coils at the system operating

Table 7.2: Measured coil impedance (in Ω) at different ports.

Tx	Coil$-x$	Coil$-y$	Coil$-z$
9.86 + j683.83	0.53 + j25.69	0.68 + j27.33	1.83 + j73.49

frequency are correspondingly evaluated as C_{reso}^{Tx}= 34.33 pF, $C_{reso}^{\text{coil}-x}$= 913.75 pF, $C_{reso}^{\text{coil}-y}$= 858.92 pF, and $C_{reso}^{\text{coil}-z}$= 319.42 pF. The nearest available SMD capacitors are mounted in series with the Tx and Rx coils following the layout shown in Fig. 7.9. To obtain a rectified output from orthogonal Rx coils, three full bridge rectifier modules (NMLU1210) are inserted in series with each Rx coil, whereas, to nullify the effect of ripples present in the rectified output voltages, a filter capacitance of 4.54 nF is inserted with each Rx coil. An anti-parallel Schottky diode (DB2S20500L) is inserted with each Rx coil to bypass it when not activated.

The experimental setup used to demonstrate the effectiveness of the lateral misalignment tolerance is depicted in Fig. 7.11. For this purpose, a programmable DC power supply (HMP2030) is employed to feed the power to a high-frequency inverter (EPC9507) that generates the feeding signal at 6.78 MHz. The output of this high-frequency inverter is supplied to the Tx antenna of the WPT system. Whereas, on the Rx side, a Keysight Digital Storage Oscilloscope (DSOX2022A) is used to measure the AC quantities. The rectified voltage at the output is measured using a Keysight multimeter (U1232A). The

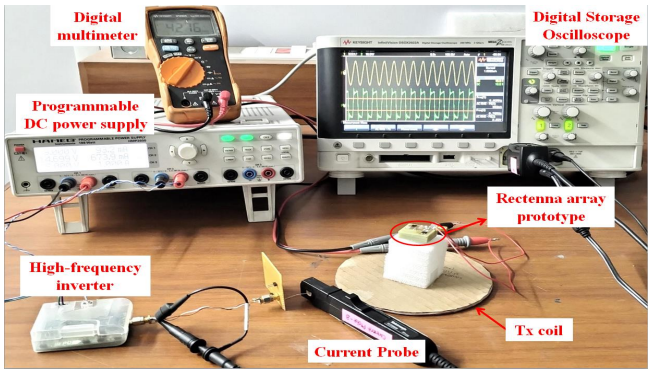

Figure 7.11: Experimental setup to measure the response of proposed Rx design.

measured current and voltage across the Tx terminals are shown in Fig. 7.12(a), which signifies that the system is operating nearly at the unity power factor. Moreover, the

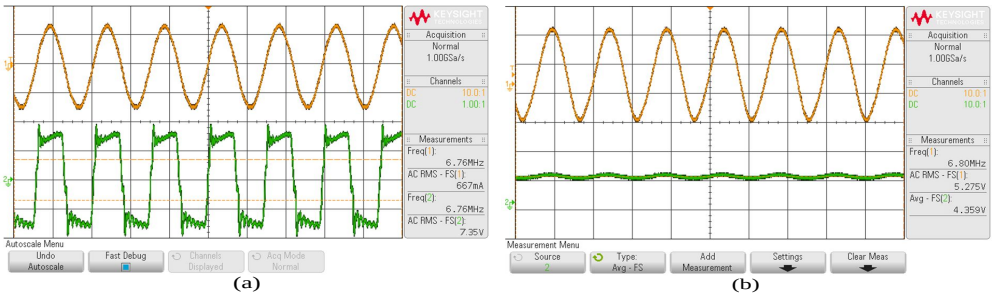

Figure 7.12: (a) Measured current and voltage across the Tx terminal, (b) Voltage induced at Rx Coil$-z$ and V_o at rectenna port.

voltage obtained at the Rx coil$-z$ and the V_o at the rectenna port under the perfectly aligned condition of the rectenna array is presented in Fig. 7.12(b). Further validation of measured V_o with the analytical V_o variation when Rx is misaligned horizontally ($y_r = 0$) and diagonally ($x_r = y_r$) is presented in Fig. 7.13. Here, both analytical and measured

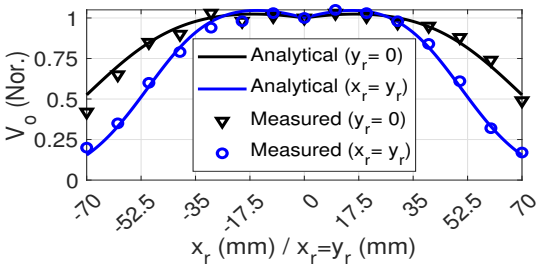

Figure 7.13: Measured V_o for a laterally misaligned rectenna along $y_r = 0$ and $y_r = x_r$.

results are self-normalized with their own V_o obtained under the perfectly aligned case. The measured results exhibit a good agreement with the analytical results. The peak voltage variation present in the proposed rectenna system is 4.8% compared to the voltage variation of 40.3% obtained in the identical Rx design case ($\alpha = 0$). This shows that the proposed rectenna provides V_o variation within the acceptable limit when the Rx is misaligned laterally and achieves a percentage uniformity of 38.18%. The load resistance

(R_L) is also optimized to deliver maximum power to the load. For this purpose, the power harnessed by the proposed rectenna is measured by inserting a variable resistor at the output terminal of the load when the rectenna unit is located at $(0, 0, 50)$ mm. Keeping the input power (P_{dc}^{in}) from a programmable DC power supply fixed at 4.90 W, the measured V_o and corresponding rectified power (P_{dc}^{r}) delivered to the load is plotted for varying R_L values as depicted in Fig. 7.14(a). The plot shows that P_{dc}^{r} is maximized for $R_L = 10\Omega$

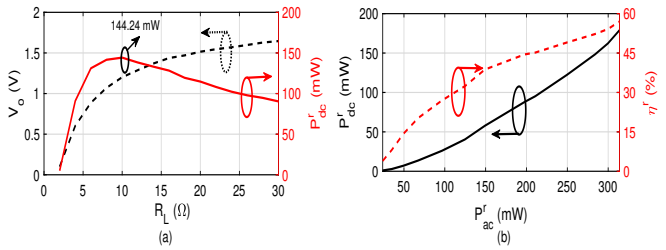

Figure 7.14: (a) Measured V_o and P_{dc}^{r} with a varying load R_L, (b) Performance measurement of utilized rectifier.

and the optimal value of P_{dc}^{r} obtained as 144.24 mW, respectively. This optimized R_L practically applies to various biomedical implant devices and portable electronic devices. Moreover, the performance of the rectifier employed in the proposed rectenna array is also evaluated by measuring the P_{dc}^{r} and rectification efficiency (η^r) versus input power to the rectifier (P_{ac}^{r}) for the Rx coil-z, and the results are depicted in Fig. 7.14(b). These measurements are carried out under the assumption of perfect alignment case of rectenna array. Here, Fig. 7.14(b) illustrates that both P_{dc}^{r} and η^r rising with increasing values of P_{ac}^{r} and the measured η^r is 53.30 %, when P_{dc}^{in} is set as 4.90 W. Furthermore, to

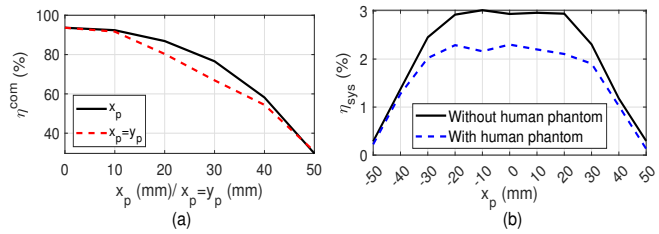

Figure 7.15: (a) Combining efficiency, (b) System efficiency versus lateral misalignment.

determine the combining losses within the rectenna array, a combining efficiency (η^{com}) is also measured, which is defined as a ratio of P_{dc}^{r} to the summation of rectified power obtained from individual coils and plotted in Fig. 7.15(a). This plot indicates that some combining loss will always be associated with the rectenna array. The system efficiency (η_{sys}) of the proposed WPT system is also evaluated, which is defined as a ratio of P_{dc}^{r} and P_{dc}^{in}. Under the perfectly aligned case, the evaluated η_{sys} is 2.94 %, whereas its variation with lateral misalignment of Rx is presented in Fig. 7.15(b). To evaluate the system's performance in a real-world scenario, a human body phantom replicating the characteristics of the human body is employed, as depicted in Fig. 7.16 and the measured η_{sys} versus lateral misalignment is shown in Fig. 7.15(b). The plot indicates a reduction in η_{sys} due to angular and longitudinal misalignment, highlighting a potential area for future

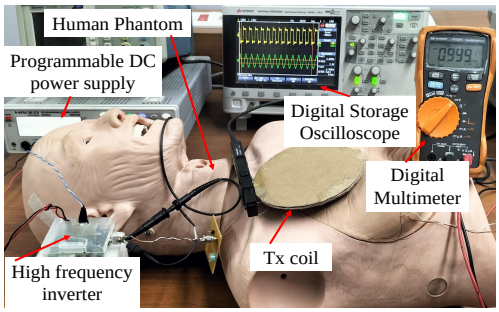

Figure 7.16: Experimental setup with human body phantom.

exploration in this study. Moreover, Fig. 7.15(b) indicates that η_{sys} is almost constant for the range $[-30, 30]$, thus providing a consistent power for the misalignment tolerance range of 60×60 mm^2. Thus, the results indicate that the proposed rectenna has a good potential to overcome the lateral misalignment problem. As a result, the power transfer performance remains consistent irrespective of the lateral movement of the Rx coil system in a wide area.

7.2 Use Case of a Planar Receiver Antenna for Drone Charging Application (Design−5B)

7.2.1 System Description and WPT Scenario

The scenario of the proposed WPT system contains a Tx coil and a set of Rx coils, which is separated by a distance h is demonstrated in Fig. 7.17(a). The Tx adopted in the this

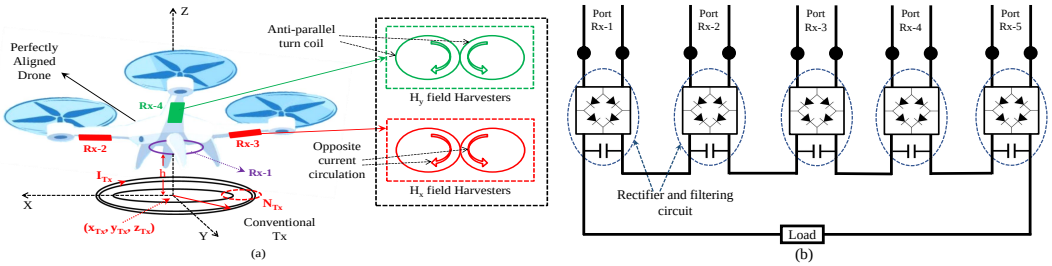

Figure 7.17: (a) Scenario of the proposed drone charging WPT system, (b) DC combining of response obtained from various Rx antennas.

work is a conventional circular coil located at (x_{Tx}, y_{Tx}, z_{Tx}) and carried a current of I_{Tx}. The radius and number of turns present in the Tx coil are designated as r_{Tx} and N_{Tx}. To exemplify the H-field components generated from the Tx coil at each point (x_r, y_r, z_r) on the Rx plane, the H-field equations for a single-turn Tx coil as presented in (2.3) is adopted. Therefore, the total H-field components (H_x, H_y, and H_z) generated at the Rx plane due to a total N_{Tx} turns of the Tx coil is given as (2.4). The H-field distribution generated by the Tx coil located at the origin, having $r_{Tx} = 70$ mm and $N_{Tx} = 5$ at the Rx plane $h = 50$ mm is calculated analytically by adopting MATLAB R2019a and plotted in Fig. 7.18 The H-field distribution signifies that the H_z component is present

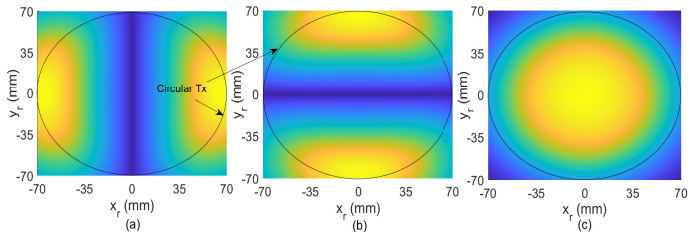

Figure 7.18: H-field distribution generated from a conventional Tx antenna at the targeted Rx region ($h = 50$ mm) (a) H_x, (b) H_y, (c) H_z.

at the center of the Tx coil, whereas the lateral fields (H_x and H_y) are present at the two extreme edges of the Tx coil. Therefore, these lateral H-field components need to be harvested optimally to improve the PTE of the conventionally WPT system (using only a single Rx coil for harvesting H_z component of H-field). To capture these lateral H-field components, the proposed Rx coil splits into five distributed Rx-coil system denoted as Rx-i $\forall$ $i \in \{1, 5\}$. Here, Rx-1 is placed between the drone's four legs and captures only the H_z component of the H-field generated by the Tx coil. In contrast, the lateral H-field components are harvested by adopting four Rx coils (Rx-2 to Rx-5) and attached to the four arms of the drone as depicted in Fig. 7.17(a).

7.2.2 Evolution of the Proposed Design Lateral Field Harvesting Coils

To harvest the lateral H-field components, two sets of anti-parallel connected coils are attached to oppositely placed coils. For instance, Rx-2 and Rx-3 are placed to the two opposite arm as shown in Fig. 7.17(a) to capture the H_x component of H-field. Similarly, Rx-4 and Rx-5 (Where, Rx-5 is hidden behind the drone, thus, not presented in Fig. 7.17)(a) are placed orthogonal to Rx-2 and Rx-3 for capturing the H_y component of H-field. The purpose of using an anti-parallel turn coil in the proposed Rx antenna is that the resultant current flows along one direction once the field is captured (from the right-hand thumb rule). However, a DC combining technique, as shown in Fig. 7.17(b), can be adapted for combining the response obtained from various Rx coils because of its advantage over AC combining. In the AC combining, the rectification is performed after combining the response obtained from distributed Rx coils, resulting in a destructive addition of H-field components and reducing the output response. Whereas, in the DC combining, the response obtained from the individual receiver is first rectified and later combining these rectified responses takes place. Further, a simulation-based study to demonstrate the field harvesting capability of the proposed anti-parallel turn coils is presented subsequently.

7.2.3 Simulation Study of Field Harvesting Coils

To verify the claim that anti-parallel turn coils have the potential to harvest the available lateral field components from a conventionally used Tx, a simulation-based study has been performed in ANSYS EM Suite 20.2. For this purpose, a layout of the proposed WPT

system was first designed in ANSYS MAXWELL, and later the same design was imported into ANSYS Simplorer to perform circuit analysis. For the sake of demonstration, the parameters of the Rx coils (Rx-2 to Rx-5) present in the proposed WPT system are selected the same as Design−1B and Design−2A. Whereas the parameters of Rx-1 are adjusted such that an equal induced voltage (V_{ind}) is obtained from all the Rx coils. Moreover, the parameters of Tx coil are taken as $r_{Tx} = 70.7$ mm and $N_{Tx} = 5$, to obtain maximum field at the Rx region ($h = 50$ mm). Also, for the sake of simplicity, a concentrated circular coil is considered on both Tx and Rx sides. Therefore, the final design parameters of the Tx and Rx coils are listed in Table 7.3. The layout of the proposed WPT scenario designed

Table 7.3: Coil parameters of the proposed WPT system.

Coil	Radius (mm)	Turn
Tx	70	5
Rx-1	70	2
Rx-2 to -5	29	11

in ANSYS MAXWELL is shown in Fig. 7.19. Later, the field harvesting capability of the

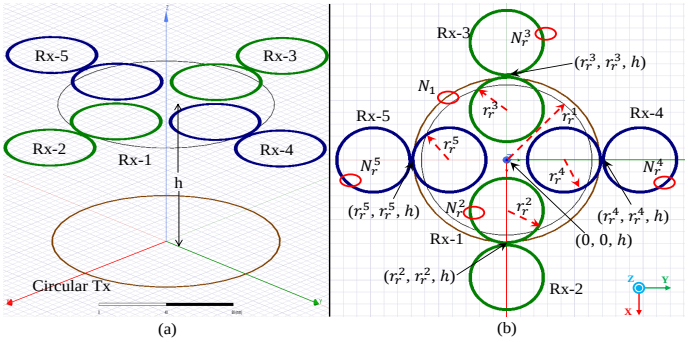

Figure 7.19: (a) Layout of the proposed WPT system in isometric view, (b) top view of the proposed Rx antenna.

proposed Rx coil is analyzed in terms of V_{ind} obtained in the Rx coil. The V_{ind} distribution when anti-parallel turn coils and planar central Rx coil are analyzed individually at the Rx region ($h = 50$ mm) are plotted in Fig. 7.20. The V_{ind} distribution of anti-parallel

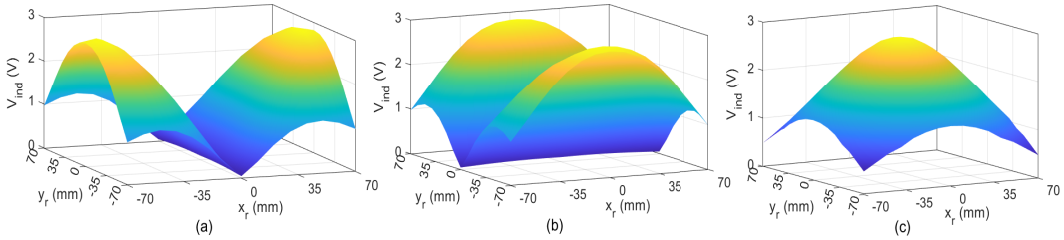

Figure 7.20: Simulated V_{ind} from (a) Rx-2 or Rx-3, (b) Rx-4 or Rx-5, (c) Rx-1.

coils is maximized at the edges of the Tx coil, which signifies the capability of the Rx coil to harvest lateral H-field components (H_x and H_y). In contrast, the central Rx coil encapsulates the vertical component of the H-field (H_z) as shown in Fig. 7.20. For better visual representation, a 2−D variation of V_{ind} with x_r is provided in Fig. 7.21. Based on the maximum V_{ind} obtained, the position of anti-parallel coils is selected as 64 mm. However,

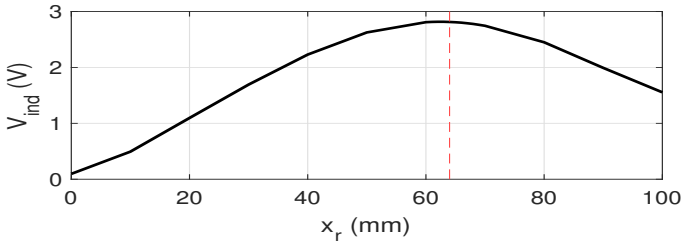

Figure 7.21: Position optimization of the proposed anti-parallel turn coil.

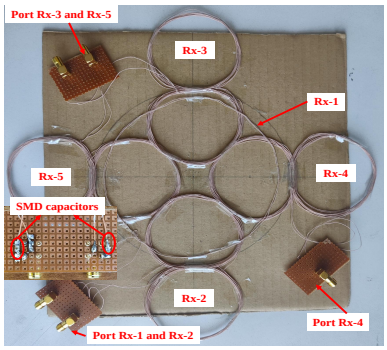

Figure 7.22: Fabricated prototype of the proposed Rx antenna.

the optimal position of the anti-parallel coil overlaps with the adjacent anti-parallel coils. Therefore, the position of anti-parallel coils is slightly adjusted by shifting at 70 mm to avoid overlapping the coils. Thus, the final position of Rx-i $\forall$ $i \in [2, 5]$ are listed in Table 7.4. Further, experimental validation of the proposed Rx antenna is presented next.

Table 7.4: Positions of anti-parallel turn coils

Rx-i	(x_r^i, y_r^i) in mm
Rx-2	(70, 0)
Rx-3	(−70, 0)
Rx-4	(0, 70)
Rx-5	(0, −70)

7.2.4 Experimental verification

The proposed Rx coil antenna having the layout shown in Fig. 7.19 is fabricated using high-frequency Litz wire as shown in Fig. 7.22. The coil parameters used for fabricating the proposed Rx remain the same as provided in Table 7.3. To resonate the Tx and Rx coils at the working frequency, the unloaded impedance of these coils is measured using an Agilent VNA (PNA-L N5230C). The measured unloaded impedance and the calculated resonating capacitance are listed in Table 7.5. The corresponding SMD capacitors are inserted in series with each coil, as shown in Fig. 7.22. Further, the performance of the fabricated prototype is verified using an experimental setup as demonstrated in Fig. 7.23. For this purpose, a programmable DC power supply (HMP2030) is used to feed the power to a high-frequency inverter (EPC9507), which generates the feeding signal. The output of this high-frequency inverter is then supplied to the Tx antenna of the WPT system. Whereas, on the Rx side, a Keysight Digital Storage Oscilloscope (DSOX2022A)

Table 7.5: Measured unloaded impedance of Tx and Rx antennas and corresponding resonating capacitance

Coil	Impedance (Ω)	resonating capacitance (pF)
Tx	$(11.07 + j756.90)$	31.01
Rx-1	$(5.12 + j109.97)$	213.46
Rx-2	$(13.15 + j1605.20)$	14.62
Rx-3	$(13.13 + j1605.47)$	14.62
Rx-4	$(13.18 + j1604.60)$	14.63
Rx-5	$(13.13 + j1604.98)$	14.63

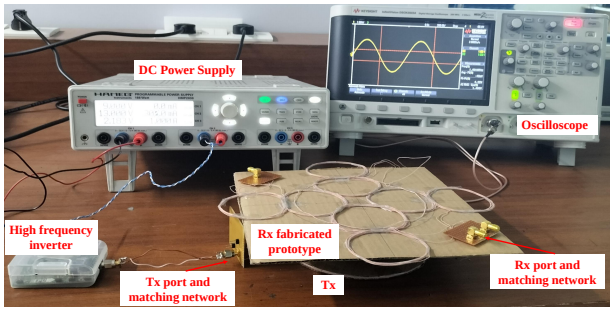

Figure 7.23: Experimental setup to verify the performance of fabricated prototype.

is utilized to measure the V_{ind} in the Rx coils. The measured V_{ind} from the central coil and anti-parallel turn coils are listed in Table 7.6. The results signifies that measured V_{ind} from

Table 7.6: Measured V_{ind} from central and anti-parallel connected turn coils.

$V_{ind}(V)$	Rx-1	Rx-2	Rx-3	Rx-4	RX-5
Simulated	22.5	22.3	22.3	22.3	22.3
Measured	22.4	21.9	22.9	23.1	22.7

various Rx ports are well corroborated with the simulated V_{ind}. Hence, it is evident that adopting anti-parallel coils along with a central Rx coil harvests all the available H-field components generated by a conventional Tx over the traditional single coil Rx. Thus resulting an improved power rating or for the same power rating increases the range of a WPT system. This proves the potential of the proposed Rx antenna. Further, combining technique and misalignment problems will be addressed in the future works.

7.3 Summary

This chapter introduced a near-field rectenna array system to address the lateral misalignment problem in a WPT system for small device powering as presented in Design−5A. The analytical framework of the magnetic field distribution originating from a conventional Tx reveals that the proposed rectenna consisting of two orthogonal Rx coils along with a traditionally used planar spiral Rx coil can effectively utilize the three orthogonal H-field components to enhance the misalignment tolerance. The rectified voltages from these orthogonal coils are efficiently combined using a DC combining technique to deliver power to the load efficiently. Optimization of the Rx coil parameters improves misalignment tolerance, demonstrating superior performance over identical Rx

antennas used in existing literature. To realize the proposed rectenna, a multi-layer PCB technology is adopted with integrated rectification and filtering circuitry, resulting in a single port rectenna structure. Experimental results indicate that the proposed rectenna achieves an impressive 38.18 % uniformity in the Rx region, with a peak voltage variation of only 4.8 %, compared to the 40.3 % variation seen in identical Rx antennas. This high degree of uniformity makes the proposed rectenna a well-suited solution for lateral misalignment-tolerant systems. Moreover, rectification and combining efficiency are also determined experimentally and obtained as 53.30 % and 93.65 %, respectively. The system efficiency is also measured in a realistic scenario as 2.30 % and remains nearly constant across the misalignment tolerance range of 60×60 mm^2. This proves the usefulness of the proposed rectenna as a compact, robust, and cost-effective solution in WPT applications for small devices.

Moreover, a use case of a planar rectenna array is presented in Design−5B, where a novel Rx antenna comprising of four sets of anti-parallel coils along with a conventionally used central receiver coil is proposed. The anti-parallel coils are designed to capture the lateral H-field components (H_x and H_y), whereas, central coil is utilized to harvest only the H_z component of H-field. Further, the position of anti-parallel turns coils are optimized to harvest the maximum available lateral fields generated from the Tx coil. To verify the claim, a fabricated prototype is then designed using a high frequency litz wire and measurement is performed using a WPT setup. The measurement result shows that the proposed anti-parallel turn coil has the capability to capture the lateral field components. Hence, proves the usefulness of the proposed antenna for drone application.

[0]**CHAPTER OUTCOMES:**

[1]. **V. K. Srivastava**, and A. Sharma, "A Coil Rectenna Array Design to Harvest All H-Field Components for Lateral Misalignment Tolerant Wireless Powering of Bio-Medical Implant Devices," in *IEEE Journal of Electromagnetics, RF and Microwaves in Medicine and Biology*, doi: 10.1109/JERM.2024.3351751.

[2]. **V. K. Srivastava**, A. Bharadwaj, and A. Sharma, "A Planar Distributed Receiver Coil Antenna Array to Encapsulate Vertical and Lateral H-Fields for Drone Wireless Charging," in *17th European Conference on Antennas and Propagation (EuCAP)*, Florence, Italy, 2023, pp. 1-5, doi: 10.23919/EuCAP57121.2023.10133370.

Chapter 8

Conclusion

8.1 Summary of the Thesis

In conclusion, this thesis provides a potential solution for mitigating all possible misalignment problems in wireless charging of bio-medical implant applications as discussed in Chapter 1. To better understand the necessity of the proposed designs, this thesis has gone through an evolutionary process followed by theoretical framework of WPT system as provided in Chapter 2. Initially, the most common misalignment problem in medical implants i.e. angular misalignment is targeted and several field forming technique is adopted to overcome this issue. For instance, in Chapter 3, 3−D rotating H-field is proposed, whereas Chapter 4 evolve a novel methodology named it as switched polarization and various potential Tx designs are suggested to generate the these fields. However, the best possible possible methodology found the one that can simultaneously localize the moving Rx implanted with the device and power up by forming magnetic beam toward it. A detailed discussion on the localization technique and its amalgamation with magnetic beam is provided in Chapter 5 and Chapter 6. Moreover, a field harvesting Rx is also provided in Chapter 7 that can overcome the misalignment problem using a conventional Tx. Furthermore, the most significant achievements of this thesis are outlined as follows:

8.1.1 Conclusions on Rotating Magnetic Field Forming Transmitters

This chapter examines the influence of 3−D polarized H-fields on the angular misalignment issue within a typical WPT application and presented in Design−1A. For this purpose, an analysis of induced voltage in the receiver due to various polarizations (2−D and 3−D) is presented. While previous work suggested spherically polarized H-field as a solution, this study demonstrates the limitations of spherical polarization and introduces an ellipsoidal polarization to completely eliminate angular misalignment. Performance comparison shows that the proposed ellipsoidal polarization significantly outperforms other polarizations in terms of induced voltage in receiver orientations, with a notable reduction in standard deviation and peak variation. Subsequently, an optimized planar multicoil antenna capable of generating an optimized 3-D ellipsoidally polarized H-field is proposed to provide an ease of placement in Design−1B. The antenna design consisting of five spatially distributed coils and three ports, is optimized to achieve maximum $S21$ between

transmitter and receiver antennas. Experimental verification confirms the antenna's ability to form a 3−D polarized H-field, effectively powering the receiver in any orientation. Compared to literature designs, the proposed antenna demonstrates superior performance in mitigating angular misalignment, showcasing a significantly lower standard deviation in RMS induced voltage. Lastly, the paper presents a 3−D polarized field-forming technique to mitigate angular misalignment in microwave power transfer systems as illustrated in Design−1C. Analyzing power transmission in various IoT node orientations, the study verifies the effectiveness of 3−D polarized E-field forming in completely eliminating angular misalignment and providing an orientation-insensitive system.

8.1.2 Conclusions on Switched Magnetic Field Forming Transmitter

This chapter investigates an innovative approach to address angular misalignment in biomedical implant applications by integrating field-forming with switching control to produce a switched polarized H-field as demonstrated in Design−2A. Unlike previous methods, this approach requires only a single-tone signal and excitation duration H-field components are controlled optimally to mitigate misalignment effectively. A planar transmitter antenna, optimized for a maximum of $S21$ with two dumbbell-shaped coils and an axial coil, achieves this field formation. Switching, facilitated by two SPDT switches, demonstrates invariant induced voltage in a rotating receiver coil, which is experimentally validated and compared with linear and circular polarization. The results show a significant reduction in the standard deviations in induced voltages, affirming the proposed antenna's high misalignment tolerance and suitability for low-cost manufacturing. This presents that the proposed Design−2A is a promising solution for orientation-oblivion wireless charging. Additionally, a planar switching integrated quadrant coil antenna is proposed to address lateral and angular misalignment issues simultaneously in near-field WPT and presented as Design−2B. Employing time switching with three DPDT switches within the antenna structure enable control over current circulations in four quadrant coils and forming a widespread switched polarized H-field. Considering various constraints, the optimization process yields an antenna design that mitigates misalignment in the Rx lateral movement region within specified zones. While lateral misalignment is completely eliminated in Zone-1, moderate mitigation is achieved in Zone-2, though challenges persist in ensuring uniformity in H-field distributions beyond these zones. The proposed antenna is also compared with the most pertinent works reported in the literature and the comparison is summarized in Table 8.1. It is inferred from Table 8.1 that the proposed antenna design provides superior functionality over the conventional designs in terms of misalignment performance, feeding complexity, antenna fabrication, and system cost. This prove the potential of proposed methodology and antenna design for overcome the angular and lateral misalignment problem simultaneously. Nonetheless, the proposed method and antenna design offer a promising solution to simultaneously tackle lateral and angular misalignment problems in WPT systems, paving the way for future improvements in uniformity across all H-field components.

Table 8.1: Comparison of the Tx antennas presented in SO−1 and SO−2 with the most pertinent works.

	Lateral/angular misalignment	Field forming schemes	Antenna structure	Switching employed	Feeding complexity	System cost	Ease of fabrication	Misalignment performance
[10]	Lateral	Widespread H_z field forming	Planar	No	Low	Low	High	Lateral- largely
[27]	Lateral	Switched H_z field forming	Planar	Yes	Moderate	Moderate	Moderate	Lateral- partial
[19, 21, 22]	Angular	3-D rotating H-field forming	3-D	No	High	High	Low	Angular- moderate
Design−1A	Angular	3-D rotating H-field forming	3-D	No	High	High	Low	Angular- complete
Design−1B	Angular	3-D rotating H-field forming	Planar	No	High	High	High	Angular- complete
Design−2A	Angular	Switched polarized H-field forming	Planar	Yes	Low	Low	High	Angular- complete
[13]	Both	Linear H-field polarization	3-D	No	Low	Low	Low	Lateral- moderate Angular- moderate
[30]	Both	Field enhancement metamaterial	3-D	No	Low	Low	Low	Lateral- partially Angular- partially
[29]	Both	Switched H-field forming	Planar	Yes	High	High	Moderate	Lateral- moderate Angular- partially
Design−2B	Both	Widespread switched polarized H-field forming	Planar	Yes	Low	Low	High	Lateral- complete Angular- moderate

8.1.3 Conclusions on Non-uniform Magnetic Field Forming Transmitter

This chapter investigates magnetic localization to predict the position and orientation of a moving Rx. For this purpose, a transceiver antenna array is initially proposed and designated as Design−3A that can localize human fingertip positions by integrating 2-coil and 3-coil magnetic resonance coupling. A hybrid optimization approach enhances

Table 8.2: Comparison study of the Tx antenna presented in SO−3 with the state-of-the-art designs.

Properties	**Design−3A**	[59]	[68]	[75]	**Design−3B**	**Design−3C**
Localization approach	MRC based	Sensor based	Electromagnetic based	FDM based	TDM based	TDM based
Employed magnetic Source	Coil based	Permanent magnet based	Coil based	Coil based	Coil based	Coil based
Localization targeted (position or orientation)	Position	Both	Both	Both	Both	Both
Structure adopted	Planar	Planar	3-D	3-D	Planar	Planar
Tx size	6.2×6.2 cm^2	15×15 cm^2	$10 \times 10 \times 10$ cm^3	$24 \times 24 \times 3.4$ cm^3	30×30 cm^2	25.5×25.5 cm^2
Design optimization	Yes	No	Yes	No	No	Yes
Average position error in mm (orientation error in degree)	-	3.89 (5.5°)	-	2.3 (0.2°)	1.22 (1.18°)	1.17 (0.87°)
fabrication complexity	Low	Low	High	High	Low	Low
Cost	Low	Low	High	High	Low	Low

sensitivity through non-uniform H-field distributions from the transmitter coil array. The receiver coils and a resonator is optimized to maintain voltage gain below a threshold, ensuring reliable localization of resonator coil movements. Experimental validation confirms agreement with simulations, showcasing the potential for hygienic touchless interfaces in various applications. In contrast, another novel approach explores magnetic localization, including the position and orientation of objects with planar receivers implanted within the human body. A switched planar multi-coil transmitter antenna is proposed and symbolized as Design−3B to address the complexity and other challenges of the prior localization scheme defined as a frequency divisional scheme, thus proving the proposed time-divisional approach with a single frequency signal a prominent solution. Analytical and experimental studies demonstrate superior localization accuracy compared to multi-frequency designs, validating advantages in accuracy and complexity. Furthermore, an optimized switching integrated overlapping coil transmitter structure is introduced and exemplified as Design−3C. The proposed Tx is optimized by adequately selecting the design parameters to enhance non-uniform H-field distributions, resulting in a miniaturized transmitter size of 27.75%. Switching circuitry enables precise coil excitation, leading to improved localization performance, reduced average position and orientation errors, and enhanced success rates compared to literature designs. Experimental results

validate the proposed transmitter's potential for near-field localization applications. The performance of the proposed Tx is also compared with the state-of-the-art designs and tabulated in Table 8.2. The parameters, such as the miniaturized Tx design and its performance presented in Table 8.2, signify that the proposed Tx outperforms the designs mentioned in the literature. This proves the usefulness of the proposed Tx structure, designed using planar technology, and its potential to localize the position and orientation of a planar Rx coil.

8.1.4 Conclusion on Magnetic Beam Forming Transmitter Antenna

This chapter introduces an array of overlapped coil Tx designed for the localization and precise directing of a magnetic beam toward a specific Rx. The design of the Tx is optimized to generate a non-uniform distribution of H-field components, utilizing spatially distributed coils to achieve accurate localization and a focused magnetic beam. Additionally, the optimal placement of coils is determined to minimize the impact of mutual coupling between adjacent coils. The optimized Tx system is then utilized to evaluate localization accuracy and magnetic beam shaping performance. A time-divisional technique is employed to gather voltage samples from the Rx across different switching combinations of the Tx coils to precisely localize the Rx. Subsequently, a machine-learning algorithm predicts the position and orientation of the Rx, resulting in average errors of 0.22 mm and 1.44°, respectively. In contrast, for powering the localized Rx, a magnetic beam is directed towards it by controlling the current within the spatially distributed coils, which is determined using particle swarm optimization. The analytical results are validated using commercial electromagnetic software and an experimental setup. A prototype of the optimized Tx, along with switching circuitry, is constructed on a cardboard sheet. Voltage samples collected from the Rx are then utilized to localize random test positions and orientations, resulting in measured average errors of 0.31 mm and 1.62° for position and orientation, respectively. Furthermore, a normalized voltage distribution is observed for various Rx positions and orientations to showcase the beam-shaping capability of the proposed Tx. The performance of the proposed Tx is also compared with the state-of-the-art designs and tabulated in Table 8.3. The comparison signifies that the proposed Tx outperforms the other literary works. These findings underscore the potential of the proposed antenna system for efficiently charging biomedical applications.

Table 8.3: Comparison study of the Tx antenna proposed in SO−4 with the state-of-the-art designs.

Properties	[75]	**Design−3B**	[34]	[37]	[38]	[39]	**Design−4A**
Targeted localization	Yes	Yes	No	No	No	No	Yes
Average position error in mm (orientation error in degree)	2.3 (0.2°)	1.22 (1.18°)	-	-	-	-	0.22 (1.44°)
Localization approach	frequency divisional	Time divisional	- -	- -	- -	- -	Time divisional
Targeted beam-shaping	No	No	Yes	Yes	Yes	Yes	Yes
Beam-shaping excitation control scheme	- -	- -	Phase control	Amplitude and phase control	Phase control	Amplitude and phase control	Amplitude control
Optimal excitation phase/ amplitude evaluation for beam-shaping	-	-	Yes	No	No	No	Yes
Maximum Rx dimension (cm)	1.3	2	-	27.6	17.8	13	2
Tx Structure adopted	3-D	Planar	Planar	3-D	Planar	Planar	Planar
Tx optimization	No	No	Yes	No	No	No	Yes
Tx size	$24 \times 24 \times 3.4$ cm^3	30×30 cm^2	60×60 cm^2	$32.8 \times 32.8 \times 32.8$ cm^3	17.8×17.8 cm^2	21.4×21.4 cm^2	17.8×17.8 cm^2
Number of excitation required	More than one	Single	More than one	More than one	More than one	More than one	Single
Circuit complexity	High	Low	High	High	High	High	Moderate
Cost	High	Low	High	High	High	High	Low

8.1.5 Conclusion on Receiver Designs for Misalignment Insensitive WPT

This chapter investigates a near-field rectenna array system to tackle lateral misalignment challenges in WPT for small device powering. Firstly, a novel rectenna design comprising two orthogonal Rx coils and a planar spiral Rx coil is proposed. Analysis reveals its effectiveness in utilizing three orthogonal H-field components to enhance misalignment tolerance. The rectified voltages from these coils are efficiently combined using DC combining, with optimized Rx coil parameters demonstrating superior performance over existing literature. Realization employs multi-layer PCB technology with integrated circuitry, yielding impressive uniformity of 38.18 % in the Rx region, significantly outperforming identical Rx antennas. Experimental results verify rectification and combining efficiency, reaching 53.30 % and 93.65 %, respectively, with consistent system efficiency of 2.30 % across a misalignment tolerance range of 60×60 mm^2. Further, a use case of a planar receiver antenna for a drone charging application is proposed, comprising four anti-parallel coils and a central receiver coil. The anti-parallel coils capture lateral H-field components (H_x and H_y), while the central coil captures the H_z component. Optimized coil positions maximize lateral field harvesting from the Tx coil. Experimental validation confirms the antenna's capability to capture lateral field components, demonstrating its suitability for drone applications. The proposed coil rectenna array is also compared with the most pertinent works reported in the literature and tabulated in Table 8.4. It is apparent from Table 8.4 that the proposed rectenna array provides superior functionality in terms of miniaturized size, design optimization, the potential to mitigate lateral misalignment problems, robustness, etc., over the Rx antennas presented in the literature. Thus, the results indicate that the proposed rectenna has a good potential to overcome the lateral misalignment problem. As a result, the power transfer performance remains consistent irrespective of the lateral movement of the Rx coil system in a wide area.

Table 8.4: Comparison of the coil rectenna array proposed in SO−5 with most prominent works.

	[86]	[91]	[92]	[93]	[94]	[95]	[96]	**Design−5A**
Tx adopted	Conventional circular coil	Conventional circular coil	Circular coil array	Conventional circular coil	Conventional square coil	Conventional circular coil	Conventional circular coil	Conventional circular coil
Maximum Tx dimension	–	180 mm	150 mm	40 mm	40 mm	25.5 mm	40 mm	141.4 mm
Working Frequency	160 KHz	100 KHz	100 KHz	1 MHz	2.2 MHz	5 MHz	13.56 MHz	6.78 MHz
Coils contained in Rx antenna	Planar Rx	Two identical orthogonal square coils	Two non-identical orthogonal square coils	Two non-identical orthogonal square coils	T shaped two identical orthogonal coils	3−D cross type receiver	spherical receiver	Three non-identical orthogonal coils
Maximum dimension of Rx coil	50 mm	100 mm	65.5 mm	20 mm	20 mm	8 mm	9.5 mm	19 mm
Separate rectifier and filter units required	Yes	Yes	Yes	Yes	Yes	Yes	No	No
Transfer distance	25 mm	110 mm	50 mm	20 mm	20 mm	100 mm	30 mm	50 mm
Antenna optimization for lateral misalignment	No	No	No	No	No	No	No	Yes
Potential to mitigate lateral misalignment	Unable to mitigate	Along single axis	Along single axis	Along single axis	Along single axis	Throughout the Rx plane	Unable to mitigate	Throughout the Rx plane
Antenna fabrication technology	Copper wire	Litz wire	Copper wire	Copper wire	Copper wire	Copper wire	Copper wire	Planar technology
Possibility of antenna mass production	Low	Low	Low	Low	Low	Low	Low	High
Robustness	Low	Low	Low	Low	Low	Low	Low	High

8.2 Future Directions

There exists significant potential for further advancements in the field of wireless charging of biomedical implants, including:

8.2.1 Development of complete system including Tx-Rx Coil Antennas

- Future research could explore integrating a high-frequency inverter module and a rectifier module into the design of Tx-Rx coil antennas to create a more compact and efficient WPT system.
- Investigation into various cost-effective composite materials could be undertaken to enhance PTE in Tx-Rx coil antennas.
- Examining a planar Rx coil antennas for biomedical implant application capable of harvesting both the vertical and horizontal magnetic field distributions, with the goal of mitigating all possible misalignment issues in biomedical implants.
- Further extension of this thesis work could involve examining the designed WPT setup to a human trial for further verification of its performance.

8.2.2 Electromagnetic Compatibility (EMC) and Electromagnetic Interference (EMI)

- An essential aspect of near-field WPT involves assessing how electromagnetic interference from nearby equipment affects the operation of the Tx-Rx coil. Ensuring that WPT performance remains unaffected by such interference makes this a crucial area for future research.

8.2.3 Developing Artificial Designed Structure

- A promising avenue in advancing efficient and affordable near-field WPT systems is the exploration of artificial materials, such as metamaterials. These materials have the potential to streamline the operation of switching circuits and detection systems.

References

[1] D. Mukherjee, S. K. Rainu, N. Singh, and D. Mallick, "A miniaturized, low-frequency magnetoelectric wireless power transfer system for powering biomedical implants," *IEEE Transactions on Biomedical Circuits and Systems*, vol. 18, no. 2, pp. 438–450, 2024.

[2] M. R. Basar, M. Y. Ahmad, J. Cho, and F. Ibrahim, "An improved wearable resonant wireless power transfer system for biomedical capsule endoscope," *IEEE Transactions on Industrial Electronics*, vol. 65, no. 10, pp. 7772–7781, 2018.

[3] Z. Miao, D. Liu, and C. Gong, "Efficiency enhancement for an inductive wireless power transfer system by optimizing the impedance matching networks," *IEEE Transactions on Biomedical Circuits and Systems*, vol. 11, no. 5, pp. 1160–1170, 2017.

[4] S. R. Khan and M. P. Y. Desmulliez, "Implementation of a dual wireless power transfer and rotation monitoring system for prosthetic hands," *IEEE Access*, vol. 7, pp. 107 616–107 625, 2019.

[5] Y. Jia, S. A. Mirbozorgi, Z. Wang, C.-C. Hsu, T. E. Madsen, D. Rainnie, and M. Ghovanloo, "Position and orientation insensitive wireless power transmission for enercage-homecage system," *IEEE Transactions on Biomedical Engineering*, vol. 64, no. 10, pp. 2439–2449, 2017.

[6] H.-J. Kim, H. Hirayama, S. Kim, K. J. Han, R. Zhang, and J.-W. Choi, "Review of near-field wireless power and communication for biomedical applications," *IEEE Access*, vol. 5, pp. 21 264–21 285, 2017.

[7] A. Sharma, G. Singh, D. Bhatnagar, I. J. Garcia Zuazola, and A. Perallos, "Magnetic field forming using planar multicoil antenna to generate orthogonal h-field components," *IEEE Transactions on Antennas and Propagation*, vol. 65, no. 6, pp. 2906–2915, 2017.

[8] I. Cortes and W.-j. Kim, "Lateral Position Error Reduction Using Misalignment-Sensing Coils in Inductive Power Transfer Systems," *IEEE/ASME Transactions on Mechatronics*, vol. 23, no. 2, pp. 875–882, 2018.

[9] A. Sharma, A. Bharadwaj, and V. K. Srivastava, "An Analytical Framework to Design Planar Transmitting Array Antennas to Mitigate Lateral Misalignment in Wireless Power Transfer Systems," *IEEE Transactions on Antennas and Propagation*, vol. 69, no. 9, pp. 5559–5569, 2021.

[10] A. Bharadwaj, A. Sharma, and C. C. Reddy, "A Multi-turn Coil Antenna with Non-uniform Clustered Turns Optimized using Q-assisted MMSE Procedure to Enhance Misalignment Tolerance in WPT Systems," *IEEE Transactions on Antennas and Propagation*, pp. 1–1, 2022.

[11] T.-H. Kim, G.-H. Yun, W. Y. Lee, and J.-G. Yook, "Asymmetric Coil Structures for Highly Efficient Wireless Power Transfer Systems," *IEEE Transactions on Microwave Theory and Techniques*, vol. 66, no. 7, pp. 3443–3451, 2018.

[12] Q. Wang, W. Che, M. Mongiardo, and G. Monti, "Wireless Power Transfer System With High Misalignment Tolerance for Bio-Medical Implants," *IEEE Transactions on Circuits and Systems II: Express Briefs*, vol. 67, no. 12, pp. 3023–3027, 2020.

[13] Z. Liu, Z. Chen, C. Peng, J. Liang, P. Xiao, L. Bian, Y. Qiu, and G. Li, "A misalignment resilient system for magnetically coupled resonant wireless power transfer," *IEEE Transactions on Antennas and Propagation*, pp. 1–1, 2020.

[14] Dongyang Wang, Yongxin Zhu, Hongliang Guo, Xinen Zhu, TingTing Mo, and Qiyu Huang, "Enabling multi-angle wireless power transmission via magnetic resonant coupling," in *2012 7th International Conference on Computing and Convergence Technology (ICCCT)*, 2012, pp. 1395–1400.

[15] D. Lin, C. Zhang, and S. Y. R. Hui, "Power and efficiency of 2-d omni-directional wireless power transfer systems," in *2015 IEEE Energy Conversion Congress and Exposition (ECCE)*, 2015, pp. 4951–4958.

[16] B. Che, F. Meng, and Q. Wu, "An omnidirectional wireless power transmission system with controllable magnetic field distribution," in *2016 IEEE International Workshop on Electromagnetics: Applications and Student Innovation Competition (iWEM)*, 2016, pp. 1–3.

[17] J. Kang, Q. Wang, Y. Wang, and W. Li, "Polarization characteristic of the magnetic field in wireless power transfer systems," *IEEE Transactions on Antennas and Propagation*, vol. 67, no. 11, pp. 7114–7120, 2019.

[18] P. Bienkowski, T. Dlugosz, V. Nichoga, and H. Trzaska, "Quasi-spherical emf polarization," in *2010 International Conference on Modern Problems of Radio Engineering, Telecommunications and Computer Science (TCSET)*, 2010, pp. 89–90.

[19] W. M. Ng, C. Zhang, D. Lin, and S. Y. Ron Hui, "Two- and three-dimensional omnidirectional wireless power transfer," *IEEE Transactions on Power Electronics*, vol. 29, no. 9, pp. 4470–4474, 2014.

[20] C. Zhang, D. Lin, and S. Y. Hui, "Basic control principles of omnidirectional wireless power transfer," *IEEE Transactions on Power Electronics*, vol. 31, no. 7, pp. 5215–5227, 2016.

[21] J. Kim, D. Kim, J. Choi, K. Kim, and Y. Park, "Free-positioning wireless charging system for small electronic devices using a bowl-shaped transmitting coil," *IEEE Transactions on Microwave Theory and Techniques*, vol. 63, no. 3, pp. 791–800, 2015.

[22] J. Feng, Q. Li, F. C. Lee, and M. Fu, "Transmitter coils design for free-positioning omnidirectional wireless power transfer system," *IEEE Transactions on Industrial Informatics*, vol. 15, no. 8, pp. 4656–4664, Aug 2019.

[23] M. Grzeskowiak, A. Diet, M. Benamara, P. Poulichet, C. Conessa, S. Protat, M. Biancheri-Astier, F. de Oliveira Alves, Y. Le Bihan, and G. Lissorgues, "Distributed diameter subcoil twisted loop antenna in nonradiative wpt," *IEEE Antennas and Wireless Propagation Letters*, vol. 17, no. 1, pp. 4–7, 2018.

[24] C. Jiang, K. T. Chau, T. W. Ching, C. Liu, and W. Han, "Time-Division Multiplexing Wireless Power Transfer for Separately Excited DC Motor Drives," *IEEE Transactions on Magnetics*, vol. 53, no. 11, pp. 1–5, 2017.

[25] M. Fu, H. Yin, and C. Ma, "Megahertz Multiple-Receiver Wireless Power Transfer Systems With Power Flow Management and Maximum Efficiency Point Tracking," *IEEE Transactions on Microwave Theory and Techniques*, vol. 65, no. 11, pp. 4285–4293, 2017.

[26] H. Qiu, T. Sakurai, and M. Takamiya, "Digital Transmitter Coil for Wireless Power Transfer Robust Against Variation of Distance and Lateral Misalignment," *IEEE Transactions on Microwave Theory and Techniques*, vol. 68, no. 9, pp. 4031–4039, 2020.

[27] P. Tan, T. Peng, X. Gao, and B. Zhang, "Flexible combination and switching control for robust wireless power transfer system with hexagonal array coil," *IEEE Transactions on Power Electronics*, vol. 36, no. 4, pp. 3868–3882, 2021.

[28] J. Li, Y. Yang, H. Yan, C. Liu, L. Dong, and G. Wang, "Quasi-Omnidirectional Wireless Power Transfer for a Sensor System," *IEEE Sensors Journal*, vol. 20, no. 11, pp. 6148–6159, 2020.

[29] B. Lee, D. Ahn, and M. Ghovanloo, "Three-phase time-multiplexed planar power transmission to distributed implants," *IEEE Journal of Emerging and Selected Topics in Power Electronics*, vol. 4, no. 1, pp. 263–272, March 2016.

[30] T. Shaw and D. Mitra, "Wireless power transfer system based on magnetic dipole coupling with high permittivity metamaterials," *IEEE Antennas and Wireless Propagation Letters*, vol. 18, no. 9, pp. 1823–1827, 2019.

[31] Q. Zhu, M. Su, Y. Sun, W. Tang, and A. P. Hu, "Field orientation based on current amplitude and phase angle control for wireless power transfer," *IEEE Transactions on Industrial Electronics*, vol. 65, no. 6, pp. 4758–4770, 2018.

[32] T. Lim and Y. Lee, "Reconfigurable coil array for near-field beamforming to compensate for misalignment in wpt systems," *IEEE Transactions on Microwave Theory and Techniques*, vol. 69, no. 11, pp. 4711–4719, 2021.

[33] J. Li, N. Kou, S. Yu, Z. Ding, and Z. Zhang, "Reconfigurable pcb coil array loaded with pin diodes for improving transmission efficiency in mcr-wpt systems," *IEEE Antennas and Wireless Propagation Letters*, vol. 22, no. 7, pp. 1667–1671, 2023.

[34] J. H. Kim, B. H. Choi, H. R. Kim, and C. T. Rim, "2-d synthesized magnetic field focusing technology with loop coils distributed in a rectangular formation," *IEEE Transactions on Industrial Electronics*, vol. 66, no. 7, pp. 5558–5566, 2019.

[35] B. H. Choi, J. H. Kim, J. P. Cheon, and C. T. Rim, "Synthesized magnetic field focusing using a current-controlled coil array," *IEEE Magnetics Letters*, vol. 7, pp. 1–4, 2016.

[36] M.-W. Kim, J. H. Kim, Y. Cho, M. Kim, B. H. Choi, K. Lee, J. Kim, G.-H. Cho, and C. T. Rim, "High-resolution synthesized magnetic field focusing for rf barcode applications," *IEEE Transactions on Industrial Electronics*, vol. 65, no. 1, pp. 597–607, 2018.

[37] Q. Zhu, M. Su, Y. Sun, W. Tang, and A. P. Hu, "Field orientation based on current amplitude and phase angle control for wireless power transfer," *IEEE Transactions on Industrial Electronics*, vol. 65, no. 6, pp. 4758–4770, 2018.

[38] N. Kang, Y. Shao, M. Liu, and C. Ma, "Analysis and implementation of 3d magnetic field shaping via a 2d planar transmitting coil array," *IEEE Transactions on Power Electronics*, vol. 37, no. 1, pp. 1172–1184, 2022.

[39] X. Li, B. Sun, J. Xu, S. Pang, and H. Li, "Design and analysis of misalignment insensitive wireless power transfer system based on multitransmitter for constant power," *IEEE Journal of Emerging and Selected Topics in Power Electronics*, vol. 11, no. 4, pp. 4536–4548, 2023.

[40] W. Chen, C. Yu, C. Tu, Z. Lyu, J. Tang, S. Ou, Y. Fu, and Z. Xue, "A survey on hand pose estimation with wearable sensors and computer-vision-based methods," *Sensors*, vol. 20, no. 4, p. 1074, 2020.

[41] A. Erol, G. Bebis, M. Nicolescu, R. D. Boyle, and X. Twombly, "Vision-based hand pose estimation: A review," *Computer Vision and Image Understanding*, vol. 108, no. 1-2, pp. 52–73, 2007.

[42] B.-S. Lin, I. Lee, S.-Y. Yang, Y.-C. Lo, J. Lee, J.-L. Chen *et al.*, "Design of an inertial-sensor-based data glove for hand function evaluation," *Sensors*, vol. 18, no. 5, p. 1545, 2018.

[43] P. Bellitti, A. D. Angelis, M. Dionigi, E. Sardini, M. Serpelloni, A. Moschitta, and P. Carbone, "A wearable and wirelessly powered system for multiple finger tracking," *IEEE Transactions on Instrumentation and Measurement*, vol. 69, no. 5, pp. 2542–2551, 2020.

[44] M. A. Ansari and D. K. Singh, "An approach for human machine interaction using dynamic hand gesture recognition," in *2019 IEEE Conference on Information and Communication Technology*, 2019, pp. 1–6.

[45] D. K. Singh, "Recognizing hand gestures for human computer interaction," in *2015 International Conference on Communications and Signal Processing (ICCSP)*, 2015, pp. 0379–0382.

[46] A. Rashid and O. Hasan, "Wearable technologies for hand joints monitoring for rehabilitation: A survey," *Microelectronics Journal*, vol. 88, pp. 173–183, 2019.

[47] B.-S. Lin, I. Lee, S.-Y. Yang, Y.-C. Lo, J. Lee, J.-L. Chen *et al.*, "Design of an inertial-sensor-based data glove for hand function evaluation," *Sensors*, vol. 18, no. 5, p. 1545, 2018.

[48] P. Bellitti, A. D. Angelis, M. Dionigi, E. Sardini, M. Serpelloni, A. Moschitta, and P. Carbone, "A wearable and wirelessly powered system for multiple finger tracking," *IEEE Transactions on Instrumentation and Measurement*, vol. 69, no. 5, pp. 2542–2551, 2020.

[49] L. Chan, R.-H. Liang, M.-C. Tsai, K.-Y. Cheng, C.-H. Su, M. Y. Chen, W.-H. Cheng, and B.-Y. Chen, "Fingerpad: private and subtle interaction using fingertips," in *Proceedings of the 26th annual ACM symposium on User interface software and technology*, 2013, pp. 255–260.

[50] Y. Ma, Z. Mao, W. Jia, C. Li, J. Yang, and M. Sun, "Magnetic hand tracking for human-computer interface," *IEEE Transactions on Magnetics*, vol. 47, no. 5, pp. 970–973, 2011.

[51] F. S. Parizi, E. Whitmire, and S. Patel, "Auraring: Precise electromagnetic finger tracking," *Proceedings of the ACM on Interactive, Mobile, Wearable and Ubiquitous Technologies*, vol. 3, no. 4, pp. 1–28, 2019.

[52] F. Santoni, A. De Angelis, A. Moschitta, and P. Carbone, "Magik: A hand-tracking magnetic positioning system based on a kinematic model of the hand," *IEEE Transactions on Instrumentation and Measurement*, vol. 70, pp. 1–13, 2021.

[53] Z. Xiao, W. Hu, C. Liu, H. Yu, and C. Li, "Noncontact human–machine interface with planar probing coils in a differential sensing architecture," *IEEE Transactions on Instrumentation and Measurement*, vol. 67, no. 4, pp. 956–964, 2018.

[54] N. Anandan and B. George, "Design and development of a planar linear variable differential transformer for displacement sensing," *IEEE Sensors Journal*, vol. 17, no. 16, pp. 5298–5305, 2017.

[55] N. Anandan, A. Varma Muppala, and B. George, "A flexible, planar-coil-based sensor for through-shaft angle sensing," *IEEE Sensors Journal*, vol. 18, no. 24, pp. 10 217–10 224, 2018.

[56] S. K. Oruganti, S. H. Heo, H. Ma, and F. Bien, "Wireless energy transfer: Touch/proximity/hover sensing for large contoured displays and industrial applications," *IEEE Sensors Journal*, vol. 15, no. 4, pp. 2062–2068, 2015.

[57] A. Sheinker, B. Ginzburg, N. Salomonski, and A. Engel, "Localization of a mobile platform equipped with a rotating magnetic dipole source," *IEEE Transactions on Instrumentation and Measurement*, vol. 68, no. 1, pp. 116–128, Jan 2019.

[58] R. Shirai and M. Hashimoto, "Dc magnetic field based 3d localization with single anchor coil," *IEEE Sensors Journal*, vol. 20, no. 7, pp. 3902–3913, 2020.

[59] H. Dai, C. Hu, S. Su, M. Lin, and S. Song, "Geomagnetic compensation for the rotating of magnetometer array during magnetic tracking," *IEEE Transactions on Instrumentation and Measurement*, vol. 68, no. 9, pp. 3379–3386, 2019.

[60] F. Fereidoony, S. P. M. Nagaraja, J. P. Santos, and Y. E. Wang, "Near-field ranging using dual mode magnetic induction," *IEEE Transactions on Antennas and Propagation*, vol. 68, no. 4, pp. 3145–3153, 2020.

[61] Y. Sui, K. Leslie, and D. Clark, "Multiple-order magnetic gradient tensors for localization of a magnetic dipole," *IEEE Magnetics Letters*, vol. 8, pp. 1–5, 2017.

[62] S. Song, C. Hu, and M. Q. . Meng, "Multiple objects positioning and identification method based on magnetic localization system," *IEEE Transactions on Magnetics*, vol. 52, no. 10, pp. 1–4, Oct 2016.

[63] S. Su, W. Yang, H. Dai, X. Xia, M. Lin, B. Sun, and C. Hu, "Investigation of the relationship between tracking accuracy and tracking distance of a novel magnetic tracking system," *IEEE Sensors Journal*, vol. 17, no. 15, pp. 4928–4937, Aug 2017.

[64] C. D. Natali, M. Beccani, N. Simaan, and P. Valdastri, "Jacobian-based iterative method for magnetic localization in robotic capsule endoscopy," *IEEE Transactions on Robotics*, vol. 32, no. 2, pp. 327–338, April 2016.

[65] K. M. Popek, T. Schmid, and J. J. Abbott, "Six-degree-of-freedom localization of an untethered magnetic capsule using a single rotating magnetic dipole," *IEEE Robotics and Automation Letters*, vol. 2, no. 1, pp. 305–312, Jan 2017.

[66] H. Chao, F. Zhongqing, R. Yupeng, C. Yueyue, L. Haixiang, W. Kai, X. Xiaodong, and B. Jianmeng, "An efficient magnetic localization system for indoor planar mobile robot," in *2015 34th Chinese Control Conference (CCC)*, July 2015, pp. 4899–4904.

[67] T. Nara, S. Suzuki, and S. Ando, "A closed-form formula for magnetic dipole localization by measurement of its magnetic field and spatial gradients," *IEEE Transactions on Magnetics*, vol. 42, no. 10, pp. 3291–3293, Oct 2006.

[68] M. N. Islam and A. J. Fleming, "An algorithm for transmitter optimization in electromagnetic tracking systems," *IEEE Transactions on Magnetics*, vol. 53, no. 8, pp. 1–8, 2017.

[69] Y. Higuchi, T. Nara, and S. Ando, "Complete set of partial differential equations for direct localization of a magnetic dipole," *IEEE Transactions on Magnetics*, vol. 52, no. 5, pp. 1–10, May 2016.

[70] D. D. Arumugam, "Through-the-wall magnetoquasistatic ranging," *IEEE Antennas and Wireless Propagation Letters*, vol. 16, pp. 1439–1442, 2017.

[71] M. Doß, L. Bungert, D. Cichon, H. Brauer, and R. Psiuk, "Localization of passive 3-d coils as an inverse problem: Theoretical analysis and a numerical method," *IEEE Transactions on Magnetics*, vol. 56, no. 4, pp. 1–10, 2020.

[72] H. Dai, S. Song, X. Zeng, S. Su, M. Lin, and M. Q. . Meng, "6-d electromagnetic tracking approach using uniaxial transmitting coil and tri-axial magneto-resistive sensor," *IEEE Sensors Journal*, vol. 18, no. 3, pp. 1178–1186, Feb 2018.

[73] P. G. Seiler, H. Blattmann, S. Kirsch, R. K. Muench, and C. Schilling, "A novel tracking technique for the continuous precise measurement of tumour positions in conformal radiotherapy," *Physics in Medicine and Biology*, vol. 45, no. 9, pp. N103–N110, aug 2000.

[74] D. D. Arumugam, "Decoupled range and orientation sensing in long-range magnetoquasistatic positioning," *IEEE Antennas and Wireless Propagation Letters*, vol. 14, pp. 654–657, 2015.

[75] W. Yang, C. Zhang, H. Dai, C. Hu, and X. Xia, "A novel wireless 5-d electromagnetic tracking system based on nine-channel sinusoidal signals," *IEEE/ASME Transactions on Mechatronics*, vol. 26, no. 1, pp. 246–254, 2021.

[76] A. Plotkin, E. Paperno, G. Vasserman, and R. Segev, "Magnetic tracking of eye motion in small, fast-moving animals," *IEEE Transactions on Magnetics*, vol. 44, no. 11, pp. 4492–4495, Nov 2008.

[77] A. Plotkin, O. Shafrir, E. Paperno, and D. M. Kaplan, "Magnetic eye tracking: A new approach employing a planar transmitter," *IEEE Transactions on Biomedical Engineering*, vol. 57, no. 5, pp. 1209–1215, May 2010.

[78] K. O'Donoghue and P. Cantillon-Murphy, "Planar magnetic shielding for use with electromagnetic tracking systems," *IEEE Transactions on Magnetics*, vol. 51, no. 2, pp. 1–12, Feb 2015.

[79] ——, "Low cost super-nyquist asynchronous demodulation for use in em tracking systems," *IEEE Transactions on Instrumentation and Measurement*, vol. 64, no. 2, pp. 458–466, Feb 2015.

[80] A. Plotkin and E. Paperno, "3-d magnetic tracking of a single subminiature coil with a large 2-d array of uniaxial transmitters," *IEEE Transactions on Magnetics*, vol. 39, no. 5, pp. 3295–3297, Sept 2003.

[81] J. Feng, Q. Li, and F. Lee, "Load Detection and Power Flow Control Algorithm for an Omnidirectional Wireless Power Transfer System," *IEEE Transactions on Industrial Electronics*, pp. 1–1, 2021.

[82] G. Simard, M. Sawan, and D. Massicotte, "High-Speed OQPSK and Efficient Power Transfer Through Inductive Link for Biomedical Implants," *IEEE Transactions on Biomedical Circuits and Systems*, vol. 4, no. 3, pp. 192–200, 2010.

[83] X. Li, J. Hu, Y. Li, H. Wang, M. Liu, and P. Deng, "A Decoupled Power and Data-Parallel Transmission Method With Four-Quadrant Misalignment Tolerance for Wireless Power Transfer Systems," *IEEE Transactions on Power Electronics*, vol. 34, no. 12, pp. 11 531–11 535, 2019.

[84] Z. Zhang, H. Pang, C. H. T. Lee, X. Xu, X. Wei, and J. Wang, "Comparative Analysis and Optimization of Dynamic Charging Coils for Roadway-Powered Electric Vehicles," *IEEE Transactions on Magnetics*, vol. 53, no. 11, pp. 1–6, 2017.

[85] K. Kim, H.-J. Kim, D.-W. Seo, and J.-W. Choi, "Magnetically Decoupled Modular Coil Array for Dynamic Wireless Power Transfer With Magnetic Beamforming," *IEEE Access*, vol. 10, pp. 42 121–42 140, 2022.

[86] M. Machnoor, P. Kosta, M. Monge, and G. Lazzi, "Rectifier Design for Highly Loaded Inductive Wireless Power Transfer Systems for Biomedical Applications," *IEEE Journal of Electromagnetics, RF and Microwaves in Medicine and Biology*, vol. 6, no. 4, pp. 574–579, 2022.

[87] T. P. G. v. Nunen, R. M. C. Mestrom, and H. J. Visser, "Wireless Power Transfer to Biomedical Implants Using a Class-E Inverter and a Class-DE Rectifier," *IEEE Journal of Electromagnetics, RF and Microwaves in Medicine and Biology*, vol. 7, no. 3, pp. 202–209, 2023.

[88] D. K. Biswas, N. Saha, and I. Mahbub, "Wirelessly Powered 3-D Printed Headstage Based Neural Stimulation System for Optogenetic Neuromodulation Application," *IEEE Journal of Electromagnetics, RF and Microwaves in Medicine and Biology*, vol. 7, no. 1, pp. 24–31, 2023.

[89] D. K. Biswas, N. T. Tasneem, and I. Mahbub, "Effects of Coaxial-Lateral and Coaxial-Angular Displacements on Link Efficiency of a Wirelessly Powered Optogenetic Implant: Design, Modeling, and Experimental Validation," *IEEE Journal of Electromagnetics, RF and Microwaves in Medicine and Biology*, vol. 3, no. 4, pp. 269–275, 2019.

[90] J. P. W. Chow, N. Chen, H. S. H. Chung, and L. L. H. Chan, "Misalignment Tolerable Coil Structure for Biomedical Applications with Wireless Power Transfer," in *2013 35th Annual International Conference of the IEEE Engineering in Medicine and Biology Society (EMBC)*, 2013, pp. 775–778.

[91] X. Tian, K. T. Chau, W. Liu, and C. H. T. Lee, "Analysis of Multi-Coil Omnidirectional Energy Harvester," *IEEE Transactions on Magnetics*, vol. 57, no. 2, pp. 1–6, 2021.

[92] Z. Zhang and K. T. Chau, "Homogeneous Wireless Power Transfer for Move-and-Charge," *IEEE Transactions on Power Electronics*, vol. 30, no. 11, pp. 6213–6220, 2015.

[93] L. Qian, K. Qian, Y. Shi, H. Xia, J. Wang, and Y. Xia, "TSV Based Orthogonal Coils With High Misalignment Tolerance for Inductive Power Transfer in Biomedical Implants," *IEEE Transactions on Circuits and Systems II: Express Briefs*, vol. 68, no. 6, pp. 1832–1836, 2021.

[94] J. P. W. Chow, N. Chen, H. S. H. Chung, and L. L. H. Chan, "An Investigation Into the Use of Orthogonal Winding in Loosely Coupled Link for Improving Power Transfer Efficiency Under Coil Misalignment," *IEEE Transactions on Power Electronics*, vol. 30, no. 10, pp. 5632–5649, 2015.

[95] S. R. Khan, S. K. Pavuluri, G. Cummins, and M. P. Y. Desmulliez, "Miniaturized 3-D Cross-Type Receiver for Wirelessly Powered Capsule Endoscopy," *IEEE Transactions on Microwave Theory and Techniques*, vol. 67, no. 5, pp. 1985–1993, 2019.

[96] A. Basir, I. A. Shah, and H. Yoo, "Sphere-Shaped Implantable Receiver Coil for Misalignment-Resilient Wireless Power Transfer Systems for Implantable Devices," *IEEE Transactions on Antennas and Propagation*, pp. 1–1, 2022.

[97] M. N. Sadiku, R. Bansal, C. Christopoulos, K. R. Demarest, A. Weisshaar, N. N. Rao, M. Horenstein, M. Popovic, Z. Popovic, M. Kolbehdari *et al.*, *Fundamentals of engineering electromagnetics*. CRC press, 2018.

[98] Z. Luo and X. Wei, "Analysis of Square and Circular Planar Spiral Coils in Wireless Power Transfer System for Electric Vehicles," *IEEE Transactions on Industrial Electronics*, vol. 65, no. 1, pp. 331–341, 2018.

[99] D. M. Pozar, *Microwave engineering: theory and techniques.* John wiley & sons, 2021.

[100] A. Sharma, I. J. G. Zuazola, A. Gupta, A. Perallos, and J. C. Batchelor, "Non-Uniformly Distributed-Turns Coil Antenna for Enhanced H-Field in HF-RFID," *IEEE Transactions on Antennas and Propagation*, vol. 61, no. 10, pp. 4900–4907, 2013.

[101] Z. Luo and X. Wei, "Analysis of Square and Circular Planar Spiral Coils in Wireless Power Transfer System for Electric Vehicles," *IEEE Transactions on Industrial Electronics*, vol. 65, no. 1, pp. 331–341, 2018.

[102] U.-M. Jow and M. Ghovanloo, "Design and Optimization of Printed Spiral Coils for Efficient Inductive Power Transmission," in *2007 14th IEEE International Conference on Electronics, Circuits and Systems*, 2007, pp. 70–73.

[103] ——, "Modeling and Optimization of Printed Spiral Coils in Air, Saline, and Muscle Tissue Environments," *IEEE Transactions on Biomedical Circuits and Systems*, vol. 3, no. 5, pp. 339–347, 2009.

[104] Y.-L. Lyu, F.-Y. Meng, G.-H. Yang, B.-J. Che, Q. Wu, L. Sun, D. Erni, and J. L.-W. Li, "A Method of Using Nonidentical Resonant Coils for Frequency Splitting Elimination in Wireless Power Transfer," *IEEE Transactions on Power Electronics*, vol. 30, no. 11, pp. 6097–6107, 2015.

[105] C. A. Balanis, *Antenna theory: analysis and design.* John wiley & sons, 2016.

[106] A. Bharadwaj, A. Sharma, and C. C. Reddy, "An Unconventional Measurement Technique to Estimate Power Transfer Efficiency in Series–Series Resonant WPT System Using S-Parameters," *IEEE Trans. Instrum. Measur.*, vol. 71, pp. 1–9, 2022.

[107] S. Hosur, Z. Kashani, S. K. Karan, S. Priya, and M. Kiani, "MagSonic: Hybrid Magnetic-Ultrasonic Wireless Interrogation of Millimeter-Scale Biomedical Implants With Magnetoelectric Transducer," *IEEE Trans. Biomed. Circu. Syste.*, vol. 18, no. 2, pp. 383–395, 2024.

[108] I. C. on Non-Ionizing Radiation Protection *et al.*, "ICNIRP Statement on the "Guidelines for Limiting Exposure to Time-varying Electric, Magnetic, and Electromagnetic Fields (up to 300 GHz)"," *Health physics*, vol. 97, no. 3, pp. 257–258, 2009.

[109] J. Robinson and Y. Rahmat-Samii, "Particle swarm optimization in electromagnetics," *IEEE Transactions on Antennas and Propagation*, vol. 52, no. 2, pp. 397–407, 2004.

[110] U. Anwar, O. A. Ajijola, K. Shivkumar, and D. Marković, "Towards a Leadless Wirelessly Controlled Intravenous Cardiac Pacemaker," *IEEE Transactions on Biomedical Engineering*, vol. 69, no. 10, pp. 3074–3086, 2022.